Chapter 3. Beamline Engineering

3.1 Front-End Design

3.1.1 Front-End Overview

3.1.1.1 Beamline floor plan & installation overview

The front-ends are located tangentially to the storage ring, and most of their components are installed inside the storage ring tunnel. Their primary function is to provide an ultra-high vacuum (UHV) connection between the storage ring and the beamline located outside the shielding wall. Since all synchrotron radiation extracted from the storage ring must pass through the front-end before reaching the experimental station, the front-end serves as the interface between the storage ring and the Photon Transfer Line (PTL).

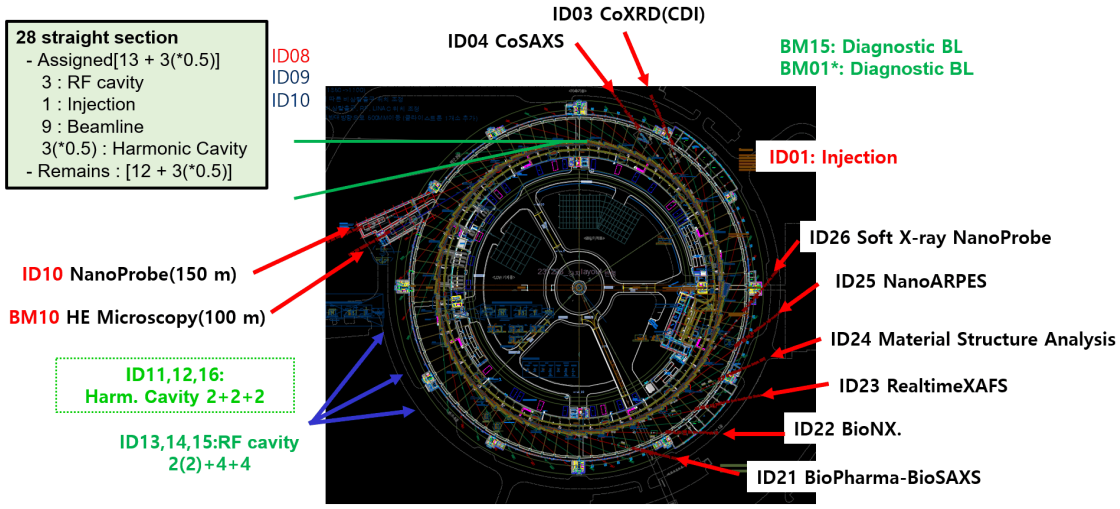
In the Korea Light Source (KLS) Phase I, the storage ring consists of a total of 28 straight sections. Among them, synchrotron radiation can be extracted from 21 sections, excluding three RF cavity sections, one injection section, and three harmonic cavity sections. Each sector is equipped with one insertion device (ID) beam port and one bending magnet (BM) beam port. <Figure 3.1.1.1> shows the locations of the ten beamlines planned for Phase I, while a typical front-end layout for one sector is illustrated in <Figure 3.1.1.2>.

Thermal simulations indicate that most of the synchrotron radiation heat load is absorbed within the front-end. In addition, potential beam missteering scenarios were considered during the thermal analysis to design an efficient cooling channel capable of safely removing the deposited heat [1].

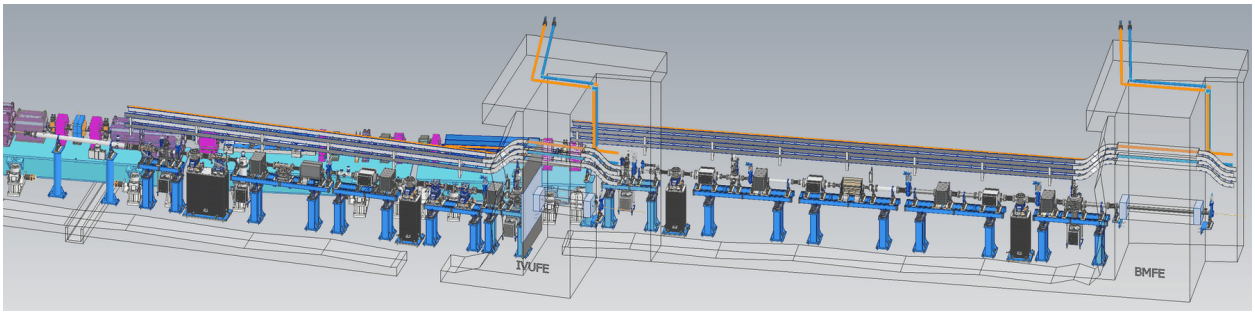
To deliver the central cone from the storage ring to the PTL, the front-end must precisely control the beam profile. When required, it must also be capable of completely blocking both the photon beam and synchrotron radiation while maintaining the UHV environment.

The KLS Phase I requires three types of front-ends:

- IVU Front-End (IVUFE) for an in-vacuum undulator of period length (16, 20, 22, and 24 mm).



<Figure 3.1.1.1> Beamline locations in Phase I.



<Figure 3.1.1.2> Layout of ID and BM front-end.

- EPU Front-End (EPUFE) for an elliptically polarizing undulator of period length (78 and 98 mm).
- Bending Magnet Front-End (BMFE) for a bending magnet source.

The specifications and principal characteristics of the undulators to be used for each beamline are summarized in <Table 3.1.1.1>.

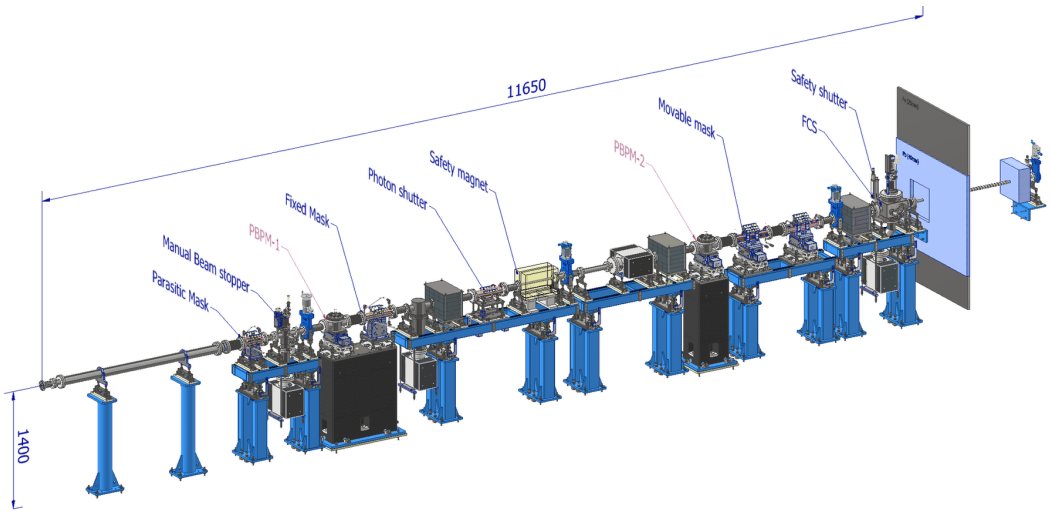
<Table 3.1.1.1> Photon beam parameters of each undulator type.

Type of undulator	IVU16	IVU20	IVU22	IVU24	EPU78	EPU98	BM
Beamline [#]	ID24	ID04 ID21 ID22	ID03	ID10 ID23	ID26	ID25	BM10
Period length [mm]	16	20	22	24	78	98	–
Periods	185	148	134	123	44	36	
Length [m]	3.0	3.0	3.0	3.0	3.62	3.6316	
$K_{\max}$ value	1.172	1.904	2.315	2.745	KV6.948 KC4.390 KH5.652	KV9.238 KC6.070 KH8.043	1.811
$B_{\max}$ [T]	0.785	1.021	1.127	1.225	BV0.954 BC0.602 BH0.776	BV1.010 BC0.663 BH0.879	2
$\mathrm{Gap}_{\min}$ [mm]	5	5	5	5	15	15	–
$\varepsilon_{1\mathrm{st}}$ [eV]	5628.6	2696.1	1876.6	1327.8	77.49[V] 96.0[C] 114.84[H]	35.5[V] 40.9[C] 46.49[H]	
Total Power [kW]	7.38	12.49	15.16	17.93	12.65[V] 10.08[C] 8.37[H]	13.75[V] 11.87[C] 10.44[H]	0.65
Max. Power density [kW/mrad^2]	154.3	164.2	165.2	165.4	46.5[V]	38.02[V]	0.216 kW/mrad (linear)
Central radiation (1σ) [mrad]	$\Sigma_{x'}$ 0.00679 $\Sigma_{y'}$ 0.00626	$\Sigma_{x'}$ 0.00930 $\Sigma_{y'}$ 0.00892	$\Sigma_{x'}$ 0.01100 $\Sigma_{y'}$ 0.01068	$\Sigma_{x'}$ 0.01293 $\Sigma_{y'}$ 0.01265	$\Sigma_{x'}$ 0.04837[V] $\Sigma_{y'}$ 0.04830[V] $\Sigma_{x'}$ 0.04348[C] $\Sigma_{y'}$ 0.04340[C] $\Sigma_{x'}$ 0.03977[H] $\Sigma_{y'}$ 0.03969[H]	$\Sigma_{x'}$ 0.07246[V] $\Sigma_{y'}$ 0.07241[V] $\Sigma_{x'}$ 0.06745[C] $\Sigma_{y'}$ 0.06740[C] $\Sigma_{x'}$ 0.06333[H] $\Sigma_{y'}$ 0.06327[H]	
Natural radiation [mrad]	$\Sigma_{x'} = 0.279$ $\Sigma_{y'} = 0.128$	$\Sigma_{x'} = 0.279$ $\Sigma_{y'} = 0.128$	$\Sigma_{x'} = 0.279$ $\Sigma_{y'} = 0.128$	$\Sigma_{x'} = 0.279$ $\Sigma_{y'} = 0.128$	$\Sigma_{x'} = 0.279$ $\Sigma_{y'} = 0.128$	$\Sigma_{x'} = 0.279$ $\Sigma_{y'} = 0.128$	$\pm$1.5[H] $\pm$0.3[V]
Type of Front-End	IVUFE	IVUFE	IVUFE	IVUFE	EPUFE	EPUFE	BMFE

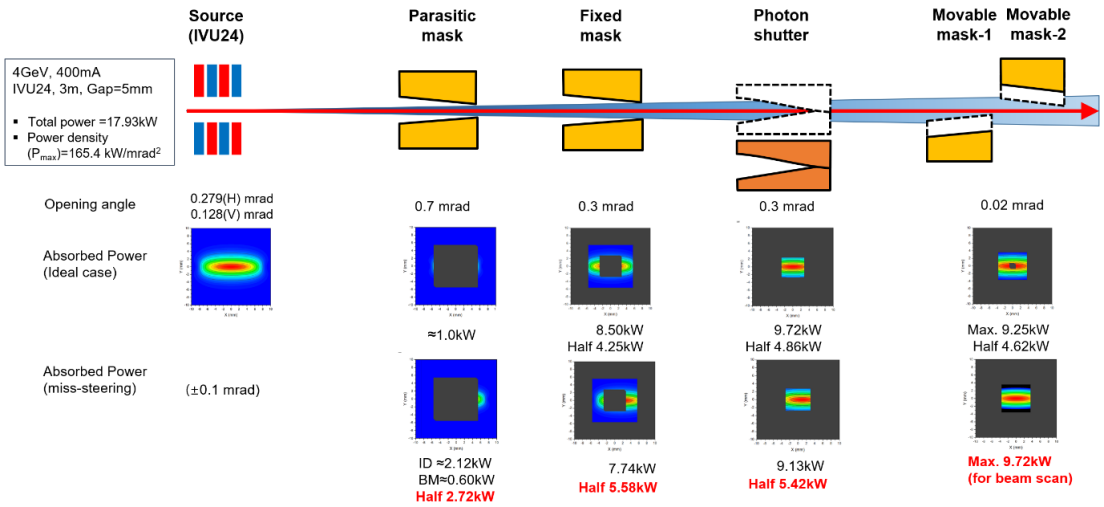
※ For EPU98, 36 is the rounded display of the final specified 35.75 periods; its length entry is the final array length of 3.6316 m. Other length entries are device lengths. The retained source calculation uses 36 regular periods and a regular magnet length of 3.528 m.
※ The divergence values calculated above refer to the first harmonic of the central cone.
※ For the bending magnet the quoted $\pm$1.5 mrad (H) $\times$ $\pm$0.3 mrad (V) is the opening aperture at the exit of the storage-ring vacuum chamber, not a natural emission angle; the horizontal fan of a dipole is continuous.
※ Orbit interlock condition of electron Beam Position Monitors (e-BPMs) for the ID is set to $\pm$0.1 mrad angle and $\pm$400 μm in position offset.

3.1.1.2 In-Vacuum Undulator Front-End

The IVU front-end was designed based on the IVU24, which produces the maximum heat load among the insertion devices [2]. The design heat-load condition corresponds to the storage ring operating at an electron beam energy of 4 GeV with a stored beam current of 400 mA and an undulator gap of 5 mm. The corresponding heat-load parameters are summarized in <Table 3.1.1.1>. Under these operating conditions, the major front-end components were designed to withstand a peak power density of 165.4 kW/mrad^2 and a total power of 17.93 kW. As shown in <Figure 3.1.1.3> and <Figure 3.1.1.4>, each major component is designed to absorb the incident heat load according to its distance from the source and the beam divergence [1].



<Figure 3.1.1.3> Detailed layout of IVU front-end.



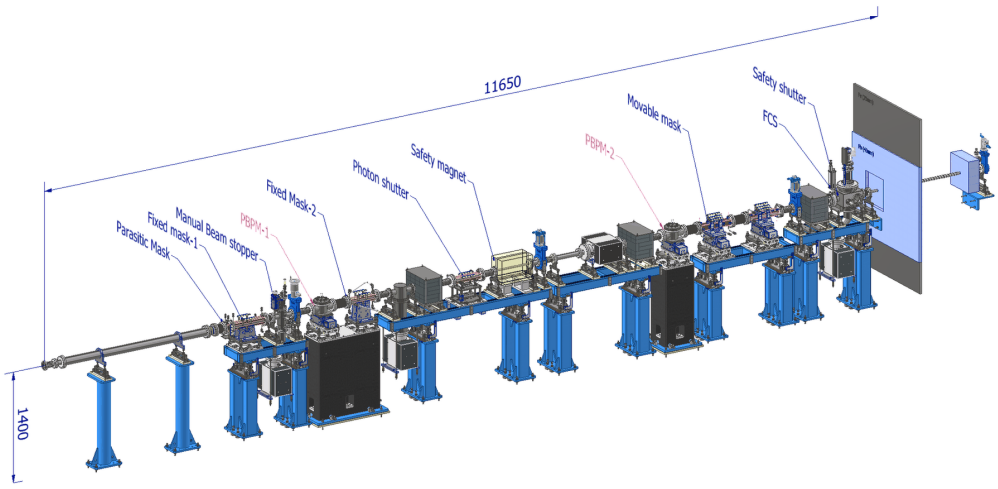
<Figure 3.1.1.4> Each positional heat-load on the IVUFE components.

3.1.1.3 Elliptically Polarizing Undulator Front-End

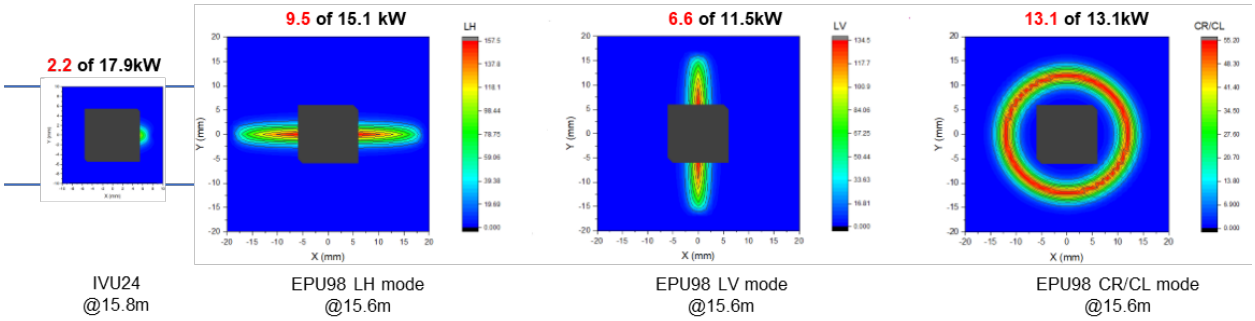
The EPU front-end has a configuration that is largely identical to that of the IVU front-end. However, the circular polarization mode must also be considered in the design. Under circular mode operation, more than 99% of the total heat load is concentrated on the parasitic mask, making it impractical for the parasitic mask alone to withstand the thermal load (see <Figure 3.1.1.6>). Therefore, an additional Extra Fixed Mask was incorporated into the front-end design to distribute and absorb the heat load according to the characteristics of the EPU radiation [1]. Since the heat loads under the horizontal and vertical polarization modes do not exceed the IVU design conditions, the same front-end configuration as the IVU type was adopted (see <Figure 3.1.1.5>).

The installation length of the ID front-end at Port A is approximately 11.65 m. Precision components are supported on granite bases to ensure mechanical stability, while the remaining components are mounted on adjustable girders and support structures. The principal components of the front-end include the Photon Beam Position Monitor (PBPM), Fixed Mask, Photon Shutter, and Movable Mask:

- The PBPM is a non-intercepting diagnostic device that precisely measures the position and intensity of the photon beam.
- The primary function of the Fixed Mask is to absorb unwanted radiation surrounding the central cone.
- The Photon Shutter completely blocks the main photon beam when operated



<Figure 3.1.1.5> Detailed layout of EPU front-end.



<Figure 3.1.1.6> Circular mode heat-load on the “Extra Fixed Mask” of EPU front-end.

in conjunction with the Safety Shutter.

- A pair of Movable Masks defines the central cone to an aperture of approximately 1 mm × 1 mm before the beam is delivered to the PTL [2].

The remaining front-end components and their functions are summarized in <Table 3.1.1.2>.

<Table 3.1.1.2> Devices and functions for ID front-ends.

Components	Distance from source [mm]	Function
Parasitic Mask	15,840	Unnecessary white beam absorption
(Extra Fixed Mask)	15,900	Absorption for full beam in Circular mode (applies to EPUFE only)
Manual beam stopper	16,195	Bending magnet beam absorption for vacuum accident or maintenance, gate valve protection
PBPM-1	16,880	Photon beam position monitoring device (to ensure beam stability and detect any drift or misalignment)
Fixed Mask	17,355	Unnecessary beam absorption outside the central cone
Photon Shutter	18,800	Fully block the main beam (interlock with Safety Shutter)
Safety magnet	19,480	Clearing magnet for electron dumping
PBPM-2	21,785	
Movable Mask	22,927	The central cone transport to the PTL area (photon beam shaping to 1×1 mm)
Fast Closing Shutter		Shutter that closes quickly in the event of a vacuum accident
Safety Shutter	24,145	Fully block the radiations (interlock with Photon Shutter)

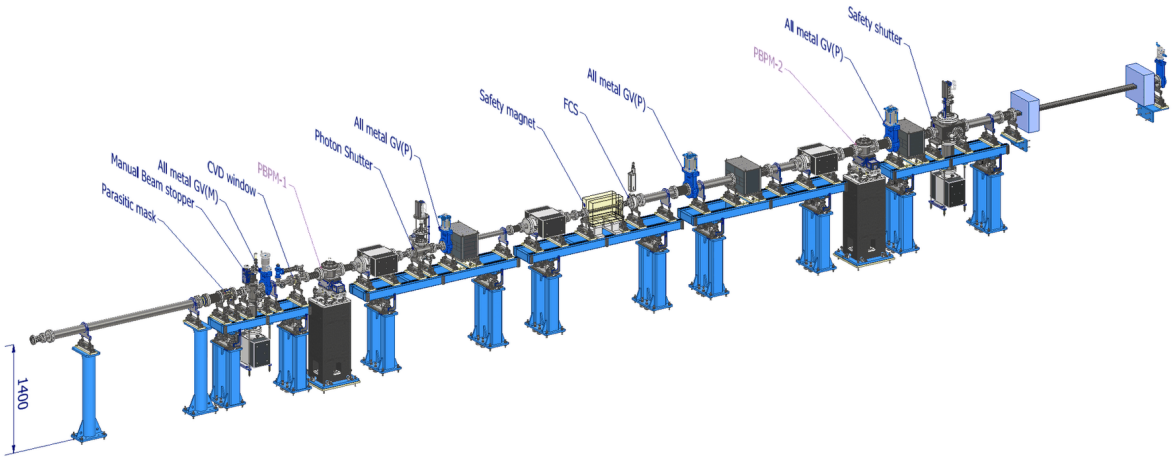
3.1.1.4 Front-End for BM

Although the BM source generates a relatively high total power, most of the synchrotron radiation is absorbed within the storage ring. Only the remaining portion of the bending magnet radiation, passing through the limited aperture at the exit of the storage ring vacuum chamber, enters the BM front-end. Considering the linear power density of 0.216 kW/mrad, as summarized in <Table 3.1.1.3>, the heat load on each BM front-end component is estimated to be less than 500 W [1]. Therefore, the beam size is defined solely by the Parasitic Mask to satisfy the beamline requirements.

The BM beamline is a long beamline approximately 100 m in length, extending to the end-station, and is based on the white beam generated from the center bend of the storage ring and the Longitudinal Gradient Bending Magnet (LGBM). In the front-end section, most of the beam passes through without interception, while in the PTL section, the beam shape is defined using a white beam slit.

<Table 3.1.1.3> Heat load of BM source.

Type of Front-End	BMFE
Total radiated power (storage ring)	1,358 kW
Power through the ±1.5 mrad opening aperture	648 W
Partial power in Front-End area	468 W
Linear power density	0.216 kW/mrad
White beam divergence	Horizontal ±1.5 mrad Vertical ±0.3 mrad



<Figure 3.1.1.7> Detailed layout of BM front-end.

The total installation length of the BM front-end at Port B is approximately 14.15 m (see <Figure 3.1.1.7>). Precision components are supported on granite bases to ensure mechanical stability, while the remaining components are mounted on adjustable girders and support structures. The principal components of the BM front-end include the Photon Beam Position Monitor (PBPM), Parasitic Mask, and Photon Shutter. The functions of the major BM front-end components are summarized as follows:

- The PBPM is a non-intercepting diagnostic device that precisely measures the position and intensity of the photon beam.
- The Parasitic Mask defines the bending magnet beam aperture while absorbing unwanted synchrotron radiation outside the required beam acceptance.
- The Photon Shutter completely blocks the main photon beam when operated in conjunction with the Safety Shutter.

The overall configuration of the BM front-end and the functions of its components are summarized in <Table 3.1.1.4>.

<Table 3.1.1.4> Devices and functions for BM front-end.

Components	Distance from source	Function
Parasitic Mask	11,690	Defining white beam divergence
Manual beam stopper	12,160	Bending magnet beam absorption for vacuum accident or maintenance, gate valve protection
CVD window	12,745	Isolating the vacuum (observing the shape of the white beam)
PBPM-1	13,260	Photon beam position monitoring device (to ensure beam stability and detect any drift or misalignment)
Photon Shutter	14,572	Fully block the main beam (interlock with Safety Shutter)
Safety magnet	17,170	Clearing magnet for electron dumping
Fast Closing Shutter		Shutter that closes quickly in the event of a vacuum accident
PBPM-2	20,920	
Safety Shutter	22,120	Fully block the radiations (interlock with Photon Shutter)

3.1.2 Design Requirements & Criteria

3.1.2.1 Basic requirements

The front-end of the beamline must be designed, manufactured, and installed to sufficiently satisfy basic requirements [1].

The vacuum level of the front-end must be equal to or better than that of the storage ring, and a device capable of quickly isolating the vacuum of the storage ring and beamline must be installed to protect against vacuum accidents in the storage ring or beamline. An interlock system must be installed for rapid isolation. The vacuum level of the front-end is recommended to be 5×10^{-9} Torr during storage ring operation and 5×10^{-10} Torr when the storage ring is not in operation. To satisfy this vacuum level, ion pumps of sufficient capacity must be installed appropriately in the front-end.

Generally, the rupture pressure wave that occurs due to a vacuum accident is classified as a shock wave, and the speed of the shock wave for air is known to be about 1,000 m/s and for helium about 2,000 m/s. The front-end must detect this shock wave pressure and delay it using the Fast Closing Shutter (FCS) before it reaches the storage ring. At the same time, the gate valve between the storage ring and the beamline must be closed to protect the vacuum in the storage ring from shock waves. When the FCS closes due to a vacuum accident and then the photon shutter closes, the radiation can heat the blade of the FCS for several seconds. Considering this case, the material of the shutter blade must be carefully selected.

The front-end must minimize the range of bremsstrahlung radiation emitted from the storage ring during beamline experiments. In addition, when the safety shutter is activated, bremsstrahlung radiation must be completely shielded within the shielding wall, thereby protecting beamline users from bremsstrahlung radiation and providing a biologically safe experimental environment.

The vacuum components directly exposed to synchrotron radiation must be cooled using Low Conductivity Water (LCW) to prevent vacuum deterioration and damage. In addition, the glancing angle must be used to reduce the heat load intensity while supplying sufficient low-conductivity water for cooling. LCW usually has a purity (resistivity) of 1 MΩ·cm or more and has high temperature precision, so it is used as a coolant in devices exposed to synchrotron radiation.

The operating status of the front-end must be configured so that it can be detected by various types of sensors. Several conditions, such as UHV condition,

shock wave detection, air pressure monitoring, LCW flow condition, and the positions of various switching devices, should be closely monitored.

Since the bremsstrahlung radiation value is very high inside the storage ring, it causes hardening of materials such as rubber and plastic. Therefore, seals or hoses made of elastomer or Buna-N must not be used, and metal seals and metal cooling pipes must be used; the permitted and prohibited UHV materials, including the restricted polymer grades and the metal-gasket flange requirement, are listed in the front-end vacuum analysis report [3].

All vacuum components of the front-end are for UHV. Therefore, electropolishing and vacuum chemical cleaning must be performed, and the metal joining method must be limited to TIG welding, vacuum brazing, electron beam welding, etc. In particular, when connecting the cooling water line in a vacuum, the connection part must be designed so that it is not directly exposed to the vacuum when the cooling water leaks. These fabrication, cleaning and joining requirements, together with the leak-rate, residual-gas and outgassing criteria used to accept each finished component, follow the beamline UHV equipment fabrication standard issued with the front-end vacuum analysis [3].

3.1.2.2 Material properties

The key material properties of copper alloys used for effective heat load cooling are summarized in <Table 3.1.2.1>. In general, oxygen-free high-conductivity (OFHC) copper, GlidCop, and CuCrZr are widely used in international accelerator facilities, with CuCrZr emerging as the preferred choice in recent years [3].

Although GlidCop and CuCrZr exhibit similar material properties, CuCrZr offers several advantages in terms of cost, delivery time, and material loss, making it more favorable in practical applications. As a result, CuCrZr was prioritized over GlidCop in the thermal analysis wherever applicable, taking productivity into consideration as well [1].

<Table 3.1.2.1> Comparison of copper alloys material properties.

	OFHC (C1010)	GlidCop (AL-15)	CuCrZr (C18150)
Young's modulus [GPa]	117	130	136
Thermal Conductivity [W/m·K]	383	365	330
Melting point [°C]	1,083	1,083	1,081
Tensile strength [MPa]	254	483	550
Yield strength [MPa]	78	455	500
Coefficient of thermal expansion [μm/m/°C]	17 (20–300 °C)	16.6 (20–150 °C)	18.6 (20–300 °C)
Density [g/cm^3]	8.9	8.9	8.94
Softening temperature [°C]	150 (150–200)	300 (300–400)	300 (250–400)
Allowable stress [MPa]	100	340	400

※ The allowable stress is applied between 50–70% based on yield strength.
※ The softening temperature is applied at about 50% of the melting temperature.

3.1.2.3 Cooling design

The thermal load applied to the beamline components was evaluated considering the missteering case, in which the beam may deviate up to 0.1 mrad from the nominal trajectory [1]. Under this condition, both the average (avg.) and maximum (max.) heat loads were calculated and applied to the thermal analysis. The design criteria for the heat-absorbing components are summarized as follows.

The thermal analysis was performed using both average and maximum beam power densities. The surface temperature of the heat absorber must remain below the softening temperature of the material (typically $<$ 250–300 °C). For the cooling water velocity, the following design guidelines were considered:

- According to ISO and Korean Industrial Standards (KS) design standards, the cooling water velocity is recommended to be up to $\sim$3 m/s in order to prevent erosion, vibration, and fatigue of the cooling channels.
- In plant engineering practices (ASME) and nuclear design codes (RCC-MR), a more conservative velocity of $\sim$2 m/s is typically recommended.

The wall temperature of the cooling channel must remain below the saturation temperature of water at the operating pressure (e.g., $T_{\mathrm{sat}} \approx 150$ °C at 5 bar). The critical heat flux (CHF) was evaluated to ensure safe operation, and an appropriate

beam incidence angle was selected to maintain sufficient margin from the CHF limit.

3.1.2.4 Radiation safety & shielding

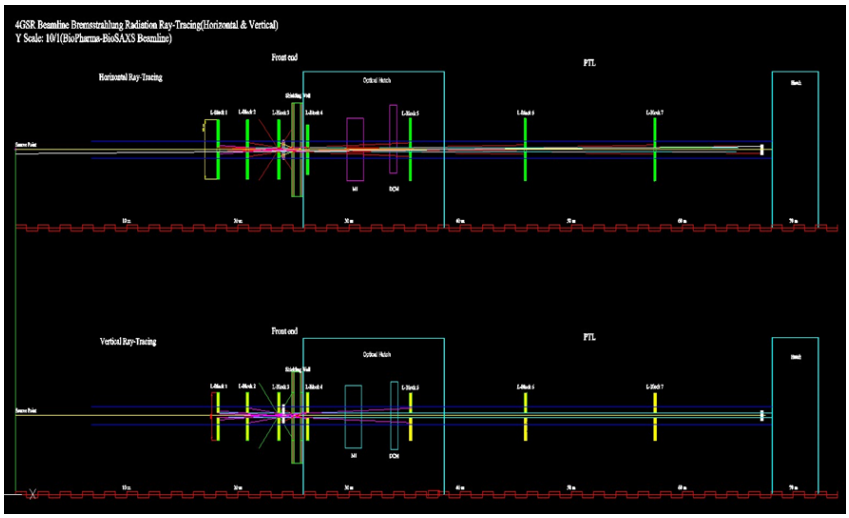
The front-end has a Safety Shutter (or bremsstrahlung shutter) and a lead collimator as devices to protect against radiation. The Safety Shutter and lead collimator used to prevent radiation leakage must take the following into consideration. In the injection mode, the shielding calculation must reflect radiation generated by the loss of electrons at multiple injected points within the storage ring tunnel, radiation generated by the loss of the entire electron beam at one point, gas bremsstrahlung, and scattered radiation from secondary sources. In the stored mode, radiation generated by the complete loss of the electron beam at any point, gas bremsstrahlung, and radiation generated by the gradual loss of electrons in orbit must be taken into account.

The requirements for Safety Shutter and shields to protect against the above-mentioned radiation and the guidelines for their design can be summarized as follows:

- The Safety Shutter must be closed during the injection time and when the beamline is not in use. The lead collimator and collimating spool must be constructed in a way that can minimize radiation penetration.
- In order to have enough space for the beamline equipment, the structure must be as compact as possible.
- A shielding thickness equivalent to 200 mm lead should be maintained in any direction within the storage ring tunnel.
- The Safety Shutter should be manufactured to a size that can block the photon beam and should be made of 200 mm thick tungsten.
- The Safety Shutter should be installed as close to the shielding wall as possible to minimize the size of the leakage angle.

The Safety Shutter is usually installed at the front-end, i.e., in front of the shielding wall. This is to maximize the shielding of the bremsstrahlung radiation, and in order to block the bremsstrahlung radiation generated from the storage ring into the vacuum spool, appropriate lead blocks should be installed in the front-end and the optical hutch. At the same time, the aperture size of the collimating

spool should be minimized to ensure the safety of users in the experimental hall. The aperture size of the collimating spool should be determined by sufficiently considering the effect of ground motion, and the bremsstrahlung ray tracing (horizontal, vertical) in <Figure 3.1.2.1> shows the quantity and location of lead blocks installed in the IVU beamline [1].

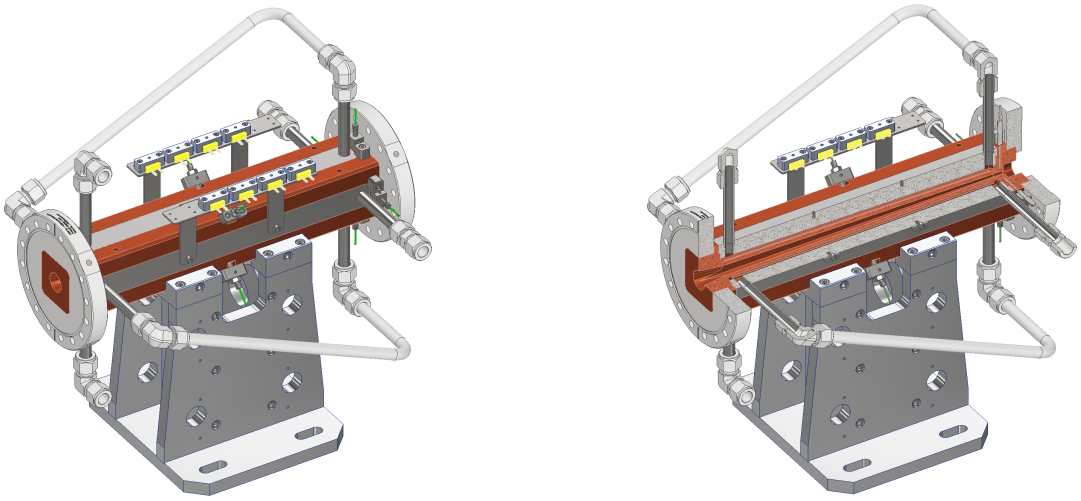


<Figure 3.1.2.1> Bremsstrahlung ray tracing of IVU beamline.

3.1.3 Front-End Components

3.1.3.1 Fixed Mask

The Fixed Mask directly absorbs the primary high heat load radiation from the front-end and is constructed of CuCrZr. Its role is to block unnecessary radiation and prevent damage to major components located downstream of the beam. A cooling water pipe with an outer diameter of 1/2 inch was applied, and a glancing angle was applied to reduce the heat load per unit area [1]. A K-type thermocouple was installed near the opening to detect whether the mask is overheated. <Figure 3.1.3.1> shows the assembly drawing and internal shape of the Fixed Mask, and its detailed specifications are summarized in <Table 3.1.3.1>.



(a) (b)

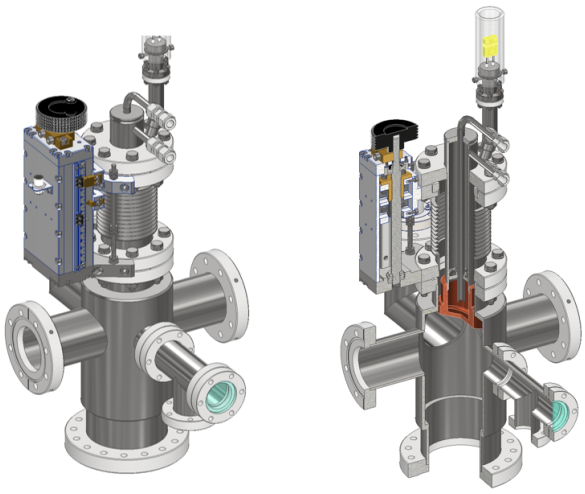
<Figure 3.1.3.1> Fixed Mask assembly: (a) outside view, (b) inside view.

<Table 3.1.3.1> Fixed Mask specification.

	IVU, EPU
Base material	CuCrZr
Incidence angle [°]	0.8
Beam defining aperture (Inlet / Outlet) [mrad]	0.7 / 0.3
Exit aperture size [mm]	5.21(H) × 5.21(V)
Cooling pipe [inch]	1/2
Cooling channel [ea]	2, direct cooling
Flange size [inch]	CF 6
Thermocouple	K-type, 8 ea (2-lines)

3.1.3.2 Manual Beam Stopper

The manual beam stopper is designed primarily to block only the BM beam and must be operated while the ID is fully opened. OFHC is used as the material and the incident angle is 20° to reduce the heat load. <Figure 3.1.3.2> shows the internal shape and assembly layout of the manual beam stopper, and its detailed specifications are summarized in <Table 3.1.3.2>.



<Figure 3.1.3.2> Manual beam stopper assembly.

<Table 3.1.3.2> Manual beam stopper specification.

	IVU	EPU	BM
From the source [mm]	16,195	16,195	12,160
Incidence angle [°]	20	20	20
Beam size [mm]	11.34(H) × 4.86(V)	16.20(H) × 4.86(V)	24.27(H) × 3.64(V)
Driving	Manual handle, with ball screw	Manual handle, with ball screw	Manual handle, with ball screw
Cooling pipe [inch]	3/8	3/8	3/8
Cooling channel [ea]	1, direct cooling type	1, direct cooling type	1, direct cooling type
Flange size [inch]	CF 4.5	CF 4.5	CF 4.5
Base material	OFHC	OFHC	OFHC
Thermocouple	K-type, feedthrough (1 pair)	K-type, feedthrough (1 pair)	K-type, feedthrough (1 pair)
Vacuum	UHV compatible, with welded bellows, window (2.75 inch)	UHV compatible, with welded bellows, window (2.75 inch)	UHV compatible, with welded bellows, window (2.75 inch)

3.1.3.3 Photon Shutter

The Photon Shutter is a critical front-end component designed to completely intercept the photon beam, thereby protecting downstream components during vacuum accidents and maintenance periods. The aperture uses CuCrZr material, and the incidence angle is designed to be as small as possible to lower the power density of the beam and minimize the heat load [1].

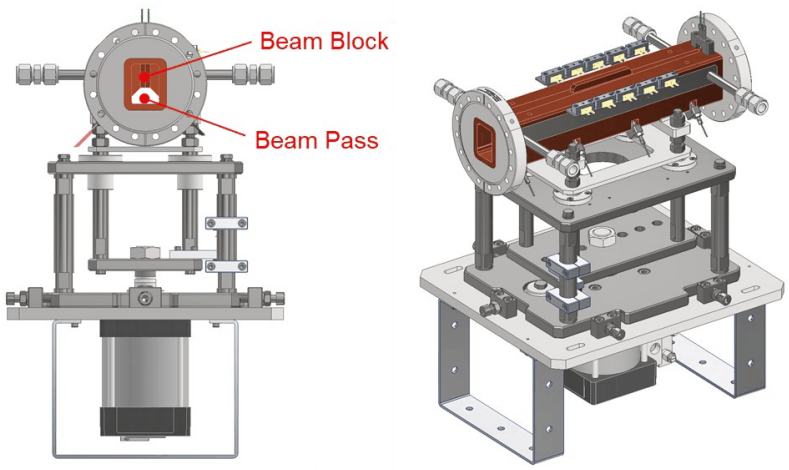
The Photon Shutter is driven by a vertically oriented pneumatic cylinder. Under routine operation, the typical opening and closing time is approximately 2 seconds. However, in the event of a vacuum accident, a fast-closing mode is required to rapidly block the photon beam simultaneously with the closure of the FCS.

To enable this function, an emergency exhaust valve is installed to rapidly vent the compressed air from the pneumatic cylinder. The valve is designed to operate in response to the FCS interlock signal. With this fast-closing mode, the Photon Shutter closing time is expected to be reduced to less than 100 ms.

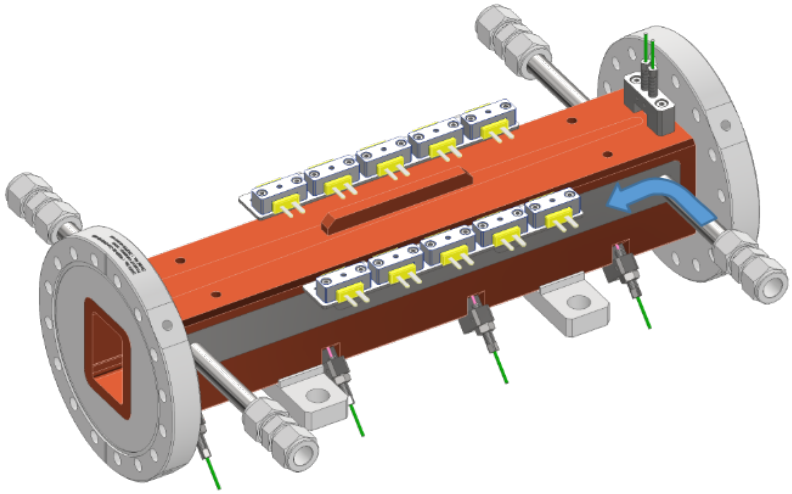
For the IVU-type front-end, it is essential to verify the safety and structural integrity of the region where the photon beam is completely intercepted. <Fig-

ure 3.1.3.3> and <Figure 3.1.3.4> show the assembly drawing of the Photon Shutter for the IVU and EPU front-ends, while <Figure 3.1.3.5> presents the assembly drawing of the Photon Shutter for the BM front-end. The corresponding specifications are summarized in <Table 3.1.3.3> and <Table 3.1.3.4>, respectively.

(a) In-Vacuum Undulator & Elliptically Polarizing Undulator type



<Figure 3.1.3.3> IVU Photon Shutter and actuating system.

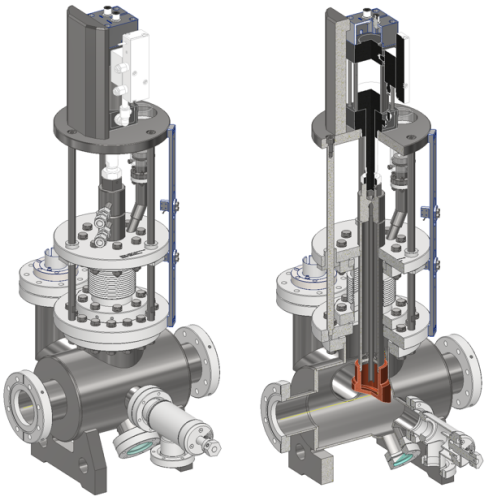


<Figure 3.1.3.4> Photon absorber parts (IVU & EPU).

(b) Bending Magnet type

<Table 3.1.3.3> Photon Shutter specification (IVU & EPU).

	IVU & EPU
From the source [mm]	18,800
Incidence angle [°]	1.6
Beam size [mm]	5.64(H) × 5.64(V)
Entrance aperture size [mm]	11.8(H) × 22.0(V)
Cooling pipe [inch]	1/2
Cooling channel [ea]	2, direct cooling type
Flange size [inch]	CF 6
Base material	CuCrZr
Thermocouple	K-type, 15 ea (3-lines)
Pneumatic cylinder	DDV-50x50-DC24V (with solenoid valve, sensor)
Pneumatic pressure	5 bar
Pneumatic damping	In each end position
Vacuum	UHV compatible



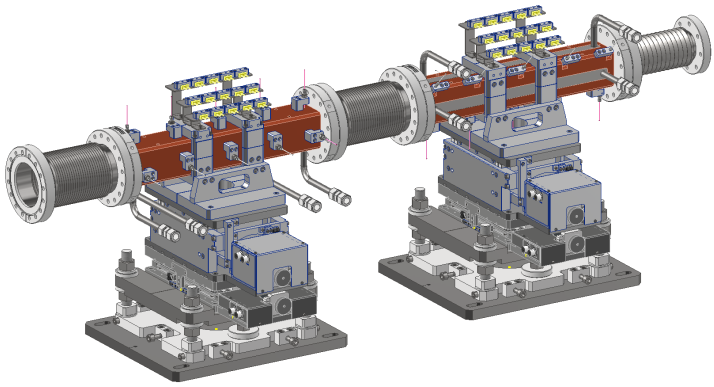
<Figure 3.1.3.5> BM Photon Shutter assembly.

<Table 3.1.3.4> Photon Shutter specification (BM).

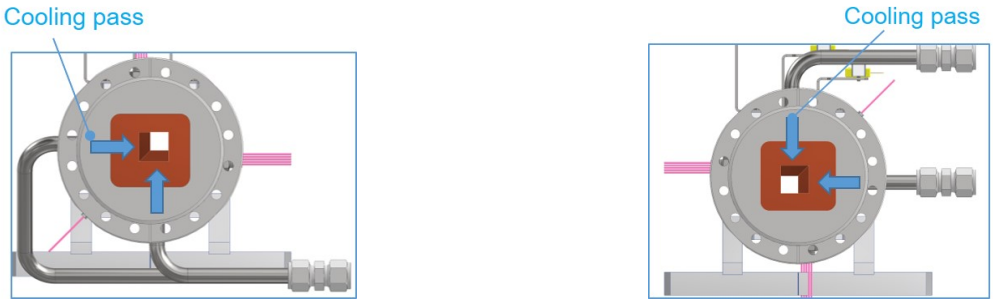
	BM
From the source [mm]	14,572
Incidence angle [°]	20
Beam size [mm]	29.22(H) × 4.38(V)
Aperture size [mm]	⌀60
Cooling pipe [inch]	3/8
Cooling channel [ea]	1
Flange size [inch]	CF 4.5
Base material	OFHC
Thermocouple	K-type, feedthrough (1 pair)
Pneumatic cylinder	DDV-50x50-DC24V (with solenoid valve, sensor)
Pneumatic pressure	5 bar
Pneumatic damping	In each end position
Maximum closing speed	50–600 mm/sec
Solenoid	24V DC
Vacuum	UHV compatible, with welded bellows, window (2.75 inch)

3.1.3.4 Movable Mask

The Movable Mask functions as a slit to remove unwanted radiation before the photon beam is delivered to the downstream optical components. It is also designed to completely intercept the photon beam when required. The blade geometry was designed to accommodate various beam conditions corresponding to different experimental requirements [1]. In addition, the Movable Mask is equipped with a motorized X–Y stage that provides remote positioning with micrometer-level precision. To enable indirect beam position monitoring, multiple temperature sensors are installed along the longitudinal direction of the mask body, with three rows of five sensors each. By analyzing the temperature distribution, the beam position can be estimated during operation. <Figure 3.1.3.6> and <Figure 3.1.3.7> show the internal structure and the assembled layout of the Movable Mask, respectively, and its detailed specifications are summarized in <Table 3.1.3.5>.



<Figure 3.1.3.6> Movable Mask assembly.

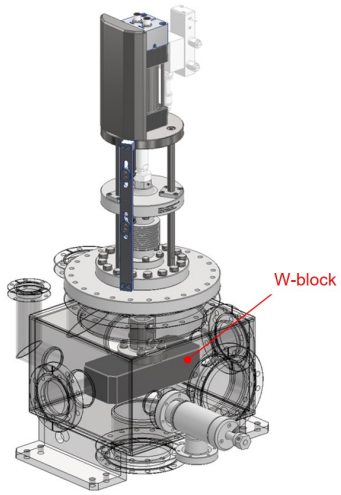


(a) (b)

<Figure 3.1.3.7> Movable Mask cooling path: (a) 1st Movable Mask cooling path, (b) 2nd Movable Mask cooling path.

<Table 3.1.3.5> Movable Mask specification.

	IVU & EPU
Incidence angle [°]	1.2
Beam size [mm]	6.88(H) × 6.88(V)
Cooling pipe [inch]	1/2
Cooling channel [ea]	2, direct cooling type
Flange size [inch]	CF 6
Base material	CuCrZr
Blade material	Tungsten with polished knife edges
Blade roughness [μm]	<1.0
Thermocouple	K-type, 15 ea (3-lines)
Slits parallelism [°]	<0.1
Moving control	With X–Y stage
Moving resolution [μm]	±1.0



<Figure 3.1.3.8> Safety Shutter assembly.

3.1.3.5 Safety Shutter

The Safety Shutter has the function of completely shielding the bremsstrahlung radiation inside the concrete shielding wall when the beamline is not in operation even during normal operation of the storage ring, or when the FCS is suddenly closed due to a vacuum accident in the beamline. Since the Safety Shutter does not have a cooling system, it must be interlocked with the Photon Shutter. <Figure 3.1.3.8> shows the assembly layout of the Safety Shutter, and its detailed specifications are summarized in <Table 3.1.3.6>.

<Table 3.1.3.6> Safety Shutter specification.

	IVU24	BM
From the source [mm]	24,145	22,120
Incidence angle [°]	90	90
Cooling	Non-cooled	Non-cooled
Stroke [mm]	50	50
Shutter size [mm]	80W × 50H × 200L	80W × 50H × 200L
Shutter material	W-alloy (W90.2%, Ni6.86%, Fe2.94%)	W-alloy (W90.2%, Ni6.86%, Fe2.94%)
Pneumatic cylinder	DDV-50x50-DC24V (with solenoid valve, sensor)	DDV-50x50-DC24V (with solenoid valve, sensor)
Pneumatic pressure	5 bar	5 bar
Pneumatic damping	In each end position	In each end position
Maximum closing speed	50–600 mm/sec	50–600 mm/sec
Vacuum	UHV compatible, with welded bellows	UHV compatible, with welded bellows

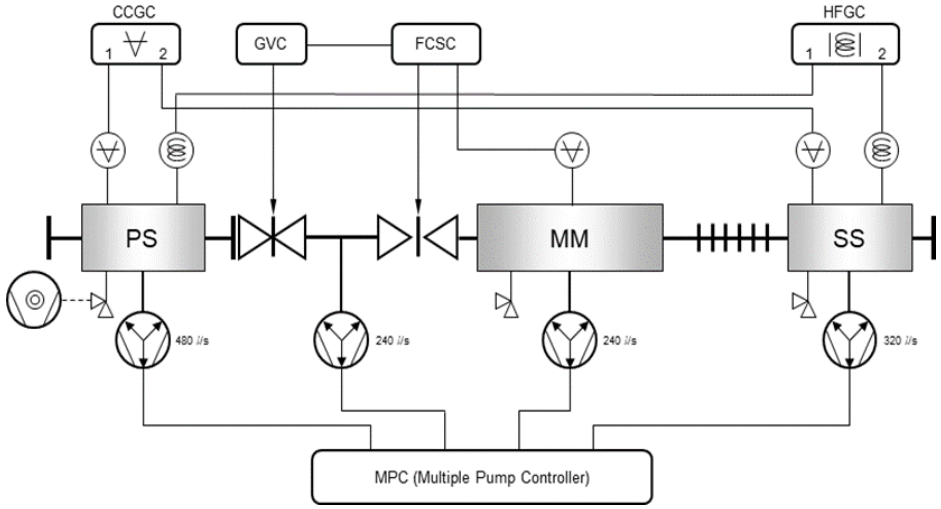
3.1.4 Vacuum System of Front-End

3.1.4.1 Purpose

The installation of a beamline vacuum system is the most basic matter in beamline construction, and a well-designed vacuum system is an important matter for the operation and maintenance of the beamline. Therefore, it is necessary to verify the roles and functions of the ion pumps, gauges, and pumping stations that are essential for maintaining the installed vacuum system, and it is also important to consider the appropriate quantity. The KLS beamline can be largely divided into three parts: the front-end, the optical hutch (OH), and the experimental hutch (EH), and each part has a different vacuum system. In particular, since the front-end section is connected to the storage ring chamber, appropriate vacuum conditions must be set, and an interlock system must be installed in preparation for vacuum accidents [4].

The front-end acts as a bridge between the storage ring and the beamline, so the vacuum condition of one side directly affects the other side. Therefore, in order to operate the storage ring stably, the vacuum condition of the front-end must always be better than that of the storage ring. The vacuum condition of the front-end is designed to be 2×10^{-10} Torr or less when the storage ring is not operated, but in practice it should be maintained at 5×10^{-10} Torr or less when the storage ring is not operated, and 5×10^{-9} Torr or less when the beamline is operated.

In order to satisfy the above conditions, all vacuum components must meet the conditions, and materials that can be heat treated up to 200 °C must be selected to obtain the desired vacuum level [3]. In addition, rubber seals that are easily hardened by radiation must not be used within the storage ring. The vacuum system is divided into a vacuum measuring system, vacuum vessel and valve, and exhaust system as shown in <Figure 3.1.4.1>.

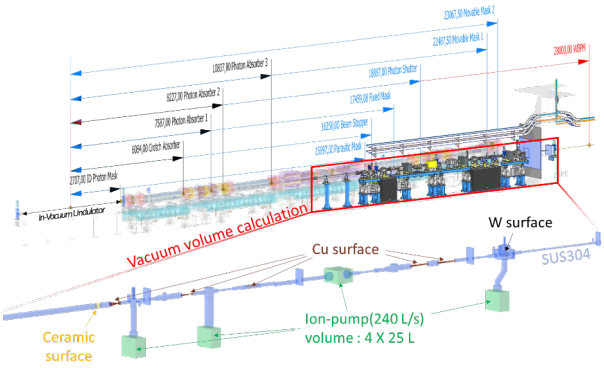


<Figure 3.1.4.1> Diagram of front-end vacuum system. (PS: Photon Shutter, MM: Movable Mask, SS: Safety Shutter, CCGC: Cold Cathode Gauge Controller, HFGC: Hot Filament Gauge Controller, FCSC: Fast Closing Shutter Controller, GVC: Gate Valve Controller.)

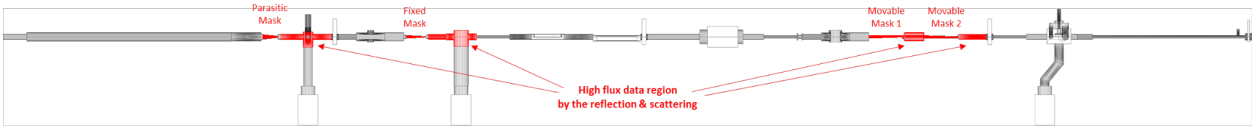
3.1.4.2 Vacuum Analysis for Front-End

To maintain the UHV environment during beamline operation, ion pumps are strategically distributed throughout the front-end section. Since the vacuum performance is significantly influenced by the materials of the vacuum chambers and beam-intercepting components, a comprehensive vacuum analysis was performed [3].

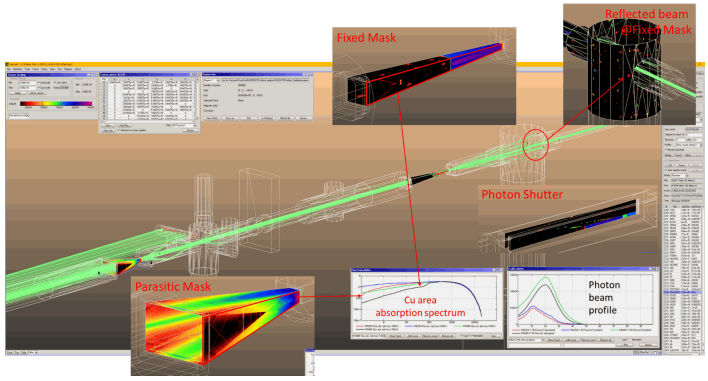
<Figure 3.1.4.2> illustrates the locations of the ion pumps and the materials used for the beam-intercepting components in the front-end. The vacuum analysis considered photon reflection and scattering at the major components, whose layout and details are shown in <Figure 3.1.4.3> and <Figure 3.1.4.4>, respectively. The resulting pressure distributions evaluated before bake-out, after bake-out, and during beam operation are shown in <Figure 3.1.4.5> [3].



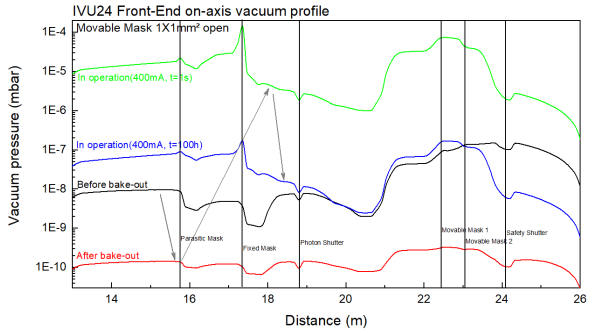
<Figure 3.1.4.2> Pumping area and materials.



<Figure 3.1.4.3> Layout of reflection and scattering points.



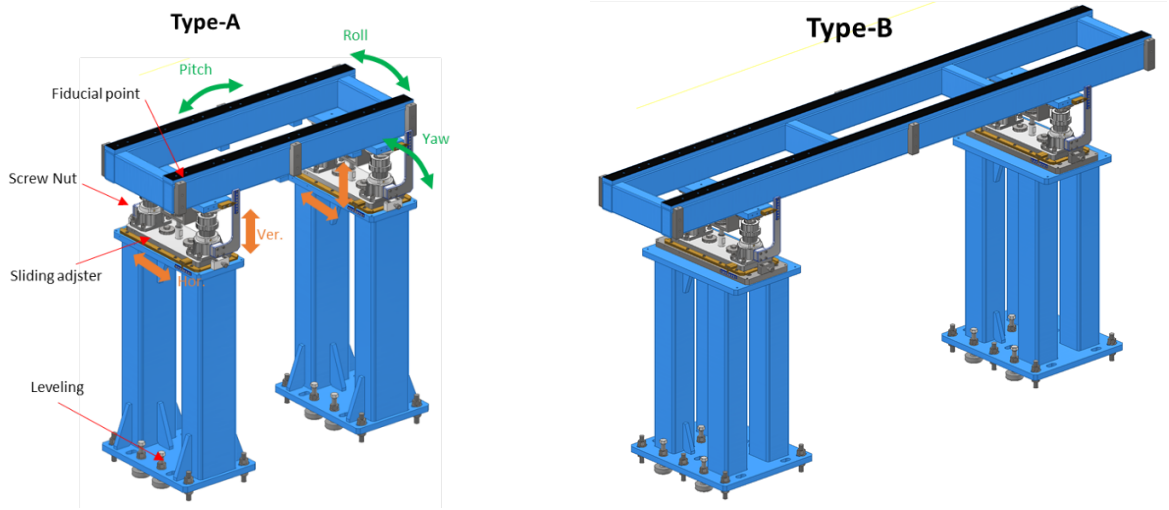
<Figure 3.1.4.4> Details of reflection and scattering points.



<Figure 3.1.4.5> Vacuum profile of front-end.

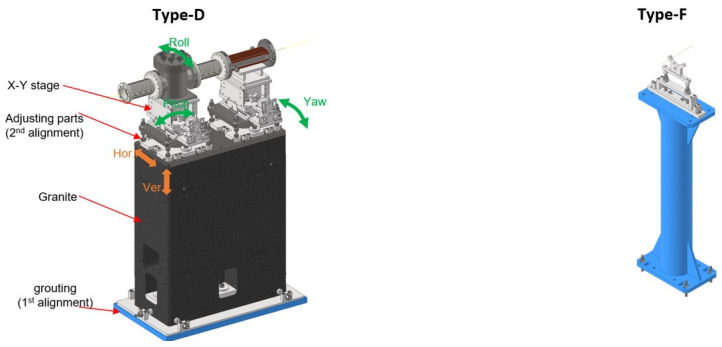
3.1.5 Girder & Support

The girder and support structures provide mechanical mounting and alignment for the beamline vacuum components. It must be manufactured to meet the design requirements such as precision adjustment device, vibration absorption, and thermal expansion absorption. The girder system uses a screw-jack at the bottom for rough adjustment, and detailed adjustments are made at the top. In particular, since the front-end has limited space, it is useful to apply an integral girder for efficient alignment. <Figure 3.1.5.1> and <Figure 3.1.5.2> show the integral girder systems applied to the beamline. The support structure is designed to have the rigidity to withstand vacuum and seismic loads. The inside of the girder system is filled with dry sand to pursue a vibration-proof effect, and the surface is applied with powder coating that is economical, corrosion-resistant, and durable.



(a) (b)

<Figure 3.1.5.1> Integral girder systems: (a) Type-A, (b) Type-B.



(a) (b)

<Figure 3.1.5.2> Integral girder systems: (a) Type-D, (b) Type-F.

3.1.5.1 Table of specification

The specifications of the integral girder systems (Type-A, B, D, F) are summarized in <Table 3.1.5.1>.

<Table 3.1.5.1> Girder & support specification.

	Type	A	B	D	F
1	Size [mm]	∼2000 × 340/380 × 115	∼4000 × 340/380 × 115	$L \times 380 \times 1040$	150A #40 Pipe
2	Load capacity [tonf]	2	5	–	–
3	Vertical motion	Vertical, Pitch, Roll direction Screw Jack: 4ea/set (Stroke: ±25 mm)	Vertical, Pitch, Roll direction Screw Jack: 4ea/set (Stroke: ±25 mm)	Vertical: ±10 mm	Vertical: ±24 mm
4	Horizontal motion	Horizontal, Yaw direction LM Guide & Ball Screw (Stroke: ±24 mm)	Horizontal, Yaw direction LM Guide & Ball Screw (Stroke: ±24 mm)	Horizontal: ±20 mm	Horizontal: ±12 mm
5	Anti-vibration	Grouting between ground and stand, Filling dry sand in stand & frame	Grouting between ground and stand, Filling dry sand in stand & frame	Grouting between ground and stand	Filling dry sand in stand & frame
6	Drive type	Manual (motor and encoder attachable)	Manual (motor and encoder attachable)	Manual	Manual
7	Indicate	Indicating X and Y directions	Indicating X and Y directions	–	–
8	Etc.	Fixing clamp, level indicator, Fiducial Post	Fixing clamp, level indicator, Fiducial Post	Fixing clamp, level indicator, Fiducial Post	

※ L: variable, depending on the installation location.

References

[1] Jongha Park et al. High Heat Load Front-End Mechanical Design and Thermal Analysis Report. Internal Document PAL-INT/ME-2026-003. Pohang Accelerator Laboratory, June 2026.

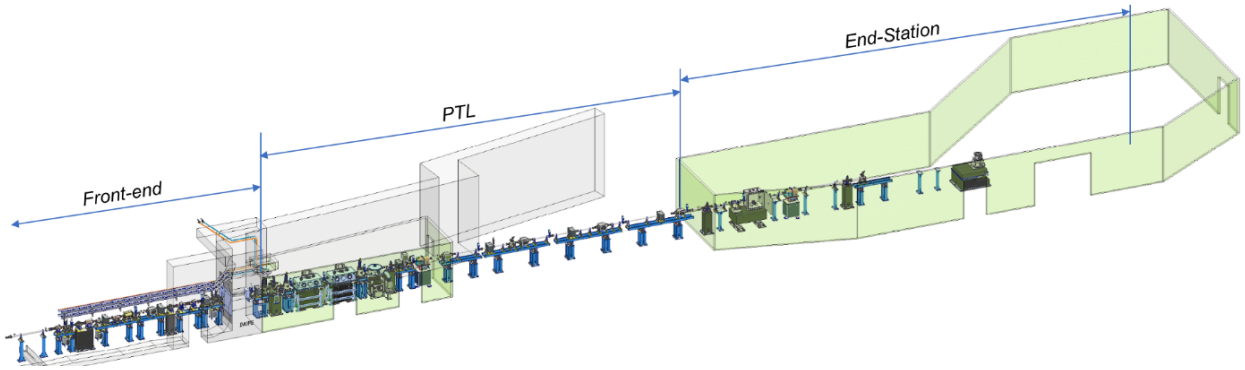
[2] Hyungseok Choi and Jongha Park. Beamline Photon Source Analysis Report. Internal Document PAL-INT/ME-2026-007. Pohang Accelerator Laboratory, July 2026.

[3] Hyungseok Choi and Jongha Park. 4GSR Front-End Vacuum Analysis Report. Internal Document PAL-INT/ME-2026-009. Pohang Accelerator Laboratory, Aug. 2026.

[4] Minho Seo and Chaesoon Lee. 4GSR Beamline Interlock System Design Report. Internal Document PAL-INT/EE-2026-012. Pohang Accelerator Laboratory, July 2026.

3.2 Photon Transfer Line Components

As illustrated in the example in <Figure 3.2.0.1>, a typical beamline consists of three main sections: the front-end, the Photon Transfer Line (PTL), and the end-station. The PTL and end-station are respectively enclosed within radiation-shielding hutches (the optical and experimental hutches). Since optical components and experimental instruments in the PTL vary depending on specific beamline characteristics and measurement techniques, the PTL descriptions in this report focus on standardized components common across multiple beamlines.



<Figure 3.2.0.1> Beamline layout (example).

The types and functions of these common components are summarized in <Table 3.2.0.1>, while their detailed design and structural features are described in the corresponding sections.

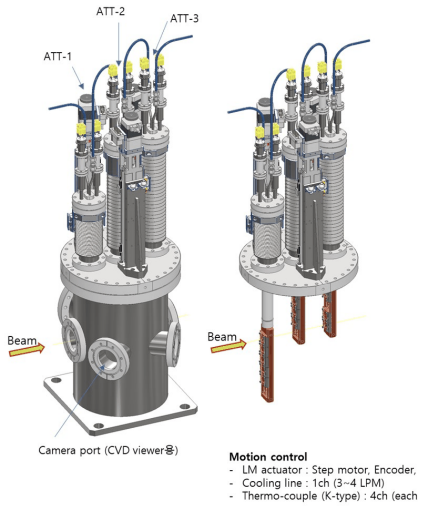
3.2.1 Attenuator

The white-beam attenuator is equipped with three actuator assemblies installed within a single vacuum chamber to accommodate the beam trajectory. Each actuator supports a filter holder suspended from the actuator shaft, and cooling water is supplied to the holder through the central shaft to efficiently remove the absorbed heat (<Figure 3.2.1.1>). The holder, cooling-channel and motion-system design is given in the white beam attenuator design report [1].

Each filter holder can accommodate up to five filters. Carbon and aluminum alloy are used as the primary filter materials for beam attenuation. The last filter holder can be optionally equipped with a CVD diamond screen to allow visual observation of the beam position. In addition, thermocouples are installed at every filter mounting position to continuously monitor the filter temperature and ensure that the allowable operating temperature is not exceeded.

<Table 3.2.0.1> Common components in the PTL area.

Components	Type of source	Function
Attenuator (cooling type)	White beam	White-beam attenuation using carbon and aluminum-alloy filters to adjust the transmitted energy range.
Slit (cooling type)	White beam	Micrometer-level beam size and profile adjustment for white-beam applications.
Slit (non-cooling type)	Mono beam	Micrometer-level beam size and profile adjustment for monochromatic beam applications.
Exit slit	Mono beam	Nanometer-level beam size and profile adjustment for delivering monochromatic beams to soft X-ray experimental stations.
Screen monitor	White beam	White-beam position and profile monitoring.
Screen monitor	Mono beam	Monochromatic beam position and profile monitoring.



<Figure 3.2.1.1> Attenuator system assembly.

The main specifications of the attenuator system are summarized in <Table 3.2.1.1>; the commissioning and operating heat-load cases listed there are the conditions used for the thermal analysis of the filter set [1].

<Table 3.2.1.1> Attenuator system specification.

Parameter	Commissioning mode	Operating mode
Operation conditions	IVU24, 100 mA, Gap 12 mm, @26.7 m	IVU24, 400 mA, Gap 5 mm, @26.7 m
Beam size [mm]	2.0 (H) × 2.0 (V)	1.2 (H) × 1.2 (V)
Thermal load range [W]	61.6	322
Chamber mount flange [inch]	CF 12	CF 12
Holder	3 channels, OFHC (cooling flow rate = 3 L/min)	3 channels, OFHC (cooling flow rate = 3 L/min)
Holder aperture size [mm]	d 15	d 15
Moving control	Stepping motor with LM actuator	Stepping motor with LM actuator
LM actuator resolution [μm]	± 3	± 3
Linear encoder	MS15 TTLx200	MS15 TTLx200
Encoder accuracy [μm]	± 5	± 5
Cooling pipe [inch]	1/4 (hose and fitting)	1/4 (hose and fitting)
Thermocouple	K-type, feedthrough	K-type, feedthrough
Structure materials	STS304, Al6061, Al5052	STS304, Al6061, Al5052
Filter materials	Carbon (0.5, 1, 2, 4, 6, 8t); Aluminum (0.3, 0.5, 0.9, 1.9, 2.7, 5t); CVD diamond (0.4–0.5t)	Carbon (0.5, 1, 2, 4, 6, 8t); Aluminum (0.3, 0.5, 0.9, 1.9, 2.7, 5t); CVD diamond (0.4–0.5t)

A Interlock condition of attenuator system

The temperature limits and the carbon pre-filter sequence referred to below are based on the thermal analysis of the filter materials [1]. To ensure safe operation, the following interlock functions should be implemented:

- Filter operation shall be enabled only when either the commissioning mode or operation mode is selected.
- During normal operation, aluminum-alloy filters shall be inserted only after the 6-mm-thick carbon filter has been positioned in the beam path.
- If the measured temperature exceeds the predefined limit, the filter holder shall be automatically moved to the empty position and remain disabled until the temperature returns to a safe operating range.
- During operation mode, filter exchange should be permitted only after the Photon Shutter has been closed.

3.2.2 Slit

3.2.2.1 White beam slit for In-Vacuum Undulator type

The white beam slit is used to define the beam profile. Specifically, it adjusts the beam size delivered from the front-end before entering the monochromator. Accurate control of the white beam requires tungsten blades with low surface roughness and high flatness, and a cooling system capable of withstanding the thermal load.

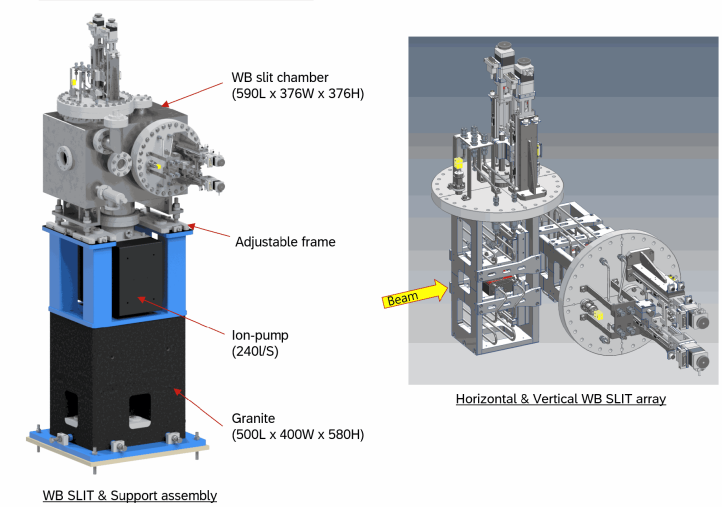
This slit is used widely in both ID and BM beamlines. Depending on the needed beam shape, the aperture shape and cooling channel design can be different at each location.

The white beam slit for the IVU source consists of a single vacuum chamber incorporating independent horizontal and vertical subassemblies mounted on dedicated mounting flanges. To define the central cone with millimeter-scale dimensions, the slit apertures must provide micrometer-level positioning accuracy over a short travel range of approximately ± 10 mm.

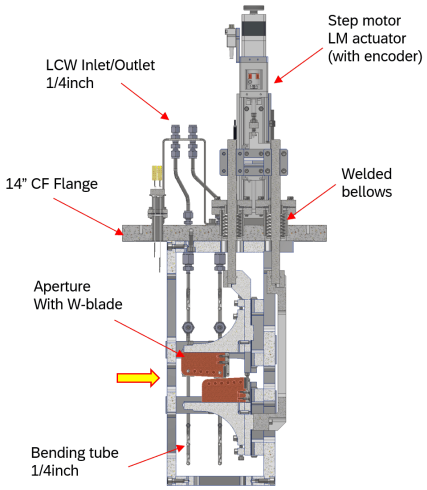
The design is based on a CF14 mounting flange. Outside the vacuum chamber, each aperture is actuated by a linear motion actuator system. Inside the vacuum chamber, the aperture is guided by cross-roller guides within a rigid rectangular frame to ensure smooth motion and high positioning stability.

Each aperture is fabricated from a copper alloy and incorporates a tungsten blade bonded to its rear surface. This dissimilar-material joint enables efficient heat removal from the blade edge exposed to the white beam. To achieve precise beam definition, the blade edge is polished to a surface roughness of Ra 0.8 μm or better. Cooling water is supplied to the aperture through a dedicated vacuum feedthrough located on the front side of the main mounting flange.

A key feature of this design is the cooling-water supply system. Instead of using bellows, the cooling lines are constructed from multi-bent stainless-steel tubes that elastically accommodate the required aperture travel while remaining within the elastic deformation range of the tubing. This approach eliminates the need for separate cooling-line bellows, thereby reducing both the installation space and manufacturing cost. In addition, minimizing the number of mechanical joints improves the overall structural reliability of the system. The overall assembly and detailed geometry are shown in <Figure 3.2.2.1> and <Figure 3.2.2.2>, respectively.



<Figure 3.2.2.1> White beam slit assembly (IVU type).



<Figure 3.2.2.2> Detailed geometry of the white beam slit (IVU type).

<Table 3.2.2.1> summarizes the specifications of the IVU-type white beam slit.

<Table 3.2.2.1> White beam slit (IVU type) specification.

Parameter	White beam slit
Applicable beamline	IVU, EPU
Thermal load range [W]	< 550 (expected)
Flange size [inch]	CF 14
Beam size control range [mm]	30 (H) $\times$ 30 (V)
Aperture material	CuCrZr
Blade material	Tungsten with polished knife edges
Blade roughness [μm]	Ra 0.8
Blade flatness [μm]	< 1
Moving control	Stepping motor with LM actuator
LM actuator resolution [μm]	$\pm$ 3
Linear encoder	MS15 TTLx200
Encoder accuracy [μm]	$\pm$ 5
Cooling pipe [inch]	1/4
Cooling line feedthrough method	Multi-bent tube (no bellows)
Thermocouple	K-type, feedthrough
Structure materials	STS304, Al6061, Al5052
Tube materials	STS304, C1010

3.2.2.2 White beam slit for Bending Magnet upstream type

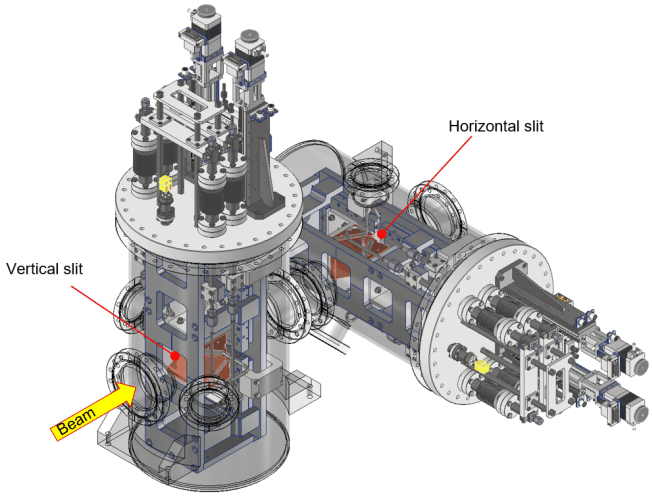
Unlike the IVU source, the BM source exhibits a linearly distributed power density over a relatively wide radiation fan. Most of the BM radiation is transmitted through the front-end rather than being absorbed, allowing the white beam to be delivered as close as possible to the end-station [2].

The white beam slit for the BM source consists of separate horizontal and vertical vacuum chambers. Owing to the broad emission of the BM source, the required travel range of the slit apertures increases with distance from the source.

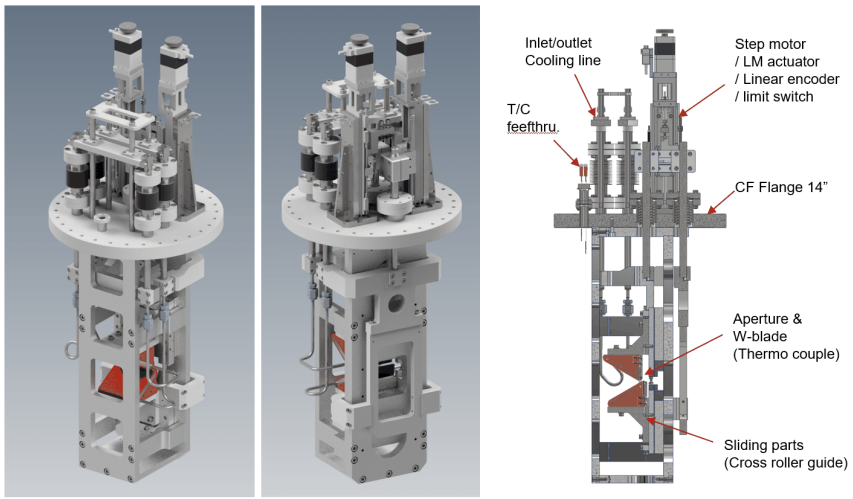
The design is based on a CF14 mounting flange. Outside the vacuum chamber, each aperture is actuated by a linear motion actuator system. Inside the vacuum chamber, the aperture is guided by cross-roller guides within a rigid rectangular frame to ensure smooth motion and high positioning stability.

Each aperture is fabricated from a copper alloy and incorporates a tungsten blade bonded to its rear surface for efficient heat removal from the blade edge. To

achieve accurate beam definition, the blade edge is polished to a surface roughness of Ra 0.8 μm or better. Cooling water is supplied to the aperture through a dedicated welded-bellows feedthrough mounted on the side of the main flange. Inside the vacuum chamber, the feedthrough line is mechanically constrained by a support arm so that it follows the aperture motion, allowing the cooling line to move synchronously throughout the full opening and closing stroke. The overall assembly and detailed geometry are shown in <Figure 3.2.2.3> and <Figure 3.2.2.4>, respectively.



<Figure 3.2.2.3> White beam slit assembly (BM upstream type).



<Figure 3.2.2.4> Detailed geometry of the white beam slit (BM upstream type).

<Table 3.2.2.2> summarizes the specifications of the BM upstream-type white beam slit.

<Table 3.2.2.2> White beam slit (BM upstream type) specification.

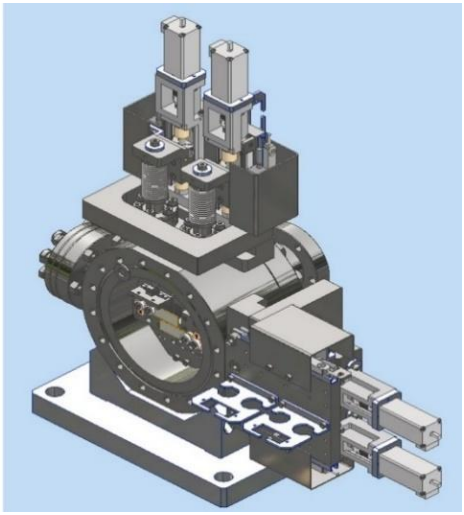
Parameter	White beam slit
Applicable beamline	BM (Upstream type)
Thermal load range [W]	< 470 (expected)
Flange size [inch]	CF 14
Beam size control range [mm]	60 (H) $\times$ 30 (V)
Aperture material	CuCrZr
Blade material	Tungsten with polished knife edges
Blade roughness [μm]	Ra 0.8
Blade flatness [μm]	< 1
Moving control	Stepping motor with LM actuator
LM actuator resolution [μm]	$\pm$ 3
Linear encoder	MS15 TTLx200
Encoder accuracy [μm]	$\pm$ 5
Cooling pipe [inch]	1/4
Cooling line feedthrough method	Welded-bellows feedthrough (moves with aperture)
Thermocouple	K-type, feedthrough
Structure materials	STS304, Al6061, Al5052
Tube materials	STS304, C1010

3.2.2.3 Mono beam slit

The slit plays a role in precisely controlling the beam size applied to the optical device. Therefore, it must be designed, assembled, and installed with great precision. In particular, the blade that comes into contact with the beam must be precisely machined to reduce radiation scattering. The slit is installed in front of the optical device (double-crystal monochromator (DCM), mirror) located in the optical hutch, and is also installed inside the experimental hutch where the experimental device is located.

<Figure 3.2.2.5> shows the internal shape and assembly layout of the mono beam slit.

Specification	
Blade material:	Tunsten with polished knife edges
Slits parallelism:	< ± 0.1 degree
Blade surface roughness:	< 1um
Aperture:	10 x 10 mm(overlapping blades)
Step resolution:	0.1 um (driver control)
Encoder resolution:	0.05 um
Repeatability:	< 0.2 um



<Figure 3.2.2.5> Mono beam slit assembly.

3.2.3 Photon Beam Diagnostics

The requirements for the diagnostic systems were defined by considering both the characteristics of the photon beam and the intended diagnostic functions. <Table 3.2.3.1> summarizes the physical quantities measured by each diagnostic device and their corresponding impact on the photon beam.

<Table 3.2.3.1> Physical parameters to be diagnosed by the photon beam diagnostic devices planned for use at the KLS, and the effects of these devices on the photon beam.

Name of Diagnostics		Diagnostic objects					Effect on beam		
		Position	Size	Intensity	Spatial profile (Shape)	Spectrum	Nondestructive	Attenuative	Fully blocked
White Beam Profile Monitor 1	DDB-XBPM	○	△				√		
	Spectral Intensity Monitor			○				√	
White Beam Profile Monitor 2	WB Screen Monitor		△	△	○				√
	WB Screen Monitor		△	△	○				√
White Beam Profile Monitor 3	WB Screen Monitor		△	△	○				√
	MB Screen Monitor		▲	▲	●				√
Mono Beam Profile Monitor	MB Screen Monitor		▲	▲	●				√
	Wire Current Monitor		●	▲				√	
	MB Intensity Monitor			●					√
End-station Diagnostics	MB Screen Monitor		▲	▲	●		√		
	scDBPM	●		▲			√		
	QBPM	●		▲		▲	√		
	MB Intensity Monitor			●			√		

○ : White beam main purpose △ : White beam indirect use ● : Mono beam main purpose ▲ : Mono beam indirect use

※ DDB-XBPM: diamond detector blade X-ray beam position monitor; scDBPM: single-crystal diamond beam position monitor; QBPM: quadrant beam position monitor; WB: white beam; MB: mono beam.

3.2.3.1 White Beam Diagnostics

The White Beam Diagnostic System is generally designed for two primary purposes: to align the front-end components and to intercept and characterize the photon beam before it enters the optical systems. Consequently, the thermal load and cooling efficiency relative to the white beam power density profile [3] are critical design considerations. The system requirements have been established to ensure both undistorted diagnostic performance and precise beamline alignment. To ensure the system can withstand the maximum thermal load even in the absence of preliminary alignment, the design adheres to the IVU24 front-end Photon Shutter standards [2]. This includes applying equivalent criteria for thermal load capacity, cooling performance, and vacuum integrity. The specifications for each white beam diagnostic device are summarized in <Table 3.2.3.2>.

<Table 3.2.3.2> Design requirements of the white beam diagnostics.

Name of diagnostics		Vacuum range	Temp. range	Cooling	Beam contact material	Mechanical			Signal		
						Translation range	Angle range	Resolution	Readout type	Bias voltage	Resolution
WB Profile Monitor 1	DDB-XBPM	UHV	<600 °C	2 channels (series) 10 L/min	scDiamond	None	None	None	3×4 channels current signal	4 channels 100 V	Scale of ~10 μA
	WB Screen Monitor	UHV	<290 °C	1 channel 10 L/min	CuCrZr	H: None V: 100 mm	None	H: None	Pinhole CMOS camera	None	Scale of ~0.1 μm
WB Profile Monitor 2	WB Screen Monitor	UHV	<290 °C	1 channel 10 L/min	CuCrZr	H: None V: 200 mm	None	H: None	Pinhole CMOS camera	None	Scale of ~0.1 μm
WB Profile Monitor 3	WB Screen Monitor	UHV	<290 °C	1 channel 10 L/min	CuCrZr	H: None V: 200 mm	None	H: None	Pinhole CMOS camera	None	Scale of ~0.1 μm
	MB Screen Monitor	UHV	<290 °C	1 channel 10 L/min	CuCrZr phosphor	H: None V: 200 mm	None	H: None	CCD camera	None	Scale of ~0.1 μm

※ DDB-XBPM: diamond detector blade X-ray beam position monitor; WB: white beam; MB: mono beam.

For all diagnostic devices that measure current signals, electrical insulation is important, and tri-axial cables are used to ensure a high signal-to-noise ratio. Additionally, for devices with applied bias, the middle shield layer of the tri-axial cable is maintained at the same potential as the bias voltage to minimize signal leakage current.

The white beam diagnostic system measures the beam intensity and beam profile by reading the current signals generated from a beam-intercepting target. The beam-intercepting surface is fabricated from CuCrZr. When irradiated by synchrotron X-rays, the CuCrZr surface produces X-ray fluorescence (XRF) and photoelectrons. The beam profile can be observed by imaging the X-ray fluorescence with a camera, while the beam intensity is determined from the photoelectron-induced current signals. <Figure 3.2.3.1> illustrates the typical configuration of the white-beam diagnostic system.



(a) Water-cooling current monitor (b) White beam screen monitor

<Figure 3.2.3.1> White beam diagnostic system: (a) water-cooling current monitor, (b) white beam screen monitor.

3.2.3.2 Mono Beam Diagnostics

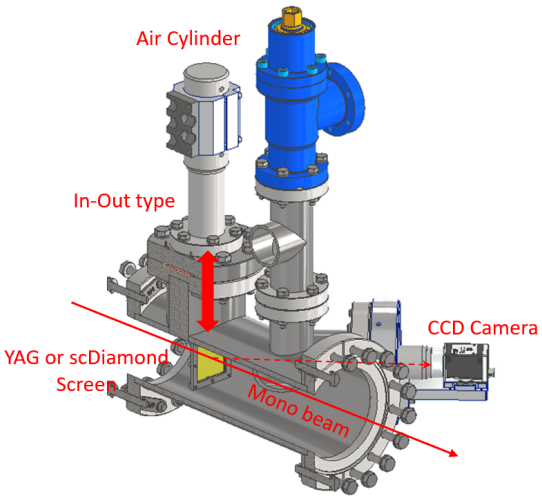
The requirements for the mono beam diagnostic system are summarized in <Table 3.2.3.3>. Detailed specifications may be further refined based on the optical components used in each beamline PTL section and the specific photon beam parameters required by the end-station. As with the white beam diagnostics, electrical insulation is critical to maintaining an optimal signal-to-noise ratio. In particular, the ion chamber requires extreme caution due to the application of high

bias voltages. For this device, the use of high-voltage rated cables is mandatory.

<Table 3.2.3.3> Design requirements of the mono beam diagnostics.

Name of diagnostics		Vacuum range	Temp. range	Cooling	Beam contact material	Mechanical			Signal		
						Translation range	Angle range	Resolution	Readout type	Bias voltage	Resolution
MB Profile Monitor	MB Screen Monitor	UHV	<290 °C	None	CuCrZr PD	H: 150 mm V: 150 mm	None	–	CCD camera	None	Scale of ~0.1 μm
	Wire Current Monitor	UHV	<1700 °C	None	W-wire	H: 150 mm V: 150 mm	None	–	2 channels current signal	None	Scale of ~1 μA
	MB Intensity Monitor	UHV	<290 °C	None	CuCrZr PD Au-mesh	H: None V: 200 mm	None	H: None	1 channel current signal	None	Scale of ~10 μA
End-station Diagnostics	MB Screen Monitor	UHV	<600 °C	None	scDiamond YAG	H: None V: 200 mm	None	H: None	CCD camera	None	Scale of ~0.1 μm
	scDBPM	HV	<600 °C	None	scDiamond	H/V ±5 mm	None	–	4 channels current signal	±10 V	Scale of ~1 μA
	QBPM	HV	<600 °C	None	Metal foil scDiamond PD	H/V ±5 mm	H/V ±1°	–	4 channels current signal, CCD camera	None	Scale of ~1 μA
	MB Intensity Monitor	0.7 bar	None	None	gas	None	None	None	2 channels current signal	2 kV	Scale of ~1 μA

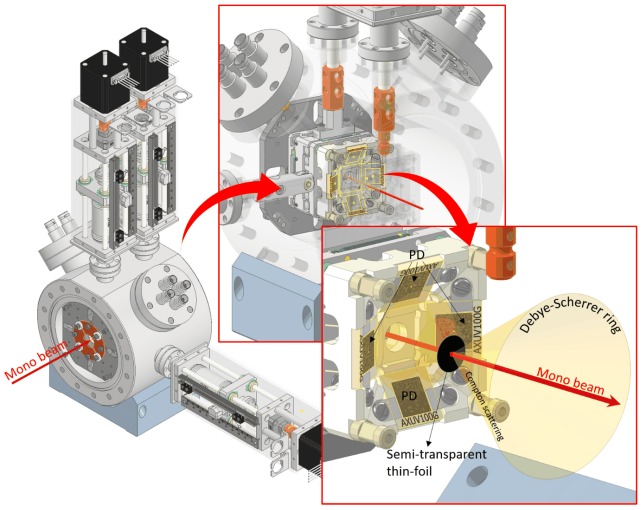
※ PD: photodiode; YAG: yttrium aluminum garnet; scDBPM: single-crystal diamond beam position monitor; scDiamond: single-crystal diamond; QBPM: quadrant beam position monitor; WB: white beam; MB: mono beam.



<Figure 3.2.3.2> YAG and scDiamond screen monitors utilized for mono beam profile characterization.

<Figure 3.2.3.2> illustrates the YAG and scDiamond (single-crystal diamond) screen monitors used for mono beam profile characterization. To ensure distortion-free profile diagnostics, these diagnostic devices require high-performance camera specifications. Specifically, a high frame rate and superior optical sensitivity are essential; additionally, a pinhole aperture may be required depending on the luminance of the mono beam.

<Figure 3.2.3.3> illustrates the Quadrant Beam Position Monitor (QBPM) used for precise diagnostics of the mono beam position. Designed for hard X-ray beamlines, this diagnostic device determines the beam center by detecting the Debye-Scherrer rings and Compton scattering emitted when the mono beam is incident on an ultra-thin metal foil. The system utilizes AXUV100G photodiodes, which are characterized by their fast response times and optimized for X-ray and electron detection. The composition of the thin metal foil is selected based on specific beamline requirements. Furthermore, by precisely analyzing the well-defined Debye-Scherrer rings of the selected metal foil, it is possible to back-calculate the wavelength of the mono beam.



<Figure 3.2.3.3> Configuration of the QBPM utilized for mono beam position monitoring.

References

[1] Jongha Park and Jaeyong Shin. White Beam Attenuator Design Report. Internal Document PAL-INT/ME-2026-005. Pohang Accelerator Laboratory, June 2026.

[2] Jongha Park et al. High Heat Load Front-End Mechanical Design and Thermal Analysis Report. Internal Document PAL-INT/ME-2026-003. Pohang Accelerator Laboratory, June 2026.

[3] Hyungseok Choi and Jongha Park. Beamline Photon Source Analysis Report. Internal Document PAL-INT/ME-2026-007. Pohang Accelerator Laboratory, July 2026.

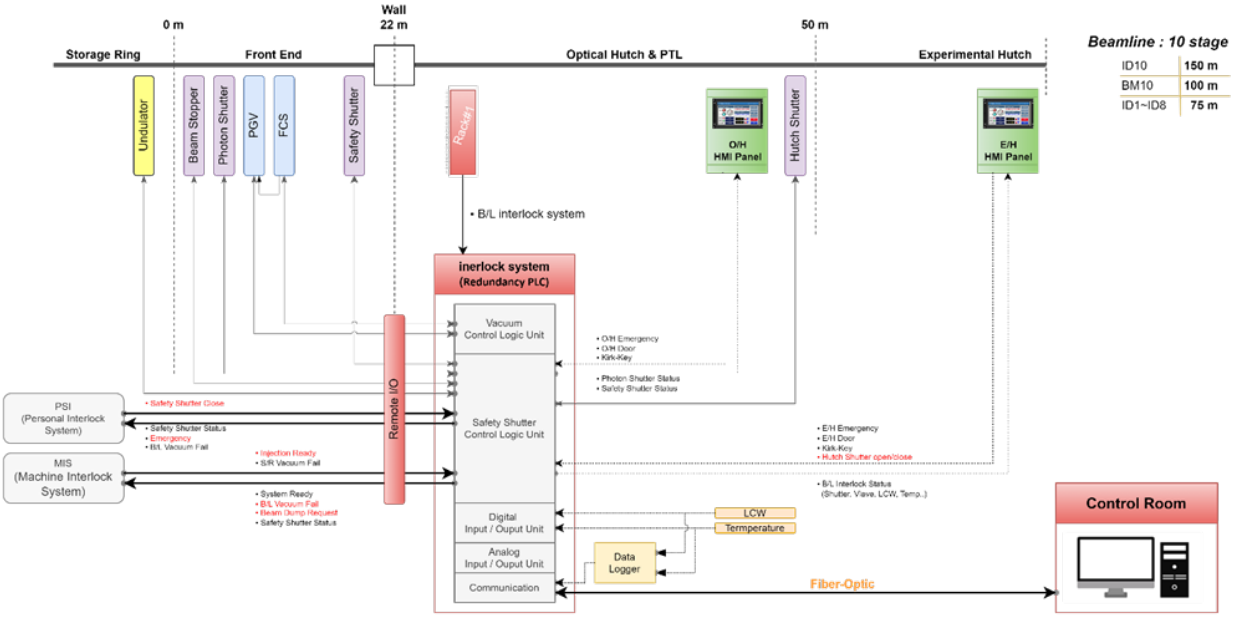
3.3 Interlock System

3.3.1 Beamline Interlock System

The interlock system is a core protective mechanism that ensures the safety of personnel and equipment during accelerator and beamline operations. It is composed of coordinated devices that serve two distinct but complementary functions:

- **PSI (Personnel Safety Interlock):** This system protects personnel by halting beam operation or preventing access whenever there is a risk of radiation exposure.
- **MIS (Machine Interlock System):** This system protects accelerator and beamline equipment. It halts operation upon detecting abnormal states or system faults—such as vacuum degradation or cooling failure—thereby preventing hardware damage and ensuring machine integrity.

These two systems operate in coordination, performing real-time monitoring and control to ensure safe and uninterrupted operation of the entire beamline and storage ring.



<Figure 3.3.1.1> Concept diagram of the beamline interlock system.

<Figure 3.3.1.1> provides a visual overview of the physical layout and signal flow of the interlock system along the full length of the beamline (0 m to 150 m). Signals from sensors, shutters, valves, and modules monitoring temperature and cooling water are transmitted to the programmable logic controller (PLC) via Remote I/O.

Both the Optical Hutch and Experimental Hutch are equipped with local human-machine interface (HMI) panels, enabling localized monitoring. The Control Room oversees the entire system via fiber-optic communication for real-time signal acquisition and monitoring.

3.3.1.1 System Components and Monitoring Items

The interlock system is integrated with various sensors and control modules located at key junctions of the storage ring and beamline, where interlock conditions may arise. The primary parameters monitored or controlled include:

- **Vacuum Status:** Real-time monitoring of high-vacuum conditions in the beamline
- **Safety Shutters and Valve Control:** Status verification and emergency closure
- **Cooling Water (LCW) and Temperature:** System shutdown in case of low flow or high temperature
- **Storage Ring Status:** Coordinated interlock actions upon abnormal storage ring operation
- **Radiation Safety and Emergency Access:** Access control and status monitoring for the Optical and Experimental Hutches

3.3.1.2 System Design Standards

The interlock system is designed to satisfy the following engineering standards:

- **Reliability:** Must function stably even in unexpected situations
- **Fail-Safe Design:** Should default to a safe state automatically upon failure
- **Redundancy:** Redundant design for key components such as PLCs, sensors, and communication lines to prevent total system failure

- **Shielded Cabling and EMI Protection:** Shielded cables and fiber-optic communication ensure immunity from electromagnetic interference (EMI)

3.3.1.3 System Configuration and Operation

The interlock system is categorized functionally and geographically into the following modules:

- **Front-End**
  - Located between the storage ring and the beamline
  - Includes PSI/MIS modules, Remote I/O, Safety Shutter, Gate Valve, and Temperature Sensor
  - Automatically closes shutters upon abnormal vacuum or storage ring state
  - PSI/MIS warning signals are transmitted to the interlock PLC
- **Optical Hutch & PTL**
  - Equipped with HMI Panel, sensors, and interface modules
  - Serves as an intermediate interface for the Beamline Interlock System
  - Provides real-time monitoring, access control, and status display
  - Controls optical shutters and vacuum valves
- **Experimental Hutch**
  - Local HMI Panel and Emergency Sensors
  - Allows users to operate and monitor the experimental section of the beamline
  - Emergency stop switch triggers immediate shutter closure and system halt
  - Monitors temperature and LCW flow anomalies
- **Control Room**
  - Oversees the entire interlock system via Experimental Physics and Industrial Control System (EPICS)
  - Gathers long-distance real-time signals using fiber-optic links
  - Does not perform direct device control

3.3.2 Programmable Logic Controller-Based Beamline Interlock System Design

The beamline interlock system is driven by a PLC, a standard platform in industrial automation and accelerator facilities. Since various guidelines are presented for securing reliability and responding to failures of the PLC system, it is easier to configure the system than other types of controllers. The beamline interlock should be configured to protect users from beamline radiation and ensure high availability by considering device failure situations (PLC failure, vacuum accidents, component overheating, etc.).

In addition, designing for high reliability that takes into account the safety and reliability of data is essential. The connection between the local PLC and the Control Room uses the industrial Ethernet protocol (PROFINET) to communicate. It also features the ability to provide services for users by linking with EPICS input/output controller (IOC). <Figure 3.3.2.1> shows the configuration of the local PLC CPU redundancy and the Remote I/O local devices of the beamline interlock system. The local PLC is redundant with two PLCs. The two PLCs are programmed with the same content to perform the same function. The purpose of redundant control systems is to ensure that the beamline interlock operates normally through the other system even if a problem occurs in one system. In the event that both systems are inoperable, the Photon Shutter and Safety Shutter are designed to close for the safety of the user and equipment.

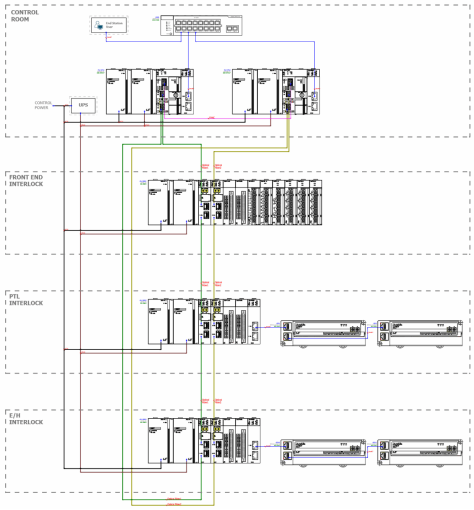
3.3.2.1 Programmable Logic Controller System Configuration Diagram

The PLC-based interlock system is organized into the following functional blocks:

- **Control Room**
  - Operator interface (HMI), EPICS IOC server, PROFINET-based Ethernet communication equipment
  - Dual connection to local PLC under UPS power supply
  - User operation at the end-station
- **Front-End Interlock**
  - I/O modules for Gate Valve and Safety Shutter control

  - Multi-channel Remote I/O expansion slots installed
  - Dual PROFINET-based communication lines (Main + Backup)

- **PTL Interlock / Experimental Hutch Interlock**
  - Remote I/O modules installed in Optical Hutch and Experimental Hutch
  - Local control by sensing signals such as temperature, LCW, vacuum, emergency stop, etc.
  - Independent control structure for Safety Shutter and Photon Shutter



<Figure 3.3.2.1> Configuration of interlock CPU redundancy and Remote I/O.

3.3.2.2 Redundancy – Dual Programmable Logic Controller Structure

The local PLC is configured in a redundant (dual PLC) structure:

- Each PLC is designed to perform the same control functions.
- Identical logic and programs are loaded into both PLCs so that, in the event of a single failure, the other PLC immediately takes over operation.
- If one of the two PLCs fails, the overall system continues to operate without interruption.

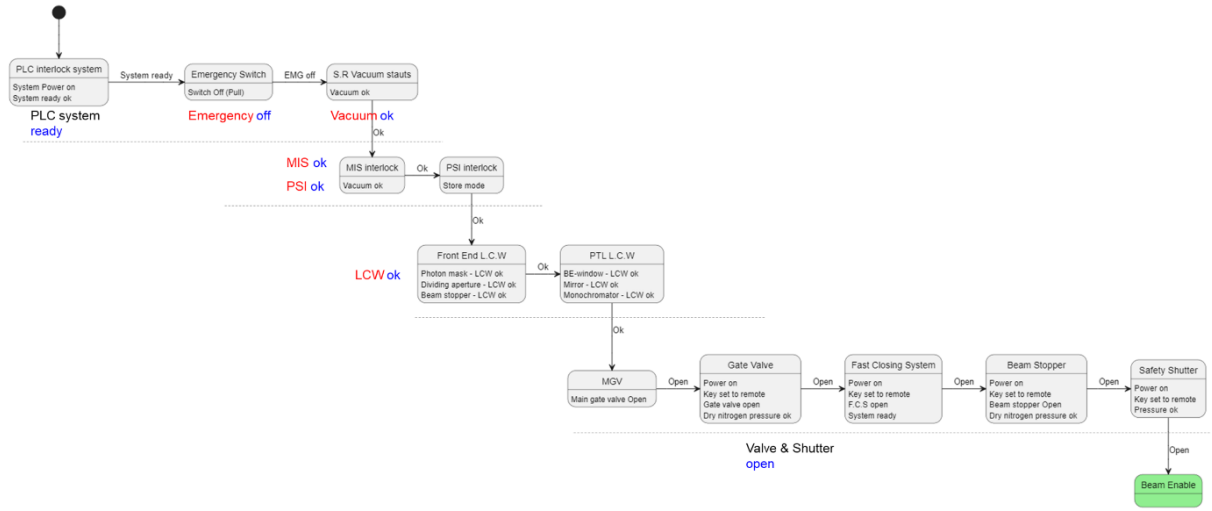
Fail-over and worst-case response:

- If both PLCs become non-functional, the Photon Shutter and Safety Shutter automatically close.
- This structure functions as the final safety mechanism to protect human life and high-value equipment.

3.3.3 Beamline Interlock Operation Sequence

This section outlines the overall operational flow of the beamline interlock system and the corresponding state transitions. The system is designed to sequentially satisfy multiple safety conditions before transitioning to the “Beam Enable” state. This ensures the safety of both personnel and equipment.

The entire sequence proceeds in the following order: PLC Interlock System ready → Emergency switch off → Vacuum OK → PSI/MIS Interlock OK → Normal LCW state → Gate Valve/Shutter open → Beam Enable.



<Figure 3.3.3.1> Interlock system operation sequence and state transition diagram.

<Figure 3.3.3.1> visualizes the conditional flow required for a PLC-based beamline interlock system to enter the Beam Enable state. The system transitions only when power status, vacuum level, emergency switches, storage ring and hutch interlocks, LCW status, and the position/status of various valves and shutters are all confirmed to be normal.

3.3.3.1 Terminology

- **Emergency signal:** A signal triggered by an emergency switch installed in the beamline or hutch, intended for immediate action in dangerous situations. Among the interlock system signals, this is the only one that operates based on user judgment rather than device status.
- **Vacuum fail:** A signal from the vacuum gauge that detects conditions outside the specified vacuum range. It is triggered when vacuum pressure exceeds

the allowable limit or if contamination occurs. Cold cathode gauges are used for monitoring, and FCS should be installed in the front-end section of each beamline branch, with at least one gauge installed downstream.

- **LCW fail:** A signal output from a flow switch installed in the cooling water (LCW) pipeline used for cooling beamline components. It is triggered when the flow rate falls below a predefined threshold.
- **MIS, PSI:** Signals exchanged between the MIS system operated from the machine control room and the beamline interlock system.

3.3.3.2 System Operation Flow

1. **PLC Interlock System Startup**
    - PLC Interlock System: System Power ON / System Ready OK
    - Ensures that the system is ready to perform interlock judgment and control
    - Requires successful power-on and initialization of PLC hardware and redundancy modules
2. **Emergency Switch Status Check**
    - Emergency Switch: Switch OFF (pulled out)
    - The Emergency Switch must not be pressed
    - Manual reset is required for the system to return to normal
    - Ensures operator safety (system is blocked if Emergency Switch is pressed)
3. **Storage Ring Vacuum Status Check**
    - Storage ring vacuum status: Vacuum OK
    - Vacuum in the storage ring must meet low-pressure criteria
    - "Vacuum OK" is set when vacuum falls below the threshold
    - If Vacuum Fail occurs $\rightarrow$ triggers interlock $\rightarrow$ automatically closes Fast Closing Shutter
4. **PSI / MIS Interlock Judgment**

- PSI (Personnel Safety Interlock): must be in normal state
- MIS (Machine Interlock System): must also be in normal state

5. **Front-End LCW Status**
   - Front-End LCW: All equipment LCW OK
   - Flow switches confirm sufficient LCW supply to the front-end masks (Parasitic Mask, Fixed Mask, and Movable Mask), the Photon Shutter, and the beam stopper [1]
   - LCW flow must be detected as normal on each line
6. **PTL LCW Status**
   - PTL LCW: beryllium window, Mirror, etc. LCW OK
   - Cooling status of optical components in PTL must be verified
   - If abnormal flow is detected in Mirror/Monochromator $\rightarrow$ LCW Fail triggered
7. **Main Gate Valve (MGV)**
   - Main Gate Valve: Open
   - Valve can be opened once vacuum is stabilized
   - Requires satisfaction of pressure and control signal conditions
8. **Gate Valve**
   - Power ON / Key Set to Remote / Dry N_2 Pressure OK
   - All conditions must be met: system powered, key in Remote position, nitrogen pressure sufficient
   - Only then can the valve be opened
9. **FCS**
   - Dedicated shutter designed to close rapidly in vacuum emergencies [1]
   - Requires “System Ready” and valid key setting
10. **Beam Stopper**
    - The beam stopper must be confirmed to be in the open position

- If this condition is not satisfied, the sequence does not proceed to the Beam Enable state

11. **Safety Shutter**
    - Only allowed to open when all conditions are satisfied
    - Automatically closes if any abnormal condition is detected
12. **Final State: Beam Enable**
    - When all conditions are met and confirmed as “OK,” the Safety Shutter opens as the final step, and the system transitions into the Beam Enable state.
    - From this point, the beam can be supplied under experimental conditions.

References

[1] Jongha Park et al. High Heat Load Front-End Mechanical Design and Thermal Analysis Report. Internal Document PAL-INT/ME-2026-003. Pohang Accelerator Laboratory, June 2026.

3.4 Beamline Control (EPICS)

3.4.1 Overview

The KLS beamline control system is responsible for controlling and monitoring the status of all hardware constituting the beamline, including optical instruments, diagnostic devices, and actuators. This section describes: (i) an EPICS-based control framework to integrate beamline devices into the accelerator standard control environment, (ii) motion and device control for applications requiring high precision and real-time performance, and (iii) the deployment plan for beam diagnostics and a vision system that enables intuitive, visual assessment of the beam condition.

3.4.2 EPICS-Based Distributed Control Framework

3.4.2.1 EPICS 7 and Input/Output Controller Development

A software engine will be established to connect all beamline devices using the accelerator standard protocol. Most beamline components, except detectors, will be implemented as Soft IOCs, and multiple IOCs will exist as device servers for each hardware device.

EPICS 7 will be adopted as the core foundation of the control system.

To improve reliability, enhance performance, and facilitate documentation during module development, standardized synApps will be actively utilized.

This approach provides a robust hardware abstraction layer enabling seamless integration of diverse beamline instrumentation and motion/actuation equipment in a distributed control environment.

3.4.2.2 Data Communication Network

Next-generation communication standards will be adopted to ensure real-time performance and reliability in control data transmission.

Communication between clients and device servers (IOCs) will use a hybrid approach combining the legacy Channel Access (CA) protocol and the latest pvAccess (PVA) protocol.

PVA, a core feature of EPICS 7, supports complex structured data communication over TCP/IP, which is highly advantageous for transmitting measured data together with associated metadata and maintaining them consistently.

PVA can operate in parallel with CA on the same network, allowing existing CA-based clients and IOCs to be used without modification. Furthermore, by packaging structured data (e.g., detector images with their metadata) into a unified payload, PVA reduces the communication bottlenecks typically encountered when transferring high-throughput detector data or complex device states.

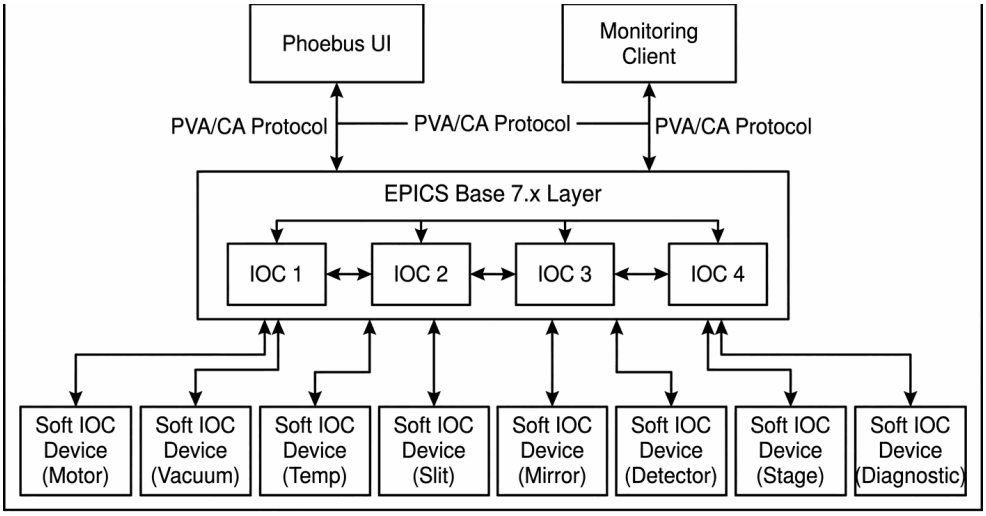
3.4.2.3 Operator User Interface Development Based on Phoebus

An integrated management interface will be developed so operators can intuitively monitor and operate the beamline.

Phoebus will be adopted as the device management and monitoring UI platform, replacing the Eclipse/RCP framework of legacy CS-Studio.

Beamline operators will be able to intuitively inspect and rapidly control device status, motor positions, vacuum levels, and temperature readings through a lightweight yet highly responsive UI.

The overall architecture of the EPICS-based distributed control framework is shown in <Figure 3.4.2.1>.



<Figure 3.4.2.1> Architecture diagram of the EPICS-based distributed control framework.

3.4.3 Motion and Device Control

3.4.3.1 EtherCAT-Based Real-Time Master (TwinCAT3) Implementation

EtherCAT, an industrial Ethernet standard, will be adopted to establish a real-time control environment with a sub-millisecond cycle time (< 1 ms). For devices requiring this deterministic performance, Beckhoff TwinCAT3 will be deployed as the real-time master, minimizing execution jitter and ensuring precise synchronization across the entire system.

To flexibly accommodate frequent changes in experimental conditions and hardware replacement, and to minimize control-network rebooting, physical wiring will follow a star topology.

For general drive systems that do not require real-time control, a TwinCAT XA-based PC-type PLC will be used to secure both stability and flexibility of the motion system.

3.4.3.2 Precision Control of Optics (Double-Crystal Monochromator/Mirror), Slits, and Motion Stages

Position control will be optimized for the DCM and mirrors, where nanometer-level precision is required.

Non-real-time motor drive systems, which account for approximately 90% of beamline control elements such as optics, slits, and sample stages, will either be consolidated with controllers in a 19-inch rack for maintainability, or installed directly on supports to reduce noise.

PLC tasks will be separated by critical device groups to simplify motor replacement or expansion, and each PLC task will be mapped 1:1 to an EPICS Soft IOC.

In particular, to satisfy motion synchronization requirements between DCM control and ID gap control, both systems will be designed using an EtherCAT/TwinCAT3-PLC combination, enabling precise synchronized control through software configuration alone without hardware modification.

3.4.3.3 Development of a High-Speed Position Synchronization System

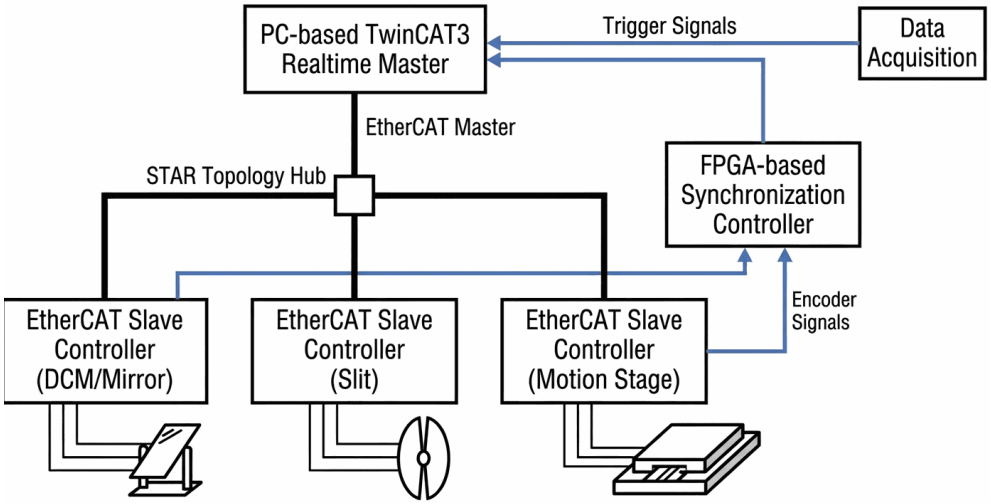
An on-the-fly high-speed scan system will be implemented to achieve hardware-synchronized triggering between continuous mechanical motion and detector

acquisition.

An FPGA-based IOC will be developed and deployed to support data counters and on-the-fly scan functions during high-speed continuous measurements.

The system receives signals generated by the incremental encoders of precision motors as real-time position synchronization inputs, precisely divides them internally, and transmits synchronized trigger signals to data acquisition instruments and detectors.

The configuration of the EtherCAT-based precision motion control system is shown in <Figure 3.4.3.1>.



<Figure 3.4.3.1> Configuration of the EtherCAT-based precision motion control system.

3.4.4 Beam Diagnostics and Vision System

3.4.4.1 Integration of GigE Vision Cameras and areaDetector

High-resolution cameras will be integrated into the control network to monitor the beam profile in real time.

Industrial cameras supporting GigE Vision/GenICam standards will be introduced to precisely determine the photon beam position from the source to the experimental end-station.

Acquired analog/digital images will be converted into digital data via EPICS areaDetector plugins and fully integrated into the IOC control network.

Cameras will be installed at locations including diamond filters for heat-load reduction, YAG screens for position diagnostics, mirrors, and the DCM. Power over Ethernet (PoE) will be applied to simplify cabling, and a dedicated independent camera network of 1 Gbit/s or higher will be established.

3.4.4.2 Real-Time Beam Position Tracking Using a Quadrant Beam Position Monitor Algorithm

A beam position monitoring algorithm will be implemented to track and correct beam motion in real time.

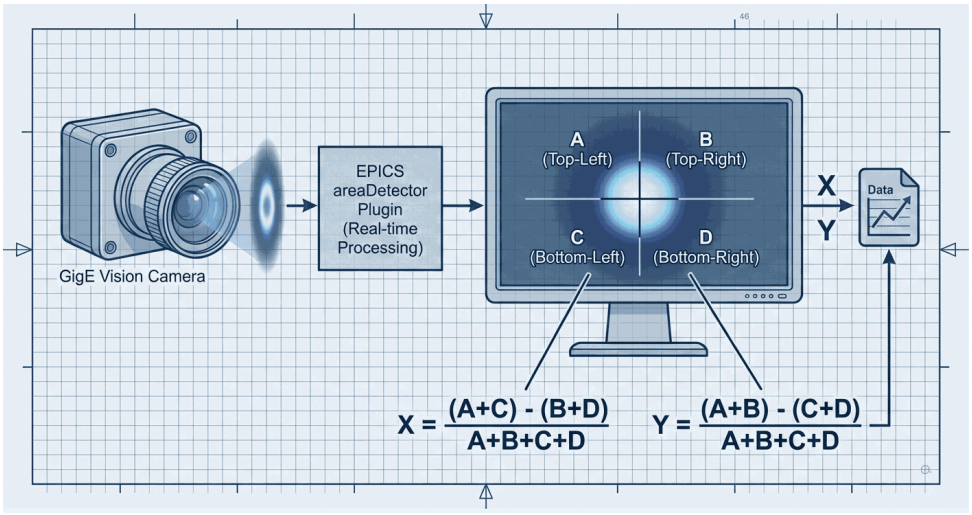
The QBPM algorithm will be applied to image frames provided by areaDetector to calculate the beam centroid position in real time.

A dedicated GUI will be provided to configure four regions of interest (ROIs)—designated as A, B, C and D—on the beam profile image, and the X- and Y-axis displacements will be continuously derived using the following equations:

$$X = \frac{(A + C) - (B + D)}{A + B + C + D}, \qquad Y = \frac{(A + B) - (C + D)}{A + B + C + D} \qquad \text{(Eq. 3.4.4.1)}$$

By optimizing the combination of camera pixel pitch and optical magnification, the system will achieve improved position resolution. This will enable precise tracking of long-term beam position drift while archiving real-time position and intensity data into the control-system archiver.

<Figure 3.4.4.1> shows a conceptual diagram of the vision system and the QBPM algorithm for beam diagnostics.



<Figure 3.4.4.1> Conceptual diagram of the vision system and QBPM algorithm for beam diagnostics.

3.5 Beamline Data Acquisition

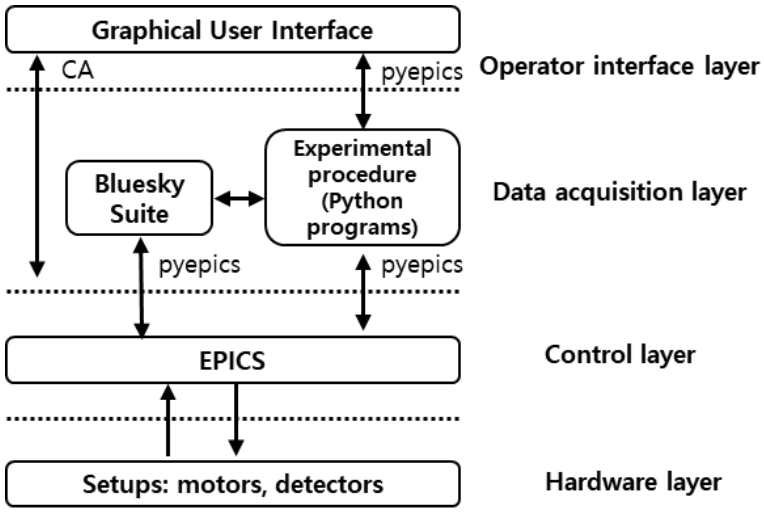
3.5.1 Data Acquisition (DAQ)

3.5.1.1 Detector Interface Integration

The detector interface layer is built on the Bluesky ecosystem, in which each software component plays a well-defined role:

- Ophyd: Abstraction of hardware devices (motors, counters/timers, detectors, instruments, etc.).
- Bluesky: Executes DAQ procedures according to experimental plans using the abstracted hardware.
- Suitcase & Databroker: Store and manage data acquired through Bluesky.

By using Ophyd, Bluesky, Suitcase, and Databroker, a standardized interface can be designed. Equipment such as EPICS PV-based devices, serial/socket devices, custom controllers, and various detectors and motion stages can be abstracted uniformly via Ophyd and then controlled in a consistent manner from Bluesky, as illustrated in <Figure 3.5.1.1>.

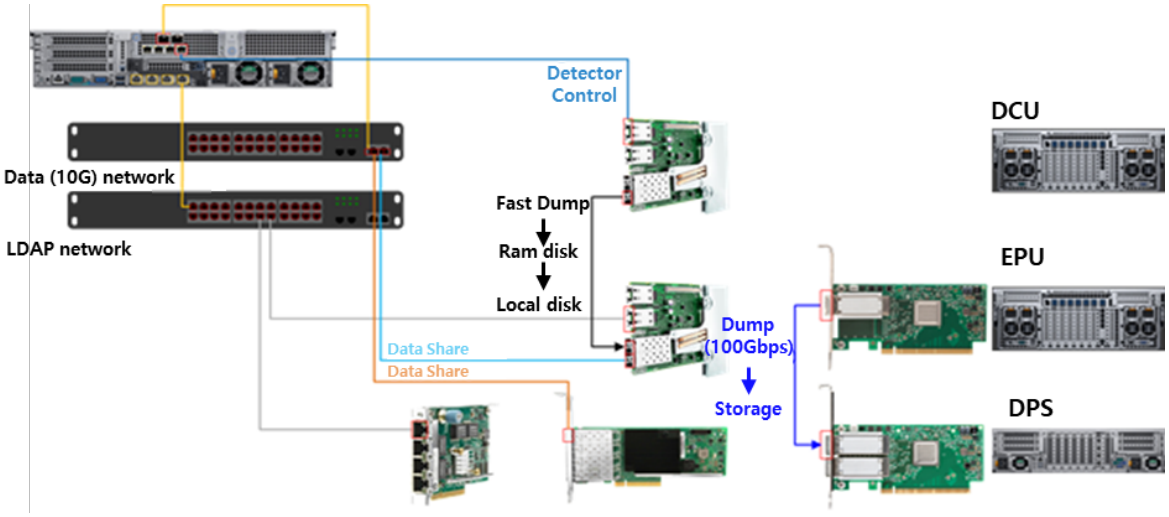


<Figure 3.5.1.1> Control (EPICS) & DAQ (Bluesky) standard framework relationship diagram.

3.5.1.2 High-Speed Data Streaming

DAQ streaming is designed to prevent bottlenecks even at 10/25/100 GbE and beyond by combining (i) dedicated network path separation via Virtual Local Area Networks (VLANs), (ii) near-zero-copy transfer utilizing Remote Direct Memory Access (RDMA) and RDMA over Converged Ethernet (RoCE), and (iii) a high-speed burst-absorption layer based on Non-Volatile Memory Express (NVMe) storage.

RoCE provides low-latency RDMA over lossless Ethernet, and BeeGFS can aggregate storage servers over an RDMA-capable interconnect (such as InfiniBand/RoCE) to deliver high-performance striped I/O, as shown in <Figure 3.5.1.2>.



<Figure 3.5.1.2> Configuration of network and computer system for DAQ.

3.5.1.3 Hardware Synchronization (Triggering)

From the DAQ system perspective, the beamline control system applies a control infrastructure based on EPICS IOCs and EtherCAT/TwinCAT3 PLCs, while the position-synchronized DAQ and synchronous trigger generation required for on-the-fly experiments are implemented using an FPGA-based IOC.

The position-synchronized signal generator produces divided measurement signals and synchronous triggers based on incremental encoder signals, and these signals are used to precisely align the timing of mechanical motion with detector exposure. This enables acquisition of detector data and motion position information on a common reference axis during scanning, thereby ensuring temporal and spatial consistency of the data in continuous scanning experiments.

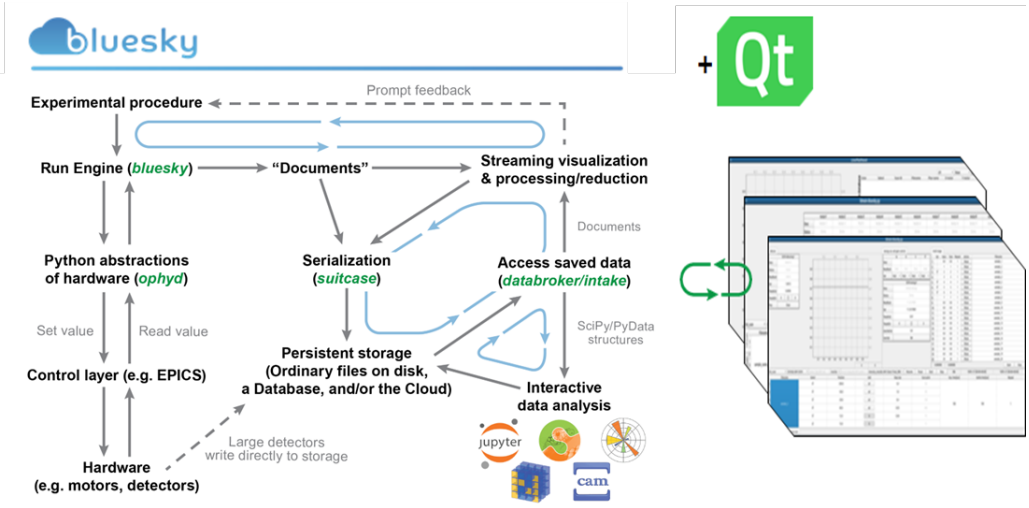
This architecture is applied as a core DAQ technology for accurate triggering,

metadata consistency, and reproducibility of repeated experiments in high-speed data acquisition environments.

3.5.2 DAQ Software

3.5.2.1 Experiment Orchestration (Bluesky Framework)

The DAQ software adopts a Bluesky-based framework for standardized data collection, processing, and analysis. Data collection is provided primarily via a CLI, and a GUI is also developed and provided for static and repetitive DAQ. The development/runtime environment is Python 3.10 or higher; Qt5 is used for the GUI and pyqtgraph for visualization, and the bluesky, ophyd, and databroker packages are used for DAQ, as illustrated in <Figure 3.5.2.1>.



<Figure 3.5.2.1> Example of DAQ processing and document system.

3.5.2.2 Real-time Data Visualization

To enable immediate verification of data quality and device status during experiments, the beamline DAQ system is equipped with an operational environment that includes real-time data visualization. The purpose of this functionality is to support users in promptly assessing the progress of the experiment and detecting any anomalies in the data, so that appropriate actions can be taken, by displaying data collected in real time from detectors, cameras, motion devices, diagnostic devices, and various instruments.

The beamline control/DAQ system integrates all beamline devices, including optical components, detectors, diagnostics, and motion devices, into a distributed control architecture based on EPICS, and is designed so that clients for monitoring, DAQ, and archiving access each device's data via CA and PVA.

The real-time visualization function consists broadly of a real-time image viewer, real-time trend plotting, device status monitoring screens, and an integrated operator GUI. The image viewer allows real-time inspection of beam shape, position, intensity distribution, and alignment status based on images produced by cameras and imaging detectors, and is used as a means to detect, at an early stage, beam position changes, optical system faults, and sample alignment errors that may occur during experiments.

Data stored at the beamline are designed to be searchable and visualizable via Phoebus and web browsers, and a raw data export function and Python interface are provided so that users can reprocess and further analyze the data during or immediately after experiments.

3.5.2.3 Data Cataloging & Metadata Management

A System Overview

In beamline experiments, various types of metadata, such as energy, temperature, pressure, sample information, detector settings, and scan conditions, are generated together with the raw data. This design establishes a Data Cataloging & Metadata Management system to manage these experimental conditions and measurement data in an integrated manner. The system links a Bluesky–Ophyd–Databroker-based DAQ framework with an HDF5-based storage structure so that the metadata catalog and raw data files are consistently connected.

B Storage and Management Structure

Experimental data are stored in HDF5 format and, where possible, managed hierarchically using a NeXus-compatible structure. Metadata are stored in three categories: management metadata such as data identifiers, user information, and beamline information; experimental metadata such as energy, temperature, pressure, sample name, scan conditions, and exposure time; and operational metadata such as transfer status, processing history, and analysis parameters. This enables joint preservation of data and experimental conditions, as well as systematic tracking of data creation and usage history.

C Search and Utilization

Through a Databroker-based metadata catalog, users can search for data using conditions such as energy, temperature, pressure, sample name, beamline, experi-

mental technique, and measurement period. The search results are linked to the corresponding HDF5 data files and post-processing outputs, enabling immediate post-experiment data inspection, condition-based comparative analysis, search for similar experiments, and reuse of long-term archived data. This system improves data reproducibility, discoverability, and usability, while providing a foundation for future expansion to data centers and automated analysis environments.

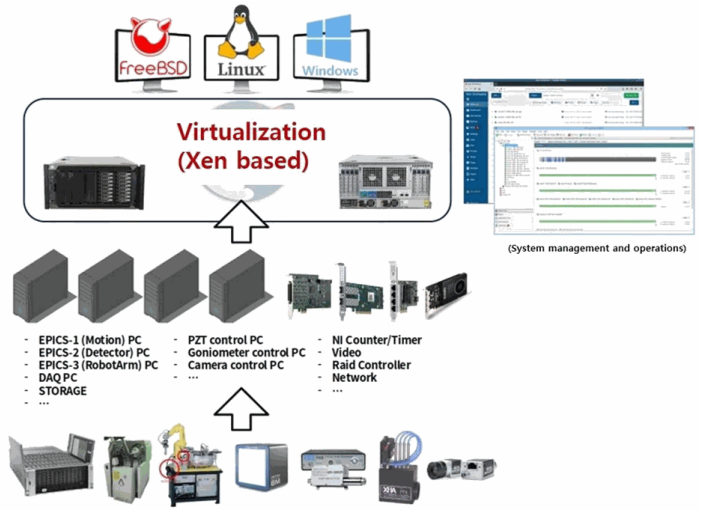
3.5.3 Beamline Computer System

3.5.3.1 Virtualized Computing Environment

The beamline computing environment combines control devices, detectors, DAQ, and analysis software, resulting in complex operating system and software dependencies. To address this, the KLS computing infrastructure is built as a hybrid architecture that combines server virtualization with a container-based analysis environment. Multiple virtual machines are created on top of a powerful central server and operated separately by function, with a strategy for rapid image-based recovery in the event of failures.

The server virtualization layer is implemented with XCP-ng-based virtualization servers, where beamline control, DAQ support, monitoring, databases, and web services are each operated in independent VMs. This standardizes the heterogeneous software environments across devices and enables rapid deployment and recovery using snapshots and templates. The analysis layer is implemented as a container environment based on Docker and Apptainer: web-based services and lightweight applications are provided via Docker, while large-scale scientific computing and reproducibility-focused analyses are provided via Apptainer.

This architecture enhances environmental reproducibility, maintainability, and fault tolerance, and, when integrated with the data center's high-speed network and common DAQ infrastructure, provides a scalable analysis platform. In addition, by validating virtualization performance, security, and data processing workflows in a dedicated testbed in advance, the stability of actual beamline operations can be ensured, as illustrated in <Figure 3.5.3.1>.



<Figure 3.5.3.1> Virtualization application of the beamline computer system.

3.5.3.2 High-Performance Storage (NFS/BeeGFS)

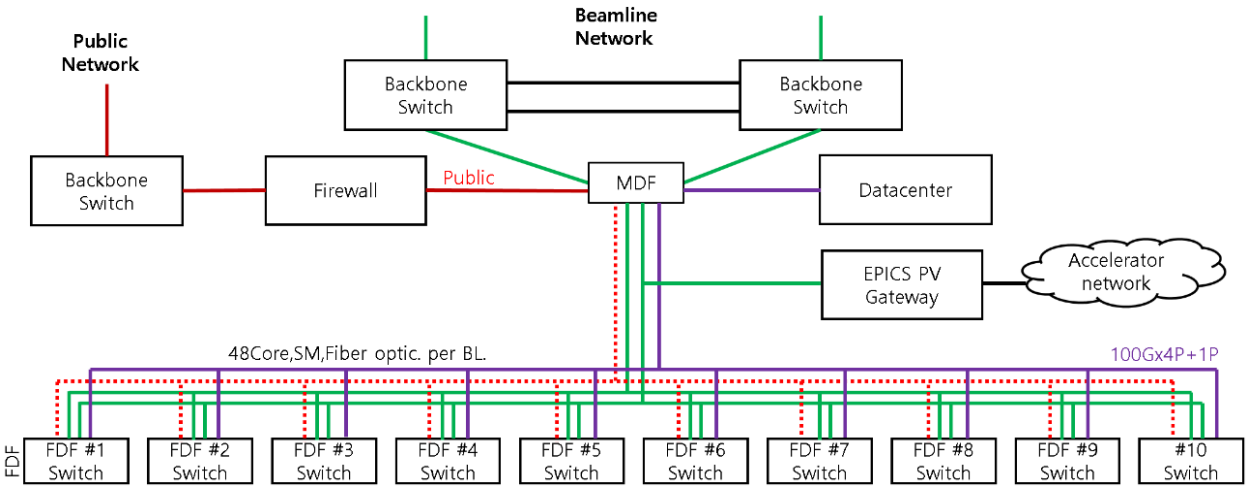
To reliably store large-volume experimental data in real time and make it available for subsequent analysis, a high-performance storage system is established by integrating the beamlines with the central data center. An NFS-based file-sharing system is applied to user home directories, shared workspaces, and analysis result sharing in order to ensure accessibility and ease of operation.

Meanwhile, large raw data generated by detectors are written at high speed to the central storage via a parallel file system such as BeeGFS, which distributes the data across multiple storage nodes. This simultaneously secures real-time data-writing performance and parallel access from many compute nodes, thereby realizing a data-center-based research environment in which DAQ, storage, and analysis are integrated.

3.5.3.3 Dedicated DAQ Network (VLAN)

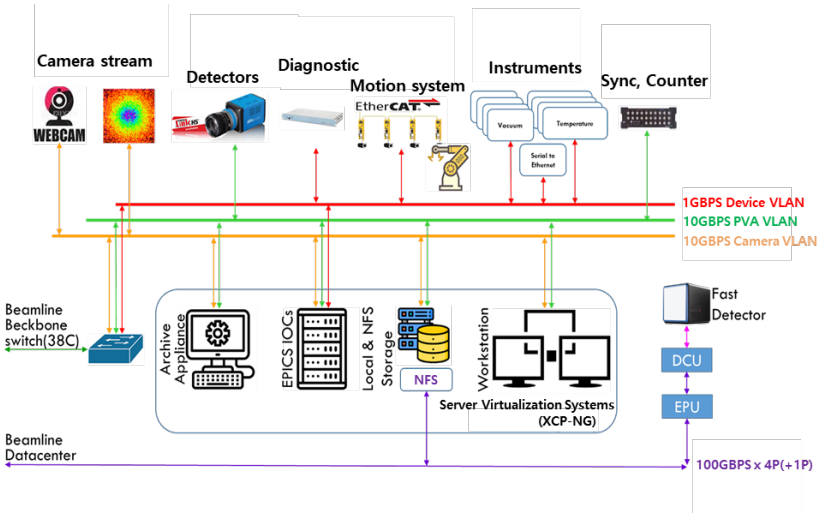
The beamline network is designed according to the basic principle of functional separation into a control network, a camera network, and a DAQ network. The control network is used for device configuration, control, and status monitoring. The DAQ network serves as a dedicated data path that enables high-speed storage and transfer of large 2D/3D experimental data generated by detectors and feeds analysis results from the data center back to the experimental system. To this end, a core switch is installed in the data center, and 48-core optical fiber cables are laid to each beamline. Considering image-intensive beamlines, 10 Gbps

links are applied. In addition, four 100 Gbps links are secured for direct storage to the central data center, and one additional spare link is planned for future analysis-feedback traffic, ensuring scalability, as shown in <Figure 3.5.3.2>.



<Figure 3.5.3.2> Configuration of the entire beamline control network.

Within each beamline, VLANs are configured according to device characteristics to logically separate the camera network (10 G), the Ethernet device network for motion, vacuum, etc. (1 G), and the detector and EPICS networks (10 G). This VLAN-based separation prevents traffic generated in one device group from unnecessarily propagating to others, thereby avoiding interference between control signals and large-volume experimental data and enabling stable data transfer and bottleneck prevention. Data exchange with the accelerator control system is handled through a dedicated EPICS PV Gateway, which enhances both security and traffic-management efficiency, as shown in <Figure 3.5.3.3>.



<Figure 3.5.3.3> Configuration of each beamline network.

3.6 Utility

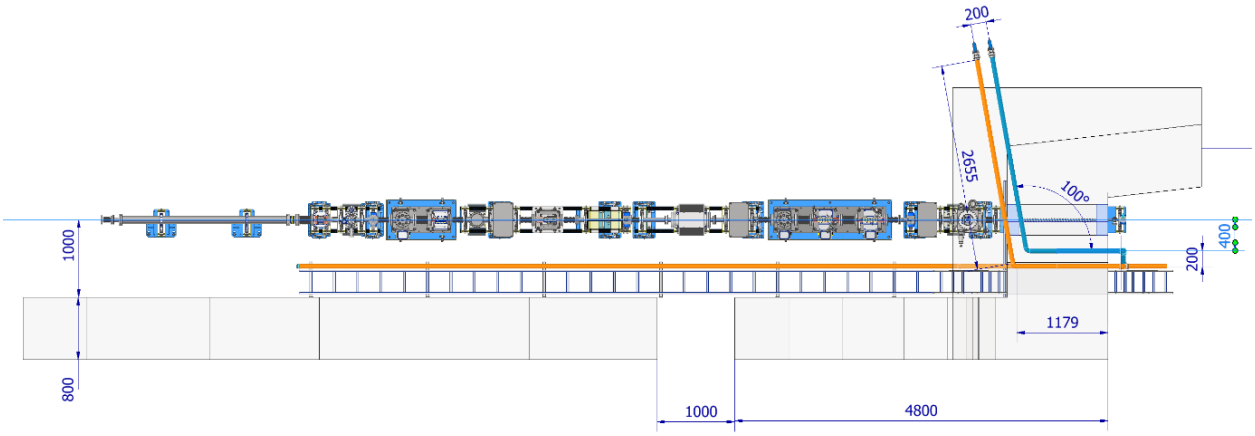
3.6.1 Low Conductivity Water (LCW)

3.6.1.1 Installation for LCW

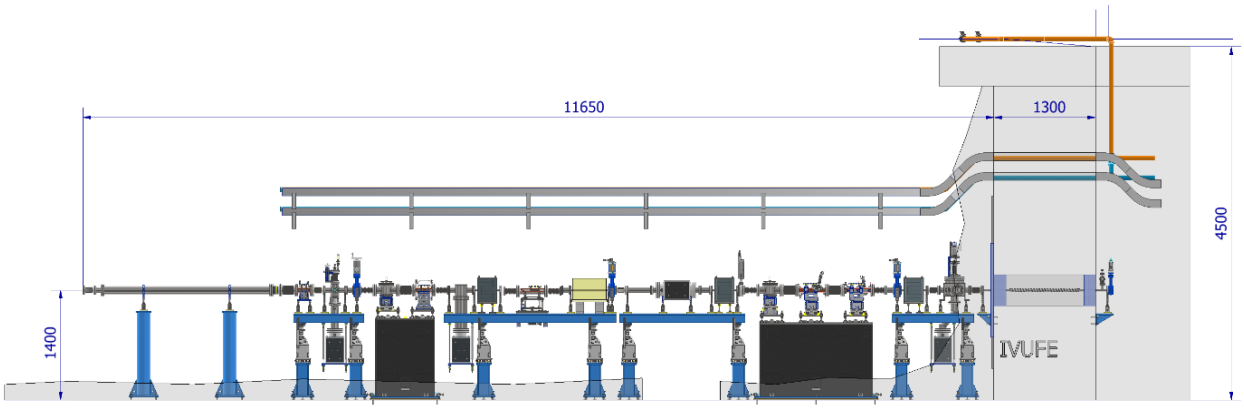
The LCW distribution system for the beamlines shall be installed with sufficient mechanical rigidity to minimize vibration transmitted to precision equipment. Although eliminating vibration sources is the most effective approach, increasing the structural stiffness of the piping system is also essential to minimize vibration displacement and prevent vibration from propagating to adjacent equipment.

The routing of the LCW supply and return piping for the front-end is illustrated in the plan and side views at Port A (<Figure 3.6.1.1> and <Figure 3.6.1.2>) and at Port B (<Figure 3.6.1.3> and <Figure 3.6.1.4>), with an example utility installation shown in <Figure 3.6.1.5> and the routing at the concrete shielding wall shown in <Figure 3.6.1.6>. Considering the limited installation space, both the supply and return lines are planned to be installed at a height of approximately 2.5 m or higher above the floor and supported by the cable-tray support structures.

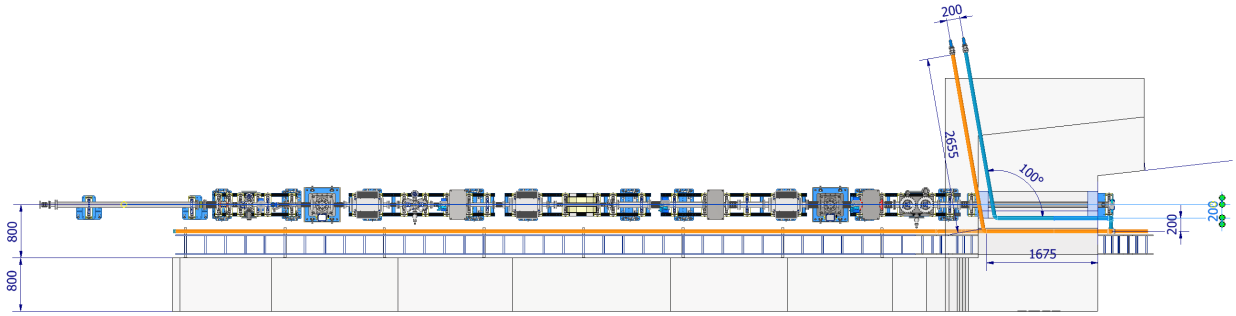
The main LCW distribution piping for the PTL is also planned based on the cable-tray elevation. Cooling water will be distributed through the main piping network to provide the required flow to each beamline component.



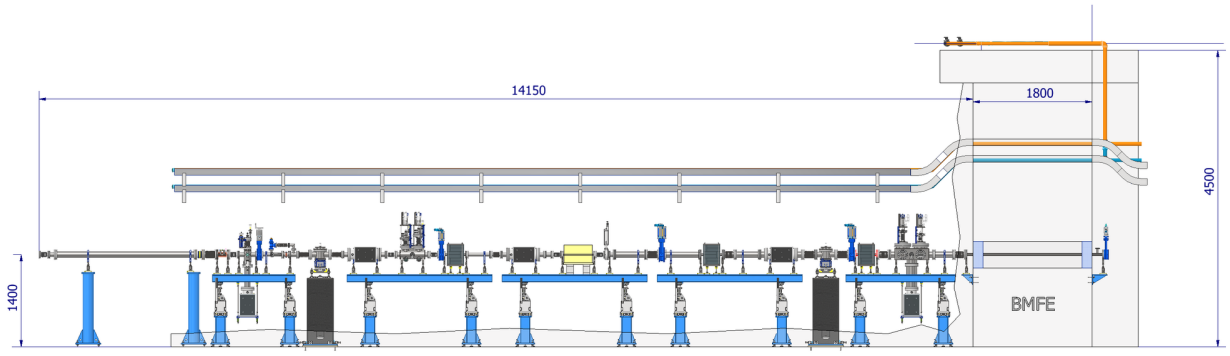
<Figure 3.6.1.1> LCW supply routing for the front-end at Port A (plan view).



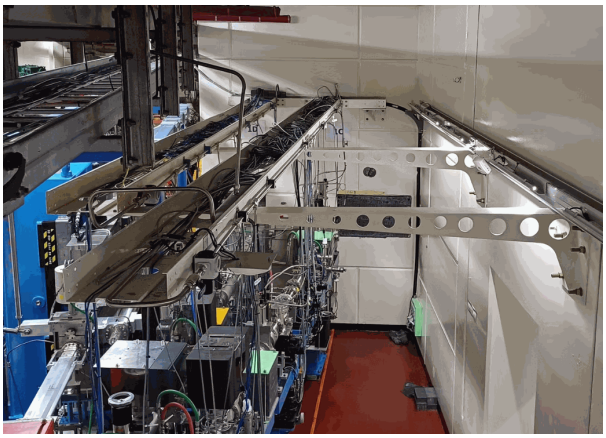
<Figure 3.6.1.2> LCW supply routing for the front-end at Port A (side view).



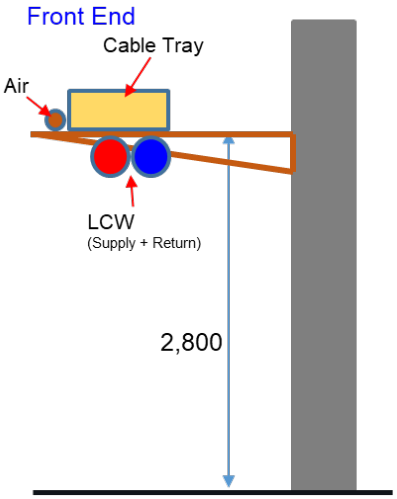
<Figure 3.6.1.3> LCW supply routing for the front-end at Port B (plan view).



<Figure 3.6.1.4> LCW supply routing for the front-end at Port B (side view).

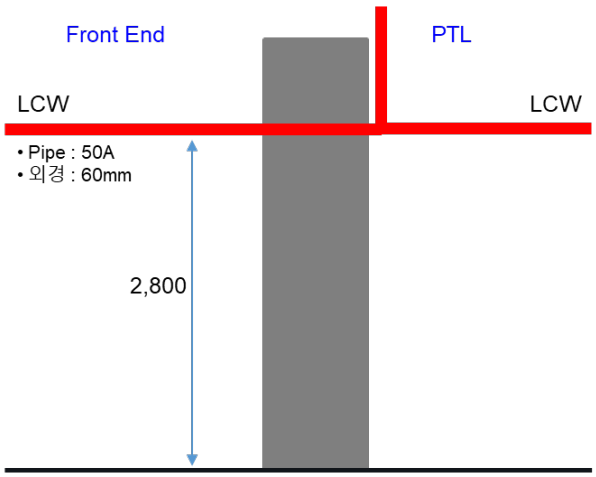


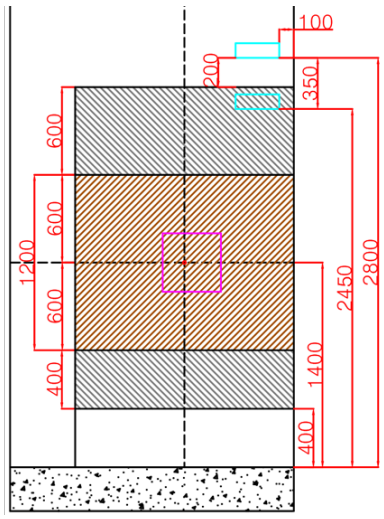
(a)



(b)

<Figure 3.6.1.5> Example utility installation in the front-end. (a), (b) Representative views of the LCW piping arrangement.





<Figure 3.6.1.6> LCW routing at the concrete shielding wall.

3.6.1.2 Leak prevention measures

In general, water leakage most frequently occurs at fitting connections. In most cases, leakage is caused not by defective fittings themselves but by human error during the assembly and tightening process. In addition, flexible hoses may become hardened and deteriorate over time, increasing the risk of damage and subsequent leakage.

To minimize these risks, periodic inspection and preventive maintenance are essential. In particular, the fitting assembly process should be carefully monitored, and post-installation inspections, including pressure tests and bubble leak tests, should be performed to verify the integrity of all connections and ensure reliable operation.

3.6.1.3 Required flow rate (at ID beamline)

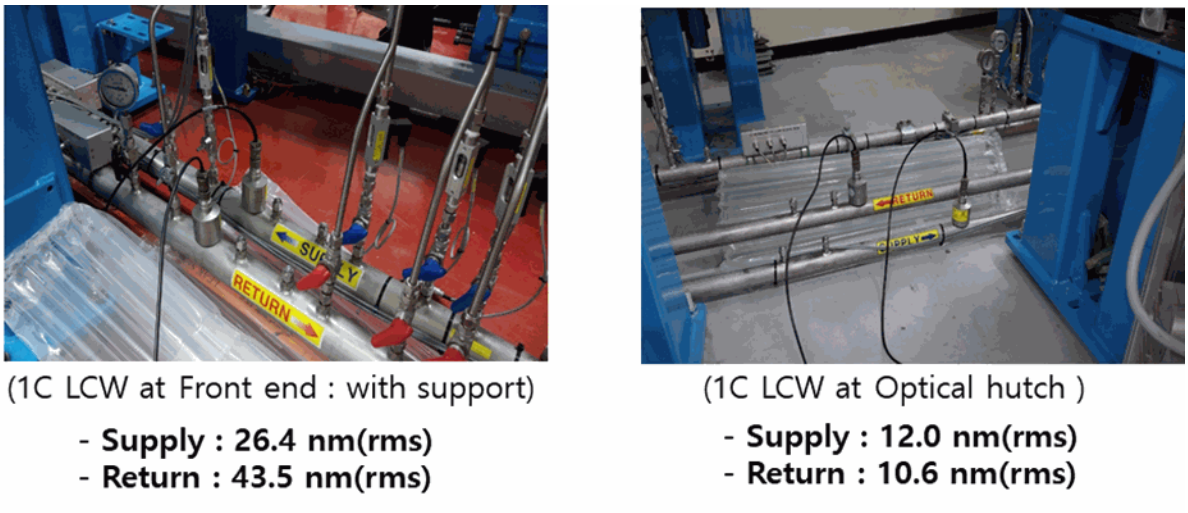
For the ID beamlines, the required cooling water flow rates and outlet temperatures for each component are determined following the corresponding thermal loads [1], as summarized in <Table 3.6.1.1>.

<Table 3.6.1.1> Total flow rate supplied to each component (ID beamline LCW cooling).

Location	Components	Beam power (kW)	Efficiency	Heat load (kW)	ΔT (°C)	Flow rate of item (L/min)	Flow rate (m^3/h)	Inlet temp. (°C)	Outlet temp. (°C)	No. of ports	Flow rate per port (L/min)
Front-end	Parasitic Mask	1.0		1.0	3	10		25	28	2	5
Front-end	Beam Stopper	1.0		1.0	3	6		25	28	1	6
Front-end	PBPM-1	0.03		0.03	0	5		25	25	1	5
Front-end	Fixed Mask	7.7–8.5		8.5	11.5	14		25	36.5	2	7
Front-end	ID Photon Shutter	9.1–9.7		9.7	8	20		25	33	2	10
Front-end	PBPM-2	0.03		0.03	0	5		25	25	1	5
Front-end	Movable Mask-1	4.3–9.7		9.7	14	20		25	39	2	10
Front-end	Movable Mask-2	4.3–9.7		9.7	14	20		25	39	2	10
Front-end	Sum			39.66		100	6				
PTL	Filter	0.16	0.3	0.048	0	5		25	25	1	5
PTL	White beam slit	0.112	1	0.112	0	10		25	25	4	2.5
PTL	White beam BPM	0.03	0.3	0.009	0	10		25	25	2	5
PTL	High Heat Load Mirror	0.112	1	0.112	0	9		25	25	6	1.5
PTL	White beam BPM	0.03	0.3	0.009	0	10		25	25	2	5
PTL	Horizontal DCM	0.112	1	0.112	1	3		25	26	2	1.5
PTL	White beam screen/stop	0.112	1	0.112	0	5		25	25	1	5
PTL	Sum	0.668		0.514		52	3.12				
Total	Total			40.174		152	9.12				

3.6.1.4 Reference for installation

The vibration displacement of the LCW distribution system shall be measured and controlled in accordance with the acceptance criteria established from the Pohang Light Source-II (PLS-II) installation, as illustrated in <Figure 3.6.1.7>. Measurements of the PLS-II system confirmed that the vibration displacements at both the front-end and the optical hutch satisfy the specified criteria, demonstrating excellent vibration performance. Based on these results, an LCW distribution system with a similar configuration will be adopted for the KLS beamlines.



<Figure 3.6.1.7> Vibration displacements of LCW in a PLS-II beamline.

3.6.2 Liquid Nitrogen (LN_2)

3.6.2.1 Purpose

A fourth-generation synchrotron radiation source is characterized by an ultra-low electron beam emittance of less than 100 pm·rad, providing significantly higher brilliance and coherence than previous-generation light sources. Such low emittance corresponds to minimal spatial and angular spread of the electron beam, resulting in an X-ray beam with high brightness, excellent collimation, and a small beam size. These characteristics are essential for advanced applications, including high-resolution X-ray imaging, nanoscale structural analysis, and phase-contrast imaging.

To fully utilize these beam characteristics, precise control of temperature and vibration is essential for maintaining the performance of high-precision optical components. Optical elements such as monochromators, mirrors, lenses, and focusing optics are highly sensitive to thermal expansion and mechanical vibration, and even slight misalignment of the optical axis can significantly degrade beam quality. In the operating environment of a fourth-generation synchrotron source, where ultra-high-resolution measurements and nanoscale imaging are routinely performed, overall system stability is required not only for the optical components themselves but also for vibration-isolated optical tables, temperature-controlled enclosures, active cooling systems, and precision motion-control equipment.

To maintain this high-precision operating environment, a reliable liquid nitrogen (LN_2) supply system and regular maintenance activities are indispensable. LN_2 replenishment and maintenance operations should be carefully scheduled outside the beam service period to prevent temperature fluctuations, vibration disturbances, or interruptions to cryogenic cooling that could adversely affect beam stability and experimental performance.

Accordingly, the facility operation plan should include a comprehensive maintenance strategy covering the LN_2 replenishment cycle, equipment inspection schedule, and availability of backup systems. By maintaining a stable thermal and mechanical environment, the KLS will provide users with highly reproducible and reliable experimental conditions.

A X-ray detector cooling

High-sensitivity X-ray detectors, such as high-purity germanium (HPGe) detectors and silicon drift detectors (SDDs), are typically operated at cryogenic temperatures to reduce thermal noise and improve the signal-to-noise ratio. Liquid nitrogen (LN_2) is commonly used to maintain these detectors at approximately 77 K, ensuring stable and high-performance detector operation.

B Cryogenic sample environment

In structural biology and materials science beamlines, LN_2 is used to maintain samples at cryogenic temperatures to minimize radiation damage during X-ray exposure. Cryogenic devices, such as cryo-streams and cryo-stages, preserve the original state of the samples while reducing radiation-induced degradation, thereby enabling high-resolution imaging and diffraction experiments.

C X-ray optics cooling

The high-brilliance synchrotron beam imposes a substantial heat load on X-ray optical components, including silicon monochromators and X-ray mirrors. Thermal deformation of these optics can degrade optical alignment and beam quality. To maintain precise energy selection and beam focusing, LN_2 cooling is employed to minimize thermal distortion and ensure the stable performance of the X-ray optics.

D Vacuum components cooling

LN_2 is also utilized in vacuum systems to assist in achieving and maintaining a UHV environment. By cooling cryogenic surfaces, residual gases are effectively trapped, thereby improving the vacuum level.

E Sample storage and transportation

LN_2 is widely used for the long-term storage and transportation of temperature-sensitive samples, including biological specimens and cryogenically preserved crystals. Maintaining cryogenic temperatures during storage and transport preserves sample integrity and ensures consistent experimental results.

3.6.2.2 LN_2 pipeline layout

The main LN_2 distribution pipeline shall be routed along the curvature of the storage ring to supply LN_2 to each beamline. The distribution system shall provide a continuous connection from the outdoor LN_2 storage tanks to the cryocoolers installed at individual beamlines within the experimental hall.

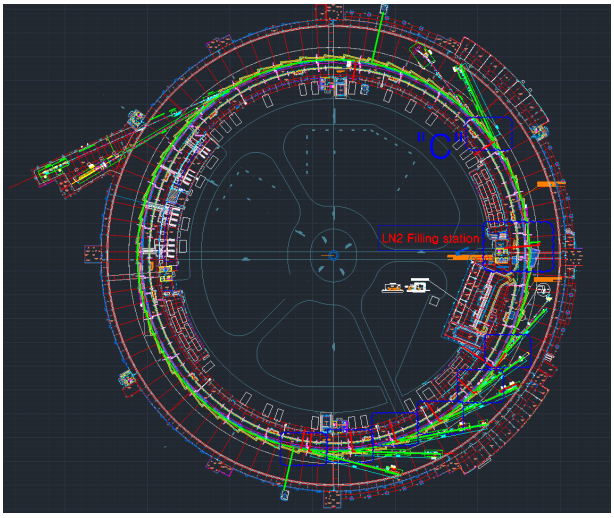
A LN_2 supply points for individual beamlines

LN_2 is supplied from a central filling station located in the infield and distributed from the storage tanks to each beamline, as illustrated in <Figure 3.6.2.1>; the connection from the LN_2 tank to the cryocooler is shown conceptually in <Figure 3.6.2.2>. The LN_2 is distributed through vacuum-insulated piping, the conceptual configuration of which is shown in <Figure 3.6.2.3> and <Figure 3.6.2.4>. Each beamline is equipped with a dedicated cryogenic module or small dewar for supplying LN_2 directly to optical components and experimental equipment. Accordingly, an independent LN_2 distribution point shall be provided for each beamline.

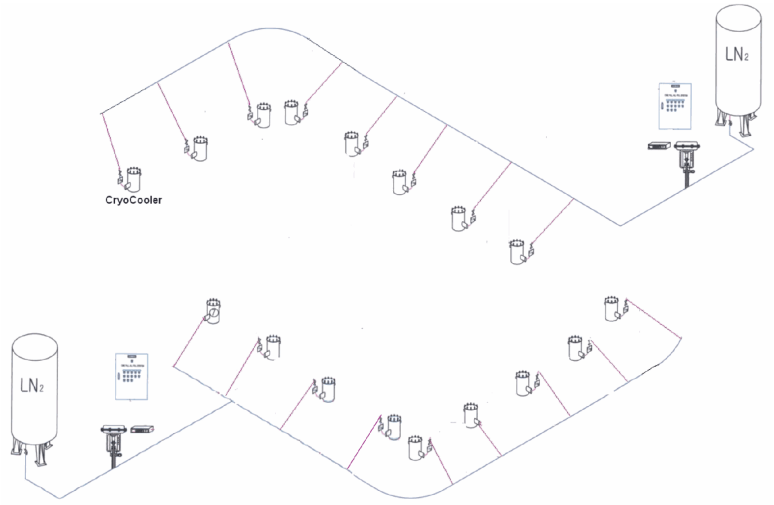
To minimize the length of the supply piping and reduce the response time of the cryogenic system, the locations of the LN_2 distribution points should be determined during the early stage of the beamline layout design in conjunction with the equipment arrangement.

B Filling station

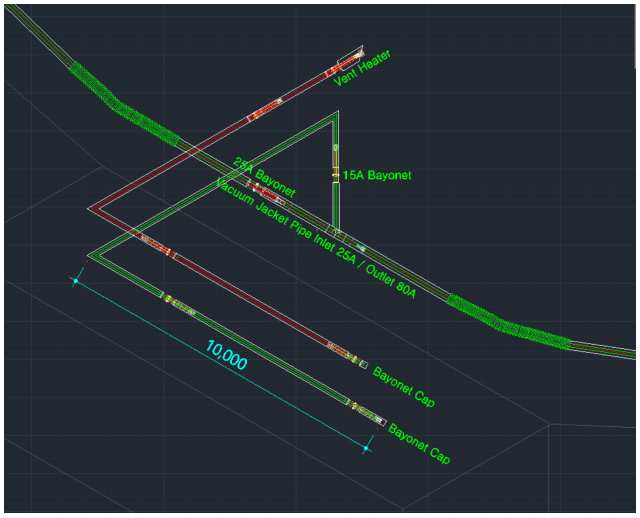
LN_2 is dispensed from a central filling station located in the infield, from which it is distributed to the individual beamlines through the vacuum-insulated piping described above. The general arrangement of the filling station is shown in <Figure 3.6.2.5>.



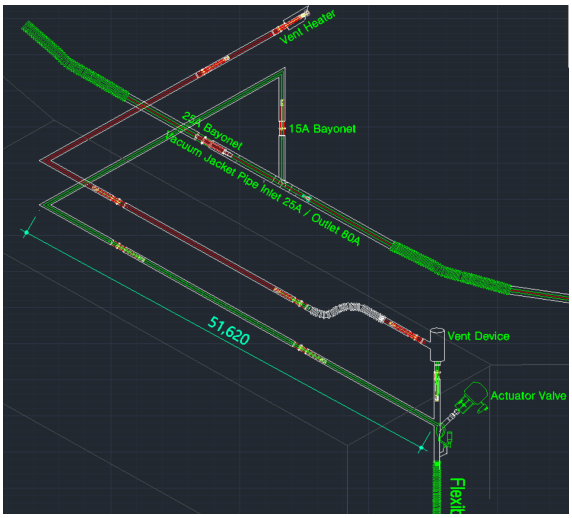
<Figure 3.6.2.1> Plan view for LN_2 supply to the beamlines.



<Figure 3.6.2.2> Conceptual diagram of the LN_2 tank to cryocooler connection.



<Figure 3.6.2.3> Vacuum-insulated piping conceptual chart (1).



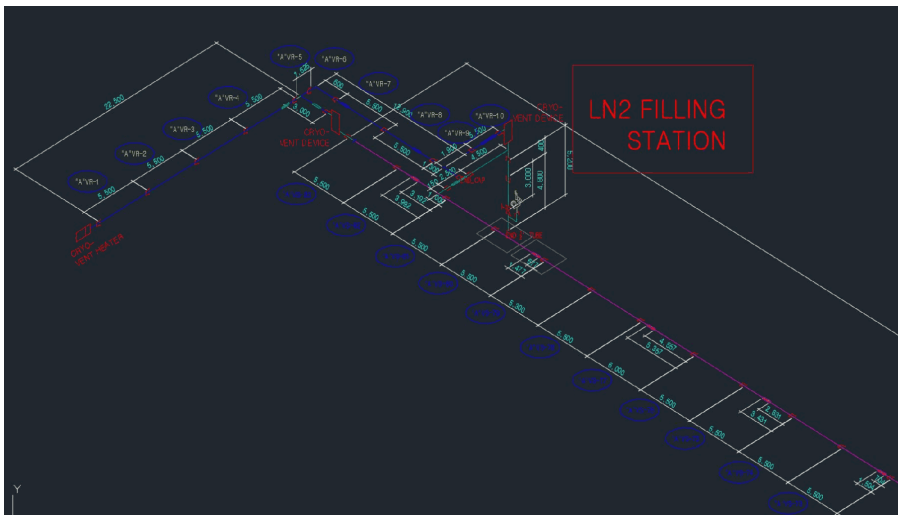
<Figure 3.6.2.4> Vacuum-insulated piping conceptual chart (2).

3.6.2.3 LN_2 design requirement

A Heat-load estimation for the LN_2 cooling system

The light sources for the initial ten KLS beamlines are summarized as follows. The hard X-ray beamlines employ IVU16, IVU20, IVU22, and IVU24 insertion devices, providing synchrotron radiation with a maximum extracted power of up to 18 kW [2]. The soft X-ray beamlines utilize EPU78 and EPU98 insertion devices, while the bending-magnet beamlines are based on a 2 T bending magnet with a critical photon energy of 21 keV.

The heat load for each beamline was evaluated based on the maximum power incident on the DCM, using the full width at half maximum (FWHM) of the central cone as the design beam size. Based on this design criterion, the total heat load on the DCMs of the initial ten beamlines is estimated to be approximately 900 W, as summarized in <Table 3.6.2.1>.



<Figure 3.6.2.5> Diagram of the LN_2 filling station.

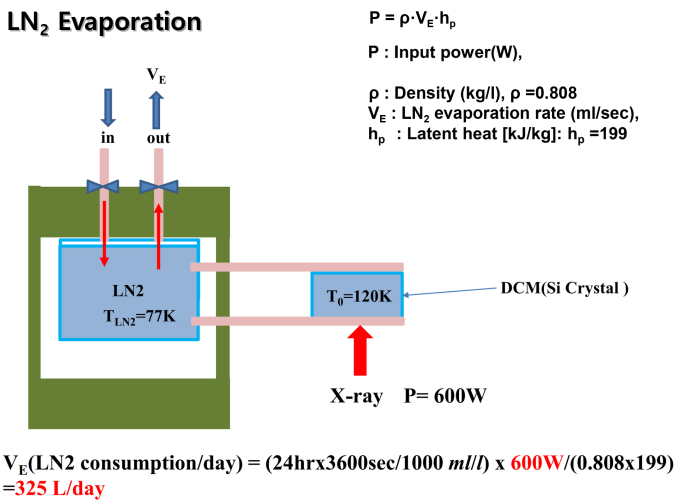
<Table 3.6.2.1> Calculation of the heat load on the DCM for each beamline.

No.	Beamline	Device	Distance from source (m)	Beam size (H×V, mm)	Max total heat load (W)	Cryocooler op. pressure (bar)
ID03	Coherent X-ray Diffraction (CoXRD)	HDCM	60	1.5×1.5	104.7	3–5
ID04	Coherent Small-Angle X-ray Scattering (CoSAXS)	HDCM	32	1×1	160	3–5 (estimated)
ID10	Nanoprobe	HDCM	32	1×1	109	3–5
BM10	High Energy Microscopy (HEM)	–	–		–	None
ID21	BioPharma-BioSAXS (BioSAXS)	DCM	32	1×1	151	3–5
ID22	Bio-Nano Crystallography (BioNX)	HDCM	50	1.36×1.3	75.9	3–4
ID23	Real-Time XAFS (RT-XAFS)	DCM	38	1.55×1.3	196.9	3–5
ID24	Material Structure Analysis (MSA)	DCM	40	1.5×1.5	223.7	3–5
ID25	NanoARPES					
ID26	Soft X-ray Nanoprobe (softNanoprobe)					
	Total				∼900	(including margin)

※ HDCM: horizontal double-crystal monochromator.

B Estimation of LN_2 consumption

The LN_2 consumption is estimated based on the thermal loads of the optical systems and experimental equipment, together with the expected operating time. For optical components requiring cryogenic cooling, such as monochromators and X-ray mirrors, the hourly LN_2 consumption is determined from the heat load of each component and the cooling efficiency of the LN_2 cooling system. The estimation procedure is illustrated in <Figure 3.6.2.6> and <Figure 3.6.2.7>.



<Figure 3.6.2.6> Schematic diagram for estimating the LN_2 evaporation in the DCM.

LN_2 Consumption per day

- Theoretical LN_2 Loss : 53 L/100W/day (≅ 2.21 L/100W/hr)
  Ex) 500 W → 270 L/day, 1500 W → 810 L/day

- ID03, ID04, ID10, ID21, ID22 ID23(Q), ID23, ID24(3,600W)
  → 450 W * 1 BLs = **245 L/day/1BLs**
  → 245 L/day * 8 BLs ≅ **2,000 L/day/8BLs**

- 1 Protein crystallography cold streams
  → 150 L/day * 1 stations = **150 L/day**

- LN_2 filling station
  → **250 L/day**

- LN_2 Transfer line
  → 2,000m * 2 W/m = 4,000 W
  → **2,160 L/day**

Total : ≅ 4,600 L/day
Total : ≅ 9,000 L/day +α (+Phase Ⅱ beamlines (16 ea) + etc)

<Figure 3.6.2.7> Calculation of the total daily LN_2 consumption.

3.6.2.4 LN_2 storage tank

The KLS LN_2 storage tanks will be installed at the southern and northern infield areas of the storage ring to supply LN_2 to the ten beamlines through the cryogenic distribution pipeline. The principal design requirements for the LN_2 storage tanks are summarized as follows.

The storage capacities of the two LN_2 tanks are 30 tons and 40 tons, respectively. Each storage tank shall be designed for a maximum design pressure of 1.0 MPa and a normal operating pressure of 0.5 MPa. The design operating temperature range shall be 77–330 K.

The storage tanks shall be designed and fabricated in accordance with the applicable ASME Code. The inner vessel, which is in direct contact with LN_2, shall be manufactured from ASTM A240 Type 304 stainless steel (or equivalent SUS 304 material), while the outer vessel shall be fabricated from structural carbon steel.

To minimize heat leakage, the annular space between the inner and outer vessels shall be at least 300 mm and insulated using a multilayer vacuum insulation system filled with perlite. This insulation system is designed to minimize heat transfer by conduction, convection, and radiation. The vacuum level shall be maintained at $\leq$0.05 Torr under warm conditions and $\leq$0.02 Torr under cold conditions, thereby limiting the daily evaporation (boil-off) rate to less than 0.3%.

In accordance with the Korean High-Pressure Gas Safety Control Act, the pressure relief system shall incorporate a three-way valve arrangement with one standby safety valve to allow maintenance without interrupting operation. Vacuum-insulated piping, including the emergency shutoff valve and flow-control valve assemblies, shall maintain a vacuum level better than 1×10^{-6} Torr to minimize heat ingress.

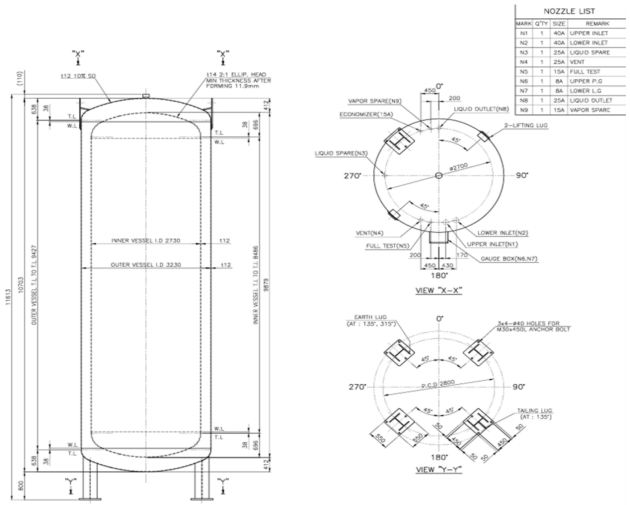
All pressure relief valves shall have a set pressure of 10 bar and shall be certified by the Korea Gas Safety Corporation (KGS).

To ensure safe operation, the LN_2 storage tanks shall be equipped with a remote monitoring and control system. The instrumentation shall enable continuous monitoring of the operating status and provide the information required for safe facility operation.

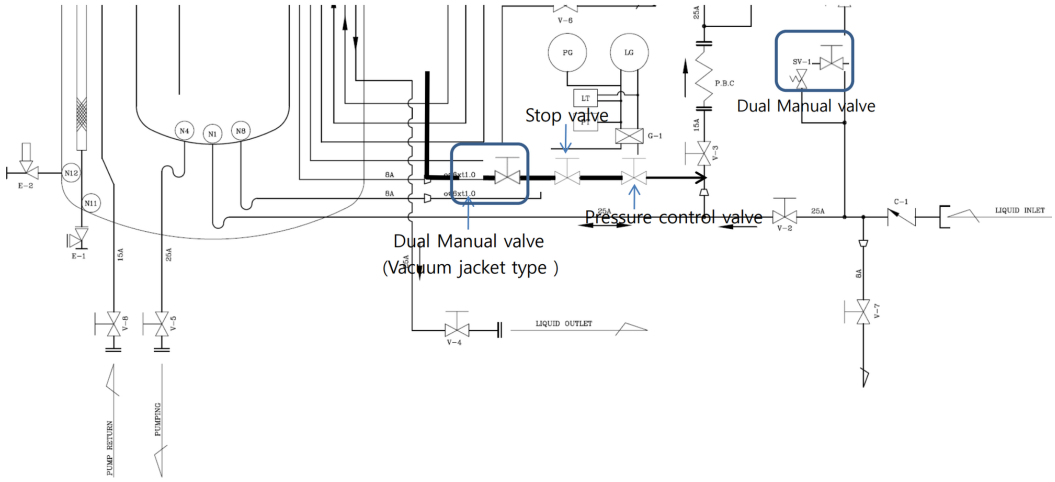
Each storage tank shall be equipped with a pressure transmitter (PT), pressure indicator (PI), level transmitter (LT), and level indicator (LI). These instruments shall support both local indication and remote monitoring through signal trans-

mission to the central control system. Instrumentation with a standard 4–20 mA output signal, such as products manufactured by Rosemount, shall be employed for system integration.

The storage-tank configuration and its pressure-control valve arrangement are shown in <Figure 3.6.2.8> and <Figure 3.6.2.9>, and the principal design values are summarized in <Table 3.6.2.2>.



<Figure 3.6.2.8> LN_2 storage tank drawing.



<Figure 3.6.2.9> Pressure-control valve diagram of the LN_2 tank.

<Table 3.6.2.2> Design values of the LN_2 storage tank.

Description	Value	Remark
LN_2 storage tank capacity	30 ton, 40 ton	One tank of each capacity
Design pressure	1.0 MPa	
Operating pressure	0.5 MPa	
Operating temperature	77–330 K	
Tank material	Inner vessel: SUS 304 Outer vessel: SS 275	
Vacuum level (storage tank)	Warm condition: $\leq$0.05 Torr Cold condition: $\leq$0.02 Torr	
Vacuum level (vacuum-insulated piping)	$< 1 \times 10^{-6}$ Torr	
Control & Manual valve	25A, KYOEI	
Safety valve	10 bar, PSV, 3-Way Type	One standby valve included
Instrumentation (PT, PI, LT, LI)	DC 4–20 mA	
Applicable code	ASME Boiler and Pressure Vessel Code, Section VIII	

3.6.2.5 Maintenance

A Optimized LN_2 refilling schedule

An optimized LN_2 refilling schedule shall be established based on the consumption pattern of each beamline. Depending on operational requirements, either an automatic refilling system or a scheduled manual refilling plan may be adopted. Refilling operations shall be performed outside the beam service period, preferably during nighttime or other scheduled maintenance windows. Considering the user operation schedule and the beamline maintenance period, LN_2 refilling shall be coordinated with the regular beamline maintenance cycle to minimize any impact on user experiments.

B Redundant supply system

A redundant LN_2 supply system shall be provided for critical equipment by installing dual dewars or backup storage tanks. This configuration shall ensure stable operation for at least 24 hours in the event of an interruption to the primary

LN_2 supply.

For operational safety, the system shall be equipped with nitrogen concentration sensors, temperature sensors, and leak detectors for continuous condition monitoring. An automatic alarm system shall immediately notify operators whenever abnormal operating conditions are detected.

C Preventive maintenance

A preventive maintenance program shall be established for all major components, including valves, vacuum-insulated piping, and thermal insulation materials. Periodic inspections shall be scheduled to ensure long-term system reliability, and maintenance activities shall be performed during non-operational periods to maintain uninterrupted beamline operation and experimental continuity.

3.6.3 Hutch

The hutch system is classified into two categories: the optical hutch and the experimental hutch. Depending on the characteristics of each beamline, these enclosures provide essential radiation shielding during beamline operation. The optical hutch accommodates various optical components and diagnostic equipment, whereas the experimental hutch houses the experimental apparatus used for scientific research.

The configuration and dimensions of each hutch are determined based on the requirements of the corresponding beamline. Since the radiation shielding specifications are largely common among the beamlines, standardization of the hutch design is an important consideration. Depending on the radiation shielding requirements, the hutch may be constructed from reinforced concrete or modular steel shielding panels incorporating lead. The entrance door may be either a manual sliding type or a swing type. Whenever practical, a large access door or removable roof panels should be provided to facilitate the installation and maintenance of large experimental equipment. In addition, shielding windows, safety interlocks, electrical panels, gas-cylinder ports, exhaust hoods, and removable lead blocks shall be installed at appropriate locations; the placement of the hutch access-control and emergency-stop devices is specified in the beamline interlock system design report [3]. The overall dimensions and configuration of each hutch shall be determined according to the specific requirements of each beamline.

3.6.3.1 Radiation shielding criteria

The shielding materials and required thicknesses for the hutches were determined based on the radiation shielding analysis performed for the beamlines. For the optical hutch, local shielding shall be provided around components that may be directly exposed to the X-ray beam in order to satisfy the prescribed radiation dose limits. The resulting design criteria are summarized in <Table 3.6.3.1>.

<Table 3.6.3.1> Design criteria for radiation shielding.

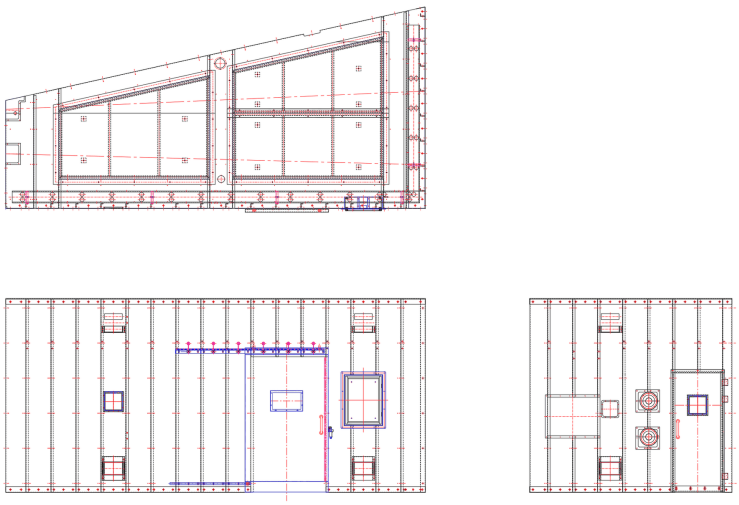
Radiation shielding material	Optical hutch	Experimental hutch
Fe	6 mm	5 mm
Pb	3 mm	–

3.6.3.2 Structure of the optical hutch

The optical hutch is located at the entrance of the PTL, where the X-ray beam is transported to the monochromator and other optical components. Since this region is exposed to a relatively high radiation level, the optical hutch provides the primary radiation shielding between the storage-ring shielding wall and the downstream optical system.

The optical hutch consists of three principal shielding surfaces: the front wall containing the main entrance door, the side walls, and the roof. Each wall is assembled from modular shielding panels approximately 400 mm in width. Every panel adopts a three-layer sandwich structure consisting of steel–lead–steel to achieve the required shielding performance.

To improve structural rigidity, both longitudinal edges of each panel are bent to form stiffening flanges, and the panels are assembled using a modular overlapping configuration. This structural concept is similar to that successfully employed in the PLS-II optical hutch and will be adopted as the reference design for the beamlines. An example design is shown in <Figure 3.6.3.1>.



<Figure 3.6.3.1> Example design of the optical hutch (PLS-II).

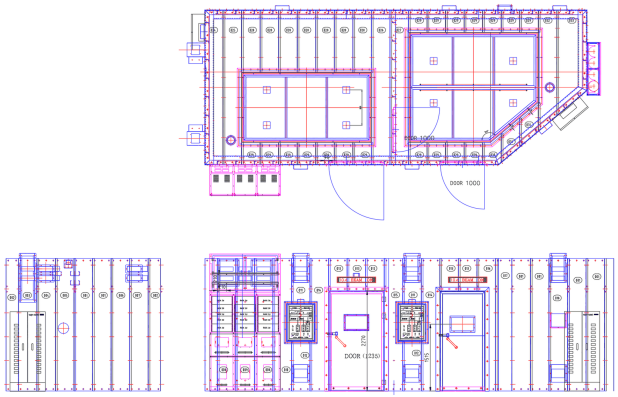
3.6.3.3 Structure of the experimental hutch

The experimental hutch encloses the end-station, where the X-ray beam interacts with the sample during experiments. Radiation shielding is particularly important for hard X-ray beamlines because scattered radiation generated during experiments must be effectively contained. Consequently, experimental hutches

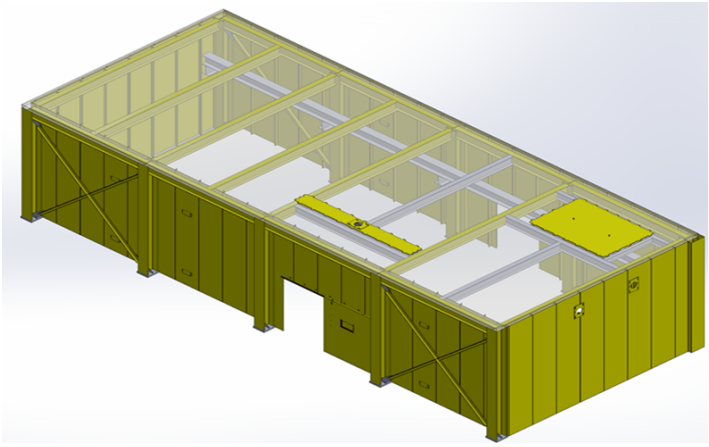
are required for hard X-ray beamlines, whereas they are generally not required for soft X-ray beamlines.

The experimental hutch consists of five shielding surfaces: the front wall containing the main entrance, the rear wall, two side walls, and the roof. The wall construction follows the same modular panel concept as that of the optical hutch, with the panel composition determined by the shielding criteria in <Table 3.6.3.1>.

Because the experimental hutches of the beamlines are expected to be significantly larger than those of PLS-II, additional structural reinforcement may be required. Adequate stiffness shall be achieved by installing structural H-beams at appropriate intervals to ensure long-term mechanical stability and provide a stable experimental environment. Example designs are shown in <Figure 3.6.3.2> and <Figure 3.6.3.3>.



<Figure 3.6.3.2> Example design of the experimental hutch (PLS-II).



<Figure 3.6.3.3> Example design of the experimental hutch (PAL-XFEL).

References

[1] Jongha Park et al. High Heat Load Front-End Mechanical Design and Thermal Analysis Report. Internal Document PAL-INT/ME-2026-003. Pohang Accelerator Laboratory, June 2026.

[2] Hyungseok Choi and Jongha Park. Beamline Photon Source Analysis Report. Internal Document PAL-INT/ME-2026-007. Pohang Accelerator Laboratory, July 2026.

[3] Minho Seo and Chaesoon Lee. 4GSR Beamline Interlock System Design Report. Internal Document PAL-INT/EE-2026-012. Pohang Accelerator Laboratory, July 2026.

Chapter 4. Beamline Science and Application

4.1 Introduction

4.1.1 Initial 10 Beamlines

The Phase-I beamline portfolio for the Korea Light Source (KLS) consists of ten beamlines, strategically selected through a rigorous review process. This selection was informed by utilization patterns at PLS-II and the unique beam characteristics of the KLS. The Beamline Technology Review Committee(Chair: Prof. Hyunjung Kim), composed of experts across diverse scientific and technological disciplines, played a central role in defining priorities and ensuring alignment with national research needs.

The ten Phase-I beamlines are listed in <Table 4.1.1.1>. Among them, three are designated as industry-priority beamlines: ① BioPharma-BioSAXS (Bio-Pharmaceutical and Bio Small-Angle X-ray Scattering) ② Material Structure Analysis ③ Soft X-ray Nanoprobe

These three beamline selections for the KLS are strategically chosen to maximize early, high-value impact across life sciences, advanced materials research, and nanoscience, ensuring alignment with both global research trends and critical Korean national industrial needs. A core focus is placed on high-throughput technologies and industrial applicability to accelerate commercialization and strengthen the domestic supply chain.

- **BioPharma-BioSAXS:** Accelerating Domestic Drug Discovery

The BioPharma-BioSAXS beamline is designed to directly address the surging demand within the Korean pharmaceutical and bio-industry for structural biology R&D. Its capability for high-throughput and automated workflows will significantly accelerate drug discovery pipelines, providing critical insights into the structure and interactions of biomolecules, including challenging membrane proteins. This positions the beamline as a vital bridge between academic research

and industrial application, facilitating the localization and rapid development of novel biopharmaceuticals and anti-cancer drugs.

- **Material Structure Analysis:** Strengthening the Material Industry

The Material Structure Analysis beamline responds to the increasing importance of the precise structural characterization of crystalline and polycrystalline materials essential for next-generation technologies. By combining high-resolution powder diffraction with in-situ measurement under temperature, gas, and electrochemical control, it follows structural change as it occurs. Typical subjects are the phase transitions and redox processes of battery cathodes and electrolytes during charge and discharge; the active phases of catalysts and electrocatalysts during reaction; and, under controlled temperature, pressure, and atmosphere, the behaviour of functional ceramics, oxides, polymers, structural metals, and materials for extreme environments. The beamline therefore supports key national industrial areas — rechargeable batteries (including all-solid-state cells) for electric vehicles and energy storage, hydrogen and green ammonia, semiconductors and sensors, and the automotive, shipbuilding, aerospace, and steel industries — while its multi-sample, high-throughput configuration additionally serves the phase identification and quantitative phase analysis on which manufacturing quality control depends. This is crucial for optimizing core components and materials, thereby aligning with national efforts to enhance the competitiveness and self-reliance of the Materials, Components, and Equipment industry.

- **Soft X-ray Nanoprobe**: Enabling Next-Generation Nanoelectronics

The Soft X-ray Nanoprobe beamline serves as a flagship facility, providing unique capabilities for nanoscale chemical and electronic state analysis. It is built around two branches: an imaging branch combining Scanning Transmission X-ray Microscopy (STXM) with ptychography to reach spatial resolutions of a few tens of nanometres, and a spectroscopy branch providing high-throughput X-ray Photoelectron Spectroscopy (XPS) and X-ray Absorption Spectroscopy (XAS). Covering 90 to 2600 eV, the beamline reaches the K edges of light elements and the L edges of transition metals, which reflects the global strategic race in quantum materials, catalysis, and nanoelectronics. This facility will empower researchers and engineers to probe functional states with element-specific sensitivity at interfaces, providing the fundamental data required to accelerate the development of

high-performance semiconductor devices and advanced sensors crucial for the national IT and future technology sectors.

The remaining seven are fundamental research beamlines: ④ Nanoscale Angle-Resolved Photoemission Spectroscopy (NanoARPES) ⑤ Coherent X-ray Diffraction (CoXRD) ⑥ Coherent Small-Angle X-ray Scattering (CoSAXS) ⑦ Real-Time X-ray Absorption Fine Structure (Real-Time XAFS) ⑧ Bio-Nano Crystallography (BioNX) ⑨ High Energy Microscopy (HEM) ⑩ Nanoprobe

These seven beamlines are dedicated to fundamental research, strategically selected to support leading-edge scientific research across multiple disciplines and capitalize on the unique properties of a 4th-generation storage ring, namely its ultra-high brightness and coherence. These capabilities are essential for addressing the grand challenges in quantum science, dynamical processes, and complex biological structures worldwide.

- **Nanoscale Angle-Resolved Photoemission Spectroscopy (NanoARPES)**

The NanoARPES beamline combines spatially selective ARPES with photon-energy and polarization control for quantum and low-dimensional materials. Its capillary-focused nanoARPES branch has a beam-size target of at most 1 μm FWHM, complemented by a microARPES branch with approximately 10×10 μm FWHM illumination. The beamline supports measurements of small flakes, heterogeneous domains, moire and heterostructure regions, and electrically controlled devices. The illumination footprint, sample positioning, and mapping response together determine spatial selectivity.

- **Coherent X-ray Diffraction (CoXRD)**

The CoXRD beamline is dedicated to exploiting the high spatial coherence of the KLS to realize non-destructive 3D structural imaging in crystalline and nanostructured materials. Utilizing advanced coherent diffraction techniques (e.g., Bragg Coherent Diffraction Imaging), it enables the precise visualization of lattice distortions, internal strain fields, and defects at the nanoscale. This capability is paramount for global efforts in materials engineering, nanotechnology, and energy device development, where structural integrity dictates performance.

- **Coherent Small-Angle X-ray Scattering (CoSAXS)**

The CoSAXS beamline will leverage X-ray coherence for probing nanoscale dynamics and fluctuations in soft and hard condensed matter. Applying X-ray Photon Correlation Spectroscopy (XPCS), it allows for time-resolved studies of motion and changes in materials like polymers, colloids, and complex fluids. This facility provides unique, dynamic insights into processes such as self-assembly and phase transitions, which are essential to modern soft matter physics and the development of functional nanostructured systems.

- **Real-Time X-ray Absorption Fine Structure (Real-Time XAFS)**

The Real-Time XAFS beamline establishes a powerful platform for real-time chemical state analysis. It is optimized for high-speed, high signal-to-noise ratio acquisition, enabling *in-situ* and *operando* studies of the local electronic and structural environments during reaction and operation. This is a critical global trend, providing essential mechanistic data for advancing catalysis, energy storage materials (batteries, fuel cells), and functional oxides.

- **Bio-Nano Crystallography (BioNX)**

The BioNX beamline is designed to push the boundaries of structural biology by extending macromolecular crystallography (MX) capabilities to nano- and micro-crystals. By integrating advanced micro-focus optics and detection systems, it addresses a key limitation in conventional MX, enabling the structure determination of challenging targets such as membrane proteins and complex biomolecular assemblies. This significantly accelerates drug discovery and fundamental life science research.

- **High Energy Microscopy (HEM)**

The HEM beamline will exploit high-energy X-rays for deep-penetration microscopy and tomography. This enables the non-destructive 3D imaging of large or dense samples under realistic conditions. It plays a critical role in the global trend of analyzing structural integrity in industrial components, engineering materials, and fully assembled energy devices, providing multi-scale insights into internal architectures and operational stress.

- **Nanoprobe**

The Nanoprobe beamline will offer multi-modal nanoscale characterization by integrating X-ray fluorescence (XRF), X-ray absorption spectroscopy (XAS), diffraction-based methods, as well as Nano-Coherence imaging and Nano-Scanning imaging, achieving spatial resolutions down to tens of nanometers, facilitating correlative studies of chemical composition, electronic states, and structural features, making it a vital tool for applications in catalysis, nanomaterials, and environmental sciences, while enhancing understanding and development across these critical scientific fields.

<Table 4.1.1.1> lists the ten Phase-I beamlines. For each of them the specifications of the preliminary feasibility report are set alongside those of the present detailed design, so that the changes made during the design phase remain visible; the feasibility-report column records the original plan and is therefore not updated.

<Table 4.1.1.1> Specifications of the Initial 10 Beamlines of the KLS.

Beamline	**Preliminary Feasibility Report Specifications**	**Detailed Design Specifications**	**Application**	**Remarks**
1. BioPharma-BioSAXS (Industry-Priority)	Beam Energy: from 8 to 23 keV Experimental Method: Bio-SAXS	Beam Energy: from 8 to 23 keV Experimental Method: Solution SAXS Beam Size: 132 (H) × 125 (V) μm at the 67 m sample position (detector-focused mode); 40 × 10 μm^2 in sample-focused mode Resolution: d-spacing from 8 to 3800 Å (SAXS) * $\triangle E/E \leq 2 \times 10^{-4}$ Light Source: IVU20	Bio	Energy: from 8 to 23 keV SDD (Sample-to-Detector Distance) up to 8 m Automation system implemented
2. Material Structure Analysis (Industry-Priority)	Beam Energy: from 5 to 40 keV Experimental Method: XRD (Powder XRD), XAFS	Beam Energy: from 17 to 45 keV, operated at a fixed energy of 33 keV Experimental Method: High-resolution powder XRD (HRPD), in-situ XRD Beam Size: about 20 (H) × 5 (V) μm (focused) to about 1 × 1 mm^2 (unfocused) Resolution (at 33 keV): HRPD, multi-analyzer stage $< 0.01°$ (estimated about 0.006° or better, Section 4.2.7.6 B); in-situ XRD, two-dimensional detector $\approx 0.05°$; $\Delta E/E < 2 \times 10^{-4}$ Light Source: IVU16	Material, Energy, Chemical, Semiconductor, Manufacturing	Implementation of HRPD and in-situ XRD experimental methods

(continued on next page)

(Table 4.1.1.1 continued)

Beamline	Preliminary Feasibility Report Specifications	Detailed Design Specifications	Application	Remarks
3. Soft X-ray Nanoprobe (Industry-Priority)	Beam Energy: 90 to 2600 eV Beam Size: ≤100 nm (imaging) 5 × 5 μm² (Spectroscopy) Experimental Method: XPS, XAS	Beam Energy: from 90 to 2600 eV Beam Size: from 20 to 30 nm at 250 eV (imaging branch); about 5 × 5 μm² (spectroscopy branch) Resolution: resolving power above 8,000 over the operating range Experimental Method: STXM, Ptychography (imaging branch); XPS, XAS (spectroscopy branch) Light Source: EPU78	Semiconductor, Material	Designed with two branch beamlines Grating coverage: LEG from 90 to 600 eV, MEG from 400 to 1200 eV, HEG from 1000 to 2600 eV
4. NanoARPES	Beam Energy: from 0.1 to 2 keV Beam Size: <100(H) × 100(V) nm² Spatial Resolution: ≤30 nm Experimental Method: Nano-ARPES	Beam Energy: from 50 to 2000 eV Beam Size Targets (FWHM): ≤1 μm (nanoARPES); about 10 × 10 μm (H×V, microARPES) Nominal resolving power targets: about 15,000 (high-flux grating); about 30,000 (high-resolution grating) Experimental Method: ARPES Light Source: EPU98	Semiconductor, Material	Designed with two branch beamlines Grating coverage: from 35 to 215 eV (HF, HR) and from 115 to 2005 eV (HE) Capillary nanoARPES baseline; mirror-focused microARPES HE primarily for rapid XPS checks FZP, spin and MBE expansion interfaces
5. CoXRD	Beam Energy: from 3 to 30 keV Beam Size: ≤1 μm Experimental Method: XRD, CDI	Beam Energy: from 5 to 30 keV Beam Size: about 1 μm (KB); about 100 μm (CRL); about 100 nm (FZP) Experimental Method: XRD, CDI Light Source: IVU22	Semiconductor, Material, Geology, Chemistry	Micrometer beam focusing with the KB pair Sub-100 nm focusing option with a Fresnel zone plate

(continued on next page)

(Table 4.1.1.1 continued)

Beamline	Preliminary Feasibility Report Specifications	Detailed Design Specifications	Application	Remarks
6. CoSAXS	Beam Energy: from 4 to 40 keV Experimental Method: SAXS/WAXS (Including GI Method), XPCS	Beam Energy: from 8.4 to 30 keV; primary operation from 9 to 12 keV Beam Size: about 13 (H) × 4 (V) μm FWHM (XPCS, CRL focused) Resolution: $\triangle E/E < 1 \times 10^{-4}$ Experimental Method: SAXS/WAXS (Including GI Method), XPCS Light Source: IVU20	Material, Chemistry	Securing Coherent Beam. (Wave front preserve)
7. Real-Time XAFS	Beam Energy: from 5 to 40 keV Experimental Method: XAFS	Beam Energy: from 4 to 30 keV Beam Size: about 50 (H) × 50 (V) μm^2 at the 60 m focal plane Resolution: $\triangle E/E < 1.4 \times 10^{-4}$ Experimental Method: XAFS, XES Light Source: IVU24	Energy, Environment, Material, Geology	Consideration of Advanced Hard X-ray Spectroscopy Techniques
8. BioNX	Beam Energy: from 5 to 20 keV Resolution: ≤1 Å Experimental Method: MX	Beam Energy: from 8 to 25 keV (DCM); from 10 to 15 keV (DMM) Beam Size: from 1 × 1 to 50 × 50 μm^2 (FWHM) Resolution: from 0.7 to 3.5 Å * $\triangle E/E < 2 \times 10^{-4}$ Experimental Method: MX (SSX, ISX, HTS) Light Source: IVU20	Bio	Optimized from 8 to 25 keV NanoMX Supports Drug Development

(continued on next page)

(Table 4.1.1.1 continued)

Beamline	Preliminary Feasibility Report Specifications	Detailed Design Specifications	Application	Remarks
9. HEM	Beam Energy: from 5 to 100 keV Resolution: 0.1 μm (at 100 m reference) Experimental Method: Projection Imaging	Beam Energy: from 20 to 150 keV Beam Size: up to 200 (H) × 30 (V) mm at the sample Resolution: from 0.3 to 0.5 μm Experimental Method: Projection Imaging Light Source: Center bend Sample Position: 100 m from the source, in the satellite building	Material, Energy, Bio	Bending magnet, ±1.5 mrad opening aperture Excludes Near-Distance Hutch (Uses White Light)
10. Nanoprobe	Beam Energy: from 5 to 25 keV Experimental Method: Ptychography, XRS, XRF	Beam Energy: from 5 to 25 keV (Si(111) double-crystal mode); from 12 to 25 keV (Si(311) channel-cut mode) Beam Size: ≤50 nm Resolution: $\triangle E/E < 1.5 \times 10^{-4}$ Experimental Method: Ptychography, XRF Light Source: IVU24	Semiconductor, Material, Energy, Environment, Chemistry	Pursues Nano Beam Focusing Designed for 5f-Block Elements and RI Materials → Experiments Possible After Radiation Safety Protocol Preparation

4.1.2 Beamline Design Strategy

Phase-I KLS beamline program has established a transparent, community-driven foundation validated through rigorous peer review. Beamlines will build on this foundation with a strategic, science-driven expansion that emphasizes global competitiveness, integrated operation, and sustainable growth.

Key elements of this strategy include:

- **Community-Driven Design Validation**
  - From 2023 to 2024, a series of user workshops and working group reviews enabled iterative refinement of beamline parameters.
  - Engagement with international conferences and peer review ensured alignment with global scientific standards.
- **Consensus-Based Decision Making**
  - Public hearings and technical presentations involved researchers, industry, government agencies, and international partners, thereby ensuring technical feasibility and financial accountability.
  - Oversight by the Ministry of Science and ICT and budgetary adjustments by the Ministry of Economy and Finance secured institutional robustness.
- **Transparency and International Peer Review**
  - Regular design-sharing meetings and presentations at academic conferences enhanced transparency and community trust.
  - External reviews (e.g., MAC, Joint Workshops) provided international benchmarking and validation of design quality.
- **User-Driven Expansion Roadmap**
  - Beamlines will target unaddressed frontier areas such as tender X-ray science, high-energy X-rays, coherent imaging, and time-resolved dynamics.
  - New beamlines will be aligned with emerging science in quantum materials, energy conversion, catalysis under operando conditions, biological imaging, and AI-driven experiments.

- **Integrated Operation and Data Platforms**
  - The data management, remote access, and AI-assisted experiment frameworks piloted in Phase-I will be fully implemented in Phase-I.
  - Cross-beamline interoperability will enable multi-modal and correlative experimental approaches.
- **Global Competitiveness and Collaboration**
  - Beamlines will secure a unique scientific niche relative to major global 4th-generation facilities.
  - Opportunities for joint beamline development and shared-access programs will position the KLS as an international hub for advanced photon science.
- **Incremental and Performance-Based Expansion**
  - Rather than launching all beamlines simultaneously, Phase-II will adopt a staged approach: evaluating Phase-I outcomes, prioritizing needs, and expanding step by step.

4.1.3 Beamline Design Review Process

The development of the initial ten beamlines at the KLS has been carried out through a rigorous, multi-stage review and consultation process involving users, and domestic and international experts. Key milestones include:

2023

- Feb: KLS Beamline Utilization Workshop
- Jun: User Working Group & Design Review Workshop
- Jul: Design Presentation to the Preliminary Feasibility Beamline Technology Review Committee
- Oct: Public Hearing on Beamline Design & Parameter Finalization
- Nov: Initial 10 Beamline Design Sharing Meeting
- Dec: User Association's Experimental Apparatus Review & PAL Feedback

2024

- Apr: Phase-I Detailed Design Sharing & Korean Physical Society Presentation
- May–Jul: Detailed Design Adequacy Review (Ministry of Science & ICT, Office of Science & Technology Innovation)
- Sep: Design Sharing with User Community
- Oct: Completion of Detailed Design Budget Adjustment (Ministry of Economy & Finance)

2025

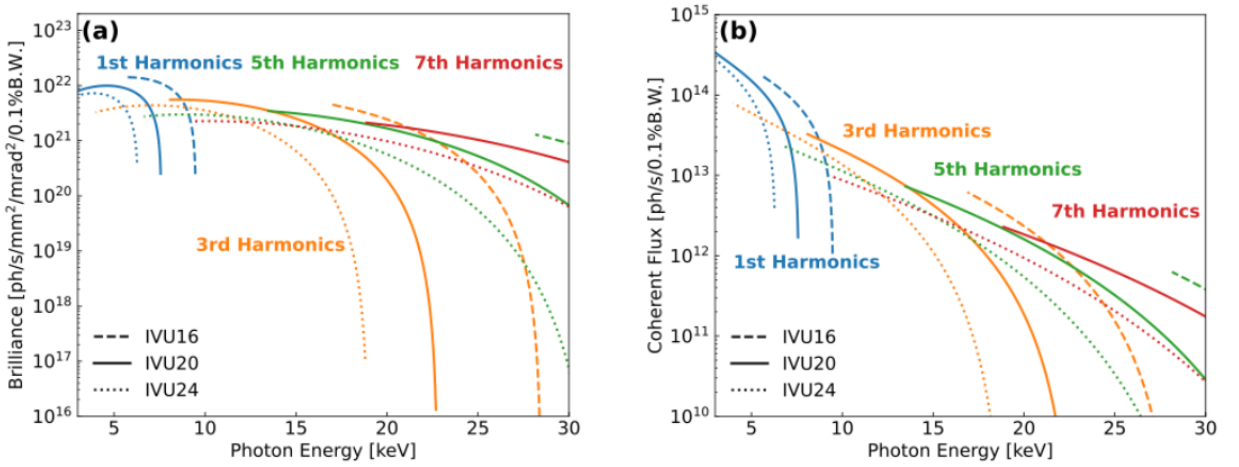
- May: Final Design Sharing Meeting
- Jun: Machine Advisory Committee (MAC) Review, International Conference, and HALF Joint Workshop
- Jul: Internal Beamline Workshop
- Sep: Publication of Beamline Design Status in Journal of the Korean Physical Society (Special Issue on Advanced Technologies)
- Oct: Dedicated Symposium at the Korean Chemical Society & Institutional Session at the Korean Physical Society

This staged process has ensured transparency, maximized user participation, and provided rigorous technical validation, establishing a solid foundation for the successful realization of the KLS beamline portfolio. Crucially, continuous user communication ensures the Phase-I beamlines are designed with inherent flexibility to accommodate future cutting-edge experimental techniques.

4.1.4 Photon Sources for Phase-I beamlines

To realize the above capabilities, the photon sources have been configured to support the ten Phase-I beamlines. The configuration consists of one bending magnet, seven in-vacuum undulators (IVUs), and two out-of-vacuum elliptically polarized undulators (EPUs). The distribution of these sources is summarized in <Table 4.1.4.1>, while the photon brilliance and flux characteristics are illustrated in <Figure 4.1.4.1>. This configuration provides broad spectral coverage and high

brilliance, enabling the KLS to address the diverse requirements of both fundamental research and industrial applications. In particular, the combination of IVUs and EPUs allows flexible polarization control and energy tunability, supporting experiments in materials science, energy and catalysis, life sciences, pharmaceutical development, and quantum material research. A detailed description of each beamline, including the light source, will be covered in Section 4.2.



<Figure 4.1.4.1> Photon brilliance and coherent flux for IVU16, IVU20, and IVU24: (a) spectral brilliance and (b) coherent flux as a function of photon energy for the 1st through 7th harmonics.

<Table 4.1.4.1> Photon source parameters for the Phase-I beamlines. All undulator values are quoted at the minimum magnetic gap and a stored current of 400 mA; for the EPUs the vertical [V], circular [C] and horizontal [H] polarization modes are listed separately. For EPU98, the final specified period count is 35.75, displayed as 36. The EPU98 length entry is the final array length of 3.6316 m; other undulator length entries are device lengths. The source calculation model uses 36 regular periods and a regular magnet length of 3.528 m. For BM10 the quoted power is that accepted by the $\pm$1.5 mrad opening aperture, obtained from the linear power density in the adjacent column. The last row gives the PLS-II IVU20 for comparison.

Undulator	Beamline #	Period Length (mm)	Periods	Length (m)	$K_{\max}$ value	$B_{\max}$ (T)	$\mathrm{Gap}_{\min}$ (mm)	1st harm. energy (eV)	Total Power (kW)	Max. Power Density (kW/mrad^2)	Photon Beam Divergence $\Sigma_{x'}/\Sigma_{y'}$ (mrad)
IVU16	ID24 Material Structure Analysis	16	185	3.0	1.172	0.785	5	5,628.6	7.38	154.3	0.00679/0.00626
IVU20	ID04 CoSAXS ID21 BioPharma ID22 BioNX	20	148	3	1.904	1.021	5	2,696.1	12.49	164.2	0.00930/0.00892
IVU22	ID03 CoXRD (CDI)	22	134	3	2.315	1.127	5	1,876.6	15.16	165.2	0.01100/0.01068
IVU24	ID10 Nanoprobe ID23 RealTime XAFS	24	123	3	2.745	1.225	5	1,327.8	17.93	165.4	0.01293/0.01265
EPU78	ID26 SX-ray Nanoprobe	78	44	3.62	K_V6.948 K_C4.390 K_H5.652	B_V0.954 B_C0.602 B_H0.776	15	77.49 [V]/ 96.0 [C]/ 114.84 [H]	12.65 [V] 10.08 [C] 8.37 [H]	46.5 [V]	0.04837/0.04830 [V] 0.04348/0.04340 [C] 0.03977/0.03969 [H]
EPU98	ID25 NanoARPES	98	36	3.6316	K_V9.238 K_C6.070 K_H8.043	B_V1.010 B_C0.663 B_H0.879	15	35.5 [V], 40.9 [C], 46.49 [H]	13.75 [V] 11.87 [C] 10.44 [H]	38.02 [V]	0.07246/0.07241 [V] 0.06745/0.06740 [C] 0.06333/0.06327 [H]
BM	BM10	-	-	0.186	-	2	-	[E_c] 21,280.8	0.65	0.216 (kW/mrad)	
PLS-II (IVU20)		20	68	1.4	1.811	0.969	5	1,618.78	2.91	22.5	0.0341/0.0171

4.2 Beamline Application

4.2.1 Coherent X-ray Diffraction (ID03)

4.2.1.1 Target Purpose and Objective

The Coherent X-ray Diffraction (CoXRD) beamline aims to provide a platform for the quantitative three-dimensional characterization of local lattice distortions and defects in crystalline materials. Its primary techniques are Bragg Coherent X-ray Diffraction Imaging (BCDI) and Bragg ptychography. Combining nanoscale strain imaging with these coherent Bragg techniques in the first phase and mesoscale structural imaging with Dark-Field X-ray Microscopy (DFXM) in a later phase, the beamline will contribute to understanding the relationship between structural disorder and functional properties in advanced materials.

The beamline is designed to make full use of the high coherence of the KLS source. The optical layout minimizes the number of optical elements and employs horizontal deflection throughout, in order to preserve the coherent wavefront and beam stability at the sample position and thereby maximize the coherent flux available for coherent diffraction experiments. The coherent flux directly governs the attainable spatial resolution and strain sensitivity of the reconstructions, as well as the range of accessible sample sizes and the time resolution of *in situ* and *operando* measurements.

The endstation is designed around a Eulerian/Kappa-type diffractometer rather than a tower-type sample stage. Although a tower-type stage offers a simpler configuration and easier integration of *in situ* experimental environments, its limited angular degrees of freedom can restrict access to reciprocal space. In contrast, the Eulerian/Kappa-type diffractometer provides multiple sample and detector rotation axes about a common center of rotation, enabling greater flexibility in diffraction geometry and access to a wider range of Bragg reflections. This configuration was therefore selected to support versatile reciprocal-space measurements for coherent X-ray diffraction imaging. This allows Bragg reflections to be reached in specular, off-specular, and in-plane geometries, and rocking curves and reciprocal-space scans to be performed about an arbitrary scattering vector, covering nearly the entire accessible reciprocal space. As a result, the beamline is not limited to BCDI but supports coherent X-ray diffraction experiments in general, including measurements on thin films, surfaces, and interfaces, and on weak or off-specular reflections. The Kappa geometry also keeps the space around the sample

open, which facilitates the integration of *in situ* and *operando* sample environments. A key objective enabled by this diffractometer is multi-reflection BCDI, in which coherent diffraction patterns are collected from several non-coplanar Bragg reflections of the same crystal. Because a single Bragg reflection is sensitive only to the projection of the displacement field onto its scattering vector, combining at least three non-coplanar reflections allows the full three-dimensional displacement field and strain tensor to be reconstructed. This enables unambiguous identification of defects, such as dislocations that are invisible in reflections for which the Burgers vector is perpendicular to the scattering vector, and a complete description of strain states in individual nanocrystals. Multi-reflection measurements require wide angular access in reciprocal space and reliable re-centering of the same crystal between reflections, all of which are addressed in the diffractometer design.

Bragg ptychography extends coherent Bragg diffraction imaging beyond isolated crystals to extended samples such as thin films, heterostructures, and devices, where the crystal is larger than the illuminating beam size. By scanning the focused beam across the sample with overlapping illumination positions while recording coherent diffraction patterns around a Bragg peak, the strain and lattice-tilt distributions of extended crystalline regions can be reconstructed without the size restriction of conventional BCDI. The focused beam delivered by the KB mirror system and Fresnel Zone Plate (FZP), together with high-precision sample scanning, provides the basis for these measurements. In addition, the reconfigurable experimental setup of the end-station allows the beamline to support microbeam X-ray diffraction experiments, providing opportunities to investigate structural evolution and phase transitions in confined systems such as nanowires or patterned sample. These capabilities extend the applicability of the beamline beyond coherent imaging by enabling complementary studies of local structural changes under various external stimuli.

In the second phase of development, the beamline will be expanded to incorporate DFXM by installing a compound refractive lens (CRL) objective in a far-field geometry and 1D-CRLs upstream of the sample for depth profiling. The end-station and detector flight path are designed with the flexibility required for DFXM experiments, including sufficient sample-to-detector distance and detector rotation capability for dark-field imaging. This expansion will enable direct, non-destructive mapping of lattice strain and orientation in deeply embedded grains and domains, complementing the coherent Bragg imaging capabilities and

establishing the CoXRD beamline as a platform for multiscale characterization of materials.

In the longer term, the energy tunability of the beamline offers a route toward element-specific (resonant) BCDI, in which coherent diffraction data are recorded near the absorption edges of selected elements. As fluorescence background, reduced coherent flux near absorption edges, and challenges associated with resonant BCDI reconstruction remain significant obstacles, this capability is considered a future development goal rather than a first-phase objective.

4.2.1.2 Photon Source

The photon source for the ID03 Coherent X-ray Diffraction beamline is a 3 m long in-vacuum undulator with a period of 22 mm (IVU22, 134 periods). Operating with a gap range of 5 – 18 mm, corresponding to a deflection parameter K of 2.31 – 0.30, the IVU22 covers a continuous photon energy range of 5 – 30 keV by tuning the gap across successive odd harmonics. At the minimum gap of 5 mm and a storage-ring current of 400 mA, it generates a maximum total power of 15.165 kW with a peak power density of 165.3 kW/mrad^2.

The ID03 source parameters are summarized in table 4.2.1.1. Owing to the low emittance of the KLS storage ring, the IVU22 provides a high degree of transverse coherence. The coherence properties of the beam at the sample, and the coherence and flux modes selected by the slit upstream of the KB mirror, are described in section 4.2.1.4 Beamline Optics. Detailed insertion-device specifications and performance calculations are maintained in the photon source technical document [1].

<Table 4.2.1.1> ID03 Coherent X-ray Diffraction Beamline source parameters, (400 mA, K_{max} and the maximum total power at 5 mm gap)

Undulator	**Period (mm)**	**Length (m)**	**Gap size (mm)**	K_{max}	**Max total power (kW)**	**Power density (kW/mrad^2)**
IVU22	22	3	5 – 16	2.315	15.165	165.3

4.2.1.3 Front-End

The front-end (FE) components of the beamline are designed to satisfy the following thermal criteria, in accordance with the KLS beamline FE design and the high heat load front-end design report [2]:

- The thermal stress induced by the heat load shall not exceed the yield strength of the material.
- The temperature rise induced by the heat load shall not exceed the softening temperature of the material.
- The temperature of the cooling-channel wall in contact with the low-conductivity water (LCW) shall remain below the boiling point of water.

The maximum total power of 15.165 kW generated by the IVU22 [1] is progressively reduced along the FE. The first fixed mask, with an opening angle of 0.3 mrad, absorbs ~6.75 kW, and the second fixed mask, located downstream with an opening angle of 0.23 mrad, absorbs additional power. Near the end of the FE, upstream of the photon shutter, the front-end movable mask at 22.5 m limits the beam to its 3σ full width at 6 keV, corresponding to an opening of approximately 0.75×0.75 mm^2. As a result, the power transmitted to the photon transfer line (PTL) is reduced to approximately 182 W.

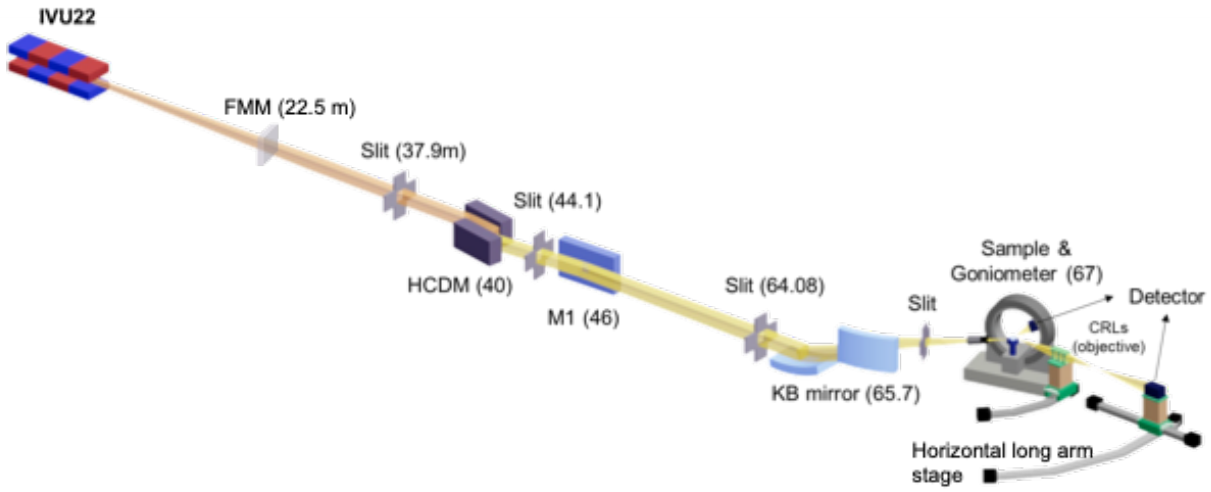
4.2.1.4 Beamline Optics

The optical performance of the beamline was simulated using ShadowOui and XOPPY within the OASYS environment, together with SPECTRA. The focal spot sizes of the Kirkpatrick–Baez (KB) mirror system were calculated with the HYBRID method, and the photon flux was evaluated at photon energies of 6, 10, 15, and 30 keV. To deliver the maximum possible flux in flux mode, all optical components are designed to accept the beam up to its 3σ full width at 6 keV, hereafter referred to as 3σ.

A Overall optical layout and component roles

The beamline incorporates three main optical components. A horizontal double-crystal monochromator (HDCM) at 40 m monochromatizes the beam, and a high harmonic rejection mirror (HHRM) at 46 m suppresses higher harmonics transmitted by the monochromator. A KB mirror pair, consisting of a vertical focusing mirror (VFM) at 65.08 m and a horizontal focusing mirror (HFM) at 65.7 m, then focuses the beam to a micrometer-scale spot at the sample.

The beamline layout minimizes the number of optical elements in order to preserve the wavefront against thermal load, vibration, and other environmental perturbations. The HDCM and the HHRM both deflect the beam horizontally.



<Figure 4.2.1.1> Schematic layout of the CoXRD beamline.

Because the vertical source size is about four times smaller than the horizontal one, angular vibration of an optical element in the vertical plane would broaden the effective source far more severely than the same vibration in the horizontal plane. Horizontal deflection therefore minimizes vibration-induced source broadening.

The HFM is located 1.3 m upstream of the sample, providing sufficient working distance to accommodate various *in situ* and *operando* sample environments. The sample position, defined as the center of rotation of the diffractometer, is accordingly set at 67 m. An 8 m long flight path is located downstream of the sample and is designed to rotate horizontally by up to 45° toward the ring. The current design is provisional and may be revised in response to ongoing discussions and future technical requirements.

To provide a range of beam sizes for different experimental requirements, additional focusing optics are planned. A CRL stack installed at approximately 50 m will provide a beam of about 100 μm at the sample, and a Fresnel zone plate (FZP) at approximately 66.8 m will provide a focused beam of approximately 200 nm.

Diagnostic devices and other optical components not shown in figure 4.2.1.1 are listed in table 4.2.1.2 together with their positions and specifications. Slits and diagnostic devices are installed upstream and downstream of each main optical component, and a quadrant beam position monitor (QBPM) at the end of the optical hutch (48.2 m) monitors the position of the beam entering the experimental hutch.

<Table 4.2.1.2> Components of the CoXRD beamline listed in beam order, with their distances from the source.

Distance (m)	Location	Component	Description
0	Storage ring	IVU22	Period 22 mm, length 3 m
22.5	Front-end	Movable mask (FMM)	4-way slit, water cooling; mechanical design and thermal analysis [2]
28	Optical hutch	White-beam attenuator	CVD diamond, 2 sets, water cooling
29		White-beam screen monitor	Diamond window, water cooling; fluorescent metal screen, current signal output
29.5		White-beam PBPM	4-blade type, water cooling
37.9		White-beam slit	4-way slit, water cooling, super-polished blades
38.6		White-beam screen monitor	Diamond window, water cooling; fluorescent metal screen, current signal output
40		HDCM	Si(111)/Si(311), fixed exit, LN_2 cooling
41.7		White-beam screen monitor	Diamond window, water cooling; fluorescent metal screen, current signal output
42.1		Mono-beam screen monitor	YAG window; fluorescent metal screen, current signal output
44.1		Mono-beam slit	4-way slit
44.5		Mono-beam screen monitor	YAG window; fluorescent metal screen, current signal output
46		HHRM	Plane mirror, 3-stripe coating (Si, Rh, Pt)
47		Mono-beam slit	4-way slit
47.6		Mono-beam screen monitor	YAG window; fluorescent metal screen, current signal output
48.2		QBPM	Ti foil 1000 nm, Ni foil 500 nm, Au foil 1000 nm, Ni foil 1000 nm
50–51	Experimental hutch	CRLs	Diamond lens stack
62		Mono-beam screen monitor	YAG window; fluorescent metal screen, current signal output
62.8		QBPM	Ti foil 1000 nm, Ni foil 500 nm, Au foil 1000 nm, Ni foil 1000 nm

(continued on next page)

(Table 4.2.1.2 continued)

Distance (m)	Location	Component	Description
64.08		Mono-beam slit	4-way slit, super-polished blades
65.08		VFM	3-stripe coating (Si, Rh, Pt); vertical focusing
65.7		HFM	3-stripe coating (Si, Rh, Pt); horizontal focusing
		Be window	Double-side polished, 127 μm thick
		Mono-beam slit	4-way slit
		Attenuator	2 sets, 8-channel (Al, Mn + block or Si wafer)
		QBPM	Ti foil 1000 nm, Ni foil 500 nm, Au foil 1000 nm, Ni foil 1000 nm
66.8		FZP	W or Au zone plate
67		Diffractometer	Eulerian/kappa type; LM-guide or air-bearing base plate
67.5–70		2D detector	Motorized, mounted on the diffractometer
68.5–76.5		Flight path	8 m, horizontal rotation up to 45°

B Mirror parameters and mirror/mechanism required performance

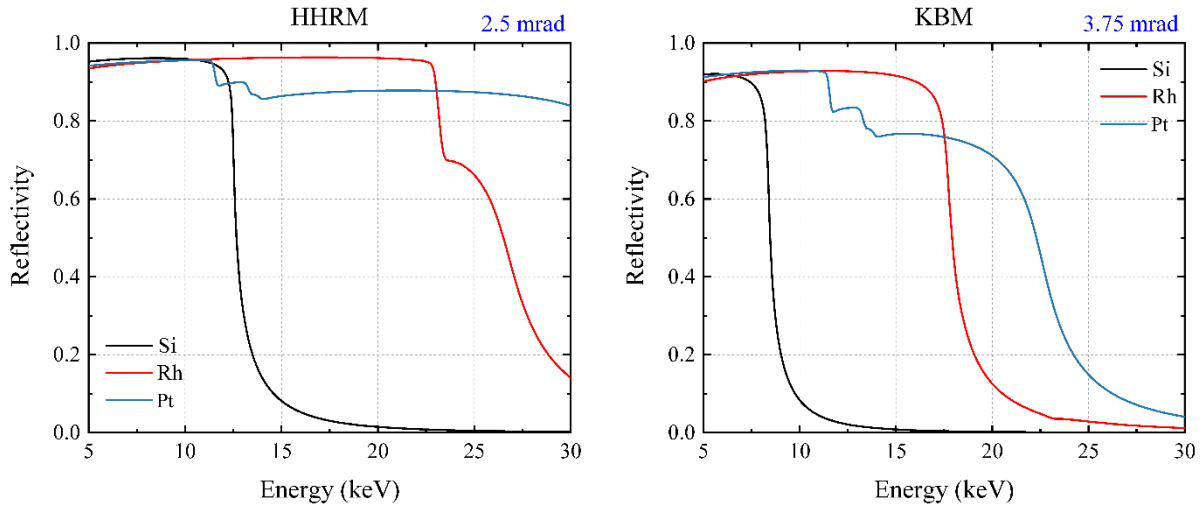
As listed in <Table 4.2.1.3>, the HHRM is a plane mirror that deflects the beam horizontally toward the experimental hall. At an incidence angle of 2.5 mrad, the 3σ beam at 46 m produces a footprint of approximately 580 mm, which is accommodated by the 600 mm long mirror. The mirror carries three coating stripes of Si, Rh, and Pt, which together cover photon energies up to 30 keV (figure 4.2.1.2).

The KB mirrors are 600 mm long with an effective optical length of 560 mm and operate at an incidence angle of 3.75 mrad, giving a geometric acceptance of 2.1 mm. This matches the 3σ beam size at the KB mirror position, so that the full beam can be accepted in flux mode. As shown in figure 4.2.1.2 (right), the reflectivity of the KB mirrors extends up to 20 keV, which covers the energy range used for coherent diffraction experiments. Measurements above 20 keV are therefore performed with the unfocused beam.

All mirrors are specified with a tangential slope error below 0.1 μrad RMS and a surface roughness below 0.2 nm RMS. These strict requirements arise because

<Table 4.2.1.3> ID03 mirror specification.

Parameter	HHRM	VFM	HFM
Installation location (m)	46	65.08	65.7
Reflection direction	Horizontal (towards the hall)	Vertical (upward)	Horizontal (towards the ring)
Mirror surface shape	Plane	Elliptical cylinder	Elliptical cylinder
Incident angle	2.5 mrad	3.75 mrad	3.75 mrad
Tangential radius	> 100 km (plane)	994.7 m	679.9 m
Sagittal radius	> 100 km (plane)	> 100 km (cylinder)	> 100 km (cylinder)
Substrate material	Si	Si	Si
Mirror size (L × W × T)	600 × 50 × 50 mm^3	600 × 50 × 50 mm^3	600 × 50 × 50 mm^3
Coating material	Si, Rh, Pt (50 nm)	Si, Rh, Pt (50 nm)	Si, Rh, Pt (50 nm)
Coating strip number	3	3	3
Coating stripe width	10 mm (W), per stripe	10 mm (W), per stripe	10 mm (W), per stripe
Tangential slope error	< 0.1 μrad RMS	< 0.1 μrad RMS	< 0.1 μrad RMS
Sagittal slope error	< 5 μrad RMS	< 2 μrad RMS	< 2 μrad RMS
Roughness	< 0.2 nm RMS (HSF)	< 0.2 nm RMS (HSF)	< 0.2 nm RMS (HSF)
Cooling method	None	None	None
Mirror bender	None	None	None
Mirror surface height	1400 mm	1400 mm	1404.65 mm
Motor axis	Pitch, roll, yaw, x, y, z	Pitch, roll, yaw, x, y, z	Pitch, roll, yaw, x, y, z
Manual axis (granite base)	Pitch, roll, yaw, x, y, z	Pitch, roll, yaw, x, y, z	Pitch, roll, yaw, x, y, z



<Figure 4.2.1.2> Reflectivity of the Si, Rh, and Pt coating stripes of the HHRM at an incidence angle of 2.5 mrad (left) and of the KB mirrors at 3.75 mrad (right).

the focal spot at the sample is on the order of 1 μm, so that wavefront distortions caused by slope errors and surface roughness directly degrade the focused beam. The simulated focusing performance including these effects is presented in figure 4.2.1.3.

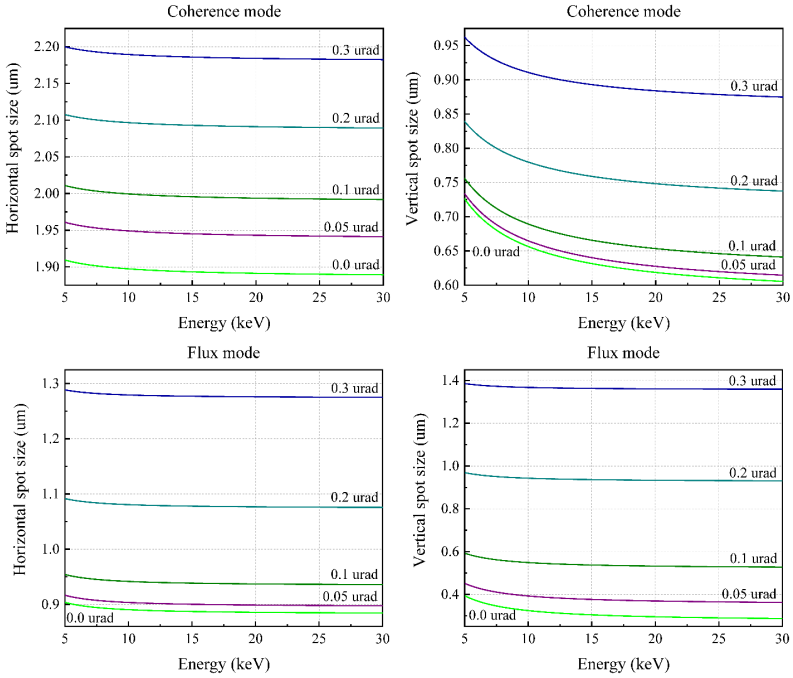
The focal spot size at the sample was calculated with the HYBRID method, which combines geometrical ray tracing with a wave-optical treatment of diffraction. Three contributions determine the spot size: source demagnification, the diffraction-limited focus, and the slope error of the KB mirrors. Source demagnification is the geometric reduction of the source size by the ratio of the mirror-to-sample distance to the source-to-mirror distance, which is about 1/51 for the HFM and 1/34 for the VFM. Because it depends only on the source size and these distances, this contribution is the same in coherence mode and flux mode.

The diffraction-limited focus is the smallest spot achievable for a given wavelength and numerical aperture. Although the source size and the focusing geometry are identical in both modes, the numerical aperture differs because it is set by the slit at 64.08 m upstream of the KB mirrors. In coherence mode, the slit opening is adjusted according to the energy-dependent transverse coherence length, resulting in a variable numerical aperture. In contrast, flux mode utilizes the full 2.1 mm acceptance of the KB mirrors, maintaining a constant numerical aperture. Finally, slope errors arising from mirror fabrication cause deviations from the ideal surface figure, which distort the wavefront and broaden the focal spot. Since slope errors are inherent to all mirrors and generally become harder to control as the mirror length increases, minimizing them is essential.

The relative importance of demagnification and diffraction differs between the two modes. In coherence mode, the small slit opening makes the diffraction-limited term dominant over demagnification. In flux mode, the large and fixed aperture makes demagnification the dominant contribution to both the horizontal and vertical spot sizes.

The resulting focal spot sizes including the slope error are shown in figure 4.2.1.3. In coherence mode, a slope error of 0.1 μrad broadens the spot by less than 5%, since the spot size is already dominated by the diffraction-limited term, which is less sensitive to slope error. In flux mode, the horizontal broadening likewise remains within 5%. The vertical spot in flux mode, however, is highly sensitive to slope error. Because the small vertical source is strongly demagnified by the VFM, the ideal vertical spot is intrinsically very small, and even a slope

error of 0.1 μrad increases the vertical spot size by approximately 50% compared to the theoretically calculated value. Taking all contributions into account, the final focal spot size is approximately 2 μm (H) × 700 nm (V) in coherence mode and approximately 950 nm (H) × 600 nm (V) in flux mode.



<Figure 4.2.1.3> Simulated focal spot sizes at the sample in coherence and flux modes, including the effect of the slope error of the KB mirrors.

In addition to the KB mirror system, focusing optics based on CRLs and FZPs are planned to extend the scientific capabilities of the beamline. The specifications of these optics listed in tables 4.2.1.4 to 4.2.1.6 were obtained from OASYS simulations, and their positions and detailed parameters may be revised in subsequent design iterations.

As summarized in table 4.2.1.4, the CRL stack consists of spherical or parabolic diamond lenses with a web thickness of 0.05 mm and an aperture of 2 mm. To provide a beam of about 100 μm at the sample for each photon energy, the number of lenses and the stack position are adjusted, using 4 lenses at 51 m for 6 keV, 6 lenses at 50.5 m for 8 keV, and 10 lenses at 50 m for 10 keV. The resulting beam size at the sample is approximately 98 × 98 μm^2 (H × V) at 6 keV and 97 × 107 μm^2 at 10 keV, providing a moderately focused beam suitable for microbeam XRD and related experiments.

For sub-micron focusing, two FZP designs are considered, with geometric

<Table 4.2.1.4> Specifications of the CRLs at 6, 8 and 10 keV. All lenses are diamond lenses with a web thickness of 0.05 mm and an aperture of 2 mm. The number of lenses and the stack position are chosen to provide a beam of about 100 μm at the sample position (67 m).

Energy (keV)	**Lens configuration**	**Position (m)**	R **(mm)**	N	**Beam size, H × V (μm)**
6	Diamond, spherical or parabolic	51	1.7	4	98 × 98
8	Diamond, spherical or parabolic	50.5	1.47	6	103 × 103
10	Diamond, spherical or parabolic	50	1.63	10	97 × 107

<Table 4.2.1.5> Specifications of the FZP designs. The positions are given for 6 keV and are adjusted with photon energy so that the focus remains at the sample position (67 m).

Parameter	**HZP-400um-120nm**	**HZPSC/HZPX-550um-50nm**
Position at 6 keV	66766.9 mm	66866.65 mm
Focal distance at 6 keV (calc.)	233.1 mm	133.35 mm
Diameter	400 μm	550 μm
Zone material	W or Au	W or Au
Zone thickness	2000 nm	1500 nm
Outermost zone width	120 nm	50 nm
Substrate material	Si_3N_4	Si_3N_4
Substrate thickness	1000 nm	1000 nm

<Table 4.2.1.6> Simulated performance of the FZPs at 6, 8 and 10 keV.

Model	**Energy (keV)**	**Focal distance, sim. (mm)**	**Beam size, H × V (nm)**	**Efficiency (%)**
HZP-400um-120nm	6	232.29	216 × 162	8.27
	8	309.72	259 × 166	25.06
	10	387.15	293 × 172	32.54
HZPSC/HZPX-550um-50nm	6	133.08	105 × 62	21.28
	8	177.44	136 × 66	30.20
	10	221.80	157 × 67	28.17

specifications listed in table 4.2.1.5 and simulated performance in table 4.2.1.6. Both FZPs use W or Au as the zone material on a 1000 nm thick Si_3N_4 substrate. At 6 keV, the HZP-400um-120nm design provides a focal distance of 232.29 mm, a focused beam size of 216 × 162 nm^2 (H × V), and a diffraction efficiency of 8.27%, while the HZPSC/HZPX-550um-50nm design provides a focal distance of 133.08 mm, a focused beam size of 105 × 62 nm^2 (H × V), and a diffraction efficiency of 21.28%.

The corresponding focal distances, beam sizes, and efficiencies at 8 and 10 keV are summarized in table 4.2.1.6.

C Double Crystal Monochromator

The specifications of the HDCM are summarized in table 4.2.1.7. The HDCM is equipped with both Si(111) and Si(311) crystal pairs, which are selected by lateral translation, to cover the photon energy range of 5–30 keV. Si(111) provides higher flux, while Si(311) provides a narrower energy bandwidth. To handle the heat load, the crystals are cryogenically cooled with liquid nitrogen through a side-cooling mechanism.

<Table 4.2.1.7> ID03 HDCM specification.

Item	Specification
Position (m)	40
Type	Fixed-exit horizontal double-crystal monochromator (horizontal deflection)
Photon energy range	5–30 keV
Crystals	Si(111) and Si(311), plane
Operating mode	Fixed exit; Si(111) or Si(311) selected by lateral crystal translation
First crystal size (L × W × H)	50 × 20 × 40 mm^3
Second crystal size (L × W × H)	60 × 20 × 40 mm^3
Beam offset	25 mm (toward the ring)
Bragg angle range (5–30 keV)	23.29°–3.78° for Si(111), 49.21°–7.25° for Si(311)
Bragg stage travel	3.78°–49.21°
Bragg angle resolution	< 0.2 μrad
Slope error	< 1 μrad RMS
Roughness	< 0.5 nm RMS
Cooling	LN_2, side cooling
Motion axes	Bragg, gap, roll, pitch, piezo roll and pitch

D Beam conditions at the sample per optical configuration

The beamline provides two operational modes, coherence mode and flux mode, which differ in the degree of coherence of the beam delivered to the sample. The mode is selected by the slit at 64.08 m upstream of the KB mirrors. In coherence mode, the slit opening is matched to the transverse coherence length at the given photon energy, so that a fully coherent beam is delivered to the sample. In flux mode, the slit is opened to the 2.1 mm acceptance of the KB mirrors in order to

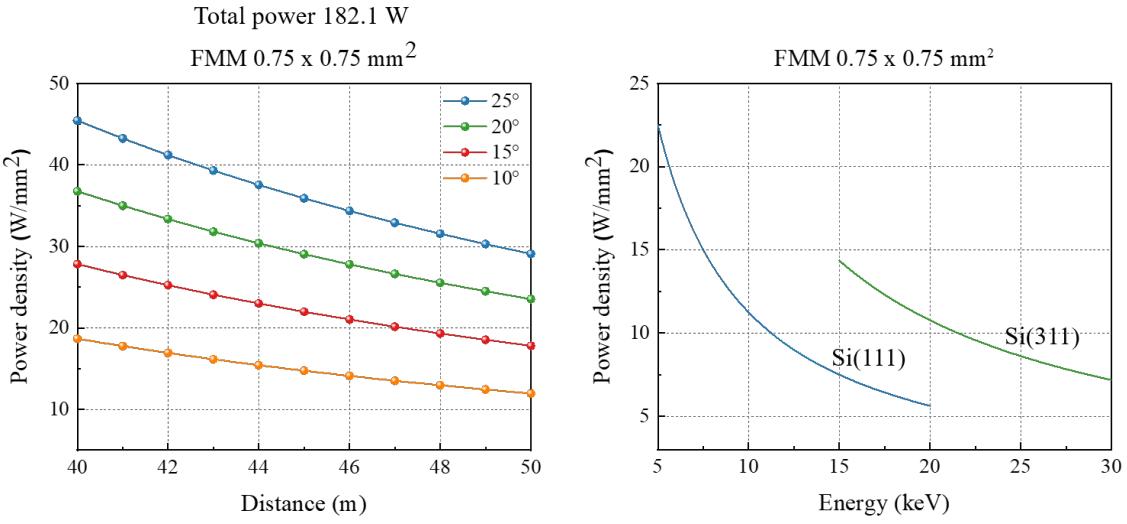
maximize the photon flux. The resulting flux at the sample is summarized in table 4.2.1.8.

<Table 4.2.1.8> Flux at the sample in coherence and flux mode with the KB mirrors, calculated for ideal optics at a storage-ring current of 400 mA.

Mode	Photon energy (keV)	Flux (ph/s)	Harmonic
Coherence mode	6	4.58×10^{12}	3
	10	1.94×10^{12}	3
	15	5.12×10^{11}	5
Flux mode	6	1.44×10^{14}	3
	10	1.04×10^{14}	3
	15	5.67×10^{13}	5

E Heat Load

This section discusses the heat load on the HDCM, which is the first optical element in the beamline and therefore absorbs most of the heat load.



<Figure 4.2.1.4> Calculated power density on the HDCM as a function of distance from the source (left) and as a function of photon energy at 40 m (right).

The power incident on the HDCM is defined by the opening of the front-end movable mask (FMM). With the operational opening of 0.75×0.75 mm^2, corresponding to the 3σ beam size at 6 keV, the total incident power is approximately 182.1 W. The absorbed power density depends on the beam footprint on the first crystal. At low photon energies, the Bragg angle is large and the footprint becomes small, and the footprint also decreases when the HDCM is placed closer to the

source. Both cases lead to a higher power density. Figure 4.2.1.4 (left) shows the calculated power density as a function of distance from the source, and the HDCM is accordingly placed as far downstream as possible within the optical hutch. Figure 4.2.1.4 (right) shows the absorbed power density as a function of photon energy at the HDCM position of 40 m.

According to the specifications provided by the monochromator manufacturer, the allowable power density is approximately three times higher than the maximum value shown in figure 4.2.1.4, indicating that the expected power density is well within the acceptable operating range. Although the total incident power is slightly higher than the nominal power rating of commercially available HDCMs, the HDCM can be relocated further downstream in the future if necessary, increasing the beam footprint and reducing the absorbed power density.

F Beam Diagnostics and Alignment

To ensure reliable beam alignment and stable operation, beam diagnostic devices will be installed upstream and downstream of the major optical components throughout the beamline. The beam screens provide both fluorescent beam imaging and drain current measurement, so that they can be used for beam alignment during commissioning and maintenance.

Separate screens are planned for white-beam and monochromatic-beam diagnostics. White-beam screens will be installed upstream of the HDCM and immediately downstream of it. Although the beam downstream of the HDCM is monochromatic during operation, a white-beam screen at this position facilitates monochromator alignment during initial commissioning. CVD diamond is planned for the white-beam screens because of its excellent thermal resistance, while YAG or equivalent scintillators will be used for monochromatic-beam diagnostics.

QBPMs will serve as the primary beam diagnostic devices during routine operation. A UHV-compatible QBPM at the end of the optical hutch (48.2 m) continuously monitors the incident intensity I_0 and the beam position. These measurements are used for the alignment of optical components and slits and provide real-time monitoring of beam stability during operation. A second QBPM at 62.8 m, immediately upstream of the KB mirrors, monitors the beam intensity and position before focusing. Since the two QBPMs are separated by approximately 15 m, the beam trajectory and angular deviation can be determined from the measured positions,

enabling accurate evaluation and correction of the alignment of the upstream optical components. A third QBPM downstream of the KB mirrors monitors the beam just before the sample. The QBPMs employ polished transmission foils with typical thicknesses of 0.5 or 1 μm, and the foil material and thickness are selected according to the photon energy to provide sufficient signal while minimizing beam attenuation and wavefront distortion.

<Table 4.2.1.9> Beam height and horizontal offset at each component. The horizontal offset is positive toward the experimental hall and negative toward the ring.

Component	Distance (m)	Height (mm)	Horizontal (mm)	Remark
IVU22	0	1400	0	Reference
HDCM	40	1400	0	Fixed offset of 25 mm toward the ring
HHRM	46	1400	25	Deflection toward the hall, incidence 2.5 mrad
QBPM	62.8	1400	59	–
VFM	65.08	1400	70.4	Upward deflection, incidence 3.75 mrad
HFM	65.7	1404.65	73.5	Deflection toward the ring, incidence 3.75 mrad
Diffractometer	67	1414.4	70.25	Sample position
Detector	67.5	1418.15	69	Minimum detector distance
Detector	70	1436.9	62.75	Maximum detector distance
Flight path	76.5	1485.65	46.5	End of flight path

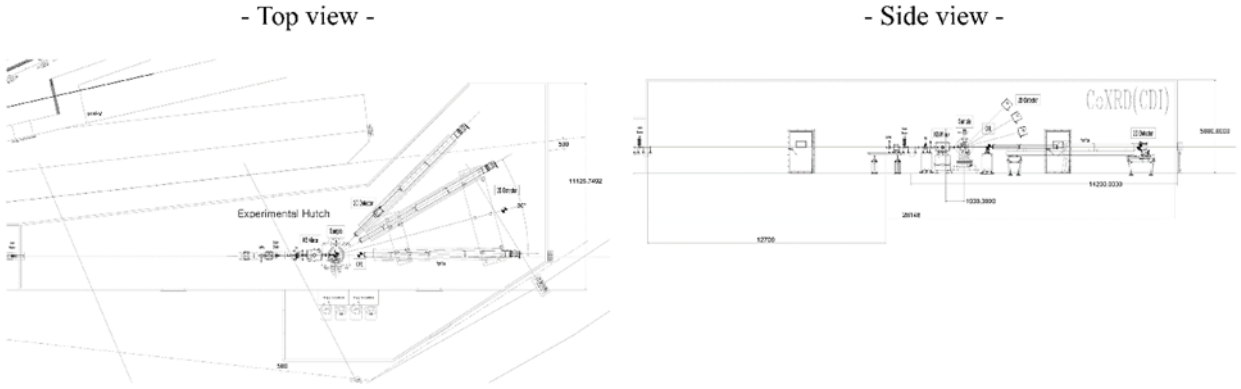
Table 4.2.1.9 summarizes the beam height and horizontal offset at each component. The beam from the IVU22 is at a height of 1400 mm, and its horizontal position is taken as the reference. With respect to the beam propagation direction, the horizontal offset is positive toward the experimental hall and negative toward the ring, and the vertical offset is positive upward.

The HDCM introduces a fixed horizontal offset of 25 mm toward the ring. The HHRM then deflects the beam toward the hall at an incidence angle of 2.5 mrad, resulting in a horizontal offset of 59 mm at the QBPM at 62.8 m. The HFM deflects the beam back toward the ring at an incidence angle of 3.75 mrad, giving a horizontal offset of 70.25 mm at the sample position. In the vertical direction, the single upward reflection by the VFM raises the beam from 1400 mm to 1414.4 mm

at the sample and to 1436.9 mm at the maximum detector distance of 70 m. The translation ranges of the optical components and the end-station are designed to accommodate these beam offsets.

4.2.1.5 Photon Transfer Line

A Hutch



<Figure 4.2.1.5> Layout of the ID03 experimental hutch (28.15 m × 10.9 m × 5 m, L × W × H).

The current layout of the experimental hutch is shown in figure 4.2.1.5. The hutch measures approximately 28.15 m in length, 10.9 m in width, and 5 m in height, providing sufficient space for the diffractometer, the detector flight path, and future experimental equipment.

The hutch height is determined primarily by the diffractometer geometry. The detector arm has a length of approximately 3 m and is required to rotate beyond 90° in the vertical plane to cover the intended range of diffraction angles. With the beam at a height of about 1.4 m at the sample, the detector reaches a height of about 4.4 m at this position. A hutch height of 5 m has therefore been adopted to provide adequate clearance for detector motion while leaving sufficient space for installation and maintenance. The hutch width is determined by the detector flight path, which rotates horizontally by up to 45° to accommodate wide-angle diffraction measurements and therefore requires a relatively large hutch footprint.

Owing to its large enclosed volume, the experimental hutch is expected to be less susceptible to rapid temperature fluctuations than a compact enclosure. The requirement for dedicated temperature control will be finalized during the detailed engineering design phase.

The experimental hutch shares one wall with the optical hutch. Although this arrangement provides an efficient beamline layout, the influence of mechanical vibration transmitted through the common wall will be evaluated during the detailed design stage. If necessary, additional vibration isolation or structural modifications will be implemented to ensure stable operation of the focusing optics and experimental instruments.

4.2.1.6 End-Station

A End-Station Mechanical Design

The end-station consists of two major systems, a diffractometer and a detector flight path. The sample is located at the center of rotation of the diffractometer at 67 m.

The diffractometer is a customized Kappa-type goniometer that combines a six-circle geometry with a nm & μm sample stage. This geometry provides multiple sample and detector rotation circles about a common center of rotation, maximizing the accessible range of reciprocal space. Bragg reflections can thus be reached in specular, off-specular, and in-plane geometries, which is essential for multi-reflection BCDI and for coherent diffraction experiments in general. The Kappa goniometer also keeps the space around the sample open for sample environments. The goniometer is designed for a maximum load of 20 kg, allowing the integration of nanopositioning stages, heating and cooling units, environmental chambers, and battery test cells for *in situ* and *operando* experiments.

The detector arm of the diffractometer carries an area detector and provides motorized translation of the sample-to-detector distance from 0.5 to 3 m. The arm rotates beyond 90° in the vertical plane, enabling flexible acquisition geometries for oversampling ratio optimization, angle-resolved measurements, and 3D-XRD.

In addition, a horizontal flight path downstream of the sample is planned as an upgrade for the second phase or the operational stage, since its full implementation within the first phase is unlikely. In the current concept, the flight path has a length of 8 m, rotates horizontally by up to 45° toward the ring, and operates under high vacuum (HV) to minimize air scattering. A large-area two-dimensional detector mounted at its end would enable wide-angle diffraction measurements, particularly the efficient acquisition of in-plane diffraction peaks. For dark-field X-ray microscopy (DFXM), a CRL objective would be installed downstream of the sample and the x-ray image detector, allowing high-resolution X-ray microscopy

using the same flight path. These specifications, as well as the techniques to be added, will be refined through future discussions with the user community and may change from the present concept.

Beyond DFXM, candidate capabilities for these later stages were proposed at the CoXRD working group meeting in January 2026. These include polarization-controlled X-ray beams and a range of *in situ* sample environments, such as cryogenic systems and magnetic-field chambers. To allow such upgrades without major reconstruction, the first-phase design reserves the necessary floor space in the experimental hutch and defines a layout compatible with future installations, including the positions of the floor rails for the flight path and of the support structures for additional equipment.

B Detector

The detection system incorporates two hybrid photon-counting area detectors, an EIGER2 X 4M and a LAMBDA 250k, together with a silicon drift detector (SDD), enabling multimodal data acquisition. The EIGER2 X 4M, with a pixel size of 75 µm and a 2068 × 2162 pixel array, provides an active area large enough to capture the full diffraction pattern typically observed in BCDI experiments. Combined with the adjustable sample-to-detector distance of 0.5 to 3 m, which allows the oversampling ratio to be tuned, it supports measurements of crystals ranging from roughly 100 nm to several micrometers in size. The LAMBDA 250k, with its smaller pixel size of 55 µm, achieves a higher oversampling ratio at a given distance, which is advantageous for coherent diffraction imaging. Its frame rate of up to 24 kHz also makes it well suited to time-resolved diffraction studies of fast structural dynamics on the millisecond time scale and below. A Timepix4-based detector, which offers the same 55 µm pixel size together with event-driven readout and sub-nanosecond time stamping, is being considered alongside the LAMBDA 250k for time-resolved measurements. The SDD will be used for XRF, GIXRF, and GIXRF-XANES measurements, and for mapping the spatial distribution of elements during Bragg ptychography.

The main parameters of the three detectors are compared in table 4.2.1.10.

As beamline construction and commissioning are still underway, the choice of detectors remains subject to change. Since procurement will take place close to completion, the detectors ultimately selected are likely to reflect the best performance available at that time.

<Table 4.2.1.10> Detectors of the CoXRD beamline.

Parameter	**EIGER2 X 4M**	**LAMBDA 250k**	**SDD**
Application	BCDI and wide-angle diffraction	Coherent diffraction imaging, time-resolved XRD	XRF, GIXRF, GIXRF-XANES, elemental mapping during Bragg ptychography
Detector type	Hybrid photon-counting pixel detector	Hybrid photon-counting pixel detector	Silicon drift detector (energy dispersive)
Sensor material and thickness	Si, 450 μm	Si	Si
Pixel pitch	75 μm	55 μm	–
Pixel format or channels	2068 × 2162	512 × 512	7 elements
Active area	155.1 × 162.2 mm^2	28 × 28 mm^2	–
Maximum frame rate	1,120 Hz (8 bit), 560 Hz (16 bit)	24,000 Hz (1 bit), 4,000 Hz (6 bit), 2,000 Hz (12 bit), < 1,000 Hz (24 bit)	–
Counter depth	32 bit image depth	1, 6, 12, or 24 bit (selectable)	–
Energy range	6–40 keV	6–25 keV	–

References

[1] Hyungseok Choi and Jongha Park. Beamline Photon Source Analysis Report. Internal Document PAL-INT/ME-2026-007. Pohang Accelerator Laboratory, July 2026.

[2] Jongha Park et al. High Heat Load Front-End Mechanical Design and Thermal Analysis Report. Internal Document PAL-INT/ME-2026-003. Pohang Accelerator Laboratory, June 2026.

4.2.2 Coherent Small-Angle X-ray Scattering (ID04)

The CoSAXS (Coherent Smal-Angle X-ray Scattering) beamline is a dedicated coherent hard X-ray scattering beamline of the KLS project, installed at sector ID04. Exploiting the high spatial coherence fraction and photon flux of the multi-bend achromat source, it delivers reliable speckle contrast for X-ray Photon Correlation Spectroscopy (XPCS) while also supporting conventional small- and wide-angle X-ray scattering (SAXS/WAXS) and grazing-incidence geometries. This chapter describes the ID04-specific design of the photon source, the front-end, the beamline optics (overall optical layout and component roles, optical layout and simulation, heat load, and beam delivery), the photon transfer line (PTL: beamline layout, hutches, and sample positions), and the end-station. Material that is common to all KLS beamlines is cited to the separate Common Technical Sections document prepared by the device team.

4.2.2.1 Target Purpose and Objective

The beamline covers a primary photon energy range of 9 to 12 keV, optimized for coherent flux in speckle based experiments, with extended access up to 30 keV for condensed matter studies requiring deeper penetration or higher wavevector transfer. Two reflective coatings (rhodium and platinum) on the High Heat Load Mirror (HHLM) suppress high harmonic contamination from IVU20 and thermal load. Two Compound Refractive Lens (CRL) transfocators provide a tunable beam size for optimizing the signal to noise ratio in XPCS and controlling the X-ray dose delivered to the sample. The design references leading coherence beamlines such as P10 at PETRA III and 8-ID at APS-U, targeting a competitive combination of coherent flux and beam size flexibility.

As a dedicated platform for coherent X-ray scattering, the beamline places particular emphasis on adaptability in both optical configuration and sample environment integration, including support for user defined or in house developed *in situ* and *operando* chambers, to serve a broad scientific program spanning soft matter, biological, and functional materials research.

A X-ray Photon Correlation Spectroscopy

XPCS is a well established technique for probing the dynamics of complex, disordered condensed matter systems, and has been applied to colloids, polymers and soft nanoparticle suspensions, metallic glasses, and water. It extends visible

light photon correlation spectroscopy into the X-ray regime, exploiting the shorter wavelength to access scattering vectors from approximately 10^{-3} to several Å^{-1} and thereby probe atomic- and nanoscale dynamics inaccessible to optical light.

Since its first experimental demonstration in 1995, dedicated XPCS beamlines have been developed at the ESRF and the APS, followed by a second generation offering higher coherent flux at PETRA III and NSLS II, and more recently at XFEL facilities such as XCS at LCLS and MID at the European XFEL.

XPCS quantifies sample dynamics through the normalized intensity autocorrelation function $g_2(q, \tau)$, whose decay rate is related to the underlying relaxation process. For example, the free particle diffusion coefficient of a Brownian system follows the Stokes-Einstein relation, or a collective diffusion coefficient applies when interparticle interactions are significant. For samples whose dynamics evolve during the measurement, the two time correlation function (TTCF) is used instead to resolve nonstationary behavior. At the COSAXS beamline, XPCS is expected to be the primary driver of the optical and end-station design, with target applications including colloidal and protein dynamics, metallic glass relaxation, and energy materials studies under operando conditions.

B Small-Angle X-ray Scattering

Small-Angle X-ray Scattering (SAXS) is one of the most established X-ray scattering techniques, tracing back to the pioneering work of Guinier in the 1930s–1950s, and remains a standard method for characterizing nanostructures from a few to several hundred nanometers across soft matter, biology, and condensed matter physics. The scattered intensity at small momentum transfer ($q \approx 0.001$–1 Å^{-1}) encodes particle size, shape, and internal structure. The low q Guinier region reflects the overall particle size through the radius of gyration, the intermediate q region reflects shape and interparticle correlations, and the high q Porod region reflects the sharpness of internal interfaces and surface morphology.

Grazing Incidence SAXS (GISAXS) extends these principles to thin films and buried interfaces using an incidence angle near the critical angle for total external reflection, and has become a key tool for in situ and operando studies of nanoparticle self assembly, block copolymer ordering, and thin film growth kinetics. Leveraging the high brilliance and coherence of the KLS source together with fast area detectors, the COSAXS beamline will support high sensitivity SAXS/GISAXS measurements of weakly scattering systems and time resolved studies, complementing

its XPCS capability within a single, multi modal instrument.

4.2.2.2 Photon Source

Among the three undulators planned for the KLS (e.g., IVU16, IVU20, IVU22, and IVU24), IVU20 provides the highest coherent flux around 9 keV, making it the source of choice for the coherence driven experiments at the COSAXS beamline. The IVU20 exhibits a spectral discontinuity between 6.8 keV and 8.08 keV, which lies below the COSAXS primary operating range of 9 to 12 keV and therefore does not affect standard operation. The COSAXS beamline covers a photon energy range of 8.4 to 30 keV, with primary operations planned at 9 to 12 keV. At this energy range, the coherent photon flux at the source is expected to be approximately 2.6×10^{13} ph/s/0.1%B.W. at 9 keV, with horizontal and vertical coherent fractions of 0.063 and 0.274, respectively. The IVU20 that will be used in the COSAXS beamline has a length of 3 m, a period of 20 mm, and a gap size adjustable between 5 and 18 mm [1]. The source parameters of COSAXS are summarized in table 4.2.2.1.

<Table 4.2.2.1> Source parameters for the COSAXS beamline (IVU20). The maximum total power and the peak power density are given at full storage ring current.

Undulator	**Period (mm)**	**Length (m)**	**Gap size (mm)**	$K_{\max}$	**Max total power (kW)**	**Power density (kW/mrad²)**
IVU20	20	3.0	5 to 18	1.904	12.49	164.2

4.2.2.3 Front-End

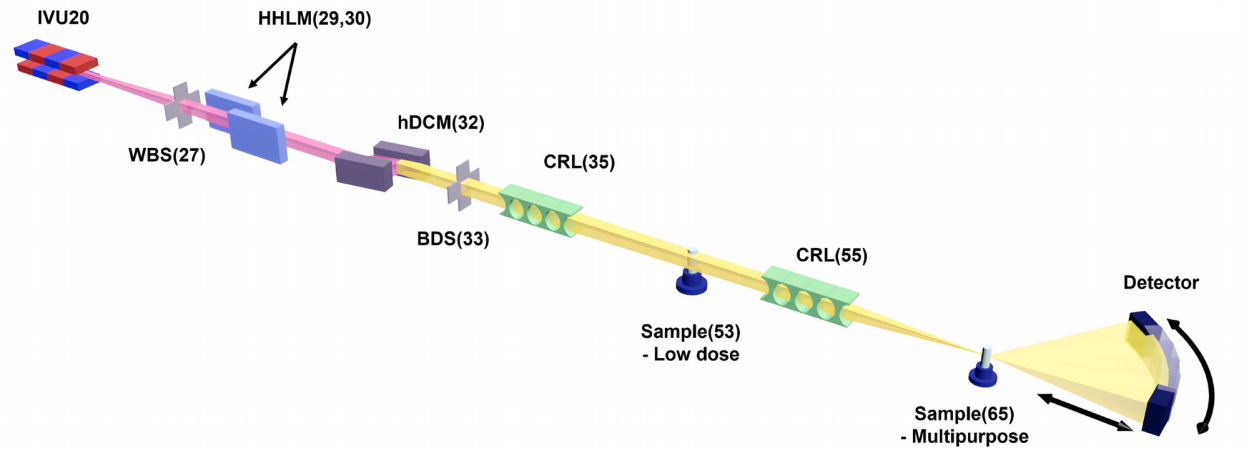
The COSAXS beamline adopts the standardized KLS High Heat Load IVU Front end [2], whose common design basis (Beamline Overview & Design Basis, and Front end & Vacuum System) is described in the separate Common Technical Sections document. For this beamline, the Front end is configured to handle up to 12.49 kW of power from the IVU20 [1]. Because preserving the X-ray wavefront is essential for maintaining coherence, the Front end design minimizes the use of windows and optics, employing components with extremely low figure and slope error to limit wavefront distortion.

4.2.2.4 Beamline Optics

A Overall optical layout and component roles

The ID04 COSAXS beamline hutch is located on the northern part of the storage ring, with a total beamline length of 79 m from the source. A shielding wall is

positioned at approximately 25 m, followed by the optics hutch extending to 36 m, which houses the white beam slits, a pair of high heat load mirrors, and the monochromator. A Beam Defining Slit (BDS) and two CRL transfocators are located at 33.7 m, 35 m, and 55 m, respectively. The experimental hutch begins at 50 m and extends 29 m downstream, housing beam position monitors, guard slits, the sample stage, and the detector system. An overview of the beamline layout is shown in figure 4.2.2.1.



<Figure 4.2.2.1> Overview of the layout of the COSAXS beamline. Component positions are given in metres from the source.

The optimal position of the focusing optics for both transmission and grazing incidence SAXS was determined analytically and validated by ray tracing from the momentum resolution requirements of each geometry. The component sequence, distances, and roles are listed in table 4.2.2.2.

The optical design of the COSAXS beamline must satisfy two distinct requirements: preservation of X-ray coherence for XPCS, and flexible focusing for SAXS/GISAXS geometries. This requires optics with minimal figure error and surface roughness, combined with careful thermal management to limit slope error degradation under the high heat load of the fourth generation source.

Two CRL transfocators (CRL1 and CRL2, at 35 m and 55 m) provide three focusing modes. CRL1 alone delivers a low divergence beam for conventional (transmission) SAXS/Ultra SAXS (USAXS); CRL2 alone provides GISAXS focusing at its optimal focal position; and a combined mode is used for XPCS, in which CRL1 provides collimation or medium focusing while CRL2 provides fine control of the beam size at the sample. A pair of High Heat Load Mirrors (HHLM), coated

<Table 4.2.2.2> Component list of the COSAXS beamline.

Distance (m)	Location	Component	Description
0	Front-End	IVU20	Period 20 mm, length 3 m
27.3–28	Optical Hutch	White-beam slit / BPM	Beam conditioning and white beam monitoring
29		HHLM 1	Rh/Pt coated high harmonic rejection mirror
30.5		HHLM 2	Rh/Pt coated high harmonic rejection mirror
32.5		HDCM	Si(111)/Si(311), LN_2 side cooled monochromator
33.7		Slit (BDS)	Beam defining slit
35		CRL1 transfocator	Beam collimation or medium focus
50	Experimental Hutch	Guard slit	Guard slit, upstream conditioning
53		Sample position 1	“Low Dose”, SDD up to 22 m
55		CRL2 transfocator	Fine focusing / GISAXS focus
64.8		Guard slit	Final beam conditioning before sample
65		Sample position 2	“Multipurpose”, SDD up to 10 m
75		2D detector	Adjustable flight tube, 3–10 m

with rhodium and platinum stripes, is positioned upstream of a Double Crystal Monochromator (DCM, Si(111)/Si(311)) to absorb the high thermal load carried by the white beam from the undulator and to suppress high harmonic content before it reaches the DCM crystals. A horizontally diffracting DCM configuration (HDCM) was selected for its resistance to pitch vibration, which is critical for the nanoscale beam pointing stability required in XPCS. Table 4.2.2.3 summarizes the beam path optical components. The specifications of the HHLM pair and of the HDCM are given in table 4.2.2.4 and table 4.2.2.5, respectively.

<Table 4.2.2.4> Specifications of the COSAXS high heat load mirror pair. Both mirrors are plane harmonic rejection optics that image no focus, so neither has a finite tangential or sagittal radius; all focusing is provided by the CRL transfocators.

Parameter	HHLM 1	HHLM 2
Installation location (m)	29	30.5
Reflection direction	Horizontal (H), towards the experimental hall	Horizontal (H), towards the ring
Mirror surface shape	Plane	Plane
Incident angle	2.4 mrad	2.4 mrad

(continued on next page)

(Table 4.2.2.4 continued)

Parameter	HHLM 1	HHLM 2
Tangential radius	$>$ 100 km (plane)	$>$ 100 km (plane)
Sagittal radius	$>$ 100 km (plane)	$>$ 100 km (plane)
Substrate material	Si	Si
Mirror size (L $\times$ W $\times$ T)	600 $\times$ 50 $\times$ 50 mm	600 $\times$ 50 $\times$ 50 mm
Coating material	Rh / Pt	Rh / Pt
Coating strip number	2 (Rh, Pt)	2 (Rh, Pt)
Coating stripe width	10 mm (W), per stripe	10 mm (W), per stripe
Tangential slope error	$<$ 0.2 µrad RMS	$<$ 0.2 µrad RMS
Sagittal slope error	$<$ 5 µrad RMS	$<$ 5 µrad RMS
Roughness	$<$ 0.2 nm RMS (HSF)	$<$ 0.2 nm RMS (HSF)
Cooling method	In-Ga bath cooling	In-Ga bath cooling
Mirror bender	None	Yes
Mirror surface height	1400 mm	1400 mm
Motor axis	Pitch, roll, yaw, x, y	Pitch, roll, x, y
Manual axis (granite base)	Pitch, roll, yaw, x, y, z	Pitch, roll, yaw, x, y, z

B Optical Layout Consideration and Simulation

The optical properties of the COSAXS beamline were evaluated using SPECTRA for source characterization, and SHADOW4 within the OASYS framework for ray tracing validation, including the coherence propagation of the focused beam at the sample position.

The position of the focusing optics for transmission SAXS and GISAXS geometries was determined by evaluating the momentum resolution,

$$\left(\frac{\Delta q}{q}\right)^2 = \left(\frac{\Delta\theta}{\theta}\right)^2 + \left(\frac{\Delta\lambda}{\lambda}\right)^2,$$

where the angular resolution $\Delta\theta$ combines the contributions of beam divergence and beam size in quadrature, $\Delta\theta = \sqrt{\Delta\alpha_i^2 + \Delta\alpha_f^2}$. For transmission SAXS, beam divergence dominates the resolution budget, favoring a low divergence beam from CRL1 alone. For GISAXS, the shallow incidence angle (typically about 0.16°) elongates the beam footprint on the sample by roughly two orders of magnitude, making the beam size contribution $\Delta\alpha_f$ dominant. Evaluating $\Delta q/q$ as a function of focusing optics position showed that the angular resolution is optimized near

<Table 4.2.2.3> ID04 COSAXS beamline optics component reference table.

Component	Distance (m)	Deflection	Type	Description
HHLM 1	29	H	Plane, Rh/Pt coated strips	Absorbs high thermal load from white beam; suppresses high harmonic content
HHLM 2	30.5	H	Plane, Rh/Pt coated strips	Absorbs high thermal load from white beam; suppresses high harmonic content
HDCM	32.5	H	Si(111)/Si(311) channel-cut	Monochromator
CRL1 transfocator	35	none	CRL stack, diamond	Collimation / medium focus
CRL2 transfocator	55	none	CRL stack, diamond	Fine focusing / GISAXS focus

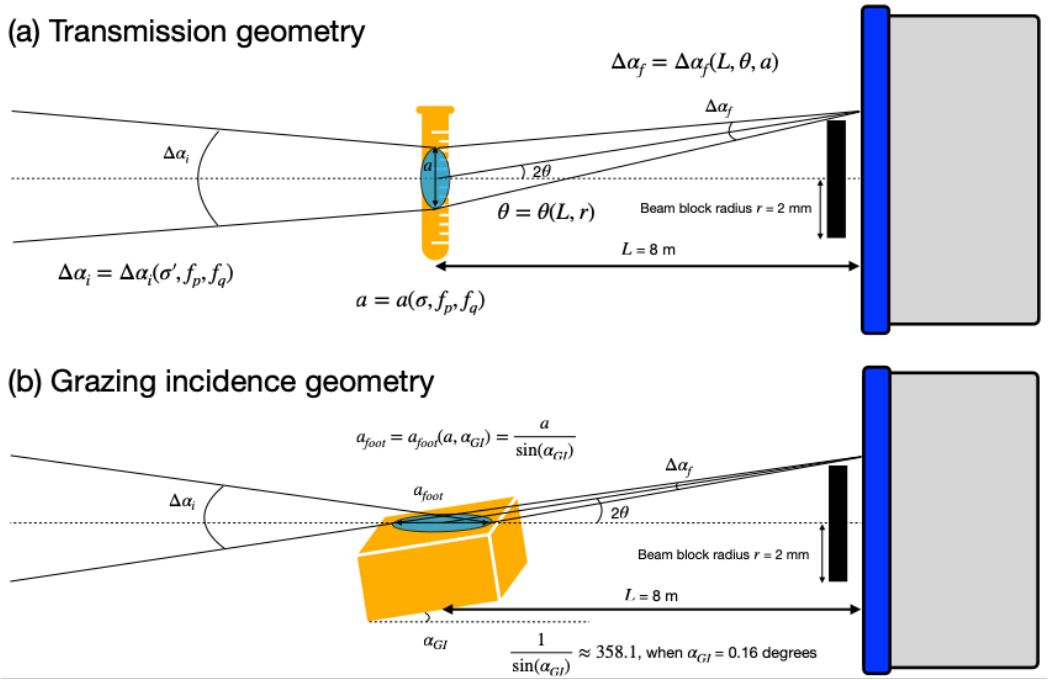
<Table 4.2.2.5> Specifications of the COSAXS horizontally diffracting double crystal monochromator (HDCM).

Item	Specification
Position (m)	32.5
Deflection / type	Horizontal (H); horizontally diffracting double crystal monochromator (HDCM)
Photon energy range	8.4 to 30 keV; primary operation 9 to 12 keV
Crystal / optical element	Si(111) / Si(311) channel-cut
Operating modes	Si(111) and Si(311) crystal sets, selectable
First crystal	Si(111)/Si(311); incident power reduced to approximately 110 W by the white beam slit and HHLM; thermal slope error near or below 1 µrad
Second crystal	Si(111)/Si(311) channel-cut
Beam offset	25 mm
Bragg angle range	Si(111): 3.78° (30 keV) to 13.61° (8.4 keV); Si(311): 7.25° (30 keV) to 26.79° (8.4 keV)
Cooling	Liquid nitrogen (LN_2) side cooling

53 m from the source, which is consistent with the CRL2 position at 55 m used for GISAXS.

Figure 4.2.2.2 illustrates the geometric quantities entering the angular resolution calculation. In the transmission geometry (a), the beam divergence $\Delta\alpha_i$ and the beam size contribution $\Delta\alpha_f$ are defined at the sample and propagate to the detector over the sample to detector distance L. In the grazing incidence geometry (b), the shallow incidence angle α_{GI} stretches the illuminated footprint on the sample to $a_{\mathrm{foot}} = a/\sin(\alpha_{\mathrm{GI}})$; for a typical grazing angle of 0.16°, this corresponds to a footprint elongation of approximately 358 times the beam size used in trans-

mission geometry, which substantially increases the beam size contribution $\Delta\alpha_f$ to the resolution.



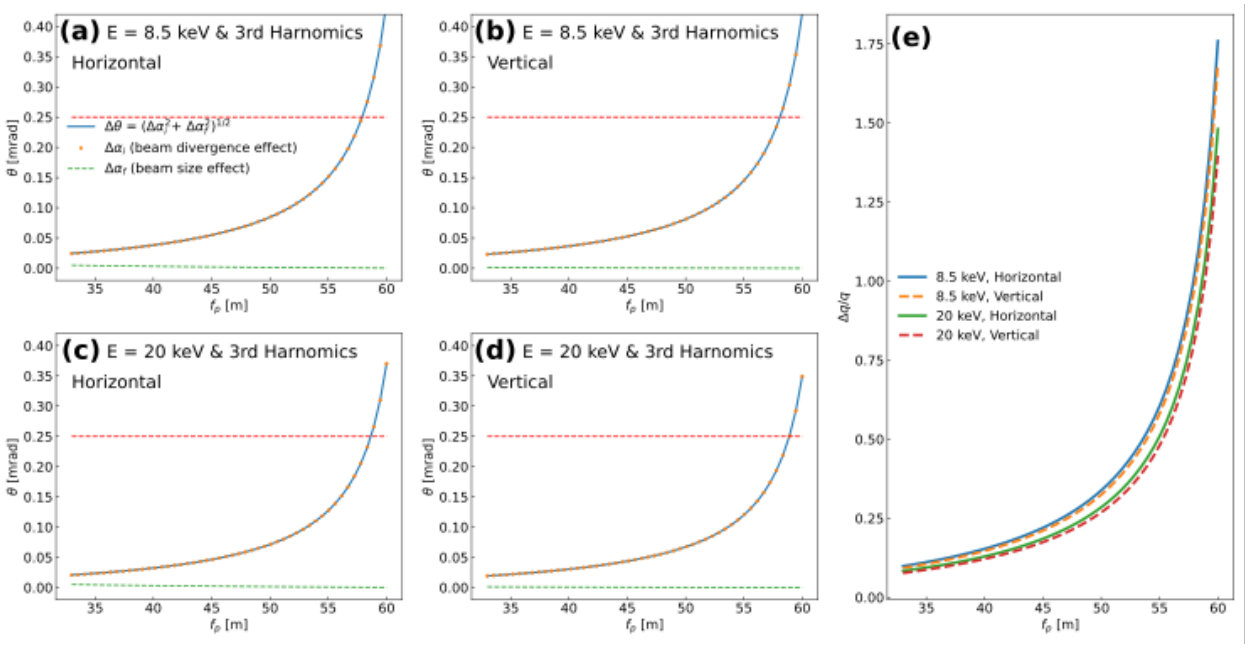
<Figure 4.2.2.2> Schematic of (a) transmission SAXS and (b) grazing incidence SAXS geometry.

Using the geometry defined above, the angular resolution $\Delta\theta$ and the relative momentum resolution $\Delta q/q$ were calculated analytically as a function of the focusing optics position f_p for the transmission geometry, shown in figure 4.2.2.3.

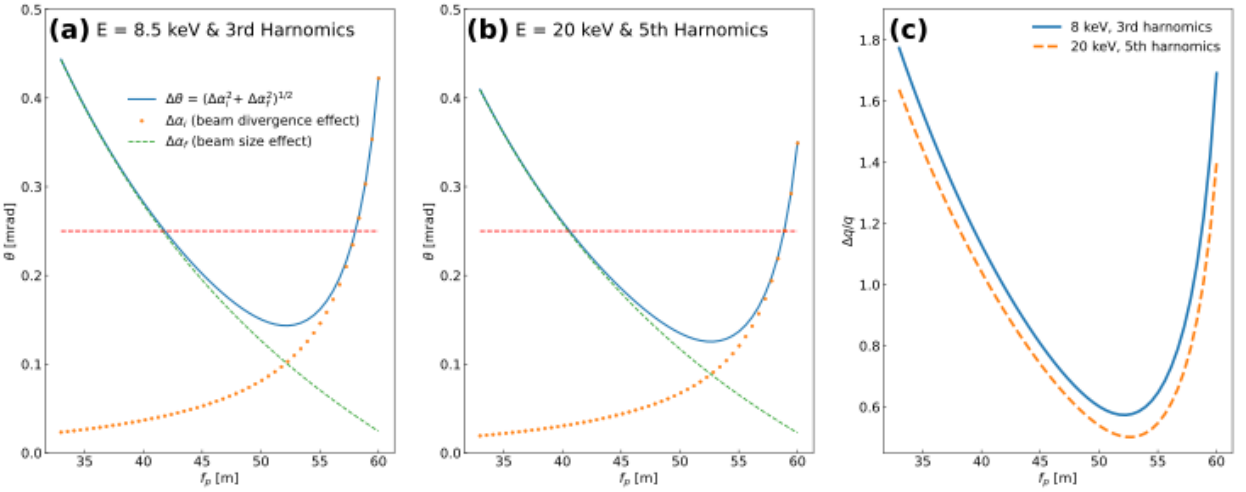
In figure 4.2.2.3(a) through (d), the solid blue line represents $\Delta\theta$, which increases gradually as the focusing optics move farther from the sample. This trend is primarily attributed to the beam divergence contribution $\Delta\alpha_i$ (orange dots), while the beam size contribution $\Delta\alpha_f$ (green dashed line) remains negligible under transmission conditions. Panel (e) summarizes the resulting $\Delta q/q$ for both photon energies and directions, confirming that a low divergence beam from CRL1 alone is sufficient to reach the target resolution for transmission SAXS.

The same analysis was repeated for the grazing incidence geometry, where the elongated beam footprint makes the beam size contribution significant. The results are shown in figure 4.2.2.4.

Unlike the transmission case, the beam size contribution $\Delta\alpha_f$ (green dashed line) is clearly pronounced at small f_p and decreases as the focusing optics move



<Figure 4.2.2.3> Angle and wavevector resolutions as a function of focusing optics position from the source, for transmission geometry at 8.5 and 20 keV in the horizontal and vertical directions.

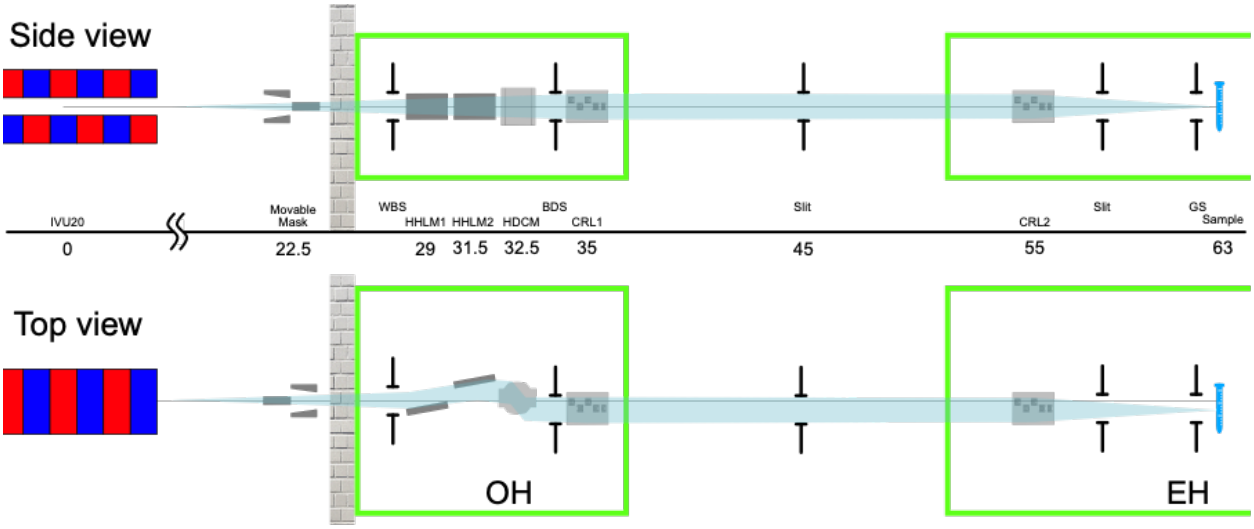


<Figure 4.2.2.4> Angle and wavevector resolutions as a function of focusing optics position from the source, for grazing incidence geometry at 8.5 and 20 keV.

farther from the sample, while the beam divergence contribution $\Delta\alpha_i$ (orange dots) increases in the opposite direction. The two contributions cross near $f_p \approx 53$ m, where the combined angular resolution $\Delta\theta$ reaches its minimum, consistent with the CRL2 position at 55 m adopted for GISAXS.

Figure 4.2.2.5 shows the resulting optical layout of the beamline, in both side

view and top view, when the beam is focused at the Multipurpose sample position for XPCS, combining the Front-End, optics hutch (OH), and experimental hutch (EH) components discussed above into a single ray-traced model.

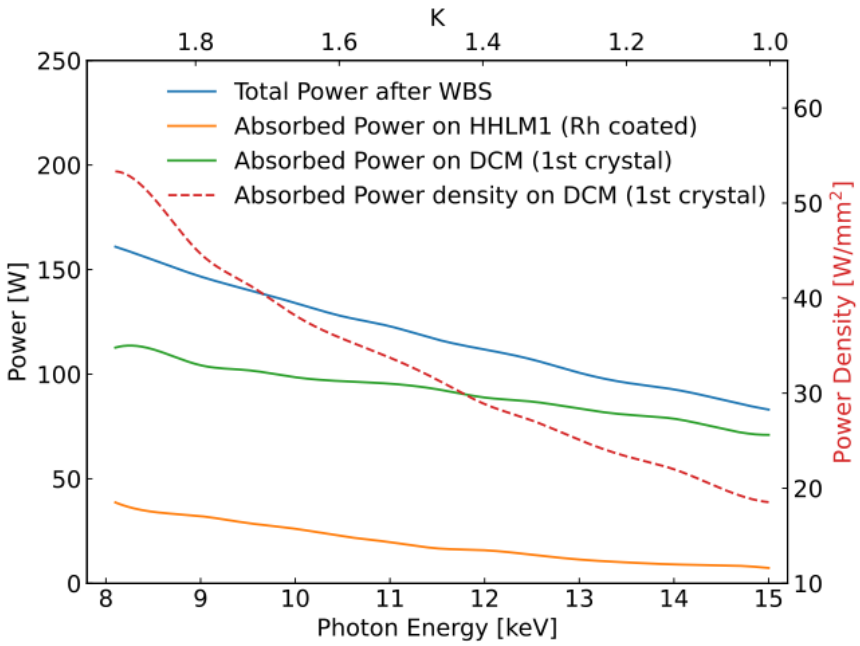


<Figure 4.2.2.5> Optical layout of the COSAXS beamline when the beam is focused at the Multipurpose sample position for XPCS.

C Heat Load Consideration

The IVU20 delivers up to 12.49 kW of total power and a peak power density of 164.2 kW/mrad² at full storage ring current [1]. The white beam slit and HHLM together reduce the power incident on the first DCM crystal to approximately 110 W, keeping the resulting thermal slope error near or below 1 µrad when combined with liquid nitrogen side cooling, consistent with heat load performance demonstrated at comparable ESRF beamlines. Thermal loading on each optical component was assessed using SRW and XOPPY.

Detailed simulations using XOPPY within the OASYS framework, accounting for the mirror grazing angle, reflectivity, and the DCM diffraction angle as a function of photon energy and undulator K value, are shown in figure 4.2.2.6. The results show that the total undulator power decreases with increasing photon energy up to 15 keV, with the Rh coated HHLM1 and HHLM2 absorbing approximately 15% and 6% of the power incident on the optics, that is of the power transmitted through the front-end aperture rather than of the 12.49 kW emitted into the full undulator radiation fan. The resulting power density on the first DCM crystal declines still more rapidly at higher photon energies, following the reduced Bragg diffraction angle of the Si(111) plane at those energies.



<Figure 4.2.2.6> Heat load calculation on the HHLM and DCM as a function of photon energy and K, from XOPPY simulations within the OASYS framework.

D Beam Delivery Specifications

Using the two CRL transfocators, the beamline targets a focused beam of approximately 4–13 μm (FWHM) for XPCS at the Multipurpose position across the 8.5–12 keV range, with independently tailored beam sizes for transmission SAXS and GISAXS geometries.

All focusing schemes were modeled using ray tracing in the OASYS framework, with results in excellent agreement with the analytic demagnification ratio $M = f_p/f_q$. For XPCS at the Multipurpose position, CRL1 and CRL2 are combined to reach a focused beam of approximately 13 μm (horizontal) by 4 μm (vertical) FWHM across 8.5 to 12 keV (table 4.2.2.6). At the Low Dose position, only CRL1 and the BDS are used, producing a larger beam to reduce X-ray dose while preserving speckle contrast over the 22 m SDD. For SAXS, either CRL1 or CRL2 is used depending on geometry: transmission SAXS uses CRL1 alone for low beam divergence, while GISAXS uses CRL2 alone, focusing near its optimal position at 55 m (table 4.2.2.7). Recent advances in large aperture diamond CRL fabrication allow CRL1 and CRL2 to transmit input beams of approximately 700 μm and 1000 μm, respectively, without significant intensity loss. The Compound Refractive Lenses are fabricated from High Pressure High Temperature (HPHT) diamond

single crystal for its thermal conductivity, mechanical strength, and radiation hardness under high coherence, high flux operation.

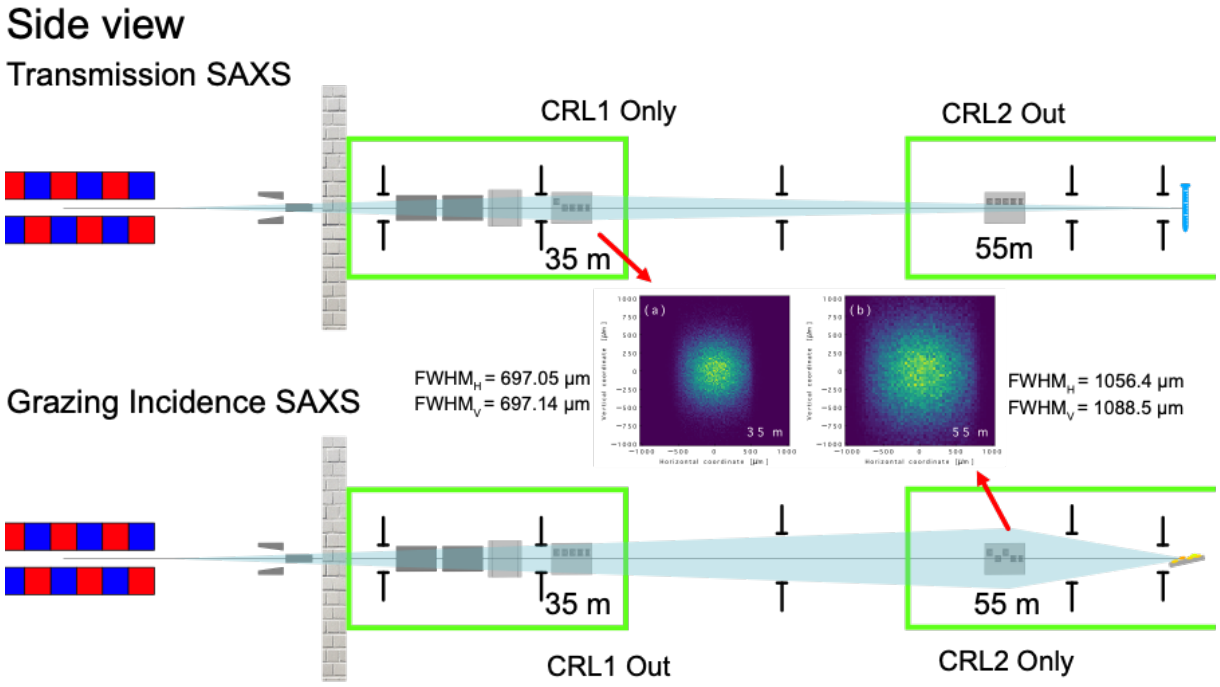
<Table 4.2.2.6> CRL configurations for XPCS at the Multipurpose position, evaluated by ray tracing (OASYS). R = apex radius of curvature; N = number of lens elements.

Energy (keV)	**CRL1 R (μm)**	**CRL1 N**	**CRL2 R (μm)**	**CRL2 N**	**Beam size, H × V (μm)**	**Transmission (%)**	**Coherent flux (ph/s/0.1%bw)**
8.5	725	1	805	4	12.97 × 4.230	22.8	6.74×10^{12}
9	650	1	723	4	12.71 × 4.052	25.3	6.56×10^{12}
10	520	1	588	4	12.75 × 3.967	30.4	6.21×10^{12}
12	350	1	412	4	12.86 × 3.743	38.0	4.55×10^{12}

<Table 4.2.2.7> CRL configurations for transmission SAXS and GISAXS geometries, evaluated by ray tracing (OASYS). R = apex radius of curvature; N = number of lens elements.

Energy (keV)	**Geometry**	**Lens configuration**	R **(μm)**	N	**Beam size, H × V (μm)**	**Transmission (%)**
8.5	Transmission SAXS	CRL1	946	3	35.9 × 11.31	35.1
20	Transmission SAXS	CRL1	455	8	33.90 × 9.215	40.7
8.5	GISAXS	CRL2	588	4	8.21 × 2.62	13.0
20	GISAXS	CRL2	430	14	8.22 × 2.28	25.4

Figure 4.2.2.7 illustrates the resulting focusing schemes for transmission SAXS and GISAXS at the Multipurpose position. For transmission SAXS, CRL1 alone is used while CRL2 is retracted from the beam, producing a beam of FWHM 697.05 × 697.14 μm at the CRL1 position (35 m). For GISAXS, CRL1 is retracted and CRL2 alone is used, producing a beam of FWHM 1056.4 × 1088.5 μm at the CRL2 position (55 m); this larger input beam is consistent with the approximately 1000 μm aperture used by CRL2 discussed above.



<Figure 4.2.2.7> Focusing schemes for transmission SAXS (upper) and grazing incidence SAXS (lower), with corresponding beam profiles at the sample position.

4.2.2.5 Photon Transfer Line

A Beamline layout and hutches

The ID04 COSAXS beamline hutch is located on the northern part of the storage ring, with a total beamline length of 79 m from the source. A shielding wall is positioned at approximately 25 m, followed by the optics hutch extending to 36 m, which houses the white beam slits, a pair of high heat load mirrors, and the monochromator. A Beam Defining Slit (BDS) and two CRL transfocators are located at 33.7 m, 35 m, and 55 m, respectively. The experimental hutch begins at 50 m and extends 29 m downstream, housing beam position monitors, guard slits, the sample stage, and the detector system. An overview of the beamline layout is shown in figure 4.2.2.1.

B Sample positions

The beamline provides two sample positions to serve complementary experimental needs. A “Low Dose” position at 53 m offers a sample to detector distance (SDD) of up to 22 m, and a “Multipurpose” position at 65 m offers an SDD of up to 10 m with a detector arm that swings up to 45° to access WAXS geometry. This two position scheme follows the approach adopted at leading XPCS beamlines

worldwide, including 8-ID at APS-U (SDD 22 m) and CoSAXS at MAX IV (17 m). The Low Dose position, combined with a larger beam size, allows radiation sensitive samples such as proteins and polymers to be measured with reduced X-ray dose while maintaining sufficient speckle contrast, whereas the Multipurpose position offers finer control of beam size to access a broader range of momentum transfer and scattering geometries.

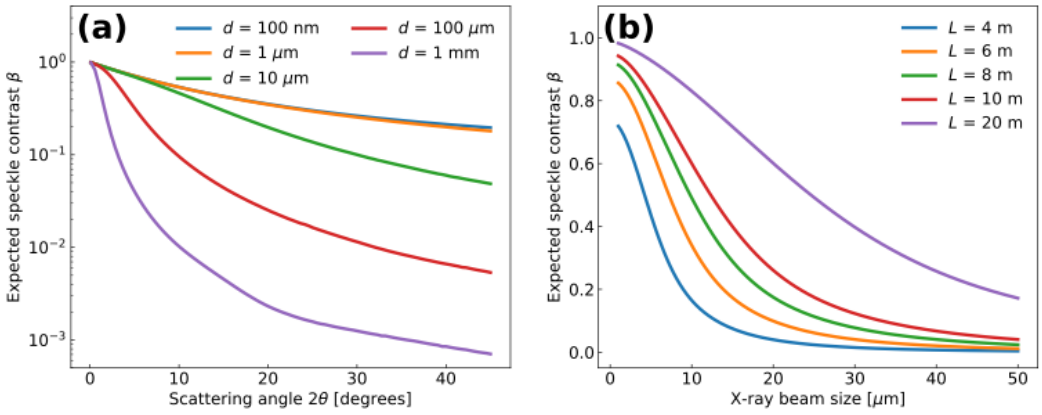
The beamline measurement strategy for XPCS is centered on optimizing the speckle contrast β to improve the signal to noise ratio (SNR), expressed as SNR $= \beta\bar{k}\sqrt{N_f N_p}$, where $\bar{k}$, N_f, and N_p denote the averaged scattering intensity, the number of frames, and the number of detector pixels within a region of interest, respectively. Because $\bar{k}$ is largely fixed by the coherent photon flux and the scattering cross section of the sample, optimizing β is the primary design lever available at the beamline.

β depends on the longitudinal coherence length ξ_l, the sample thickness, the detector pixel size, the scattering angle, the sample to detector distance (SDD), and the coherent beam size at the sample. The longitudinal coherence length is governed by monochromaticity, $\xi_l = \lambda^2/(2\Delta\lambda)$, and is approximately 0.5 to 2.5 μm at 10 keV for the Si(111)/Si(311) HDCM crystals. The target criterion for the COSAXS beamline is to tune the beam size and SDD to achieve β of approximately 0.2 to 0.3 during beamtime preparation.

For the Low Dose position (SDD up to 22 m), this yields an expected speckle contrast of about 20% with a beam size of approximately 20 to 150 μm^2, a maximum scattering angle of 0.52° (detector arm at 0°), and a maximum accessible q of 0.041 Å^{-1} at 9 keV. For the Multipurpose position (SDD 0.25 to 10 m via the adjustable vacuum flight tube), the beam size can be tuned between approximately 5 and 30 μm^2 (with an additional CRL considered in future for even smaller beams), the detector arm can rotate up to 45° with the WAXS detector stage located 0.25 m downstream of the sample, and the maximum accessible q reaches 3.4 Å^{-1} at 9 keV.

The speckle contrast can be decomposed as $\beta = \beta_{\mathrm{cl}}(a, d, \theta, \lambda, \Delta\lambda) \times \beta_{\mathrm{res}}(a, L, \lambda)$, where β_{cl} represents the effect of the transverse and longitudinal coherence length, and β_{res} corresponds to the finite angular resolution of the experimental setup. Figure 4.2.2.8 shows the estimated β calculated for the COSAXS beamline configuration.

Figure 4.2.2.8(a) shows the estimated β as a function of scattering angle 2θ for various sample thickness d, with fixed parameters photon energy E = 9 keV, SDD



<Figure 4.2.2.8> Estimated speckle contrast β (a) as a function of scattering angle for various sample thickness, and (b) as a function of X-ray beam size for various sample to detector distance.

L = 10 m, coherent beam size a = 1 μm, and detector pixel size P = 75 μm using a Si(111) DCM. The gradual decrease of β at larger θ originates from the optical path length difference along the beam direction, which becomes more significant once the sample thickness exceeds the longitudinal coherence length of approximately 1 μm under these conditions. Figure 4.2.2.8(b) shows the expected β as a function of beam size a for various SDD L, with fixed parameters E = 9 keV, d = 1 mm, and P = 75 μm. As both panels show, β remains sufficiently high in the SAXS regime for reasonable sample thicknesses and moderate beam sizes, supporting the standard XPCS configuration of the COSAXS beamline.

4.2.2.6 End-Station

A Scientific Scope

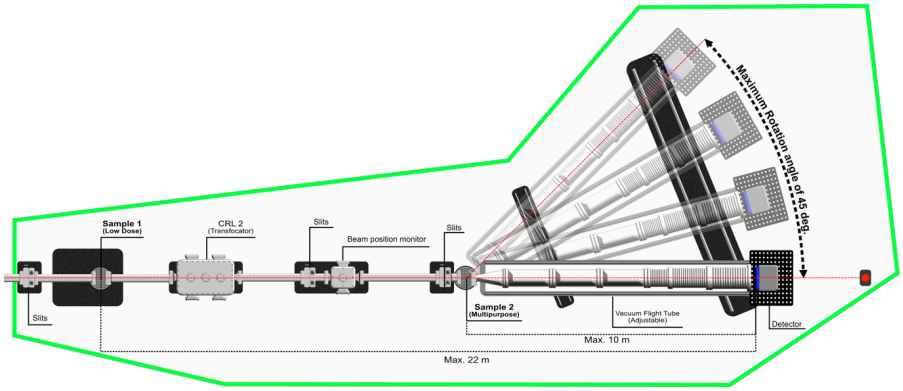
The COSAXS end-station is designed to support both dynamic (XPCS) and structural (SAXS/GISAXS/WAXS) measurements within a single, reconfigurable instrument. It provides adjustable sample to detector distance, a range of sample environments including a high speed piezo sample scanner to mitigate radiation induced sample damage during XPCS, and a microfluidic platform for in situ synthesis and structural studies, together with a detector system selected to balance dynamic range against frame rate.

B Instrument Definition

The core instrument consists of a PI hexapod mounted on a Huber two circle goniometer for sample alignment, a vacuum flight tube with a travel range adjustable between 3 and 10 m to accommodate the variable SDD, and an area detector mounted on a rotatable stage enabling scattering angles up to 45° for WAXS access. Solid state attenuators (CVD diamond, silicon, and germanium, selected according to photon energy) and motorized guard slits are installed upstream of the sample to protect the optics and detector and to minimize parasitic background.

C Instrument Location

The instrument is located in the experimental hutch spanning 50 to 79 m from the source. An overview of the end-station layout is shown in figure 4.2.2.9.



<Figure 4.2.2.9> Overview of the COSAXS experimental end-station.

D Instrument Specifications

Candidate 2D area detectors for the COSAXS end-station were surveyed among current photon counting and charge integrating technologies (e.g., EIGER2, Lambda, and Jungfrau, together with emerging high frame rate designs), balancing dynamic range against frame rate for XPCS applications. Final detector selection

will depend on continued technology development and the specific scientific requirements at the start of operation.

Ongoing developments in detector technology have produced several advanced X-ray area detectors capable of high frame rates with minimal dead time. Table 4.2.2.8 summarizes state of the art 2D area detectors surveyed in 2025 for possible implementation at the COSAXS beamline. The EIGER2X detector offers a high dynamic range and large sensitive area suited to routine scattering experiments, while detectors such as SPARTA, Rigaku XSPA, TEMPUS, CITIUS, and Jungfrau target the microsecond to millisecond regime required for fast XPCS. Final selection will depend on continued technology development and the beamline's scientific requirements at the start of operation.

<Table 4.2.2.8> Specifications of 2D area X-ray detectors for the COSAXS beamline. The EIGER2 X entry denotes the product family rather than a fixed module size.

Parameter	EIGER2 X family	Lambda	SPARTA	Rigaku XSPA	TEMPUS	CITIUS	Jungfrau
Role / technique	Routine scattering	TBD	Fast XPCS (µs–ms)	Fast XPCS (µs–ms)	Fast XPCS (µs–ms)	Fast XPCS (µs–ms)	Fast XPCS (µs–ms)
Detector type / detection principle	Hybrid photon-counting pixel detector	Hybrid photon-counting pixel detector	Integrating pixel detector	Hybrid photon-counting pixel detector	Hybrid photon-counting pixel detector	Integrating pixel detector	Integrating pixel detector
Sensor material / thickness	Si, 450 µm	Si, GaAs or CdTe (selectable)	Si, 500 µm	Si	Si, 300 µm	Si, 650 µm	Si, 320 or 450 µm
Pixel pitch	75 × 75 µm	55 × 55 µm	200 × 200 µm	76 × 76 µm	55 × 55 µm	72.6 × 72.6 µm	75 × 75 µm
Pixel format / channels	1028 × 1062 (1M) to 4148 × 4362 (16M)	512 × 512 (250k)	128 × 512	1024 × 512 (500k); 1024 × 1024 (1M)	448 × 512 (single chip)	384 × 728 per module	1024 × 512 per module
Active area	77.1 × 79.7 mm² (1M) to 311.1 × 327.2 mm² (16M)	28 × 28 mm²	25.6 × 105.2 mm²	77.8 × 38.9 mm² (500k); 77.8 × 77.8 mm² (1M)	6.94 cm² (single chip)	27.9 × 52.9 mm² per module	76.8 × 38.4 mm² per module
Maximum frame rate	0.5–2 kHz	1–24 kHz	up to 6 MHz (burst)	up to 970 kHz (burst)	40 kHz (event: 200 ps)	17.4 kHz	2.2–150 kHz (burst)

(continued on next page)

(Table 4.2.2.8 continued)

Parameter	EIGER2 X family	Lambda	SPARTA	Rigaku XSPA	TEMPUS	CITIUS	Jungfrau
Image / dynamic range	32 bit	1–24 bit (rate dependent)	1:10^4 ph/pixel/frame @ 12.4 keV	1–16 bit (rate dependent)	8 or 16 bit	1:1800 ph/pixel/frame @ 12 keV	1:10000 ph/pixel/pulse @ 12 keV
Detector-supported energy range	6–40 keV	6–25 keV (Si); 8–75 keV (GaAs); 8–150 keV (CdTe)	3–15 keV	4.5–30 keV	TBD	5–30 keV (1.5–5 keV on request)	From ∼2 keV; upper limit set by the sensor
Sample-to-detector distance	3–22 m	3–22 m	3–22 m	3–22 m	3–22 m	3–22 m	3–22 m
Remarks	Double gating, dual energy threshold	N/A	AGIPD based, dynamic gain switching	N/A	Under development	High saturation count rate (600 Mcps/pixel)	Dynamic gain switching

References

[1] Hyungseok Choi and Jongha Park. Beamline Photon Source Analysis Report. Internal Document PAL-INT/ME-2026-007. Pohang Accelerator Laboratory, July 2026.

[2] Jongha Park et al. High Heat Load Front-End Mechanical Design and Thermal Analysis Report. Internal Document PAL-INT/ME-2026-003. Pohang Accelerator Laboratory, June 2026.

4.2.3 Nanoprobe (ID10)

4.2.3.1 Target Purpose and Objective

The ID10 Nanoprobe beamline operates over the 5–25 keV energy range and delivers a hard X-ray nano-beam smaller than 50 nm. This nano-beam enables deconvolution microscopy techniques that achieve 20 nm elemental maps together with sub-10 nm ptychography, allowing quantitative nanoscale analysis of the elemental distribution and material structures in a localized region. The 5–25 keV range supports quantitative nano-spectroscopy of most transition metals and rare-earth elements, and its high penetrating power allows them to pass through gas environments and windows for environmental control, enabling *in-situ*, synthesis, and operating-condition studies. To support such work the beamline is designed to provide a long working distance of 50 mm despite the tens-of-nanometer beam size, which makes it straightforward to insert devices providing high and low temperatures, gas and liquid environments, and electric or magnetic fields for *in-situ*/*operando* materials research.

The primary experimental method is multi-modal imaging that simultaneously performs 2D/3D X-ray fluorescence (XRF) and 2D/3D ptychography; auxiliary techniques include diffraction mapping and nano-XANES. The scientific objectives focus on tracking reactions and defect-growth processes in energy materials and catalyst systems, and on the quantitative nanoscale analysis of complex functional materials in realistic manufacturing and operating environments. To accommodate the trend toward larger systems built by spreading and stacking nano-components, high-speed precision nano-stages are introduced so that larger areas can be investigated at the nanoscale. The key criterion of mechanical design is to keep the beam size, intensity and position instability delivered to the sample below 10 %.

That single figure governs the whole design, and table 4.2.3.1 carries it down to the tolerance each subsystem is built to. Two key criteria are worth stating explicitly, because every later number rests on them: the 0.2 μm position budget at the secondary-source aperture is one tenth of the 2 μm smallest aperture opening, and the 5 nm budget at the sample is one tenth of the sub-50 nm probe.

<Table 4.2.3.1> Flow-down of the 10 % instability driver to the tolerance each subsystem is specified to, and where each is shown to be met. The Maréchal criterion admits a 20 % loss of peak intensity (Strehl ratio 0.8) against 10 % of beam broadening; the two are the two halves of one criterion, not two versions of it.

Quantity at the sample	Derived tolerance	Specified in	Shown to be met by
Beam size	Broadening $< 10\,\%$; peak intensity loss $< 20\,\%$ (Maréchal)	Mirror slope, figure and roughness limits, table 4.2.3.4	Ray trace and tolerance derivation
Beam position	< 5 nm r.m.s.	Per-element σ_{vib}, table 4.2.3.5	Measured site floor and the isolated hutch slab, section 4.2.3.5
Beam position at the SSA	$< 0.2\,\mu$m	Secondary-source scheme; NBPM at 58.5 m	Position instability converted to intensity instability and corrected on I_0
Beam intensity	Within 10 %	Front-end slit-position feedback, section 4.2.3.3	Ion-gas chamber (I_0) at 148 m
Mechanical resonance	$f_1 > 70$ Hz at the mirror surface	table 4.2.3.5	Structural finite-element analysis
Thermal drift	Hutch 0.1 °C; enclosure < 0.02 °C/h	section 4.2.3.5	Concrete hutch with HVAC; water-cooled enclosure

4.2.3.2 Photon Source

The photon source for the ID10 Nanoprobe beamline is IVU24. The common insertion-device design basis (period and gap optimization, K-value, brilliance and power analyses) is described in the separate Common Technical Sections document and in the in-vacuum undulator design for the first-phase beamlines [1], as well as in the beamline photon source analysis report [2]; only the ID10-specific basics are stated here. The undulator has a magnetic period of 24 mm, a total device length of 3.0 m, and is installed at the center of the straight section. The minimum magnetic gap is 6 mm, chosen as the effective gap that delivers continuous coverage of the 5–25 keV range with the highest brilliance. Under the maximum stored current of 400 mA, the maximum beam power passing through a $2 \times 2\,\mathrm{mm}^2$ mask at 23 m is 0.96 kW, while the maximum total power emitted at the 6 mm effective gap is 12 kW. The ID10-specific source parameters are summarized in table 4.2.3.2.

<Table 4.2.3.2> ID10 Nanoprobe insertion-device source parameters at the beam port. The undulator is installed at the center of the straight section and the values are given for the maximum stored current of 400 mA. The gap size quoted is the effective minimum gap of 6 mm that delivers continuous 5–25 keV coverage. "Mask power" is the beam power transmitted through the $2 \times 2\,\mathrm{mm}^2$ front-end mask at 23 m, as opposed to the total emitted power.

Undulator	Period (mm)	Length (m)	Gap size (mm)	$K_{\max}$	Max total power (kW)	Power density (kW/mrad^2)	Mask power at 23 m (kW)
IVU24	24	3.0	6	2.27	12	135	0.96

4.2.3.3 Front-End

The ID10 Nanoprobe beamline adopts the standardized KLS IVU Front-End (FE). The common FE design basis (three-mask heat-load layout, fixed and movable masks, beam stopper, photon shutter, beam-position diagnostics, and the 0.5 T safety magnet) is described in the separate Common Technical Sections document; the mechanical design and thermal analysis of the beam-intercepting components are given in the high-heat-load front-end design report [3]. Only the nanoprobe-specific values that form the basis for the downstream optics are stated here.

The FE is rated for the standard 18 kW heat load [3, 2]. Although the IVU has a mechanical minimum gap of 5 mm, the effective minimum gap required to provide the full 5–25 keV range is 6 mm; consequently the effective maximum total power of the ID10 IVU is 12 kW. The FE diagnostics provide slit-position feedback that keeps the beam intensity at the sample stable within 10 %, and the 0.5 T safety magnet deflects any electron beam entering the FE out of the beam path so that it cannot reach the optical hutch. The acceptance defined by the FE optics is 37 μrad, corresponding to a $1 \times 1\,\mathrm{mm}^2$ aperture at 27 m; it admits about 185 W of the 0.96 kW that passes the $2 \times 2\,\mathrm{mm}^2$ front-end mask at 23 m (table 4.2.3.2). That acceptance and that power are the photon-beam input used for the optics heat-load analysis in section 4.2.3.4.

4.2.3.4 Beamline Optics

This section consolidates the detailed optics design of the ID10 Nanoprobe beamline. All optical simulations were performed with Shadow3 in the OASYS environment. Simulations were carried out primarily at 10 keV (the most frequently used energy) and at 20 keV for comparison. Because the X-ray source parameters provided by OASYS do not account for the electron-energy dispersion, the source

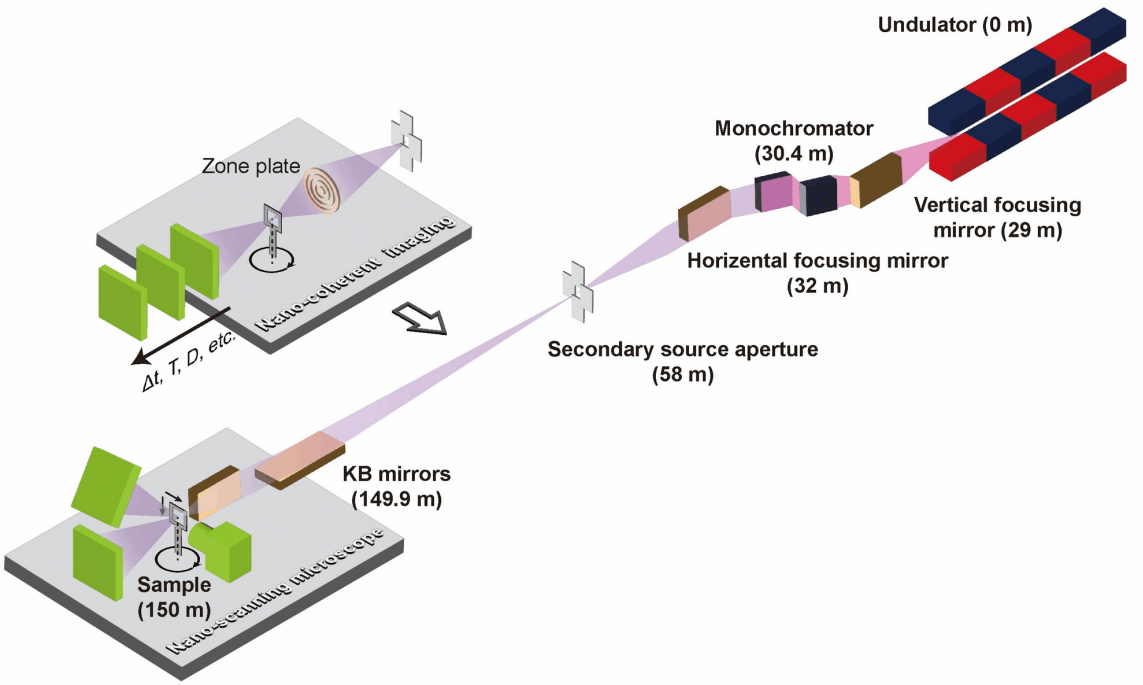
parameters used here were taken from SPECTRA as a geometry source in OASYS; the SSA aperture size and photon-flux calculations were performed with an in-house MATLAB script. The section proceeds from the optical layout and the reasoning that fixes the beamline length, through the mirror and monochromator specifications, to the beam delivered to the sample and the heat load the optics must carry; the stability budget these tolerances serve is set out in table 4.2.3.1.

A Overall optical layout and component roles

The optical layout of the beamline is shown in figure 4.2.3.1, with the component longitudinal positions listed in table 4.2.3.3. Two horizontal-deflection mirrors focus the beam in both the vertical and horizontal directions onto a secondary-source aperture (SSA); the SSA is then adjusted to the required experimental conditions and the beam is directed to the two end-stations. The layout incorporates a secondary-source focusing scheme that allows a flux-versus-coherence trade-off using the SSA: it trades the required transverse coherence for flux and converts positional instability into intensity instability. Intensity instabilities are readily compensated with diagnostic devices such as an ion chamber, whereas positional instabilities would require large computational effort to correct; this design is therefore well suited to a scanning-microscopy nanoprobe.

The 150 m beamline length is set by two design requirements. First, a working distance of about 50 mm must be preserved at the sample so that bulky *in-situ* environments can be accommodated, which fixes the image distance of the HKB, the last optic before the sample, at $q \approx 100$ mm. Second, the secondary-source aperture (SSA) must lie in the 2–50 μm range that is reachable with standard aperture/slit specifications; this is why M1 and M2 image the source onto the SSA with near-unit (1:1) magnification: a 1:1 image places the secondary-source size, and hence the required SSA aperture, in that practical 2–50 μm range, which fixes the SSA at 58 m (table 4.2.3.8). Demagnifying a 2–50 μm secondary source down to the target sub-50 nm focus then calls for a demagnification of about 900 in the horizontal and about 300 in the vertical; at the corresponding HKB and VKB image distances of 100 and 310 mm, both call for an object distance of about 90 m between the SSA and the KB (table 4.2.3.4). Placing the KB ∼90 m downstream of the SSA (58 m) therefore puts it at ∼149.9 m and the sample at 150 m (table 4.2.3.3).

The component order follows from the secondary-source scheme together with heat-load management. The high-heat-load mirror M1 (HHLM, 29 m) takes the white-beam power first and suppresses the higher harmonics before the beam



<Figure 4.2.3.1> Schematic of the ID10 Nanoprobe beamline. The IVU24 source feeds the vertical-focusing mirror M1 (29 m), the horizontal combined double-crystal and channel-cut crystal monochromator (30.4 m) and the horizontal-focusing mirror M2 (32 m); the two mirrors focus the beam onto the secondary-source aperture (SSA, 58 m), and the KB optics (149.9 m) deliver the nano-beam to the sample (150 m). The SSA is adjusted to the required experimental conditions and directs the beam to the two end-stations.

reaches the HDCM/HCCM (30.4 m), which selects the photon energy; the horizontal-focusing mirror M2 (HFM, 32 m) then completes the focusing so that M1/M2 form a near 1:1 image of the source at the secondary-source aperture (SSA, 58 m). A long, low-vibration mono-beam transport then carries the beam past the removable monitors and the flexible Endstation 1 (137–148 m) to the nano-KB pair (M3; VKB 149.7 m and HKB 149.9 m), for the final nano-focus onto the fixed multi-modal end-station (Endstation 2, 150 m). Keeping the high-heat-load and coarse-focusing optics early, where the beam is large and mechanically robust, and the nano-focusing KB last, immediately upstream of the sample, limits the propagation of figure and vibration errors into the focus.

B Mirror parameters and mirror/mechanism required performance

The complete ID10 mirror specification is given in table 4.2.3.4. For the HHLM, the HFM and the nano-KB pair (VKB and HKB), the table defines, on a single sheet,

<Table 4.2.3.3> Component-by-component layout of the ID10 Nanoprobe beamline (distance from source, location, component, role).

Distance (m)	Location	Component	Description
0	Front-End	IVU24	Period 24 mm, length 3 m
28	Optical Hutch 1	White-beam slit	Up to 4 kW heat load
28.5		White-beam attenuator	Absorber set for white-beam flux control; filter set, water-cooled holder and motion design [4]
28.8		Diamond screen monitor	White-beam profile monitor; resolution < 1 µm, diamond thickness 100 µm
29		HHLM	Spherical cylinder, Pt coating, sagittal focusing
29.8		Diamond screen monitor	Resolution < 1 µm, diamond thickness 30 µm
30.4		HDCM/HCCM	Offset 12 mm
31		White-beam DBPM	Beam-size resolution $< 0.1\%$, beam-position feedback
32		HFM	Plane substrate bent to a spherical cylinder, 2 coating strips (Rh, Pt) + bare Si
35		Diamond screen monitor	Mono-beam profile monitor, resolution < 1 µm, diamond thickness 30 µm
58	Optical Hutch 2	SSA	Aperture resolution ~500 nm, aperture size 2 to 50 µm
58.5		NBPM	Resolution 100 nm, target angle resolution < 50 nrad
137	Experimental Hutch	Beam monitor	Diamond screen monitor, 1 µm resolution, removable
137–148		Endstation 1	Flexible set-up; sample position range, spanning the monitors below
147		Beam monitor	Diamond screen monitor, 1 µm resolution, removable
148		Ion gas chamber	I_0 monitor
149.7		VKB	300 mm, Pt coating
149.9		HKB	100 mm, Pt coating
150		Endstation 2	Fixed set-up

the optical geometry, the substrate, coating and surface-error requirements, the heat load and cooling, and the manipulator and mounting concept. The slope- and figure-error tolerances of the four mirrors are set, each at its own image plane, so that the beam broadens by less than 10 % and the peak intensity decreases by less than 20 % (Maréchal criterion). The HHLM is a fixed spherical-cylinder sagittal-focusing mirror; the HFM is the only bendable one, a bendable spherical-cylinder tangential-focusing mirror used both for focusing and for thermal-bump

correction; the nano-KB pair is a set of vertical and horizontal fixed-figure elliptical cylinders that produces the < 50 nm beam. The angular-vibration tolerance budget that the mirror mechanisms and the experimental-hutch environment must meet is listed separately in table 4.2.3.5.

<Table 4.2.3.4> Specifications of the ID10 HHLM, HFM, VKB, and HKB mirrors.

Parameter	HHLM	HFM	VKB	HKB
Optical geometry				
Installation location (m)	29.0	32.0	149.7	149.9
Reflection direction	H (towards the hall)	H (towards the ring)	V (upward)	H (towards the ring)
Mirror surface shape	Fixed spherical cylinder (sagittal focusing)	Plane substrate, bent to a spherical cylinder in operation	Fixed elliptical cylinder (tangential focusing)	Fixed elliptical cylinder (tangential focusing)
Object distance p (m)	29.0	32.0	91.69	91.90
Image distance q (m)	29.0	26.0	0.31	0.10
Incident angle	2.5 mrad	2.5 mrad	3.0 mrad	3.0 mrad
Tangential radius	> 100 km (cylinder)	11.48 km (bender range 8 km to > 100 km)	206.0 m	66.59 m
Sagittal radius	72.50 mm	> 100 km (cylinder)	> 100 km (cylinder)	> 100 km (cylinder)
Mirror size (L × W × T)	$600 \times 50 \times 50\,\text{mm}^3$	$600 \times 50 \times 50\,\text{mm}^3$	$300 \times 50 \times 50\,\text{mm}^3$	$100 \times 50 \times 50\,\text{mm}^3$
Substrate, coating and surface				
Substrate material		Si [001]		
Substrate orientation		$\pm 0.5^\circ$		
Coating material	Pt (50 nm)	Rh/Pt 2-strip + bare Si (50 nm)	Pt (50 nm)	Pt (50 nm)
Coating thickness tol.		30–50 nm, ± 5 nm		
Coating strip number	1 (Pt)	3 (bare Si, Rh, Pt)	1 (Pt)	1 (Pt)
Coating stripe width		10 mm (W), per stripe		
Tangential slope error	$< 0.3\,\mu$rad RMS	$0.3\,\mu$rad RMS	$0.2\,\mu$rad RMS ($0.1\,\mu$rad goal)	$0.2\,\mu$rad RMS ($0.1\,\mu$rad goal)

(continued on next page)

(Table 4.2.3.4 continued)

Parameter	HHLM	HFM	VKB	HKB
Sagittal slope error	$< 5\,\mu$rad RMS	$< 5\,\mu$rad RMS	$< 2\,\mu$rad RMS	$< 2\,\mu$rad RMS
Roughness	< 0.3 nm RMS (HSF)	< 0.3 nm RMS (HSF)	0.2 nm RMS (HSF)	0.2 nm RMS (HSF)
Figure error (RMS)	< 0.3 nm	< 0.3 nm	< 0.15 nm	< 0.15 nm
Surface quality	≤ 0.5 scratch/point per cm^2 over 99 % of active area			
Heat load and cooling				
Absorbed power P (W)	≤ 42 of ≤ 230 incident (nominal front-end aperture; 60 for an enlarged aperture)	≈ 0	≈ 0	≈ 0
Peak density (W/mm^2)	≤ 0.1	≈ 0	n/a	n/a
Cooling method	Side cooling: slot/side water (≤ 1.5 L/min)	None	None	None
Manipulator and mounting				
Mirror bender	None	Bendable	None	
Bender figure tolerance	n/a	$\Delta R/R < 10^{-3}$; force ≤ 100 mN	n/a	
Mirror surface height	1400 mm	1400 mm	1400 mm	1401.2 mm
Motor axis	5-axis (T_z, T_x, R_x, R_y, R_z)		Nano-KB alignment stage	
Lateral T_z (range / res.)	± 5 mm / $< 1.0\,\mu$m	± 5 mm / $< 1.0\,\mu$m	within KB module	
Vertical T_x (range / res.)	± 10 mm / $< 1.0\,\mu$m	± 10 mm / $< 1.0\,\mu$m	n/a	
Pitch R_x coarse (range / res.)	$-2/+5$ mrad / 1.0 μrad	$-2/+5$ mrad / 1.0 μrad	alignment pitch	
Fine pitch	Piezo (PZT); $\pm 25\,\mu$rad / $\leq 0.05\,\mu$rad		n/a	
Roll R_y / Yaw R_z (range)	± 5 mrad each	± 5 mrad each	n/a	
Manual axis (granite base)	Granite-base alignment, 6-axis ($T_x, T_y, T_z, R_x, R_y, R_z$)			
Position encoder	Absolute optical encoder			

(continued on next page)

(Table 4.2.3.4 continued)

Parameter	HHLM	HFM	VKB	HKB
Mounting concept	Kinematic mount; bellows-decoupled; granite plinth		Nano-KB pair on granite support	

<Table 4.2.3.5> ID10 per-element angular-vibration tolerance: σ_{vib} governing value, integrated PSD over 1–2500 Hz, first resonance frequency and Criterion-D static pitch.

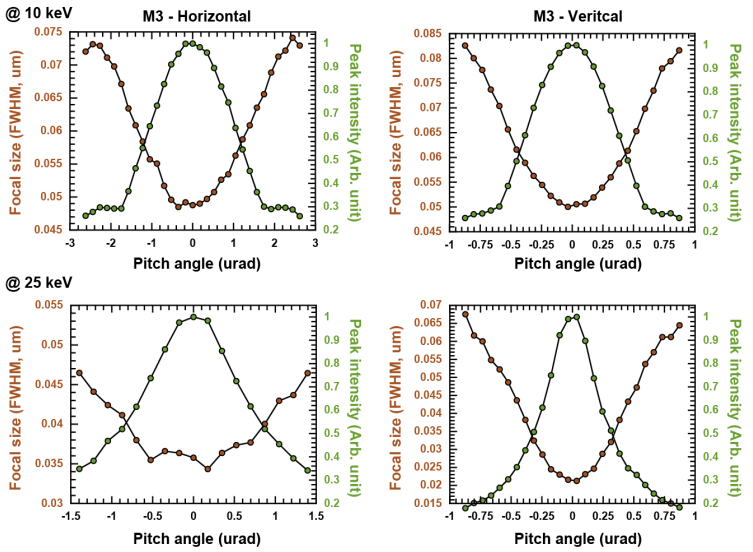
Optical element	σ_{vib} (nrad RMS)	IPSD 1–2500 Hz	First resonance	Criterion-D static pitch
HHLM	< 125 (C1)	Combined 86 (H)	> 70 Hz	n/a
DCM	< 131 (C1)	Combined 86 (H)	> 70 Hz	n/a
HFM	< 139 (A)	Combined 86 (H)	> 70 Hz	n/a
HKB	< 51 (A)	< 51 (H)	> 70 Hz	$< 0.9\,\mu$rad
VKB	< 17 (A)	< 17 (V)	> 70 Hz	$< 0.4\,\mu$rad

The required angular stability of the nano-KB (M3) was derived by simulating focal size and peak intensity versus pitch tilt: to keep both within 10 %, the pitch angular vibration must be smaller than $2.0\,\mu\mathrm{rad} \times 0.68\,\mu\mathrm{rad}$ at 10 keV and $0.4\,\mu\mathrm{rad} \times 0.2\,\mu\mathrm{rad}$ at 25 keV (figure 4.2.3.2). These angular-vibration limits define the required performance of the M3 mechanism and of the experimental-hutch vibration environment. The resulting beam at the sample position for these tolerances is shown later with the source conditions in figure 4.2.3.4.

C Double-Crystal and Channel-Cut Crystal Monochromator

A horizontal combined double-crystal and channel-cut crystal monochromator (HDCM/HCCM), with a 12 mm beam offset, is installed at 30.4 m. The Si[111] double-crystal mode covers 5–25 keV, while the Si[311] channel-cut mode covers 12–25 keV. The Si[111] first and second crystals are $60 \times 20 \times 40\,\mathrm{mm}^3$ and $75 \times 20 \times 25\,\mathrm{mm}^3$, respectively (L×W×D); the Si[311] channel-cut crystal has a 6.3 mm gap. The first crystal and channel-cut crystal are indirectly side-cooled with LN_2 through OFHC-Cu heat-exchanger blocks, and the second crystal is braid-cooled from the first assembly (table 4.2.3.6).

The HDCM/HCCM specification is given in table 4.2.3.6; its angular-vibration tolerance is listed in table 4.2.3.5.



<Figure 4.2.3.2> Focal size and peak intensity as a function of the pitch angular vibration of the M3 (nano-KB) mirrors, used to derive the angular-stability requirement.

<Table 4.2.3.6> ID10 horizontal combined double-crystal and channel-cut crystal monochromator (HDCM/HCCM).

Item	Specification
Position (ID10 layout)	30.4 m (source to monochromator)
Deflection / type	Horizontal combined double-crystal and channel-cut crystal monochromator
Photon energy range	5–25 keV (Si[111] double-crystal mode); 12–25 keV (Si[311] channel-cut mode)
Crystal / optical element	Si[111] crystal pair; Si[311] channel-cut crystal
Operating modes	Si[111] double-crystal mode / Si[311] channel-cut mode
First crystal	Si[111]: $60 \times 20 \times 40\,\mathrm{mm}^3$ (L×W×D)
Second crystal	Si[111]: $75 \times 20 \times 25\,\mathrm{mm}^3$ (L×W×D)
Channel-cut crystal	Si[311]; 6.3 mm gap
Beam offset	12 mm
Bragg rotation range	-1° to 25°
Slope error	Tangential $\leq 2\,\mu$rad RMS
Roughness	≤ 0.5 nm RMS
Cooling	First crystal and channel-cut crystal indirectly side-cooled with LN_2 through OFHC-Cu heat-exchanger blocks; second crystal braid-cooled from the first cooling blocks
Motion axes	Bragg rotation; vertical and lateral translation; second-crystal perpendicular, pitch and roll; fine-pitch and fine-roll adjustment
Sensors and encoders	Bragg: Renishaw RESA200 200-mm ring + RESOLUTE readhead, 32-bit output; out-of-vacuum axes: RESOLUTE encoders, 0.05 μm resolution; all motorized axes: encoder feedback and over-travel limit switches
Bragg drive	Worm-wheel actuated by planetary-geared stepper, closed-loop; 18 000:1 gearing, 200 steps/rev, 64× microstepping
Bragg axis	Resolution $\leq$ 0.25 μrad; repeatability $\leq$ 1 μrad; radial run-out $<$ 1.5 μm; axis wobble $\leq 25\,\mu$rad (fixed energy), $\leq 50\,\mu$rad (full range); scanning speed 0.05°/s; pitch parallelism $\leq 10\,\mu$rad
Vertical translation	Range 25 mm; resolution $\leq 2\,\mu$m; accuracy $\leq 5\,\mu$m; repeatability $\leq 10\,\mu$m
Lateral translation	Range 0–5 mm; resolution $\leq 2\,\mu$m; accuracy $\leq 5\,\mu$m; repeatability $\leq 10\,\mu$m
Second-crystal perpendicular	Range 10 mm; resolution $< 1.0\,\mu$m; repeatability $< 5\,\mu$m
Second-crystal pitch	Range $\pm 0.7^\circ$; resolution $< 0.5\,\mu$rad; repeatability $< 2.5\,\mu$rad

(continued on next page)

(Table 4.2.3.6 continued)

Item	Specification
Second-crystal roll	Range $\pm 0.7^{\circ}$; resolution $< 0.5\,\mu$rad; repeatability $< 2.5\,\mu$rad
Second-crystal fine pitch / roll	Range 100 μrad each; resolution 0.05 μrad; repeatability 0.1 μrad
Mounting concept	Granite goniometer grouted to floor with manual alignment adjusters; vacuum vessel and ion-pump interface mechanically decoupled

D Beam conditions at the sample per optical configuration

The beamline is designed to provide a reliably controllable SSA aperture for consistent experiments. For the mirror (KB) configuration, table 4.2.3.7 lists the SSA opening that yields a normalized degree of coherence $X = 0.91$ ($A\theta = \lambda/4$), where θ is the half-angular acceptance of the KB mirrors and A is the SSA opening; under these conditions ptychography in single-probe mode shows a resolution degradation below 10 %. Table 4.2.3.8 compares the RMS beam size at the SSA for different M1/M2 magnification ratios, confirming that the 1:1 ratio gives a reasonable aperture relative to the coherence-mode opening. Table 4.2.3.9 summarizes the flux and coherent fraction for the flux and coherence modes in mono-beam operation, and figure 4.2.3.3 shows the expected coherent flux delivered to the sample, including mirror reflectivity, number of reflections, SSA size, KB angular acceptance and monochromator polarization.

<Table 4.2.3.7> SSA opening size for the coherence mode ($X = 0.91$) at different photon energies.

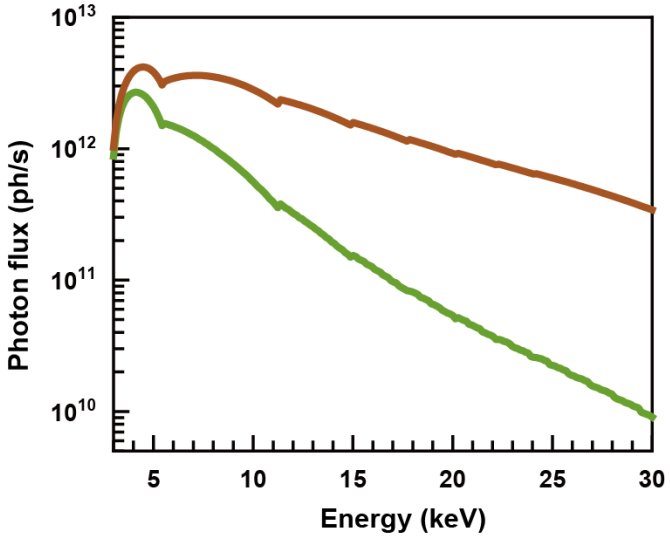
Energy	SSA-H (μm)	SSA-V (μm)
5 keV	37.98	12.63
10 keV	18.99	6.32
15 keV	12.66	4.21
20 keV	9.50	3.16
25 keV	7.60	2.53

<Table 4.2.3.8> RMS beam size at the SSA for different M1/M2 magnification ratios.

Energy	Beam size	Magnification 2:1	Magnification 1:1	Magnification 1:2
10 keV	H × V, RMS (μm)	9.5 × 2.3	19.0 × 4.5	29.4 × 7.0
20 keV	H × V, RMS (μm)	9.5 × 2.1	18.9 × 4.2	29.3 × 6.5

<Table 4.2.3.9> Beam conditions at the sample of the ID10 Nanoprobe: flux and coherent fraction in mono-beam mode. The coherence mode uses the SSA openings that give a normalized degree of coherence $X = 0.91$ (table 4.2.3.7).

Configuration	Photon energy (keV)	Flux (ph/s)	Coherent fraction	Notes
KB focus, flux mode	10	7.42×10^{13}	n/a	Total flux
KB focus, coherence mode	10	1.47×10^{13}	19.8 %	Coherent flux
KB focus, flux mode	20	2.85×10^{13}	n/a	Total flux
KB focus, coherence mode	20	1.67×10^{12}	5.9 %	Coherent flux

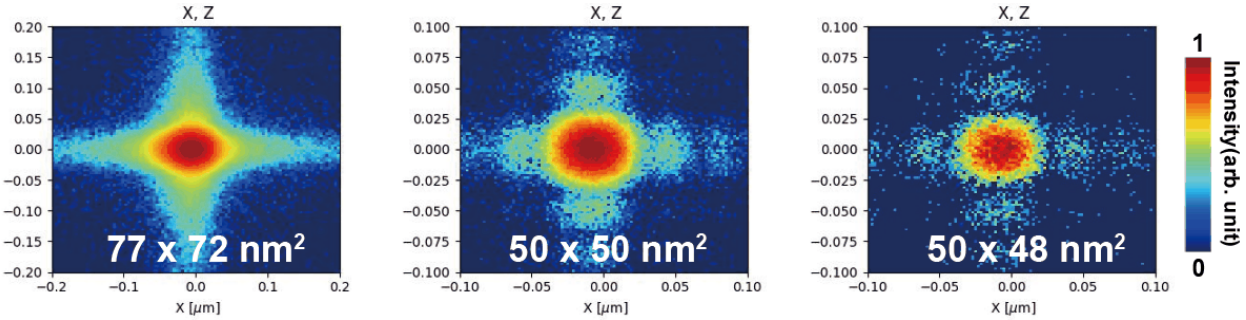


<Figure 4.2.3.3> Expected coherent flux delivered to the sample as a function of photon energy.

Figure 4.2.3.4 shows the simulated beam reaching the sample for representative SSA openings, including the mirror figure and slope errors; closing the SSA reduces the beam footprint at the sample and illustrates the flux-versus-coherence trade-off of the secondary-source scheme.

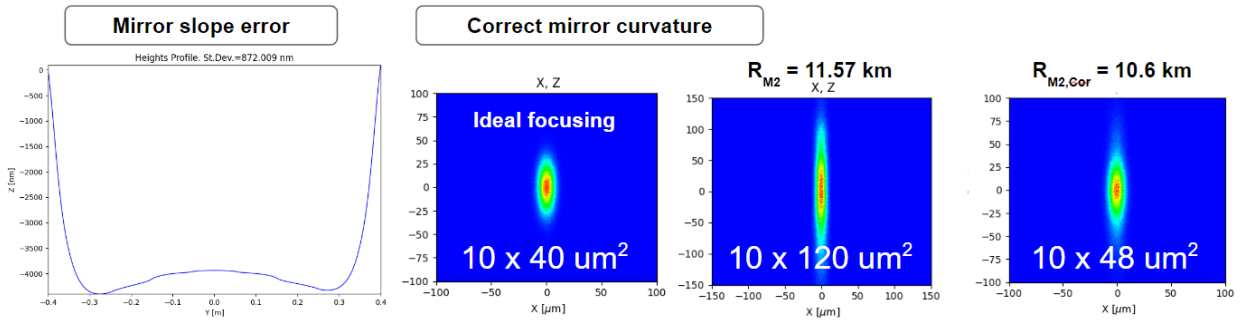
E Heat Load

A second design constraint is that the peak power density on the DCM is kept below 40 W/mm^2, the value that would distort the Si $\langle 333 \rangle$ rocking curve by $< 1\,\mu$rad. Two strategies are available to reduce the peak power density: (i) placing the DCM more than 50 m from the source, which minimises the number of optical components but limits the accepted flux; and (ii) using a High-Heat-Load Mirror (HHLM) with a notch design to absorb heat upstream, which increases the deliverable flux at the cost of requiring active correction of the HHLM thermal bump. Because rapid



<Figure 4.2.3.4> Beam simulation at the sample position including mirror figure and slope errors at 10 keV. (Left) SSA fully open; (Middle) $19.0 \times 6.3\,\mu\text{m}^2$ open; (Right) $5.0 \times 5.0\,\mu\text{m}^2$ open. The color map is logarithmic.

investigation of large samples at nanoscale resolution requires flux maximization, the ID10 design adopts the second strategy: M1 is an HHLM with a notch design and M2 is bent to compensate the residual thermal bump. Figure 4.2.3.5 shows the M1 slope-error profile at the maximum M1 absorbed power ($W_{\text{abs}} \approx 42\,\text{W}$) and the corrected beam profile at the SSA after bending M2. This thermal-bump-correction scheme can deliver a monochromatic flux above 10^{12} ph/s with a coherent flux above 10^{11} ph/s at 10 keV.



<Figure 4.2.3.5> Mirror surface profile resulting from the thermal bump on the M1 mirror (left) and the expected beam profile (V×H) at the SSA after compensation by bending M2 (right).

Whether a diamond filter is fitted is left open: it lowers the load on the downstream optics but removes a substantial part of the low-energy flux, so both cases are carried here and the choice is to be made in a later revision (TBD). The absorbed heat loads of the optical components are summarized in table 4.2.3.10 (with a 50 μm diamond filter) and table 4.2.3.11 (without it), computed with SRCalc for the 37 μrad acceptance, with the optical elements in the M1 → DCM → M2 order. M1 is Pt-coated; M2 is Si-coated for 5–10 keV, Rh-coated for 11–22 keV and Pt-coated

above that. Because the white beam reaches M1 and then the DCM, the DCM first crystal carries the largest absorbed load (up to ∼143 W) and M1 up to ∼42 W, while M2, which sees only the monochromatic beam downstream of the DCM, carries negligible heat. M1 uses the side-water cooling specified in table 4.2.3.4 (slot/side water, ≤ 1.5 L/min), the DCM first crystal is LN_2-cooled, and M2 is bent to correct the residual beam broadening at the SSA. With the notch design and cooling, the beam size is estimated to be only 2–3 times larger than ideal focusing conditions.

<Table 4.2.3.10> Calculated heat load of optical components with a 50 μm diamond filter applied. The condition columns are the photon energy; K is the corresponding undulator deflection parameter.

Component	**Location (m)**	**Parameter**	**5 keV**	**7 keV**	**10 keV**	**15 keV**	**20 keV**	**23 keV**
IVU source	0	Deflection parameter K	0.73	1.85	1.34	1.98	2.23	2.27
HHLM	29.0	Absorbed power (W)	3.1	24.4	9.5	27.8	35.4	40.8
		Peak power density (W/mm²)	7.3E-3	5.5E-2	2.2E-2	6.3E-2	8.0E-2	9.2E-2
DCM 1st crystal	30.4	Absorbed power (W)	38.2	99.1	69.8	107.8	117.8	122.3
		Peak power density (W/mm²)	13.6	25.0	12.4	11.0	10.4	9.3
HFM	32.0	Absorbed power (W)	≈ 0 (monochromatic beam downstream of the DCM)					

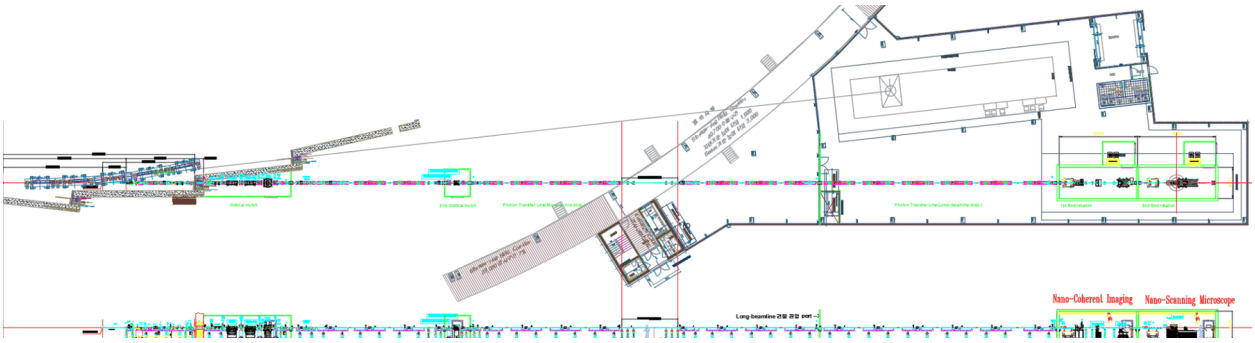
The first M1 mirror absorbs the substantial heat load; the resulting steady-state thermal distribution and the mounting (support) behavior are evaluated by finite-element analysis. The resulting M1 thermal-bump surface deformation is shown in figure 4.2.3.5.

<Table 4.2.3.11> Calculated heat load of optical components without a diamond filter. The condition columns are the photon energy; K is the corresponding undulator deflection parameter.

Component	Location (m)	Parameter	5 keV	7 keV	10 keV	15 keV	20 keV	23 keV
IVU source	0	Deflection parameter K	0.73	1.85	1.34	1.98	2.23	2.27
HHLM	29.0	Absorbed power (W)	3.9	26.8	11.6	31.2	36.5	41.8
		Peak power density (W/mm²)	9.0E-3	6.0E-2	2.7E-2	7.6E-2	8.3E-2	9.4E-2
DCM 1st crystal	30.4	Absorbed power (W)	50.0	122.4	94.9	128.6	137.9	142.5
		Peak power density (W/mm²)	17.8	30.8	16.8	13.2	12.2	10.9
HFM	32.0	Absorbed power (W)	≈ 0 (monochromatic beam downstream of the DCM)					

4.2.3.5 Photon Transfer Line

The photon transfer line (PTL) carries the beam from the FE exit through Optical Hutch 1, the long transport section, Optical Hutch 2 (SSA at 58 m) and on to the experimental hutch (135–155 m); the overall beamline floor plan is shown in figure 4.2.3.6. The PTL girder, support and vacuum standards are common to all KLS beamlines and are described in the separate Common Technical Sections document. ID10-specific PTL provisions are: white-beam transport through the white-beam slit, diamond monitors, M1 and HDCM/HCCM in Optical Hutch 1; mono-beam transport downstream of the HDCM/HCCM through the HFM (M2) and onward to the SSA; and a final transport into the experimental satellite building.



<Figure 4.2.3.6> Beamline floor plan / drawing of the ID10 Nanoprobe beamline, showing the optical hutches and the experimental hutch in the satellite building with isolated slabs.

A Mechanical Design

The intent of the mechanical design is to realize the optical layout of table 4.2.3.3 while meeting the angular-stability budget of figure 4.2.3.2 and the $f_1 > 70\,\mathrm{Hz}$ first-resonance requirement referred to the mirror surface. Each ID10 mirror is carried by a five-axis manipulator (two translations, three rotations); its per-axis drive, range, resolution and encoder, together with the mounting concept, are given in the Manipulator and mounting block of the consolidated mirror specification (table 4.2.3.4).

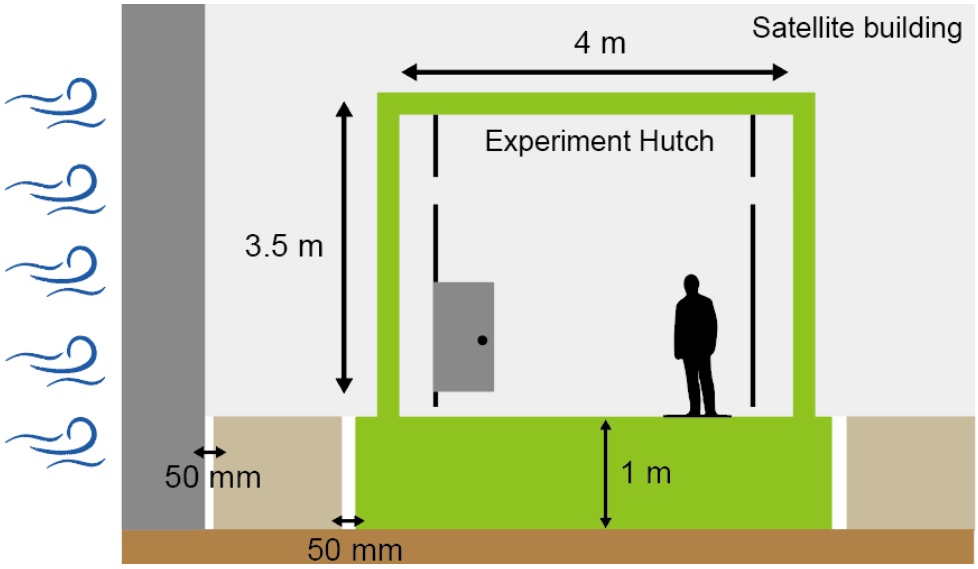
B Vacuum, Pumps and Valves

The ID10 vacuum system uses the common KLS UHV standard described in the separate Common Technical Sections document; the material, pressure, leak-rate and acceptance requirements are those of the beamline UHV fabrication standard appended to the front-end vacuum analysis report [5]. Sector isolation is provided by gate valves coordinated with the safety-interlock system: a fast-closing shutter and the photon shutter protect downstream optics in the event of a vacuum incident, with the photon-shutter fast-closing time reduced to below 100 ms by an emergency exhaust valve triggered on the fast-closing-shutter interlock signal; the interlock signals and the shutdown devices they act on are specified in the beamline interlock system design report [6]. UHV-compatible welded bellows and windows isolate the FE, optical-hutch and experimental-hutch sectors so that any sector can be vented independently for maintenance without breaking the vacuum of adjacent sectors. The detailed pump sizing, valve positions and gauge layout for the ID10 sectors are to be specified in a later revision (TBD).

C Hutch

The ID10 Nanoprobe is one of the two KLS long beamlines, and its experimental hutch is installed in a satellite building that extends from the storage ring. The beam passes through two optical hutches (OH1 for the white-beam optics and OH2 for the SSA) and into a 20 m experimental hutch spanning 135–155 m from the source. The hutch continues about 5 m downstream of the 150 m sample position so that the beam path beyond the sample is clear, which is what allows the flexible configuration to reach its longest sample-to-detector distances. Exhaust, electrical power and support facilities (LCW, compressed air, LN_2) follow the common site-infrastructure standard of the separate Common Technical Sections document; ID10-specific routing within the satellite building is to be detailed in a later revision

(TBD). The satellite building and the isolated experimental-hutch slab are shown in figure 4.2.3.7; the floor, slab and hutch structure required to meet the nanometre beam-stability budget are described in Section 4.2.3.5 E.



<Figure 4.2.3.7> Satellite building and hutch structure of the ID10 Nanoprobe beamline, showing the isolated experimental-hutch slab.

D Beam Diagnostics and Alignment

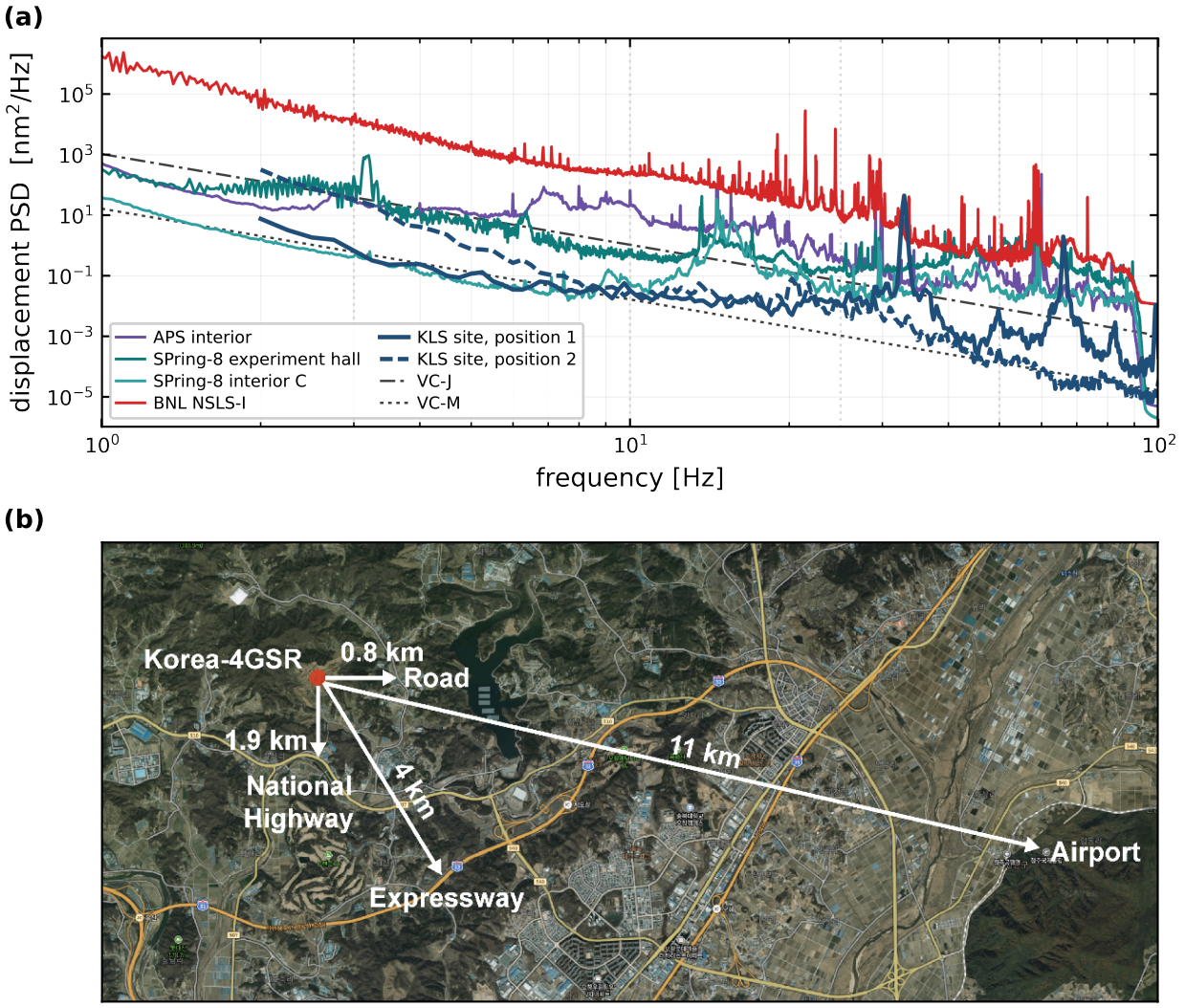
The ID10 diagnostics follow the common KLS photon-beam diagnostic standard maintained in the separate Common Technical Sections document. White-beam diagnostics are placed in Optical Hutch 1: a white-beam slit rated up to 4 kW, two diamond monitors (100 μm and 30 μm thick, $< 1\,\mu$m resolution) bracketing M1, and a white-beam DBPM at 31 m providing beam-position feedback with beam-size resolution $< 0.1\,\%$; a further diamond screen monitor at 35 m images the mono beam downstream of the HDCM/HCCM. A nano-beam position monitor (NBPM) with 100 nm resolution and a target angular resolution < 50 nrad is placed at 58.5 m in Optical Hutch 2. In the experimental hutch, removable diamond screen monitors (1 μm resolution) at 137 m and 147 m and an ion-gas chamber (I_0 monitor) at 148 m provide mono-beam diagnostics. The diagnostics directly support the secondary-source design, in which positional instability is converted to intensity instability and compensated using the I_0 ion chamber. Beam alignment uses the white-beam profile monitor in Optical Hutch 1, the diamond screen monitor immediately downstream of the white-beam slit (28.8 m), for front-end alignment, and the white-beam/nano-beam position monitors for optics alignment.

E Vibration & thermal stability

The nanoprobe mechanical design follows the rule that the instability of the beam delivered to the sample must stay below 10 % (table 4.2.3.1), which requires a beam stability better than 0.2 μm at the secondary-source aperture in Optical Hutch 2 – one tenth of the 2 μm smallest SSA opening – and better than 5 nm in the experimental hutch, one tenth of the sub-50 nm probe. Meeting this budget requires control of natural ground vibration, cultural (man-made) vibration and thermal drift, and drives the floor, slab and hutch structure of the satellite building.

The KLS ground vibration was measured at two positions on the construction site. As shown in figure 4.2.3.8, the site floor sits at the quiet end of the range spanned by operating synchrotron floors: over 2–100 Hz the two records shown carry 5.0 and 11.2 nm r.m.s. against 16.0 nm for the APS interior and 16.4 nm for the SPring-8 experiment hall, and both lie for the most part between the VC-J and VC-M generic vibration criteria. The one feature that stands out is a narrow 33 Hz line at position 1, with a harmonic at 66 Hz, which carries almost all of that record's variance above 30 Hz; with the two lines excluded its broadband level above 30 Hz is 0.8 nm r.m.s., against 1.7 to 5.0 nm at the comparison floors. Keeping the girder and stage resonances clear of that line, or damping it, is therefore the operative requirement rather than a general reduction of the floor level. The $f_1 > 70$ Hz first-resonance requirement placed on every optic (table 4.2.3.5) holds the mirror mechanisms above both the 33 Hz line and its 66 Hz harmonic. The surrounding cultural vibration sources are summarized in figure 4.2.3.8(b). To isolate the experimental hutch from these sources the nanoprobe adopts two strategies. First, the experimental-hutch slab is isolated from the surrounding slabs (figure 4.2.3.7), with an isolated-slab length of 21 m. Second, cultural vibration sources are avoided at the source: the experimental chamber uses a helium-flow environment instead of vacuum pumping, and equipment that would otherwise rely on cooling fans is replaced with water-cooled systems.

Thermal drift from hutch temperature deviation is suppressed in two stages. First, the hutch is built from 300 mm-thick concrete with an internal HVAC system; concrete has about 360 times lower thermal conductivity than a steel–lead–steel hutch, making the interior far less sensitive to external temperature changes, and the HVAC holds the hutch temperature stable to within 0.1 °C. Second, the nano-KB mirror and the sample stage are enclosed in a $2.0 \times 1.5 \times 2.0\,\mathrm{m}^3$ thermal-insulation enclosure with water-cooled panels that keep the internal temperature drift below



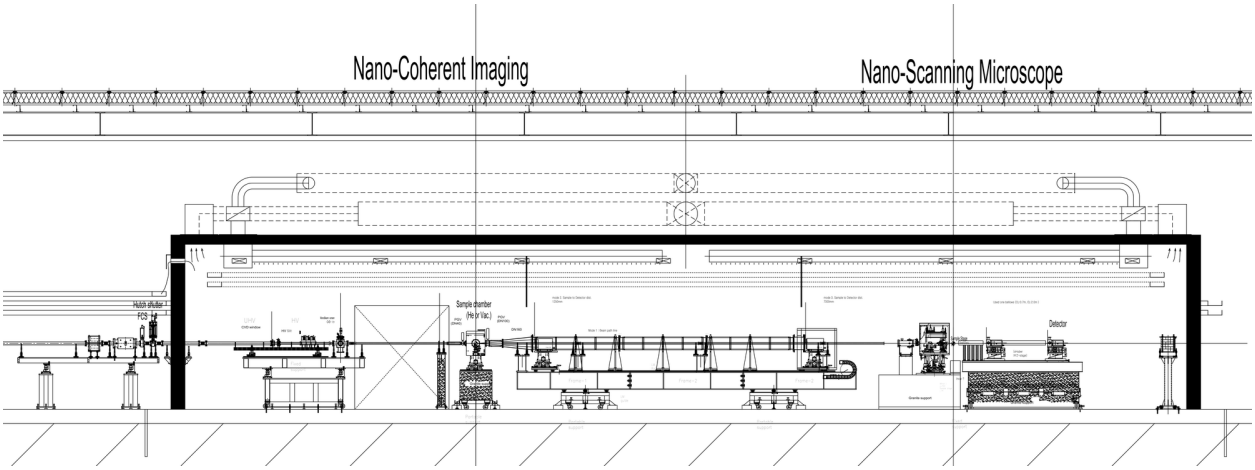
<Figure 4.2.3.8> (a) Measured vertical floor displacement PSD at the KLS construction site, one record from each of the two measured positions, against operating synchrotron floors and the VC-J and VC-M generic vibration criteria. (b) Surrounding cultural (man-made) vibration sources.

0.02 °C/h, which is the condition under which a 1 m granite block moves thermally by less than 5 nm. Installation of this enclosure will depend on the achieved HVAC performance and will follow a machine study.

4.2.3.6 End-Station

The ID10 Nanoprobe end-station provides scanning imaging in two operation modes, shown in <Figure 4.2.3.9>, which stand in line in the single 20 m experimental hutch. The first, multi-modal imaging mode, uses the nano-KB (M3, 50 mm working distance) to deliver the nano-beam to a sample at a fixed position 150 m

from the source; it provides high-resolution 2D/3D elemental maps and electron-density images by simultaneous XRF and ptychography under *in-situ*/*operando* conditions, and supports a high-speed closed-loop piezo scanner (operation rate above 20 kHz) with lightweight *in-situ* cells (target weight $\ll 100$ g). It carries 18 axes of controlled motion, including the granite yz and the detector-chamber y, and three axes set by hand. The second, flexible-setup mode works upstream of the KB, taking the beam before it reaches the KB optics and the fixed end-station, and supports sample-to-detector distances up to 6 m at 0° and up to 18 m at 45°, which the 20 m hutch accommodates with the sample at the upstream end of its travel; it offers 20 plug-and-play motor channels on 11 axes of controlled motion and a floor-rail granite-support system, with the chamber and detector stage travelling up to 5 m from the hutch wall and an additional movable granite stage for off-line preparation to reduce user-switching time.



<Figure 4.2.3.9> The two ID10 end-station configurations, Nano-Coherent Imaging and Nano-Scanning Microscope. Both stand in the single 20 m experimental hutch, the flexible Nano-Coherent Imaging set-up upstream of the KB optics and the fixed Nano-Scanning Microscope at 150 m.

A Virtual Commissioning and Control Integration

A virtual commissioning environment is used to validate the ID10 optical-alignment procedures, motor-control interfaces and scan plans before operation. It couples an optics model of the IVU24 → M1 → HDCM/HCCM → M2 → SSA → KB chain with EPICS-compatible motor records and Bluesky/Ophyd acquisition interfaces, allowing the M1/M2 alignment, monochromator alignment and energy tuning, SSA centring, KB focusing and end-station scans to be tested using

hardware-compatible control abstractions. The implementation is described in the accompanying publication [7].

B End-Station Mechanical Design

The end-station mechanical design achieves nanometer sample-position stability building on the hutch slab isolation, vibration-source mitigation and multi-stage thermal isolation described in Section 4.2.3.5 E, with a laser-interferometer head providing sample-position metrology. At its center is the sample positioning system: a multi-axis motorized coarse stage (three baseline axes, sub-micron step resolution, each exposed as an EPICS motor record for direct integration with the beamline control and automatic-alignment system) carrying a high-speed closed-loop piezo scanner that performs the actual nano-step fly-scanning at the sample. The resulting end-station instrument specification (the sample positioning system, the flexible nano-coherent-imaging configuration and the stability environment they rely on) is summarized in table 4.2.3.12.

<Table 4.2.3.12> ID10 Nanoprobe end-station instrument specification: sample positioning system of the fixed nano-scanning-microscope end-station, the flexible nano-coherent-imaging configuration, and the stability environment described in Section 4.2.3.5 E.

Parameter	Specification
Sample positioning system (nano-scanning microscope)	
Sample position	Fixed, 150 m from the source
Working distance (KB to sample)	50 mm
Coarse stage	Multi-axis motorized stage, three baseline axes
Coarse-stage step resolution	Sub-micron (per-axis values TBD)
Coarse-stage travel range	TBD
Coarse-stage control interface	One EPICS motor record per axis
Fine scanner	High-speed closed-loop piezo scanner
Piezo scanner operation rate	$>$ 20 kHz
Piezo scan range / resolution	TBD
Sample-position metrology	Laser-interferometer head
Controlled motion axes	18 (including granite yz and detector-chamber y)
Manual motion axes	3
Sample environment	Helium flow instead of vacuum pumping (cultural-vibration mitigation)

(continued on next page)

(Table 4.2.3.12 continued)

Parameter	Specification
In-situ cell weight	Target $\ll 100\,\mathrm{g}$
Flexible (nano-coherent-imaging) configuration	
Setup	Flexible; upstream of the KB optics and the fixed end-station
Sample position range	137–148 m from the source, within the 135–155 m hutch
Controlled motion axes	11
Plug-and-play motor channels	20
Sample-to-detector distance	Up to 6 m at 0°; up to 18 m at 45°
Chamber / detector stage travel	Up to 5 m from the hutch wall
Support system	Floor-rail granite support, plus a movable granite stage for off-line preparation
Stability environment	
Beam stability at the sample	$< 5\,\mathrm{nm}$
Hutch temperature stability	Within $0.1\,^{\circ}\mathrm{C}$ (HVAC, 300 mm concrete hutch)
Thermal-insulation enclosure	$2.0 \times 1.5 \times 2.0\,\mathrm{m}^3$, water-cooled panels, internal drift $< 0.02\,^{\circ}\mathrm{C/h}$

C Detector

The ID10 end-station records data with two photon-counting area detectors for coherent-imaging and diffraction techniques (ptychography, 2D/scanning XRD and SAXS-type patterns) and an X-ray fluorescence detector for elemental mapping, an area detector and the fluorescence detector operating simultaneously. A single raster scan therefore yields co-registered elemental (XRF) and structural (ptychography/diffraction) maps for three-dimensional study. Device control, data acquisition and the higher-level beamline computing and software follow the common KLS EPICS and Bluesky/Ophyd standards (see the separate Common Technical Sections document).

The 2D area detectors are DECTRIS EIGER2 X photon-counting pixel detectors with silicon sensors, in two formats: the 1M (approximately 1.1 megapixels, 1028×1062) and the 4M (approximately 4.5 megapixels, 2068×2162), both with a 75 μm pixel pitch. The 4M covers four times the area at a given sample-to-detector distance, and therefore a wider angular range, while the 1M reads out several times faster; which one is used is set by the q-range and frame rate an experiment needs. As with all EIGER2 detectors, the single-frame counter is 16-bit and the maximum frame

rate is reached only at reduced readout bit depth, while the 32-bit data depth used for image storage is obtained by auto-summation of successive frames rather than as a native high-speed readout mode; for the 1M module the maximum full-frame rate is 4,500 Hz in 8-bit readout and 2,250 Hz in 16-bit readout, and for the 4M module it is 1,120 Hz in 8-bit readout and 560 Hz in 16-bit readout. At maximum throughput, each area detector produces an uncompressed data stream of order 5 GB/s, reduced in practice by on-the-fly compression. The XRF detector is a Hitachi Vortex ME-4 silicon-drift detector (SDD) with an energy range to about 20 keV, an energy resolution of $\sim$ 130 eV at the Mn Kα line (5.9 keV), and roughly 50 mm^2 of active area; positioned at 90° to the sample, it records the full fluorescence spectrum at each scan position for nano-XRF mapping, line scans and nano-XANES of transition metals and rare-earth elements. The detector parameters and the resulting raw-data estimate are summarized in table 4.2.3.13.

<Table 4.2.3.13> ID10 end-station detectors and raw-data estimate. EIGER2 product maximum frame rates are stated for 8-bit and 16-bit readout; the beamline raw-data estimates are uncompressed and are reduced in practice by on-the-fly compression.

Parameter	**EIGER2 X 1M**	**EIGER2 X 4M**	**Vortex ME-4**
Role / technique	Ptychography, 2D/scanning XRD, SAXS-type patterns; the faster of the two area detectors	Ptychography, 2D/scanning XRD, SAXS-type patterns; wider angular coverage at a given distance	nano-XRF mapping, line scans, nano-XANES
Detector type / detection principle	Hybrid photon-counting pixel detector (DECTRIS EIGER2 X 1M)	Hybrid photon-counting pixel detector (DECTRIS EIGER2 X 4M)	Silicon-drift detector, 4-element (Hitachi Vortex ME-4)
Sensor material / thickness	Si, 450 μm	Si, 450 μm	Silicon (drift)
Pixel pitch	75 μm	75 μm	N/A (4 elements)
Pixel format / channels	1028×1062 (≈ 1.1 Mpix)	2068×2162 (≈ 4.5 Mpix)	N/A
Active area	$77.1 \times 79.7\,\mathrm{mm}^2$	$155.1 \times 162.2\,\mathrm{mm}^2$	$\approx 50\,\mathrm{mm}^2$
Maximum frame rate	4,500 Hz (8-bit) / 2,250 Hz (16-bit)	1,120 Hz (8-bit) / 560 Hz (16-bit)	One spectrum per scan point
Image / dynamic range	32-bit image depth; 16- or 8-bit readout	32-bit image depth; 16- or 8-bit readout	TBD
Detector-supported energy range	6–40 keV	6–40 keV	Up to $\sim$20 keV
Sample-to-detector distance	Up to 6 m at 0° (up to 18 m at 45°)	0.5–7 m	Positioned at 90° to the sample; distance TBD
Energy resolution	N/A	N/A	$\sim$ 130 eV at Mn Kα (5.9 keV)
Frame / spectrum size	≈ 2.1 MB/frame (16-bit)	≈ 8.9 MB/frame (16-bit)	$\sim$kB/point
Nominal raw-data rate (beamline)	$\sim$5 GB/s (uncompressed)	$\sim$5 GB/s (uncompressed)	Small
Remarks	Maximum frame rate reached only at reduced readout bit depth; raw-data rate reduced in practice by on-the-fly compression	Four times the area of the 1M at the same distance, at a correspondingly lower frame rate	Records the full fluorescence spectrum at each scan position

References

[1] Changwan Ha et al. “In-vacuum undulators for the first phase beamlines of Korea-4GSR”. In: Journal of the Korean Physical Society 85.5 (2024), pp. 371–380. DOI: 10.1007/s40042-024-01133-4. URL: https://doi.org/10.1007/s40042-024-01133-4.

[2] Hyungseok Choi and Jongha Park. Beamline Photon Source Analysis Report. Internal Document PAL-INT/ME-2026-007. Pohang Accelerator Laboratory, July 2026.

[3] Jongha Park et al. High Heat Load Front-End Mechanical Design and Thermal Analysis Report. Internal Document PAL-INT/ME-2026-003. Pohang Accelerator Laboratory, June 2026.

[4] Jongha Park and Jaeyong Shin. White Beam Attenuator Design Report. Internal Document PAL-INT/ME-2026-005. Pohang Accelerator Laboratory, June 2026.

[5] Hyungseok Choi and Jongha Park. 4GSR Front-End Vacuum Analysis Report. Internal Document PAL-INT/ME-2026-009. Pohang Accelerator Laboratory, Aug. 2026.

[6] Minho Seo and Chaesoon Lee. 4GSR Beamline Interlock System Design Report. Internal Document PAL-INT/EE-2026-012. Pohang Accelerator Laboratory, July 2026.

[7] Minho Seo et al. “Virtual commissioning of the Korea Light Source Hard X-ray Nanoprobe beamline with multilingual natural language control”. In: Journal of Synchrotron Radiation 33.5 (2026). DOI: 10.1107/S1600577526006788. URL: https://doi.org/10.1107/S1600577526006788.

4.2.4 BioPharma-BioSAXS (ID21)

The BioPharma-BioSAXS (ID21) beamline is a dedicated solution small-angle X-ray scattering (BioSAXS) beamline for the KLS project, delivering a high-flux, collimated hard X-ray beam over the 8–23 keV range for high-throughput structural analysis of biomacromolecules and biopharmaceuticals. This chapter describes the ID21-specific design of the photon source, the front-end, the beamline optics (overall optical layout, the high-heat-load mirror, the double-crystal monochromator, the bendable KB focusing mirrors, the three-slit collimation system, the optical configurations and heat load, and the beam diagnostics), the photon transfer line (PTL), and the end-station (variable q-range vacuum chamber, automated sample-changer robot, and SEC-SAXS system). Material that is common to all KLS beamlines is cited to the separate Common Technical Sections document prepared by the device team.

4.2.4.1 Target Purpose and Objective

The BioPharma-BioSAXS beamline delivers a high-flux, collimated hard X-ray beam (8–23 keV) optimized for solution-state small-angle X-ray scattering (SAXS) of biomacromolecules. Unlike X-ray crystallography, NMR, or cryo-EM, solution SAXS does not require crystallization or extreme sample preparation, enabling direct observation of conformational flexibility, folding–unfolding transitions, and transient assembly states under near-physiological conditions. The beamline covers an approximate d-spacing range of 8–3800 Å at a flux of 10^{13}–10^{14} ph/s (12.4 keV). Two selectable focusing configurations are provided using bendable KB mirrors: a detector-focused mode (132 $\times$ 125 μm^2 at the sample, FWHM) for automated high-throughput sample-changer operation, and a sample-focused mode (target approximately 40 $\times$ 10 μm^2, FWHM) for microfluidic and time-resolved studies. The two modes allow the beam size and photon density at the sample to be selected according to the experimental requirement.

The primary experimental method is solution SAXS/WAXS, complemented by in-line SEC-SAXS for real-time separation and structural analysis of heterogeneous or polydisperse samples. Scientific objectives center on the structural characterization of proteins, nucleic acids, and their complexes, particularly flexible and intrinsically disordered systems, as well as therapeutic biologics such as antibodies, antibody–drug conjugates, and biosimilars, and drug delivery platforms including lipid nanoparticles, polymer micelles, and colloidal carriers. As

an industry-priority support beamline, BioPharma-BioSAXS is built around automated sample handling and an ML-assisted data pipeline, with the overriding design driver of delivering reproducible, high-quality scattering data at throughput levels suitable for high-throughput biopharmaceutical development.

4.2.4.2 Photon Source

This beamline is primarily designed for Solution SAXS to measure biological and soft matter samples in a solution state. Based on the transmission characteristics of typical solution biological samples, the optimal operational energy range is established at 8–23 keV. The IVU20 undulator was selected as the X-ray source to cover this energy range with high flux and low divergence. IVU20 has a total length of 3 m and a 20 mm period with 148 periods. At a 5 mm gap, it achieves a magnetic field of 1.021 T (K ≈ 1.904), delivering a total radiated power of 12.49 kW and a maximum power density of 164.2 kW/mrad² [1]; the key specifications are summarized in <Table 4.2.4.1>.

<Table 4.2.4.1> ID21 BioPharma-BioSAXS insertion-device (IVU20) source parameters at the beam port. The maximum total power and power density are quoted at the 5 mm minimum gap.

Undulator	**Period (mm)**	**Length (m)**	**Gap size (mm)**	$K_{\max}$	**Max total power (kW)**	**Power density (kW/mrad²)**
IVU20	20	3.0	5–18	1.904	12.49	164.2

4.2.4.3 Front-End

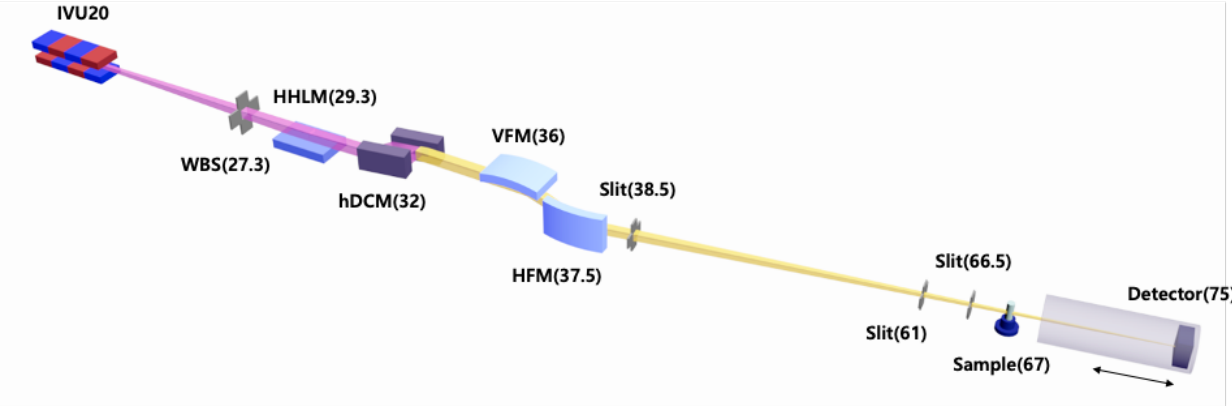
The BioPharma-BioSAXS beamline will employ the standard Front End design for the KLS in-vacuum undulator, designed to safely manage the 12.5 kW heat load generated by the IVU20 undulator at a 5 mm gap [2]. Most of the power is absorbed by three sequential water-cooled masks within the front-end section. A movable mask positioned approximately 22.5 m from the source further defines the beam to about 1 mm × 1 mm before entering the Photon Transfer Line (PTL) [1]. Through this staged attenuation, the transmitted power to the PTL is reduced to approximately 318 W, ensuring thermal stability and reliable beam transport. Detailed specifications are provided in Chapter 3.1.1.2.

4.2.4.4 Beamline Optics and Source Conditions

This section describes the beamline optics of the BioPharma-BioSAXS beamline and the source conditions it delivers to the sample, covering the overall optical layout and the roles of the individual components, the high-heat-load M1 mirror, the double-crystal monochromator, the bendable KB focusing mirrors, the three-slit collimation system, the optical configurations and their heat load, and the beam diagnostics.

A Overall Optical Layout and Component Roles

The BioPharma-BioSAXS beamline consists of three main sections: a Front End (FE), a Photon Transfer Line (PTL), and an Experimental Hutch (EH). The FE transmits the central-cone radiation from the IVU20 undulator while absorbing unwanted high-heat-load components. The PTL contains the optical components required to shape, monochromatize, and focus the X-ray beam before it reaches the experimental station; these comprise slits, a monochromator, and focusing mirrors. The entire PTL is enclosed within an Optical Hutch (OH) for radiation safety. The EH houses the sample environment and instrumentation for solution SAXS/WAXS and SEC-SAXS measurements, including an automatic sample changer. Beamline control and data analysis are carried out in a dedicated area outside the EH. The sample position is located approximately 67 m from the undulator source, and the farthest detector position is approximately 75 m. A schematic of the beamline layout is shown in <Figure 4.2.4.1>, and the main components are summarized in <Table 4.2.4.2>.



<Figure 4.2.4.1> Schematic of the ID21 BioPharma-BioSAXS beamline, showing the IVU20 source, the front-end, and the optical elements of the photon transfer line that deliver the beam to the sample (67 m) and detector (up to 75 m).

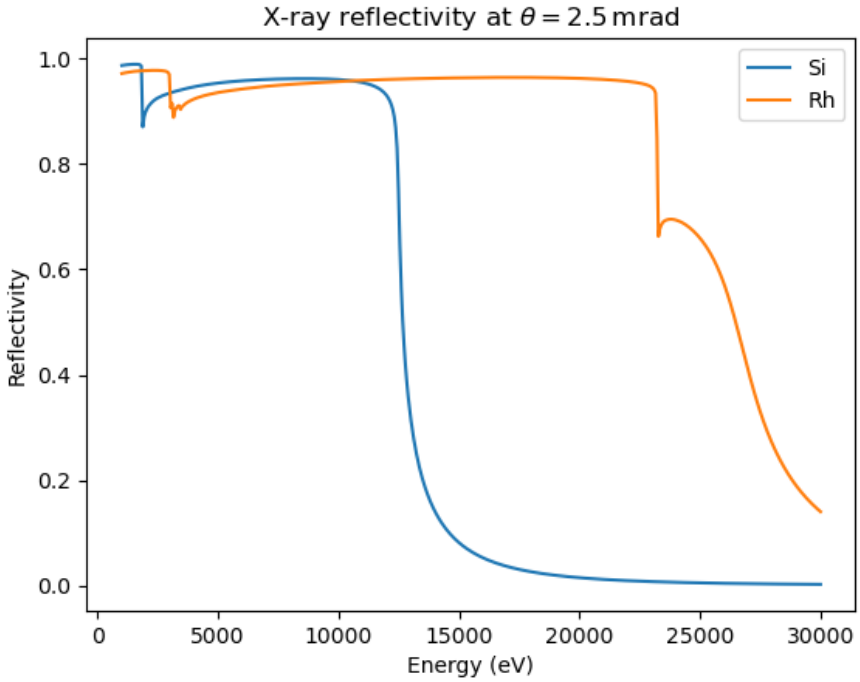
<Table 4.2.4.2> Component-by-component layout of the BioPharma-BioSAXS beamline, in beam order (distances measured from the source).

Distance (m)	Location	Component	Description
0	Front-End	IVU20	Period 20 mm, length 3 m
26.7	Optical Hutch	Attenuator	LCW cooling
27.3		White-beam slit	Incident power up to 317.6 W; transmitted power ~214.1 W at the 5 mm gap
28.1		Diamond screen monitor	White-beam screen monitor; Diamond + CCD; LCW cooling
29.3		HHLM	Eutectic-bath cooling; plane; Bare-Si / Rh coating
30.5		Diamond screen monitor	White-beam screen monitor; Diamond + CCD; LCW cooling
32		HDCM	Si(111), fixed-exit design; offset 25 mm
33.1		Mono-beam slit	4-way slit, UHV; W-blade
33.6		Diamond screen monitor	Mono-beam screen monitor; Diamond + CCD; LCW cooling
34.1		Diamond BPM (DBPM)	DCM 2nd-crystal feedback
36		VFM	Rh coating; bendable; focus 67–75 m
37.5		HFM	Rh coating; bendable; focus 67–75 m
38.5		Beam-defining slit	4-way slit, UHV; Scatterless slit; Si(100)
39		Diamond screen monitor	Mono-beam screen monitor; Diamond + CCD
61	Experimental Hutch	Collimating slit	4-way slit, HV; Scatterless slit; Si(100)
61.5		Diamond screen monitor	Diamond + CCD
65		Attenuator	Ti/Al foils
66		Ion chamber	I_0 monitor
66.5		Guard slit	4-way slit, HV; Scatterless slit; Si(100)
67		Sample environment	Arinax BioSAXS; sample-changer robot
67.5–75		Variable q-range vacuum chamber	Movable detector
67.5–75		2D SAXS detector	PILATUS4 X 2M, Si, vacuum-compatible

B M1 Mirror

The High-Heat-Load Mirror (HHLM) is positioned 29.3 m from the source and receives the white beam emerging from the front end. It reflects the beam vertically upward so that the subsequent vertical focusing mirror returns the beam to the nominal downstream beam direction.

Depending on the photon energy, the mirror uses either a bare-silicon or rhodium-coated stripe (50 nm thickness). As shown in <Figure 4.2.4.2>, the Si surface provides effective harmonic rejection in the low-energy range, whereas the Rh-coated stripe provides higher reflectivity over the higher-energy operating range up to 23 keV. Accordingly, the Si stripe is applied for operation below approximately 10 keV, and the Rh-coated stripe for operation from approximately 10 to 23 keV. The mirror is set at an incidence angle of 2.5 mrad. At 12.4 keV, which corresponds to the principal operating energy of BioSAXS experiments, the white-beam size of 4σ is approximately 0.93 mm $\times$ 0.87 mm, producing a 4σ footprint of about 349 mm $\times$ 0.93 mm (L $\times$ W) on the mirror surface. To accommodate this footprint, each coating stripe provides an optical area of at least 580 mm $\times$ 8 mm (L $\times$ W).



<Figure 4.2.4.2> Reflectivity of the Rh-coated and bare-Si mirror surfaces at a 2.5 mrad incidence angle, as a function of photon energy.

The mirror substrate (600 mm L $\times$ 50 mm W $\times$ 60 mm H, Si) employs a eutectic-bath cooling system to dissipate the absorbed heat load and minimize thermally

induced deformation. To preserve the designed beam profile and flux uniformity, the surface quality of the mirror is tightly controlled, with slope errors of < 0.2 µrad RMS (tangential) and < 0.5 µrad RMS (sagittal) and a surface roughness below 0.5 nm RMS. Detailed specifications of the HHLM, together with those of the KB focusing mirrors described below, are summarized in <Table 4.2.4.3>.

<Table 4.2.4.3> Specifications of the BioPharma-BioSAXS beamline mirrors: the high-heat-load mirror (HHLM) and the bendable Kirkpatrick–Baez focusing pair (VFM and HFM). Here p and q are the object and image distances; because the KB mirrors are benders, q is listed for both the detector-focused and the sample-focused configuration. The HHLM is a plane mirror and forms no focus. Beam sizes and footprints are 4σ values at 12.4 keV.

Parameter	**HHLM**	**VFM**	**HFM**
Installation location (m)	29.3	36	37.5
Reflection direction	Up (surface normal)	Down (surface normal)	Ring (surface normal)
Mirror surface shape	Plane	Elliptical cylinder (bendable)	Elliptical cylinder (bendable)
Incident angle	2.5 mrad	2.5 mrad	2.5 mrad
Object / image distance, p / q (m)	– (plane mirror)	Detector focus: 36 / 39; sample focus: 36 / 31	Detector focus: 37.5 / 37.5; sample focus: 37.5 / 29.5
Substrate material	Si	Si	Si
Mirror size (L × W × H)	600 × 50 × 60 mm	600 × 50 × 50 mm	600 × 50 × 50 mm
Coating material	Bare-Si, Rh (50 nm)	Rh (50 nm)	Rh (50 nm)
Coating stripe number	2	1	1
Coating stripe size (W × L)	10 × 600 mm, per stripe	10 × 600 mm	10 × 600 mm
Optical area (W × L)	8 × 580 mm, per stripe	8 × 580 mm	8 × 580 mm
Beam size (H × V)	0.931 × 0.872 mm	1.10 × 1.04 mm	1.15 × 1.00 mm
Footprint (W × L)	0.931 × 349 mm	1.10 × 416 mm	1.00 × 460 mm
Tangential slope error	< 0.2 µrad RMS	< 0.2 µrad RMS	< 0.2 µrad RMS
Sagittal slope error	< 0.5 µrad RMS	< 0.5 µrad RMS	< 0.5 µrad RMS
Roughness	< 0.5 nm RMS (HSF)	< 0.5 nm RMS (HSF)	< 0.5 nm RMS (HSF)
Cooling method	Eutectic bath	None	None

(continued on next page)

(Table 4.2.4.3 continued)

Parameter	HHLM	VFM	HFM
Mirror bender	None	Yes (focal-position adjustment)	Yes (focal-position adjustment)
Mirror surface height	1400.0 mm	1433.5 mm	1433.5 mm
Motor axis	Pitch, roll, x, y	Pitch, roll, yaw, x, y, z	Pitch, roll, yaw, x, y
Manual axis (granite base)	Pitch, roll, yaw, x, y, z	Pitch, roll, yaw, x, y, z	Pitch, roll, yaw, x, y, z

C Double-Crystal Monochromator

The double-crystal monochromator (DCM) is positioned 32 m from the source, while the sample is located at 67 m, resulting in a relatively long optical path. Given the use of automated experimental robots and microfluidic-based micro-focused setups, the beamline requires exceptionally high beam stability with minimal vibration. To meet these requirements, a horizontal-type DCM configuration is adopted, which offers superior absolute and relative pitch stability and minimizes the vibrational influence from both the cryogenic cooling system and environmental sources. The design maintains a constant beam offset of 25 mm, ensuring high beam stability.

The monochromatization is achieved by a pair of Si(111) crystals that satisfy Bragg's law, allowing continuous selection of photon energies between 8 keV and 23 keV; the corresponding Bragg angle changes from approximately 14.31° at 8 keV to 4.93° at 23 keV. The double-crystal geometry ensures that the exit beam remains parallel to the incident beam even during energy tuning, which is essential for downstream alignment and maintaining experimental repeatability. The expected energy resolution of the diffracted beam is approximately $\Delta E/E \leq 2 \times 10^{-4}$, which is suitable for BioSAXS experiments.

At 12.4 keV, the incident beam size on the first crystal is approximately 1,016 μm (H) × 952 μm (V) (4σ). The first crystal (60 mm × 25 mm) fully accepts the incoming beam, while the second crystal (150 mm length) is mounted on piezo-driven stages that allow fine pitch and roll adjustments for active feedback control. Detailed specifications of the DCM are summarized in <Table 4.2.4.4>.

A diamond beam-position monitor (DBPM) will be installed at 34.1 m from the source to detect residual beam-position fluctuations caused by angular drift.

<Table 4.2.4.4> Specification of the double-crystal monochromator (DCM).

Item	Specification
Position (m)	32.0
Deflection / type	Horizontal deflection (HDCM), fixed-exit; surface-normal direction (1st: Ring, 2nd: Hall)
Photon energy range	8–23 keV
Crystal / optical element	Si(111), both crystals
Operating modes	Fixed-exit, continuous energy tuning (8–-23 keV)
First crystal	Si(111); 60 × 25 × 50 mm (L × W × H); optical area 50 × 15 mm (L × W)
Second crystal	Si(111); 150 × 25 × 30 mm (L × W × H); optical area 140 × 15 mm (L × W); piezo-driven fine pitch/roll for feedback
Beam offset	25 mm
Bragg angle range	4.931–14.307°
Slope error	1 μrad (tangential), 1 μrad (sagittal); both crystals
Roughness	$\leq$ 0.2 nm RMS; both crystals
Cooling	Liquid-nitrogen (LN_2) side-cooling of both crystals
Motion axes	Bragg, gap, roll, pitch, piezo roll and pitch for feedback; both crystals
Beam size (H × V, 4σ)	1.02 × 0.95 mm; both crystals
Optical footprint (L × W, 4σ)	(4.13–11.87) × 0.95 mm; both crystals
Angular resolution	< 0.25 μrad; both crystals
Motor speed (°/sec)	~0.5; both crystals
Surface height (mm)	1413.5 (center); both crystals

Its signal will be used in a feedback loop driving the piezo pitch and roll stages of the second crystal, stabilizing the beam position and intensity delivered to the downstream optics and the sample position.

<Table 4.2.4.5> Specification of the DCM cryocooler.

Parameter	Specification
Cooling power	0–3,000 W
Required cooling power	< 160 W
Liquid-nitrogen flow rate	0–20 L/min (0–90 Hz)
Cooling-loop pressure	4–5 bar
Pressure stability	< 1 mbar (RMS) / < 5 mbar (PV)
Cooling-loop temperature	77–100 K

D Kirkpatrick–Baez Mirror

The KB mirror pair provides the principal focusing function of the BioPharma-BioSAXS beamline. Bendable, prefigured mirrors are adopted so that the focal position can be shifted by controlled curvature adjustment without inserting an

additional refractive focusing optic. This arrangement provides independent horizontal and vertical focusing, high photon throughput, and a comparatively simple optical layout, all of which are important for routine solution SAXS and in-line SEC-SAXS operation.

The mirrors are positioned downstream of the DCM, with the vertical focusing mirror (VFM) located at 36 m and the horizontal focusing mirror (HFM) at 37.5 m from the source. The bendable KB pair is designed to provide two primary operating configurations. In detector-focused mode, the focal point is set at approximately 75 m, corresponding to the farthest detector position; the calculated beam size at the 67 m sample position is approximately 132 μm (H) × 125 μm (V) (FWHM). This defocused sample condition reduces the photon density at the sample while maintaining a stable beam profile for automated batch BioSAXS and SEC-SAXS measurements. In sample-focused mode, the mirror curvatures are adjusted to shift the focal point to approximately 67 m, giving a beam size of approximately 40 μm (H) × 10 μm (V) (FWHM) at the sample position.

The KB mirrors cover the 8–23 keV operational range, using 50 nm Rh-coated surfaces at an incidence angle of 2.5 mrad, identical to that of the HHLM. At 12.4 keV, the calculated 4σ beam footprints are approximately 1.10 mm × 416 mm for the VFM and 1.00 mm × 460 mm for the HFM. Each mirror substrate (600 mm L × 50 mm W × 50 mm H) provides sufficient optical length for these footprints. To maintain beam quality and avoid focus broadening, the specified surface quality is a slope error below 0.2 μrad RMS (tangential) and 0.5 μrad RMS (sagittal), with a surface roughness under 0.5 nm RMS. Detailed specifications of the KB mirrors, including the image distances required for the detector-focused and sample-focused configurations, are summarized in <Table 4.2.4.3>.

E Three-Slit System

The BioPharma-BioSAXS beamline adopts a three-slit collimation system composed of a beam-defining slit, a collimating slit, and a guard slit. This configuration refines the beam geometry, minimizes parasitic scattering, and determines the smallest accessible scattering vector (q_{min}) for SAXS and WAXS experiments.

The beam-defining slit, located at 38.5 m downstream of the bendable KB mirrors, defines the beam envelope and divergence. A second scatterless slit at 61.0 m acts as the collimating slit, removing off-axis or stray radiation to ensure a uniform and well-collimated beam. The guard slit is positioned at 66.5 m, imme-

diately upstream of the sample, where it suppresses residual parasitic scattering generated by upstream optics and slit edges and so improves the signal-to-noise ratio at the detector. Each slit assembly consists of four independently adjustable scatterless silicon (100) knife edges and is operated under vacuum to minimize background and maintain alignment stability.

The same three slit stations are used in both the detector-focused and the sample-focused mode, with the slit openings adjusted according to the beam envelope in each mode. Beam-stopper sizes of 4 mm and 7 mm are planned for routine operation, providing adequate direct-beam protection while preserving access to the low-q region.

F Optical Configurations and Heat Load

(a) Beam conditions per configuration

The optical system of the BioPharma-BioSAXS beamline is designed to deliver a stable, high-flux X-ray beam optimized for solution scattering and biopharmaceutical research. The beamline employs a high-heat-load mirror (HHLM; M1 mirror) to deflect the beam upward from the undulator source. This configuration ensures that the beam height remains constant after passing through the downstream KB mirrors, resulting in a beam height of approximately 1,433.5 mm at the end-station. Following the M1 mirror, a horizontal double-crystal monochromator (H-DCM) monochromatizes the beam at a constant 25 mm horizontal offset. The monochromatized beam is then focused by a bendable Kirkpatrick–Baez (KB) mirror pair, which controls the focal position. This layout minimizes the number of focusing elements and avoids the transmission loss associated with an additional refractive optic, while ensuring stable beam alignment and high throughput during long-term operation.

Optical simulations were performed using SPECTRA to compute the undulator source spectrum and SHADOW/OASYS for ray-tracing calculations. The calculations were carried out at 12.4 keV (3rd harmonic, undulator gap = 6.86 mm), corresponding to the primary energy for solution SAXS experiments. At the source, the beam size is approximately 44 μm (H) × 10 μm (V) (FWHM) with divergences of ~19 μrad (FWHM) in both directions. Ray-tracing confirmed that the optical design provides the required beam quality, flux, and stability for both static and time-resolved BioSAXS measurements. Based on these simulation results, two operational modes are implemented to accommodate different experimental re-

quirements:

Detector-focused mode (shown in <Figure 4.2.4.1>), optimized for the automated sample changer, adjusts the bendable KB mirrors to place the focal point at approximately 75 m from the source, near the farthest detector position. At the sample position (67 m) the calculated beam size is approximately 132 × 125 μm^2 (FWHM). This mode reduces the photon density at the sample and delivers uniform X-ray exposure across the capillary volume (typically 1 mm in diameter), giving stable and reproducible scattering signals for dilute biological samples and supporting high-throughput automated measurements in routine SEC-SAXS and batch experiments.

Sample-focused mode, optimized for microfluidic experiments, adjusts the mirror curvatures to shift the focal point to the sample position at approximately 67 m, giving a calculated beam size of approximately 40 × 10 μm^2 (FWHM). This configuration provides a smaller, spatially localized beam with high photon density, suitable for time-resolved or kinetic measurements. The results of ray-tracing confirm that this optical configuration achieves the required beam quality and photon flux across the accessible energy range for both static and time-resolved BioSAXS experiments. The beam conditions delivered to the sample position (67 m) in each optical configuration are summarized in <Table 4.2.4.6>.

(b) Heat-load simulation

The heat-load management of the BioPharma-BioSAXS beamline was evaluated to ensure optical stability and prevent deformation of high-precision components under continuous high-flux operation. An HHLM is positioned upstream of the monochromator to partially absorb and dissipate the thermal power that would otherwise be concentrated on the DCM crystals, thereby minimizing slope error and preserving beam stability. Comprehensive heat-load simulations were conducted using the OASYS SRCalc and SRW modules for the IVU20 undulator. At its minimum gap of 5 mm (K = 1.904), the total radiated power is approximately 12.49 kW. At this gap, the power transmitted through the movable mask is approximately 317.6 W, and the power transmitted through the 1 mm × 1 mm white-beam (WB) slit is approximately 214.1 W. At the principal 12.4 keV operating gap of 6.86 mm (K = 1.295), the corresponding values decrease to approximately 214 W and 142.8 W.

<Table 4.2.4.6> Beam conditions delivered to the sample position (67 m) of the BioPharma-BioSAXS beamline for each optical configuration. The energy resolution is set by the Si(111) double-crystal monochromator and is common to all configurations.

Configuration	Photon energy (keV)	Beam size, H × V (μm, FWHM)	Notes
Detector-focused mode	12.4	132 × 125	KB focus at ~75 m, near the farthest detector position; defocused at the sample for uniform illumination of the 1 mm capillary; automated sample changer, batch BioSAXS and SEC-SAXS
Sample-focused mode	12.4	40 × 10	KB curvatures adjusted to focus at the 67 m sample position; microfluidic and time-resolved experiments

(c) M1 mirror thermal analysis

The M1 mirror employs a dual-coating strategy to optimize harmonic rejection and thermal durability: Bare-Si is used for the low-energy regime (below 10 keV), and Rh coating is utilized for high-energy operation (above 10 keV). Simulation results at the 5 mm minimum gap show that the absorbed power reaches 137.4 W for Bare-Si and 62.7 W for Rh, with maximum power densities of 0.315 and 0.144 W/mm^2, respectively. To manage the resulting heat load, the M1 mirror is equipped with a eutectic-bath cooling system.

(d) Double-Crystal Monochromator thermal analysis

The DCM first crystal is subjected to a maximum absorbed power of 151.4 W with a peak power density of 22.41 W/mm^2 at the 5 mm gap under the condition at 10 keV with the M1 Rh-coated stripe. To maintain crystal flatness and prevent thermal distortion under high-flux conditions, both crystals are side-cooled using a liquid-nitrogen (LN_2) circulation system. For reference, the current PLS-II DCM uses the same cryocooler specification (<Table 4.2.4.5>) and has demonstrated a heat-removal capacity of approximately 40 W/mm^2 with its existing bottom-cooled configuration. The detailed heat load and power density at each subsequent optical

element are summarized in <Table 4.2.4.7>.

<Table 4.2.4.7> Heat-load and power-density results along the beamline, at the minimum (5 mm) and operational (6.86 mm) undulator gaps.

Component	Location (m)	Parameter	Minimum gap (5 mm)	Operational gap (6.86 mm)
Undulator	0	Total power (kW)	12.49	5.76
Movable mask	22.5	Transmitted power (W)	317.6	214
WB slit	27.3	Transmitted power (W)	214.1	142.8
M1	29.3	Absorbed power (W)	137.4 (Bare-Si) / 62.7 (Rh)	23.8 (Rh)
M1	29.3	Peak power density (W/mm^2)	0.315 (Bare-Si) / 0.144 (Rh)	0.054 (Rh)
DCM, 1st crystal	32.0	Absorbed power (W)	151.4 (at 10 keV, M1: Rh coating)	119.1 (at 12.4 keV)
DCM, 1st crystal	32.0	Peak power density (W/mm^2)	22.41 (at 10 keV, M1: Rh coating)	14.24 (at 12.4 keV)
DCM, 2nd crystal	32.1	Absorbed power (W)	–	–
DCM, 2nd crystal	32.1	Peak power density (W/mm^2)	7×10^{-7}	3.53×10^{-7}

G Beam Diagnostics and Alignment

Accurately identifying the beam shape and position is essential to ensure that the X-ray beam from the light source is properly delivered to the experimental hutch. In the front-end section, two photon beam-position monitors (PBPMs) are installed to precisely measure the position and profile of the beam from the light source, integrated with the storage ring for real-time monitoring and orbit correction.

For beam diagnostics in the Photon Transfer Line (PTL) section, diamond screen monitors are installed at selected locations before and after major optical elements and downstream of selected slit stations to observe the beam profile during alignment. All of these locations are upstream of the guard slit (66.5 m), so that parasitic scattering generated while a screen is inserted does not contribute to the sample measurement once the screen is retracted and the downstream collimation is restored.

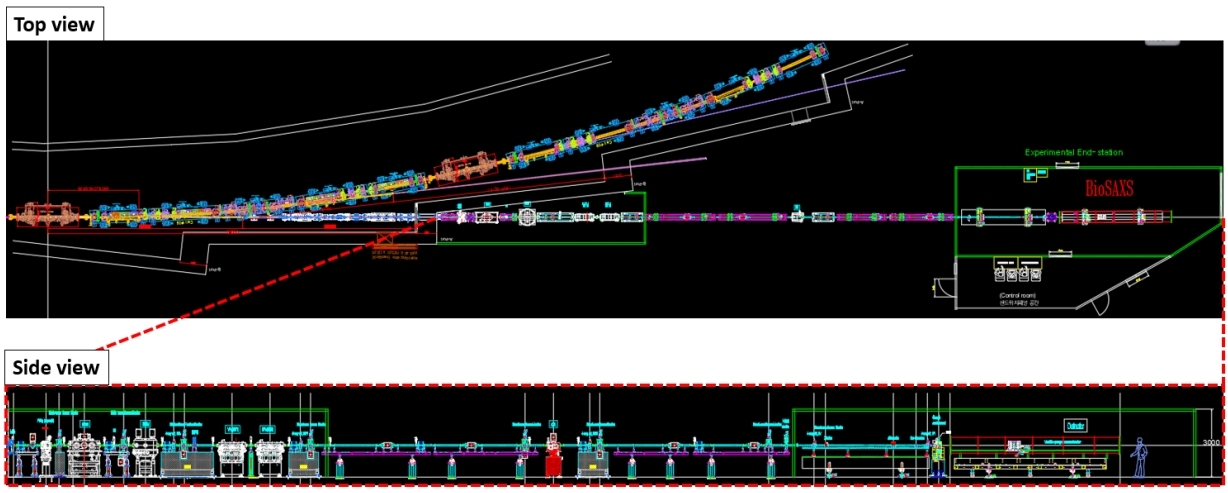
A diamond beam-position monitor (DBPM) is installed at 34.1 m, immediately downstream of the DCM, and integrated with a feedback loop on the second

crystal to compensate for angular drifts in real time. This is the principal position-sensitive feedback device in the PTL, as the DCM provides the active fine-correction mechanism (piezo-driven pitch/roll); elsewhere, direct profile observation via screen monitors is sufficient.

Finally, an ion chamber positioned upstream of the sample at 66.0 m measures the incident beam intensity for normalization with minimal additional scattering into the beam path. An upstream attenuator at 65.0 m can be used when reduced photon flux is required.

4.2.4.5 Photon Transfer Line

The overall floor plan of the BioPharma-BioSAXS beamline, including the top view and side view of the optical components from the front-end through the experimental hutch, is shown in <Figure 4.2.4.3>. Detailed PTL engineering drawings will be updated following completion of the final component and vacuum-layout design.



<Figure 4.2.4.3> BioPharma-BioSAXS beamline floor plan (top and side views).

4.2.4.6 End-Station

BioSAXS experiments increasingly require rapid and accurate structural characterization of biological macromolecules and larger assemblies over a wide size range, together with high-throughput screening and time-resolved measurements of structural dynamics. To address these requirements, the end-station will incorporate a variable-SDD vacuum flight tube (SDD up to 8 m), an automated sample-

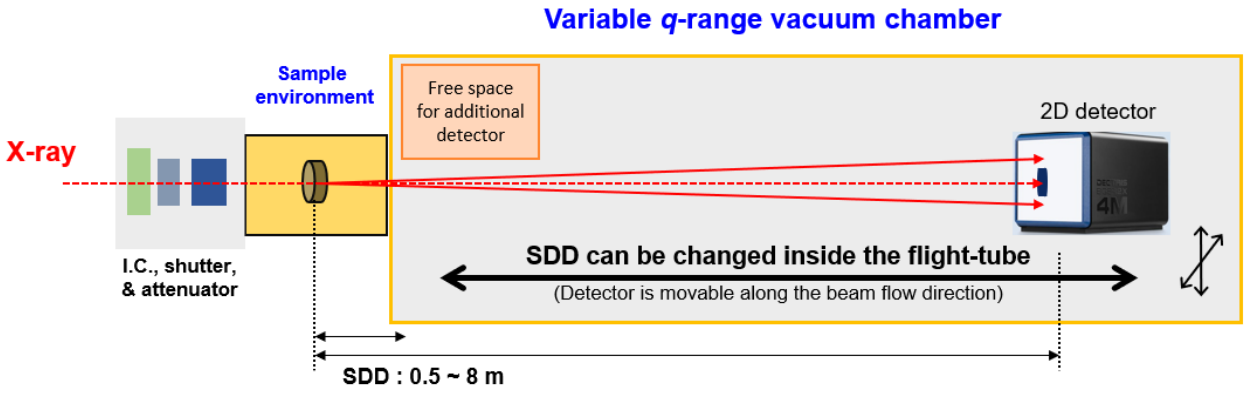
changer robot, and an integrated SEC-SAXS system. The variable-SDD configuration enables flexible q-range selection for samples ranging from proteins and protein complexes to larger assemblies such as viruses and lipid nanoparticles (LNPs). The automated sample changer supports reproducible high-throughput measurements of antibodies, formulations, and other solution samples using small sample volumes, while the SEC-SAXS system enables in-line separation and structural analysis of heterogeneous or polydisperse samples. In addition, the end-station is designed to support time-resolved measurements on millisecond-to-second timescales, depending on the available photon flux, detector acquisition rate, and sample environment.

A Variable q-range Vacuum Chamber

The solution SAXS technique acquires scattering patterns using a 2D large-area detector. Because the solution SAXS technique requires capturing scattering data across a wide range of q-values depending on the particle size of the sample, adjusting the sample-to-detector distance (SDD) is essential. A variable q-range vacuum-tube system is shown in <Figure 4.2.4.4>. The 2D detector is positioned inside the vacuum tube and can be moved along the X-ray propagation direction via a rail system, allowing the SDD to be varied up to approximately 8 m. In addition, the 2D detector can be moved vertically and horizontally relative to the incident X-ray beam, enabling precise alignment. A photodiode-type beam stop is placed in front of the detector to protect it from the direct beam. The current generated by the photodiode, which is proportional to the incident X-ray intensity, is converted into a voltage-frequency-count signal to accurately calculate the X-ray transmittance of the sample. The X-ray detectors and beam-intensity monitors of the beamline are summarized in <Table 4.2.4.8>.

B Auto Sample Changer Robot

To analyze the 3D structure of biological molecules, the BioPharma-BioSAXS beamline requires high-throughput experiments and high-speed processing of a large number of samples. To meet this demand, an automatic sample-exchange robot system will be introduced. The automatic sample-exchange robot will automatically load a minimum of 5 μL of sample into a quartz capillary and irradiate it with X-rays. A typical full cycle, including sample loading, unloading, and flow-path cleaning, takes approximately 50 s, supporting up to 96 sample positions per plate. For biomolecular samples, radiation damage from X-rays can cause sample



<Figure 4.2.4.4> Schematic diagram of the variable q-range vacuum chamber at the BioPharma-BioSAXS beamline.

<Table 4.2.4.8> Detectors and beam-intensity monitors of the BioPharma-BioSAXS beamline.

Parameter	PILATUS4 X 2M	Beam-stop photodiode	Ion chamber
Role / technique	2D SAXS scattering-pattern acquisition	Transmitted (direct) beam intensity, sample transmittance	Incident-beam intensity monitor
Detector type / detection principle	Hybrid photon-counting pixel detector	Photodiode integrated in the beam stop	–
Sensor material / thickness	Si / 450 μm	–	–
Pixel pitch	150 × 150 μm^2	Single element	Single element
Pixel format / channels	1553 × 1630 pixels (2.53 M pixels)	Single element	Single element
Beamline operating energy range	8–23 keV	8–23 keV	8–23 keV
Sample-to-detector distance	Variable, up to 8 m	–	–
Remarks	Vacuum-compatible; mounted on a movable rail for SDD adjustment, with vertical/horizontal translation for alignment	Photocurrent converted to a voltage–frequency–count signal	Non-invasive; no additional scattering into the beam path

denaturation. To minimize this effect, a flow-exposure mode is provided, in which typical transferred sample volumes of 20–35 μL flow continuously through the quartz capillary during solution SAXS measurements, with the flow rate selected according to the exposure condition.

Storage and measurement temperatures can be adjusted from 4 to 40 °C and 2 to 60 °C, respectively, depending on the characteristics of the sample. The specifi-

cations of the automatic sample-changer robot are summarized in <Table 4.2.4.9>.

<Table 4.2.4.9> Specification of the automatic sample-changer robot to be used at the BioPharma-BioSAXS beamline.

Parameter	Specification
Performance	
Solution transfer volume	5–200 μL
Typical cycle time / loading / unloading / cleaning (wash, rinse, dry)	50 s / 15 s / 15 s / 20 s
Sample containers	96-well microplates; 96-deep-well microplates; 4×8 wells Eppendorf strips (200 μL); 4×3 individual 1.5 mL wells (buffers)
Control	
Sample exposure modes	(1) Static; (2) Flow (0.05–20 μL/s)
Temperature control (exposure / storage)	2–60 °C / 4–40 °C
Control panel	Video-assisted automatic liquid positioning
Dimensions (W × H × D)	
Main unit	550 × 800 × 1100 mm^3
Fluid-management rack	837 × 576 × 900 mm^3
Control rack	712 × 576 × 900 mm^3

C SEC-MALS-SAXS System

For accurate structural analysis of solution samples, SAXS data acquisition from monodisperse samples is essential. The BioPharma-BioSAXS beamline will incorporate an in-line size-exclusion chromatography (SEC)-SAXS technique, which enables real-time separation of samples by size and molecular weight while simultaneously collecting scattering data for each component. SAXS data will be collected continuously across each SEC elution profile, so that structural information for each separated component of the mixture can be obtained. In addition, multi-angle light scattering (MALS) and dynamic light scattering (DLS) will be employed in conjunction with SEC to provide complementary molecular-weight and hydrodynamic-size information for sample-quality assessment.

References

[1] Hyungseok Choi and Jongha Park. Beamline Photon Source Analysis Report. Internal Document PAL-INT/ME-2026-007. Pohang Accelerator Laboratory, July 2026.

[2] Jongha Park et al. High Heat Load Front-End Mechanical Design and Thermal Analysis Report. Internal Document PAL-INT/ME-2026-003. Pohang Accelerator Laboratory, June 2026.

4.2.5 Bio-Nano Crystallography (ID22)

The Bio Nanocrystallography (BioNX) beamline is the first dedicated macromolecular crystallography (MX) beamline of the KLS, installed at sector ID22. It is designed to determine atomic-resolution structures of biological macromolecules such as proteins, nucleic acids and their complexes, and to support advanced techniques including serial synchrotron crystallography (SSX), in-situ crystallography (ISX) and automated high-throughput screening (HTS). This chapter describes the ID22-specific design of the photon source, the front-end, the beamline optics (overall optical layout, CRL transfocator, focusing mirrors, the horizontal double-crystal and multilayer monochromator, the chopper system, source conditions, and beam diagnostics), the photon transfer line (PTL), and the end-station. Material that is common to all KLS beamlines is cited to the separate Common Technical Sections document prepared by the device team.

4.2.5.1 Target Purpose and Objective

Macromolecular crystallography is the principal method for determining the three-dimensional atomic structures of biological macromolecules. To date, roughly 200,000 atomic-resolution structures have been deposited, about 85% of which were solved by synchrotron-based MX. These structures underpin modern molecular biology and pharmacology and are increasingly central to drug-discovery research. The BioNX beamline is designed to bring world-class MX capability to Korea by combining a high-flux, low-divergence beam from the 4th-generation storage ring with cutting-edge end-station instrumentation.

The beamline targets three core techniques, summarized below:

- **Serial synchrotron crystallography (SSX):** diffraction snapshots are collected from large numbers of microcrystals using a small, high-flux beam, and merged into a complete dataset. SSX requires a ~1 μm beam, a flux of 10^{13}–10^{14} ph/s and a fast detector, with a fixed-target sample-delivery scheme as the primary method.
- **In-situ crystallography (ISX):** crystals are measured directly in plates or 3D-printed holders without harvesting. Small wedges (~60°) are merged into a complete dataset (small-wedge synchrotron crystallography), requiring a beam of ~10 μm or less and a flux of 10^{11}–10^{12} ph/s.
- **Automated high-throughput screening (HTS):** remote, automated sample

handling and data collection enable rapid screening of large compound and fragment libraries, targeting more than 300 samples per day to accelerate drug discovery.

To realize these objectives, the beamline targets a sample-position beam size from 1×1 to 50×50 μm^2, photon energies of 8–25 keV with primary operation around 12.4 keV and 20 keV, and a flux of 10^{13}–10^{14} ph/s. Rapid beam-size changes are achieved by compound-refractive-lens (CRL) defocusing, and a horizontally deflecting Double-Crystal and Multilayer Monochromator (hDCMM) stably delivers a micron-scale, high-flux beam. The overall design goal is listed in table 4.2.5.1, and the design was benchmarked against recently upgraded international MX beamlines (table 4.2.5.2). The reference design follows the microMAX beamline at MAX-IV.

<Table 4.2.5.1> Design goal of the BioNX beamline.

Parameter	**Value**
Light source	IVU20 (3 m)
Photon energy (keV)	8 – 25
Wavelength (Å)	0.5 – 1.55
Energy resolution (ΔE/E)	$< 2 \times 10^{-4}$
Beam size (μm^2)	1×1 – 50×50 in FWHM
Photon flux (ph/s)	10^{13} – 10^{14}
Techniques	SSX, ISX, HTS
Measurement speed	> 100 Hz

<Table 4.2.5.2> Comparison of MX beamline specifications at international synchrotrons.

Parameter	KLS BioNX	ANSTO MX3	Diamond VMXm	ESRF ID29	MAX-IV micro-MAX	NSLS-II FMX
Beam size (μm^2, V×H) min	1×1	2×2	0.3×0.5	0.5×0.5	1×1.5	1×1.5
Beam size (μm^2, V×H) max	50×50	8×2	10×13	6×5	5×5	10×10
Photon flux @sample (ph/s)	10^{13}–10^{14}	6×10^{13}	$> 10^{13}$	$> 5 \times 10^{15}$ @10 keV	10^{13} (DCM); 10^{14}–10^{15} (DMM)	3.5×10^{12}
Energy range (keV)	8–25	10–15	7–28	10–25 and 35	5–25 (DCM); 10–13 (DMM)	5–30
Undulator	IVU20 (3m)	IVU17.2 (3m)	IVU21	IVU21	IVU18 (3m)	IVU21 (1.5m)
Monochromator (E resolution)	hDCMM	hDMM (0.9/0.5/ 0.3%)	hDCM	–	hDCM (2×10^{-4}); DMM (0.4/1%)	hDCM (3×10^{-4})
CRL defocus	O	O	x	–	O	O
Diffractometer	MD3-UP	MD3-UP	–	MD3-UP SSX	MD3-UP	Nelson Air SP150
Detector	EIGER2 XE 16M	Eiger2 XE 16M	EIGER2 X CdTe 9M; Pilatus3 6M	Jungfrau 4M	EIGER2 X CdTe 9M	EIGER X 16M
Operation status	Under designing	Commis-sioning	Commis-sioning	Operation	Commis-sioning	Operation

4.2.5.2 Photon Source

The primary objective of the BioNX beamline is to maximize data acquisition from challenging small crystals using a high-flux beam and short exposures, which requires a high-flux undulator. Among the three undulators planned for the KLS (IVU20, IVU22, IVU24), the IVU20 offers the highest flux and the lowest heat load, 12.49 kW [1]. The IVU20 does, however, show a spectral discontinuity between 6.8 keV and 8.08 keV that limits experiments in that range.

The BioNX beamline covers 8–25 keV with primary operation planned at 12.4 keV and 20 keV, where the flux at the sample is expected to be approximately 10^{13}–10^{14} ph/s. The IVU20 has a length of 3 m, a period of 20 mm and a gap ad-

justable from 5 to 18 mm. The source parameters are summarized in table 4.2.5.3.

<Table 4.2.5.3> Source parameters for the BioNX beamline. The maximum total power, K_{max} and power density are given at the minimum gap of 5 mm.

Undulator	Period (mm)	Length (m)	Gap size (mm)	K_{max}	Max total power (kW)	Power density (kW/mrad^2)
IVU20	20	3.0	5–18	1.904	12.49	164.2

4.2.5.3 Front-End

The front end of the BioNX beamline incorporates a high heat-load front end capable of handling up to 12 kW and specifically designed to accept the X-ray beam from the IVU20 [2]. The front end begins with the IVU20 undulator, followed by a mask at 18 m that defines the initial beam aperture before the white beam enters the optical hutch.

[To be completed in a later revision.]

4.2.5.4 Beamline Optics

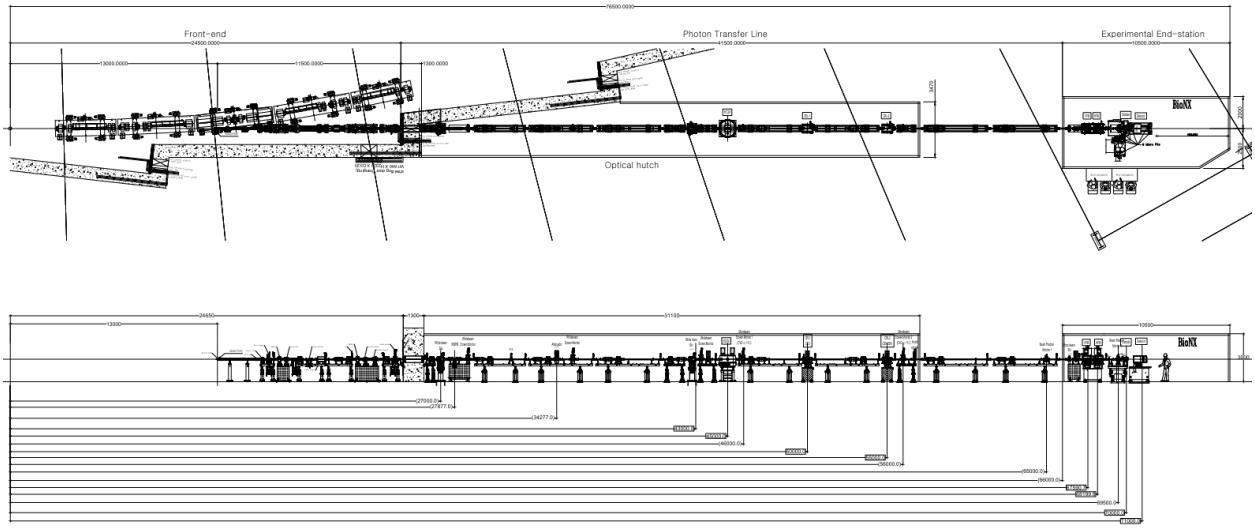
The optics conditions, monochromatize and focus the undulator beam, and define the source conditions delivered to the sample. The beamline is divided into a front end, an optical hutch where the white beam is monochromatized, a long spool, and an experimental hutch that houses the final focusing optics together with the sample and detector. The distance from the source to the sample is 70 m, with the 2D detector located within ~71 m.

A Overall optical layout and component roles

The BioNX beamline at sector ID22 spans approximately 71 m from the undulator source to the detector and is divided into four sequential sections: the front end, the optical hutch (26–57 m), the long spool (57–66 m), and the experimental hutch (66–77 m). In the optical hutch the white beam passes a 4-way UHV white-beam slit (43 m) and a retractable white-beam screen monitor with a diamond BPM (43.5 m); it is then monochromatized by the horizontal DCMM (45 m), profiled by a cooled monobeam screen monitor (46 m), passed through a heat-load chopper (48 m) and a CRL transfocator (50 m), and verified by a second monobeam screen monitor (51 m).

The long spool houses a diamond UHV beam-position monitor (BPM1, 65 m) that feeds back to the hDCMM for beam-position stabilization. The experimental

hutch integrates the final focusing optics, beam conditioning and the sample/detector environment in a single enclosure to minimize temperature-induced drift. After a 4-way UHV monobeam slit (67.2 m), a Vertical Focusing Mirror (VFM, 67.7 m) and a Horizontal Focusing Mirror (HFM, 68.4 m) focus the beam to a minimum spot of ~1 μm; a fast chopper (69 m) generates the pulsed beam, and a high-precision BPM (BPM2, 69.8 m, < 100 nm) feeds back to the HFM. The beam reaches the MD3-UP sample stage (SOC < 100 nm) at 70 m, and an EIGER2 XE 16M detector at ~71 m records the diffraction. The full optical layout is shown in figure 4.2.5.1 and figure 4.2.5.2, and all major components and locations are listed in table 4.2.5.4.

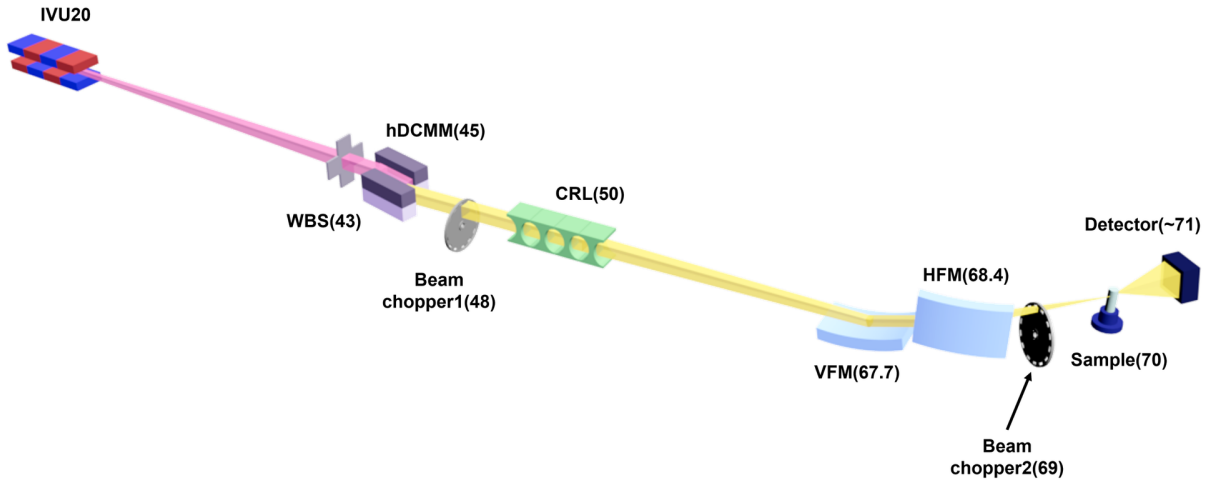


<Figure 4.2.5.1> Beamline layout of BioNX.

B Compound Refractive Lens transfocator and lens configuration

A compound refractive lens (CRL) is an array of biconcave lenses placed in series; the effective focal length is set by the number of lenses in the beam, so adding lenses shortens the focal length, moves the focus upstream of the sample and enlarges the beam at the fixed sample position. This controlled defocusing changes the beam size without re-bending the focusing mirrors, which is far faster and more stable against temperature and vibration: a critical advantage when the minimum beam size approaches ~1 μm. Recently upgraded MX beamlines (e.g., ANSTO MX3, MAX IV microMAX, NSLS-II FMX) increasingly adopt this approach, and the BioNX beamline follows it.

Beryllium, the most common CRL material, has faced production discontin-



<Figure 4.2.5.2> Optical layout of the BioNX beamline. Component positions are given in metres from the source.

uation; among the alternatives (diamond, silicon, aluminum), diamond offers transmission closest to beryllium and has been selected for the BioNX CRLs. The CRL system is implemented as a transfocator at 50 m, housing both 2D lenses (focusing in both directions) and 1D horizontal lenses selected from cassette arms. The current design uses 35 diamond lenses in three variants (table 4.2.5.5); because a CRL focal length depends on photon energy, a limited lens set and fixed, pre-validated, energy-dependent beam-size presets (approximately 1, 2, 5, 10 and 50 μm at the sample) are provided. As diamond lenses are still under active development, the final configuration may be adjusted.

C Mirror parameters and mechanism required performance

Two mirrors, the Vertical Focusing Mirror (VFM, 67.7 m) and the Horizontal Focusing Mirror (HFM, 68.4 m), focus the beam in the vertical and horizontal directions. Both are elliptical with a fixed focal length (table 4.2.5.6). To deliver a stable micron-sized beam, the mirrors are placed close to the sample and enclosed in the experimental hutch to minimize vibration and temperature fluctuation. For high-harmonic rejection the incidence angle is set to 3 mrad, and each surface is coated in three stripes of silicon, rhodium and platinum, selected according to the monochromatic energy.

<Table 4.2.5.4> Component list of the BioNX beamline, in beam order (distances measured from the source).

Distance (m)	Location	Component	Description
0	Front-End	IVU20	Period 20 mm, length 3 m
18		Mask	Defines the initial beam aperture; high heat-load front end (up to 12 kW)
43	Optical Hutch	White-beam slit	4-way slit; beam conditioning
43.5		White-beam screen monitor	Retractable; CCTV Diamond BPM; white-beam monitor
45		Horizontal DCMM	Si(111) crystal and Ru/B_4C multilayer; monochromator (monobeam)
46		Mono-beam screen monitor	CCTV; cooled; mono-beam profiling
48		Chopper 1 (heat-load chopper)	Water cooled; reduce thermal load; pulsed beam
50		CRL transfocator	2D/1D diamond lens; beam focusing
51		Mono-beam screen monitor	CCTV; cooled; mono-beam profiling
65	Spool	Beam position monitor	Diamond, feedback; beam position & profile
67.2	Experimental Hutch	Mono-beam slit	4-way slit; beam conditioning
67.7		VFM	Si / Rh (50) / Pt (50); vertical focusing
68.4		HFM	Si / Rh (50) / Pt (50); horizontal focusing
69		Chopper 2 (fast chopper)	Water cooled; pulsed-beam generation
69.8		Beam position monitor	< 100 nm resolution, feedback; beam position & profile
70		Sample stage	MD3-UP, SOC < 200 nm; diffractometer
71		2D detector	EIGER2 XE 16M; diffraction detection

<Table 4.2.5.5> Diamond CRL inventory for the BioNX transfocator.

Lens type	Radius of curvature, R (mm)	Aperture, A (mm)	Quantity (ea)
CRL-2D (ROC1)	1	2.0	5
CRL-2D (ROC6)	6	2.0	17
CRL-1D (CRL-H, 1DH)	2.1	2.0	13
Total (3 variants)	–	–	35

D Double-Crystal and Multilayer Monochromator

The monochromator is a horizontally deflecting Double-Crystal and Multilayer Monochromator (hDCMM) at 45 m, combining a Si(111) crystal pair with a Ru/B_4C multilayer pair (table 4.2.5.7). Two complementary modes are selected simply by

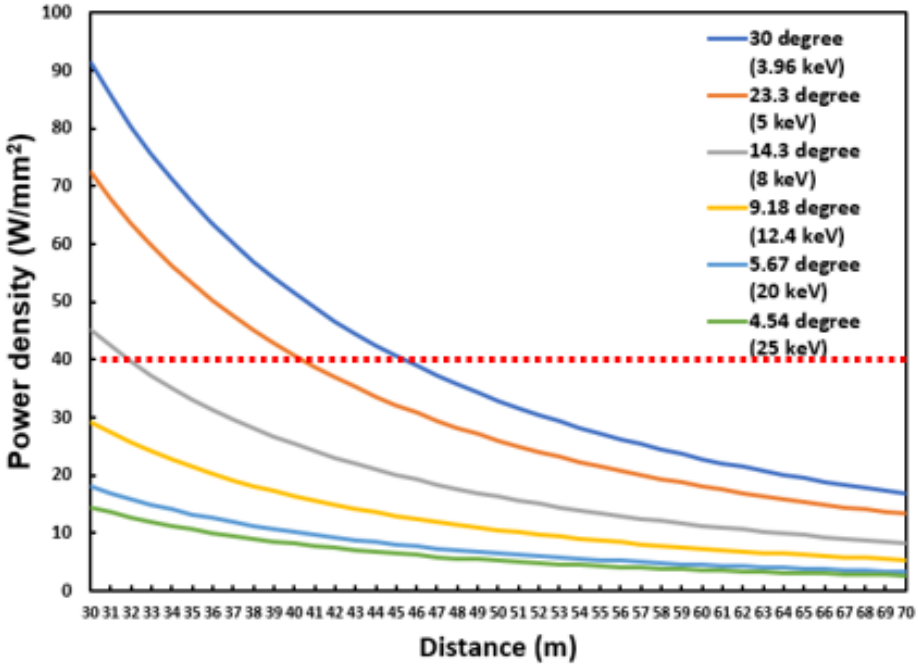
<Table 4.2.5.6> Specification of the focusing mirrors.

Parameter	VFM	HFM
Installation location (m)	67.7	68.4
Reflection direction	Vertical (upward)	Horizontal (towards the hall)
Mirror surface shape	Elliptical cylinder (tangential focusing)	Elliptical cylinder (tangential focusing)
Incident angle	3.0 mrad	3.0 mrad
Tangential radius	Ra = 35 km, Rb = 37.4 km	Ra = 35 km, Rb = 31.4 km
Sagittal radius	$>$ 100 km (cylinder)	$>$ 100 km (cylinder)
Substrate material	Silicon	Silicon
Mirror size (L $\times$ W $\times$ T)	600 $\times$ 50 $\times$ 50 mm	600 $\times$ 50 $\times$ 50 mm
Coating material	Si, Rh (50), Pt (50)	Si, Rh (50), Pt (50)
Coating strip number	3 ea	3 ea
Coating stripe width	10 mm (W), per stripe	10 mm (W), per stripe
Tangential slope error	0.2 µrad RMS (0.15 µrad goal)	0.2 µrad RMS (0.15 µrad goal)
Sagittal slope error	$<$ 5 µrad RMS	$<$ 5 µrad RMS
Roughness	0.2 nm RMS (HSF)	0.2 nm RMS (HSF)
Cooling method	Side cooling	Side cooling
Mirror bender	None	None
Mirror surface height	1400	1404.2
Motor axis	Pitch, yaw, roll, x, y, z	Pitch, yaw, roll, x, y
Manual axis (granite base)	Pitch, yaw, roll, x, y, z	Pitch, yaw, roll, x, y, z

changing the main-axis Bragg angle, without longitudinal translation. In crystal (DCM) mode the Si(111) pair gives a high energy resolution of $\Delta E/E < 2 \times 10^{-4}$ across 8–25 keV for high-resolution data collection. In multilayer (DMM) mode the Ru/B_4C pair, operated over 10–15 keV, accepts a much broader bandwidth ($\Delta E/E$ ~10^{-2}) and delivers one to two orders of magnitude more flux, which suits SSX where maximum flux in a short exposure is required. The pairs share a common rotation cradle with a single fixed exit, so the downstream optics need little realignment when switching modes.

A horizontally bouncing geometry mitigates instability from the cooling system (LN_2 pulsation, two-phase flow, pump vibration) by decoupling vertical thermal and vibrational drift from the beam pointing at the sample; it is also compact and resistant to ground vibration. The monochromator position was chosen to keep the heat load within a safe limit: the first crystal can absorb up to 40 W/mm^2, and even in the worst case (30° Bragg angle) the power density falls below this limit beyond ~45 m from the source (figure 4.2.5.3). The heat-load figures used for

this evaluation are summarized in table 4.2.5.8. The horizontal-bounce geometry, aligned with the X-ray polarization, together with the IVU20 spectral discontinuity, confines the practical range; after optimization the beamline accommodates 8–25 keV with primary operation around 12.4 keV and 20 keV.



<Figure 4.2.5.3> Power-density prediction versus distance from the source. The red dotted line marks the monochromator heat-load limit.

E Chopper system

The layout includes two choppers: a heat-load chopper (Chopper 1) at 48 m in the optical hutch and a fast chopper (Chopper 2) at 69 m in the experimental hutch. Chopper 1 reduces the thermal load on downstream optics and can generate a coarse pulsed beam; because the average power downstream of the monochromator is small (on the order of 1 W), its role is still under review and its inclusion is not yet confirmed.

Chopper 2, the fast chopper, is the primary chopper. It modulates the bunch train (selecting pulses and gating the beam at the sample) to deliver a microsecond pulsed beam for room-temperature SSX, to synchronize sample exposure with the delivery and detector systems, and to mitigate radiation damage, following the microsecond serial-crystallography approach demonstrated at ESRF-EBS ID29. The current design targets 250 Hz with a 90 μs (FWHM) pulse from a two-slit disk

<Table 4.2.5.7> Specification of the DCMM. The Ru/B_4C multilayer d-spacing is not yet fixed, so the DMM Bragg range remains TBD.

Item	Specification
Position (m)	45
Deflection / type	Horizontal bounce, fixed (constant) exit
Photon energy range	8 – 25 keV (DCM mode); 10 – 15 keV (DMM mode)
Crystal / optical element	Si(111) crystal pair and Ru/B_4C multilayer pair
Operating modes	DCM (Si(111), high resolution) / DMM (Ru/B_4C, high flux for SSX), selected by main-axis Bragg angle
First crystal	40×25×40 mm (crystal), 170×25×40 mm (multilayer)
Second crystal	70×25×25 mm (crystal), 170×25×40 mm (multilayer)
Beam offset	TBD
Bragg angle range	4.54° – 14.31° (Si(111), DCM mode over 25 – 8 keV); DMM mode TBD
Slope error	TBD
Roughness	TBD
Cooling	Liquid nitrogen (LN_2)
Motion axes	TBD
Sensors and encoders	Interferometers on crystal gap and stage vibration
Operation	Fixed-exit, closed-loop (encoder) feedback

<Table 4.2.5.8> Heat load along the BioNX beamline, evaluated for the IVU20 at its minimum gap of 5 mm. The hDCMM first crystal is rated for a peak power density of 40 W/mm^2, and its position at 45 m was chosen so that the incident power density stays below this limit even in the worst case of a 30° Bragg angle.

Component	Location (m)	Parameter	IVU20 at minimum gap (5 mm)
IVU20	0	Total emitted power (kW)	12.49
IVU20	0	Peak power density (kW/mrad^2)	164.2
Front end	18	Design power-handling capability (kW)	12
hDCMM, 1st crystal	45	Absorbed power (W)	TBD
hDCMM, 1st crystal	45	Peak power density (W/mm^2)	< 40 (design limit at a 30° Bragg angle)

at 7,500 rpm, phase-locked to the storage-ring bunch clock (table 4.2.5.9).

F Source conditions per optical configuration

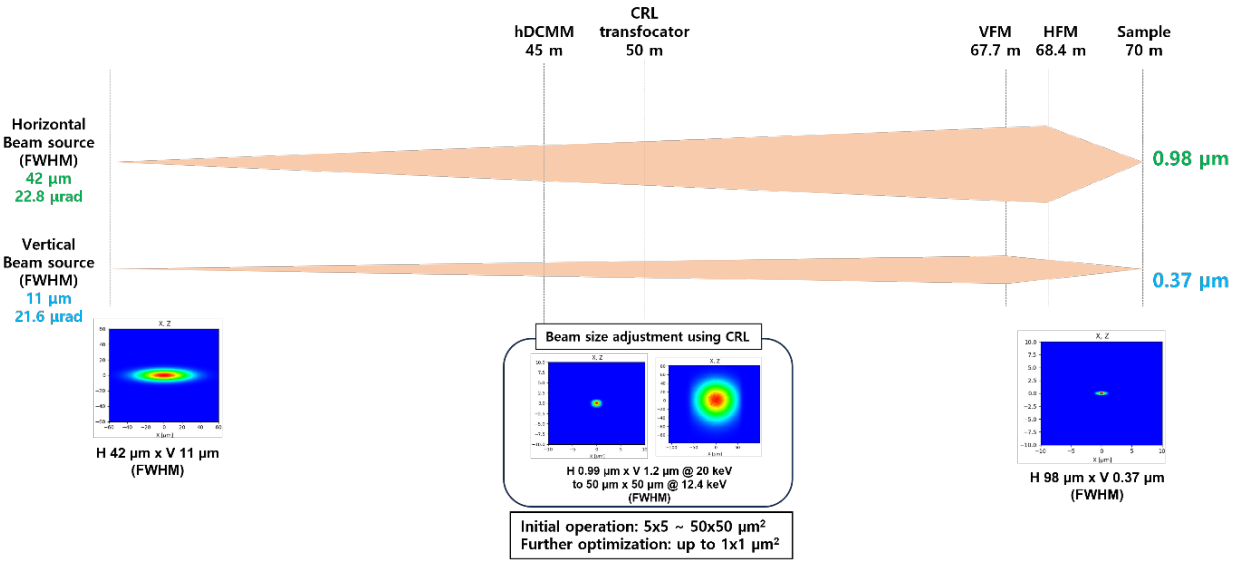
The beam-delivery design uses one-stage direct focusing without a secondary source. The IVU20 source is moderately asymmetric in size (horizontal FWHM 42 μm, vertical FWHM 11 μm) but nearly symmetric in divergence (horizontal 22.8 μrad, vertical 21.6 μrad), which allows the VFM and HFM to focus the beam directly

<Table 4.2.5.9> Specification of the fast chopper (Chopper 2).

Item	Specification
Function	Fast chopper – bunch-train modulation (pulse selection / sample-exposure gating)
Pulse repetition rate	250 Hz (X-ray pulse output)
Pulse width	90 μs (FWHM)
Rotor speed	7,500 rpm (125 Hz mechanical; 2 slits × 125 Hz = 250 Hz)
Disk	2-slit disk
Bearing	Active magnetic bearing (UHV compatible)
Synchronization	Phase-locked (PLL) to the storage-ring bunch clock

onto the sample without an intermediate aperture, reducing optical complexity and avoiding flux loss. Long-term positional stability of the micron-scale beam is provided by the horizontally bouncing hDCMM, which decouples vertical thermal drift from the beam pointing at the sample.

Without any CRL, the focusing mirrors alone produce a beam of about 0.9 × 0.3 μm^2 at the sample; inserting CRLs of different strengths enlarges the beam from roughly 1 × 1 μm^2 up to about 50 × 50 μm^2. Because a CRL focal length depends on photon energy, the same configuration does not give the same beam size at every energy, so a fixed set of pre-validated, energy-dependent beam-size presets is provided. The resulting beam conditions at the sample, computed with OASYS at 12.4 keV and 20 keV, are listed in table 4.2.5.10, and the corresponding ray-tracing and intensity distribution are shown in figure 4.2.5.4.



<Figure 4.2.5.4> Ray-tracing and simulation of beam size and intensity.

<Table 4.2.5.10> Expected beam conditions at the sample of the BioNX beamline, computed with OASYS. Each CRL configuration is given as the number of inserted 2D(ROC1)/2D(ROC6)/1DH diamond lenses.

Configuration	Photon energy (keV)	Beam size, H × V (μm, FWHM)	Flux (ph/s, 0.1% BW)	Notes
Mirrors only (CRL 0/0/0)	12.4	0.96 × 0.38	5.1×10^{14}	Minimum beam size; no CRL inserted
CRL 0/1/0	12.4	1.64 × 2.32	4.9×10^{14}	CRL defocusing preset
CRL 0/3/1	12.4	7.0 × 6.75	4.5×10^{14}	CRL defocusing preset
CRL 0/6/1	12.4	10.4 × 13.1	4.1×10^{14}	CRL defocusing preset
CRL 5/0/7	12.4	50.7 × 52.8	2.6×10^{14}	Largest preset (~50 × 50 μm^2)
Mirrors only (CRL 0/0/0)	20	1.04 × 0.37	1.4×10^{14}	Minimum beam size; no CRL inserted
CRL 0/1/0	20	1.12 × 0.96	1.38×10^{14}	CRL defocusing preset
CRL 0/3/1	20	2.23 × 2.65	1.35×10^{14}	CRL defocusing preset
CRL 0/7/4	20	6.0 × 6.0	1.27×10^{14}	CRL defocusing preset

G Beam diagnostics and alignment

Beam diagnostics are distributed along the beamline to condition the beam and provide closed-loop position feedback. In the optical hutch, a 4-way UHV white-beam slit (43 m) and a retractable white-beam screen monitor with a diamond BPM (43.5 m) condition and profile the white beam, while cooled CCTV monobeam screen monitors (46 m and 51 m) profile the monochromatized beam. A diamond UHV beam-position monitor (BPM1, 65 m) in the long spool feeds back to the hDCMM for beam-position stabilization. In the experimental hutch, a 4-way UHV monobeam slit (67.2 m) conditions the beam and a high-precision BPM (BPM2, 69.8 m, < 100 nm resolution) feeds back to the VFM, HFM. These two feedback loops (BPM1 → hDCMM and BPM2 → VFM, HFM) together ensure the long-term positional and thermal stability required for micron-scale focusing.

[To be completed in a later revision.]

4.2.5.5 Photon Transfer Line

This section covers the photon-transfer line (PTL) and the mechanical, vacuum and hutch infrastructure that support the optics and the experimental environment.

A Mechanical Design

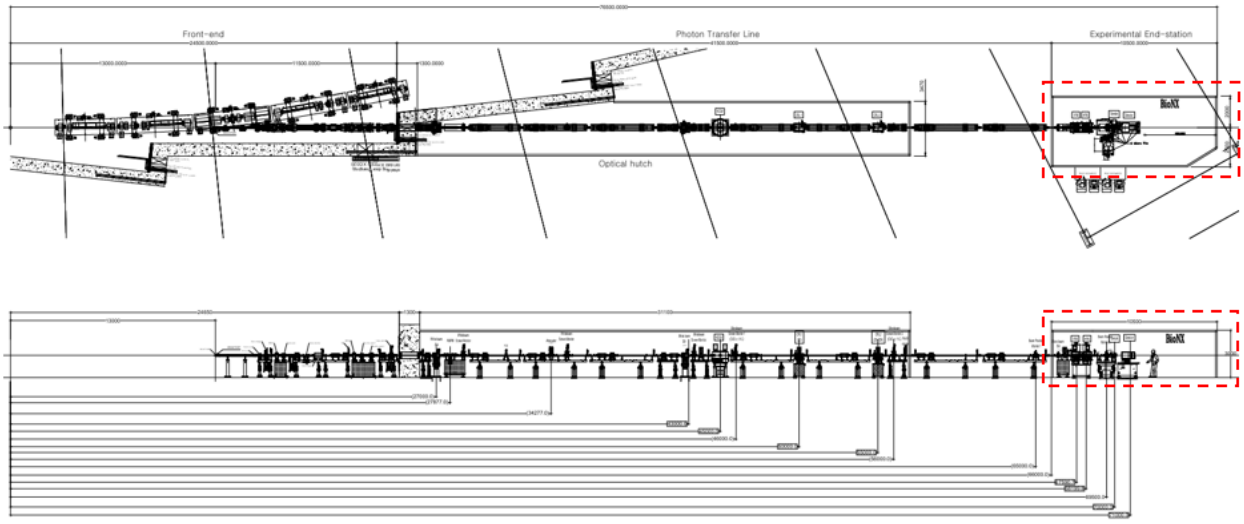
[To be completed in a later revision.]

B Vacuum, Pumps and Valves

[To be completed in a later revision.]

C Hutch and Floor Plan

The final focusing mirrors are co-located with the sample inside the experimental hutch in the ID22 section so that the focusing optics, beam conditioning and sample/detector environment share a single enclosure, minimizing temperature-induced beam drift. The ID22 section layout is shown in figure 4.2.5.5, with the experimental hutch marked by the red dotted box. A detailed floor plan and hutch dimensions will be provided later.



<Figure 4.2.5.5> ID22 section layout of the BioNX beamline. The experimental hutch is marked by the red dotted box.

D Vibration and thermal stability of the experimental hutch

Maintaining beam stability is essential when the beam is focused to a minimum size of ~1 μm. The focusing mirrors are enclosed within the experimental hutch and placed close to the sample to minimize the vibration and temperature fluctuation that would otherwise degrade beam stability, with a shot-beam stability target of ± 0.1 μm over 30 min. The horizontally bouncing monochromator further decouples vertical thermal and vibrational drift (including liquid-nitrogen pulsation, two-phase flow and pump vibration in the cooling system) from the beam pointing at the sample. A quantitative vibration and thermal-stability analysis of the experimental hutch will be added later.

[To be completed in a later revision.]

4.2.5.6 End-Station

The end-station is designed to enable both serial crystallography and high-throughput experiments in support of drug development. It provides a high flux and small beam suitable for high-quality data from nano- and micro-sized protein crystals, together with a high-precision diffractometer and an ultra-fast 2D detector for precise crystal alignment on the micron beam and for high-rate (> 100 Hz) data collection.

A Autonomous-operation strategy

For high-throughput operation the end-station supports remote sample delivery and experimentation, targeting more than 300 samples per day. A 6-axis robot arm with a double sample gripper performs rapid, automated pin exchange on the diffractometer, and an LN_2 sample-storage chamber holds approximately 600 samples. Automating sample handling and data collection reduces the time spent opening and closing the hutch, minimizes human error and the risk of ice rings, and enables consistent screening of compound libraries against target proteins. The diffractometer supports automated high-throughput screening combined with rotational crystallography.

B End-Station Mechanical Design

[To be completed in a later revision.]

C Instruments of End-Station

The end-station instruments include an optical table with beam-conditioning diagnostics, a sample diffractometer, a 2D detector, a 6-axis sample-exchange robot arm, an LN_2 sample-storage chamber and a silicon drift detector. The diffractometer supports easily interchangeable goniometer heads (including a fixed-target SSX head and a plate head), allowing rapid switching between rotational crystallography, fixed-target serial crystallography and in-situ crystallography. Four operating modes are therefore supported: rotational crystallography; fixed-target serial crystallography; in-situ crystallography; and automated high-throughput screening with rotational crystallography. Each mode can be run at cryogenic or room temperature on request.

To handle nano- and micro-sized crystals, the diffractometer requires a sphere of confusion (SOC) below 100 nm for accurate positioning on a micron beam, with a coaxial high-resolution microscope for alignment, several-hundred-nanometer precision with high repeatability, hardware triggering of the detector based on angle and position, a multi-axis (kappa/phi) goniometer to minimize spot overlap for large unit cells, and helical/raster scanning to reduce radiation damage and enable serial crystallography. The required specifications are listed in table 4.2.5.11.

<Table 4.2.5.11> Required specifications of the sample diffractometer.

Parameter	Specification
Sample alignment	
Design resolution	5 nm
Range	Y axis: 110 mm / Z axis: 6 mm / X axis: 6 mm
Static accuracy	$\pm$ 100 nm
Scan axis (Omega)	
Sphere of confusion (SOC)	< 100 nm
Rotation speed	> 100 deg/s
Design angular resolution	< 0.1 mdeg
Static accuracy	< $\pm$ 1 mdeg
Kappa range	0° – 90°
Kappa angular resolution	< 0.1 mdeg
Phi angular resolution	< 0.1 mdeg

D Detector

Diffraction is measured with a photon-counting detector offering high sensitivity and high-speed imaging above 100 Hz. To resolve diffraction from crystals

with large unit cells (membrane proteins, large complexes), the detector requires an active area of at least 300 mm so that, even when positioned farther back to separate spots, individual reflections from unit cells larger than ~1,000 Å remain resolvable while high-resolution data are collected. The required specifications are listed in table 4.2.5.12.

<Table 4.2.5.12> Required specifications of the detector, to be met by the EIGER2 XE 16M. Detector-supported energy and beamline operating energy are listed separately.

Parameter	**EIGER2 XE 16M**
Role / technique	Diffraction detection for rotational crystallography, SSX, ISX and HTS
Detector type / detection principle	Hybrid photon-counting pixel detector
Sensor material / thickness	Si, 450 µm
Pixel pitch	75 × 75 µm
Pixel format / channels	4148 × 4362
Active area	> 300 × 300 mm^2 (requirement); 311.2 × 327.8 mm^2
Maximum frame rate	1,000 Hz (8 bit) / 560 Hz (16 bit)
Image / dynamic range	32-bit image depth; 16- or 8-bit readout
Detector-supported energy range	6–40 keV
Beamline operating energy range	8–25 keV
Sample-to-detector distance	~1 m (sample at 70 m, detector at ~71 m)
Maximum count-rate capability	10^7 photons/s/pixel (1.7×10^9 photons/s/mm^2)
Remarks	An active area of at least 300 mm is required to resolve reflections from unit cells larger than ~1,000 Å; data collection above 100 Hz

E Beamline Support Facility (Sample Preparation Laboratory)

To support drug-discovery research and the goal of more than 300 crystal samples per day, an on-site sample-preparation laboratory is provided within the KLS facility so that users can prepare large quantities of samples on site rather than transporting delicate, vibration-, temperature- and humidity-sensitive crystals. The laboratory is equipped with a crystallization robot for high-volume crystal production and an automated imaging device for screening crystallization conditions, together with microscopes, incubators and lab benches.

The laboratory also supports fragment-library screening: after high-throughput crystal production, fragment-compound solutions are dispensed onto crystals for soaking, enabling on-site screening of protein–compound binding. This requires an ultrasound-based acoustic dispenser for small-volume dispens-

ing and a motorized X-Y-Z device to mount large numbers of crystals onto pins, enabling collection of a large number of crystals per hour and immediate analysis with the beamline's high-throughput screening system.

References

[1] Hyungseok Choi and Jongha Park. Beamline Photon Source Analysis Report. Internal Document PAL-INT/ME-2026-007. Pohang Accelerator Laboratory, July 2026.

[2] Jongha Park et al. High Heat Load Front-End Mechanical Design and Thermal Analysis Report. Internal Document PAL-INT/ME-2026-003. Pohang Accelerator Laboratory, June 2026.

4.2.6 Real-Time X-ray Absorption Fine Structure (ID23)

The Real-Time XAFS (ID23) beamline is a dedicated hard X-ray spectroscopy beamline of the KLS, designed for the *in-situ*/*operando* analysis of functional energy materials such as batteries and catalysts. Based on the IVU24 source and a fast direct-drive double-crystal monochromator, it covers the 4–30 keV energy range and provides two experimental modes: a fast XAFS acquisition mode and a high-resolution hard X-ray spectroscopy mode. This section describes the ID23-specific design of the photon source, the front-end, the beamline optics (overall optical layout, the M1 high-heat-load mirror, the direct-drive double-crystal monochromator, the toroidal focusing mirror, the harmonic rejection mirrors, the beam conditions at the sample, the heat load, and the beam diagnostics), the photon transfer line (PTL), and the end-station. Material that is common to all KLS beamlines is cited to the separate Common Technical Sections documents.

4.2.6.1 Target Purpose and Objective

Real-Time XAFS beamline is a dedicated hard X-ray spectroscopy beamline for the *in-situ*/*operando* analysis of materials. As one of the most versatile techniques, X-ray absorption fine structure (XAFS) provides key insights into the element-specific electronic structure and local atomic structure of diverse materials, regardless of crystallinity, concentration, and/or sample environments. Such capabilities find applications in diverse fields, such as physics, chemistry, materials science, bioscience, energy science, environmental science, geoscience, glass science, metallurgy, and mineralogy. In particular, the growing interest in functional energy materials calls for XAFS studies of chemical and structural changes in catalysts, solar cells, and batteries under *in-situ*/*operando* conditions.

The primary mission of the ID23 Real-Time XAFS beamline includes, but is not limited to, the exploration of the real-time electrochemical evolution of batteries and catalysts under *in-situ*/*operando* conditions. The Real-Time XAFS beamline provides an optimized energy range of 4–30 keV, covering the K-edges of 3d/4d-transition metals and several other critical elements for energy materials (i.e., from $Z = 20$ (Ca) to $Z = 50$ (Sn)) and L-edges of 5d-transition metals and other lanthanides (i.e., from $Z = 51$ (Sb) toward the end of the periodic table). Several key techniques of ID23 Real-Time XAFS beamline include the fast XAFS acquisition via direct-drive double-crystal monochromator (DD-DCM), also known as high-dynamic double-crystal monochromator, and diverse XAFS detection schemes:

ion chambers, passivated implanted planar silicon (PIPS) detectors, silicon drift detectors (SDD), and crystal analyzer spectrometers.

First, the DD-DCM utilizes a direct-drive torque motor for Bragg axis rotation to enable continuous energy scans, with exceptional energy scan speeds (i.e., several hundred eV per second; ~4°/s) relative to the conventional DCMs. Multi-axis motion enables the fixed-exit operation of the DD-DCM, during fast energy scans, which is a key difference from a much faster quick-XAFS with a channel-cut DCM. Efforts to synchronize the undulator gap scans with the DD-DCM energy scan would enable the tracking of the electrochemical dynamics of energy materials in several tens of seconds. Second, in addition to the conventional transmission and fluorescence detection schemes for the XAFS analysis, recent progress in high-energy-resolution fluorescence detection (HERFD) using crystal analyzers can improve spectral selectivity and suppress background, enabling studies of extremely dilute elements (e.g., trace dopant elements) in catalyst or battery materials. Moreover, HERFD-XAFS analysis further reduces the intrinsic core-hole lifetime broadening effects, thereby providing opportunities to identify the transient phases and/or reveal the minor electronic/structural modifications during the electrochemical dynamics.

Based on the primary techniques, the ID23 Real-Time XAFS beamline provides two dedicated experimental modes: a fast XAFS acquisition mode with a sub-mm scale beam, enabling the tracking of the chemical dynamics of the materials, and a high-energy-resolution detection XAFS acquisition mode with a focused beam (~50 μm), probing the electronic evolution and structural configuration of the dilute systems. Both experimental techniques will be designed to be fully compatible with the *in-situ*/*operando* sample environments (e.g., electrochemical cells, gas-environment reactors, or heating/cooling stages). Finally, crystal analyzer systems of the Real-Time XAFS beamline will enable non-resonant and resonant X-ray emission spectroscopy (XES and RXES) as auxiliary experimental techniques, providing opportunities to explore the evolution of spin-states and ligand-species under *in-situ*/*operando* conditions.

4.2.6.2 Photon Source

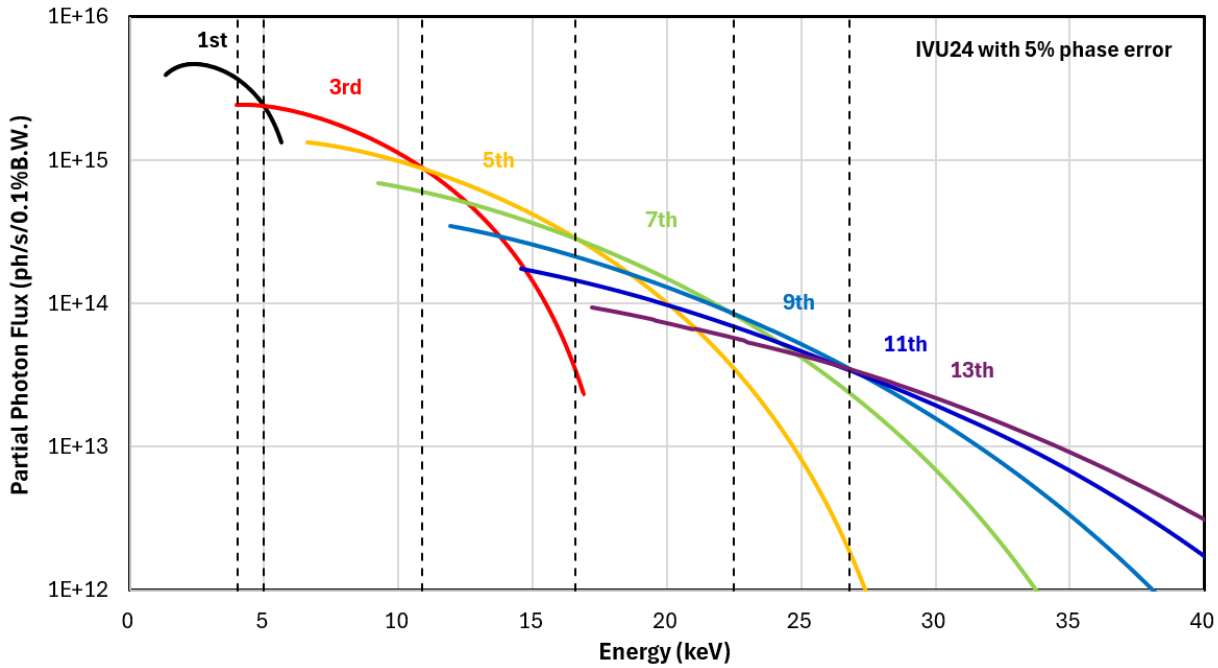
The photon source for ID23 Real-Time XAFS beamline is IVU24 with a 24 mm magnetic period and a 3.0 m device length. IVU24 exhibits no major energy discontinuities in the tuning curves, making it suitable for spectroscopy beamlines. The common insertion-device designs are described in the Common Technical Sections. Below, ID23-specific undulator features are briefly summarized (see

table 4.2.6.1). Figure 4.2.6.1 shows the partial flux curves at the 1.2 × 1.2 mm² aperture at ~27 m for the IVU24, with an assumption of the potential phase error of ~5%. In order to cover the total energy range of 4–30 keV, Real-Time XAFS beamline should access the 11th (or 13th) undulator harmonics. Vertical dashed lines at ~5, 10.9, 16.6, 22.5, 26.8 keV show the energy values where higher undulator harmonics provide better photon fluxes. The mechanical design of IVU24 provides the accessible minimum undulator gap of ~5 mm (K_{max} ~ 2.75) [1]; nevertheless, the effective minimum gap for the Real-Time XAFS beamline will be ~5.62 mm ($K_{max,eff}$ ~ 2.45) for the Ti K-edge (~4.966 keV) EXAFS collection from ~4.766 keV with the 3rd undulator harmonics. Otherwise, a minimum gap far above ~6 mm would be suitable for other undulator harmonics to provide continuous energy ranges. Given the storage ring current of ~400 mA and an effective maximum deflection parameter of ~2.45, the total power generated by the undulator source will be ~14.41 kW and the partial power at the 2 × 2 mm² mask at ~23 m will be ~1.05 kW.

<Table 4.2.6.1> IVU24 source parameters. Values are quoted at the effective minimum gap of ~5.62 mm and a storage-ring current of ~400 mA; the mechanical minimum gap is ~5 mm (K_{max} ~ 2.75). The maximum power at the front-end mask is the partial power transmitted by the 2 × 2 mm² mask at ~23 m.

Undulator	**Period (mm)**	**Length (m)**	**Gap size (mm)**	K_{max}	**Max total power (kW)**	**Max. power at FE mask (kW)**
IVU24	24	3.0	5.62	2.45	14.41	1.05

Below, we briefly discuss the features of wiggler sources at low-emittance storage rings, where spatial intensity distribution from wiggler sources becomes inhomogeneous and varies with energy. Such characteristics pose significant challenges to obtaining high-resolution EXAFS signals. Given the substantial efforts to deal with the inhomogeneous source profile and fierce heat loads from the wiggler source, ID23 Real-Time XAFS beamline will adopt the undulator as the photon source. A major drawback of the undulator arises from the relatively narrow bandwidth (e.g., ~100–150 eV), which necessitates the undulator gap scans to access the full EXAFS ranges and limits the accessible time scale via quick-XAFS techniques. Tapering the undulator magnet array would increase the bandwidth; nevertheless, significant loss in the photon flux and spatial non-uniformity pose a challenge to performing high-resolution EXAFS. ID23 Real-Time XAFS beamline, therefore, will adopt the synchronization of undulator gap scan and DCM energy scan to maximize the available flux and to provide a stable spatial beam profile.



<Figure 4.2.6.1> Partial photon flux of IVU24 undulator at the 1.2 × 1.2 mm^2 aperture at ~27 m from the source. Photon flux was calculated by considering the ~5% phase errors. Vertical dashed lines show the energy values where higher undulator harmonics provide better photon fluxes.

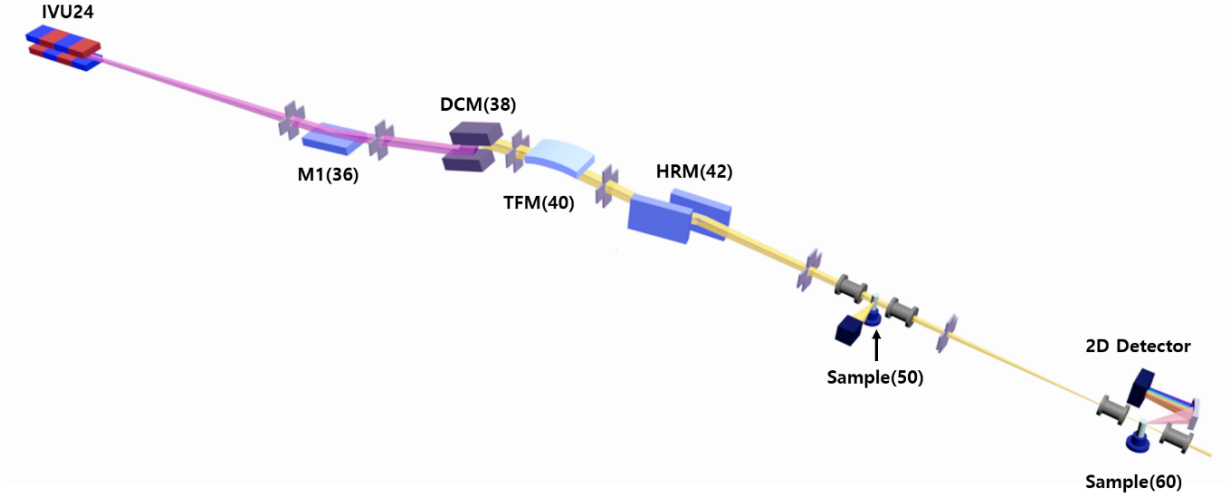
4.2.6.3 Front-End

The ID23 Real-Time XAFS beamline employs the standard IVU Front-End (FE) for hard X-ray beamlines. The common components of the FE include three-mask heat-load layout, fixed and movable masks, beam stopper, photon shutter, beam-position monitors, and 0.5 T safety magnet. Further details on the FE components are described in the Common Technical Sections and in the front-end mechanical design and thermal analysis report [2]. For the ID23 Real-Time XAFS beamline, while the FE for the standard IVU can withstand a heat load up to ~18 kW [1], IVU24 with an effective minimum gap of ~5.62 mm (i.e., extreme case for the Ti K-edge EXAFS with 3rd harmonics) produces the total heat load of ~14.41 kW, far below the heat load that can be dealt with the FE. The FE slit of 1.2 × 1.2 mm^2 at 27 m defines the angular acceptance of ~44 μrad, which has been used for the optics heat-load analysis in Section 4.2.6.4 G.

4.2.6.4 Beamline Optics

A Overall Optical Layout & Roles

Overall optical layout of the ID23 Real-Time XAFS beamline is shown in figure 4.2.6.2. The first high heat load mirror (HHLM) at 36 m vertically collimates the beam to improve the energy resolution of the double-crystal monochromator. Under extreme conditions (i.e., ~4.766 keV at $K_{\mathrm{max,eff}}$ of ~2.45), HHLM absorbs the total heat load of ~93.3 W with a peak power density of ~0.1 W/mm^2. Rh- and Pt-strips will be used for energies below and above ~23 keV, respectively, by horizontal translation of the mirror. Nominal radius for the vertical collimation corresponds to ~28.8 km at the grazing incidence angle of ~2.5 mrad, which will be achieved by the mechanical bending of the flat mirrors. Thereafter, direct-drive double-crystal monochromator at 38 m provides monochromatic X-ray toward the downstream optics. The second mirror at 40 m focuses the beam on Experimental Hutch (EH) at 60 m. A 2:1 toroidal focusing mirror (TFM), when combined with the upstream vertical collimation mirror, is known to minimize significant aberration, thereby reducing the astigmatic coma. Two toroidal mirrors with Rh- and Pt-coating will be interchangeably used to provide the reflectivity-induced glitch-free XAFS measurements over the entire energy ranges. Such scheme has been widely used at the bending magnet and wiggler beamlines. Based on the grazing incidence angle of ~2.5 mrad, tangential and sagittal radii of the toroidal mirror are ~16 km and ~66.67 mm, respectively. Because of the significant reduction in the source size, resulting focus spot size is heavily dependent on the surface quality of the mirrors. Particularly, the RMS slope error of the mirror governs the size of the vertical focus. Based on the RMS slope errors of ~0.5 μrad, ray tracing gives the final beam spot size at the focal plane at 60 m of ~50 × 50 μm^2 (H×V). Finally, a pair of harmonic rejection mirrors at 42 m and 43 m, each with three Si-/Rh-/Pt-strips, will be used to effectively minimize the 3rd harmonics from the Si(111) and Si(311) crystal monochromators. By adding separate harmonic rejection mirror pairs with variable grazing incidence angles from 2.5–8.0 mrad, HHLM and TFM could be operated without actively changing pitch angles. Monochromatic beam will be delivered to the sample positions at 50 m (experimental hutch #1: *in-situ*/*operando* chemical dynamics station) and 60 m (experimental hutch #2: high energy resolution X-ray spectroscopy station). Table 4.2.6.2 provides a summary of the beamline optics components.



<Figure 4.2.6.2> Schematic optical layout of the ID23 Real-Time XAFS beamline. The IVU24 source delivers X-ray beams to the vertical collimation HHLM (36 m), direct-drive double-crystal monochromator (38 m), toroidal focusing mirror (40 m), and a pair of harmonic rejection mirrors. Two hutches will serve distinct experimental programs, where upstream and downstream stations will be dedicated to the fast XAFS scan and high-energy resolution XAFS measurement, respectively. Component positions are given in meters from the source.

B HHLM

The HHLM at 36 m is the first optical element and the only mirror exposed to the white beam. The HHLM vertically deflects the white beam at the nominal grazing incidence angle of ~2.5 mrad. The HHLM will be mounted on the mechanical bender to vertically collimate the beam, thereby improving the energy resolution of the downstream double-crystal monochromator. At the grazing incidence angle of ~2.5 mrad, vertical collimation can be achieved at the mirror radius of ~28.8 km. Based on energy ranges, either Rh- or Pt-strips will be selected by a lateral translation for energies below and above ~23 keV, respectively. Figure 4.2.6.3 shows the mirror reflectivity for Rh- and Pt-strips at the grazing incidence angle of ~2.5 mrad. Such strip selection renders the smooth reflectivity variation over the entire energy range of 4–30 keV. A bare Si-strip would be helpful for the additional harmonic rejection; nevertheless, worst-case scenario for Si-strip leads to the significant thermal load (~200 W) of HHLM. Therefore, low-energy harmonic rejection will be performed solely by the downstream HRM pair.

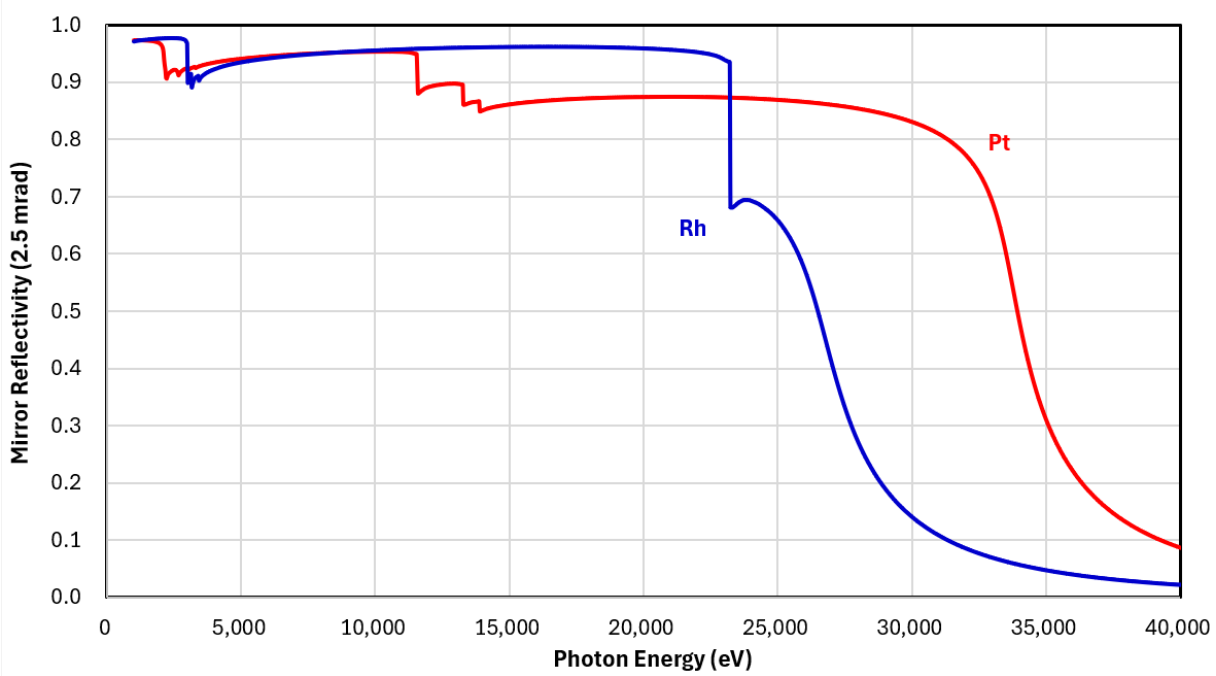
The mirror substrate (600 mm L × 50 mm W × 50 mm H, Si) will be actively

<Table 4.2.6.2> Major optical component list for the ID23 Real-Time XAFS beamline.

Distance (m)	Location	Component	Description
0	Storage ring	IVU24	Period 24 mm, length 3 m
33–35	Optical Hutch	White-beam slit / Fluorescent screen / BPM	Diagnostic modules for beam alignment
36		HHLM	Plane substrate with mechanical tangential bender, Rh-/Pt-coating strips, vertical collimation
37		Pink-beam slit / Fluorescent screen	Modules for beam alignment
38		Direct-drive DCM	Offset 15 mm, Si(111) and Si(311), LN_2 cooling
39		Mono-beam slit / Fluorescent screen / BPM	Modules for beam alignment
40		TFM	Toroidal focusing mirror with mechanical bender, Rh-/Pt-toroids with flat Si/Rh/Pt strips at the edges
41		Mono-beam slit / Fluorescent screen / BPM	Modules for beam alignment
42–43		HRM pair	Flat mirrors with Si-/Rh-/Pt-strips, variable grazing angles
44		Mono-beam slit / Fluorescent screen / BPM / Shutter	Modules for beam alignment
48	Experimental Hutch #01	Mono-beam slit / Fluorescent screen / BPM / Attenuator	Beam position feedback
50		Ionization chambers, PIPS detectors	*In-situ*/*operando* chemical dynamics station
58	Experimental Hutch #02	Mono-beam slit / Fluorescent screen / BPM	Beam position feedback
60		Ionization chambers, SDD, high-resolution spectrometer	High energy resolution X-ray spectroscopy station

water-cooled by side-cooling with indium-gallium eutectic baths, minimizing heat-induced bending of the mirrors. The surface quality of the mirror is essential for the control of vertical divergence after the HHLM. Target specifications will be slope errors of $\leq$ 0.5 µrad (tangential) and $\leq$ 5 µrad (sagittal) and a surface roughness of $\leq$ 0.2 nm RMS. At the angular acceptance of ~44 $\times$ 44 µrad^2, white beam size of ~1.45 $\times$ 1.45 mm^2 (4σ) results in the footprint of ~1.45 $\times$ 576 mm^2

on the mirror surface. Detailed specifications of the HHLM are summarized in table 4.2.6.3.



<Figure 4.2.6.3> Mirror reflectivity of the HHLM Rh- and Pt-coating strips at a grazing incidence angle of ~2.5 mrad. Strip selection maintains a smooth reflectivity variation over the entire 4–30 keV energy range (Rh- and Pt-strips used below and above ~23 keV, respectively).

<Table 4.2.6.3> Mirror specifications for the Real-Time XAFS beamline. HRM are unbent plane mirrors and therefore have infinite radii.

Parameter	HHLM	TFM	HRM pair
Installation location (m)	36	40	42/43
Reflection direction	Vertical (Up)	Vertical (Down)	Horizontal (first towards the ring, second towards the experimental hall); fixed-exit

(continued on next page)

(Table 4.2.6.3 continued)

Parameter	HHLM	TFM	HRM pair
Mirror surface shape	Plane substrate, mechanically bent to a tangential (collimating) cylinder	Toroid: substrate with pre-figured sagittal spherical curvature, mechanically bent in the tangential direction	Plane (flat, unbent)
Incident angle	2.5 mrad	2.5 mrad	2.5–8.0 mrad (variable)
Tangential radius	~28.8 km (bent)	~16 km (bent)	$>$ 100 km (plane)
Sagittal radius	$>$ 100 km (plane)	~66.67 mm	$>$ 100 km (plane)
Substrate material	Si	Si	Si
Mirror size (L $\times$ W $\times$ T)	600 $\times$ 50 $\times$ 50 mm	600 $\times$ 50 $\times$ 50 mm	600 $\times$ 50 $\times$ 50 mm
Coating material	Rh/Pt (50 nm)	Rh/Pt (50 nm)	Bare-Si/Rh/Pt (50 nm)
Coating strip number	2 (Rh, Pt)	2 (Rh, Pt)	3 (Si, Rh, Pt)
Coating stripe width	10 mm (W), per stripe	two separate toroids	10 mm (W), per stripe
Tangential slope error	$\leq$ 0.5 µrad (RMS)	$\leq$ 0.5 µrad (RMS)	$\leq$ 0.3 µrad RMS
Sagittal slope error	$\leq$ 5.0 µrad (RMS)	$\leq$ 5.0 µrad (RMS)	$\leq$ 5.0 µrad (RMS)
Roughness	$\leq$ 0.2 nm (RMS)	$\leq$ 0.2 nm (RMS)	$\leq$ 0.2 nm (RMS)
Cooling method	Side Water-Cooling	None	None
Mirror bender	Bendable	Bendable	None
Mirror surface height	1400 mm	1435 mm	1435 mm
Motor axis	Lateral translation (Rh-/Pt-strip selection)	Lateral translation (Rh-/Pt-toroid selection)	Pitch (2.5–8.0 mrad)
Manual axis (granite base)	Pitch, roll, yaw, x, z	Pitch, roll, yaw, x, z	Pitch, roll, yaw, x, z

C Double-Crystal Monochromator

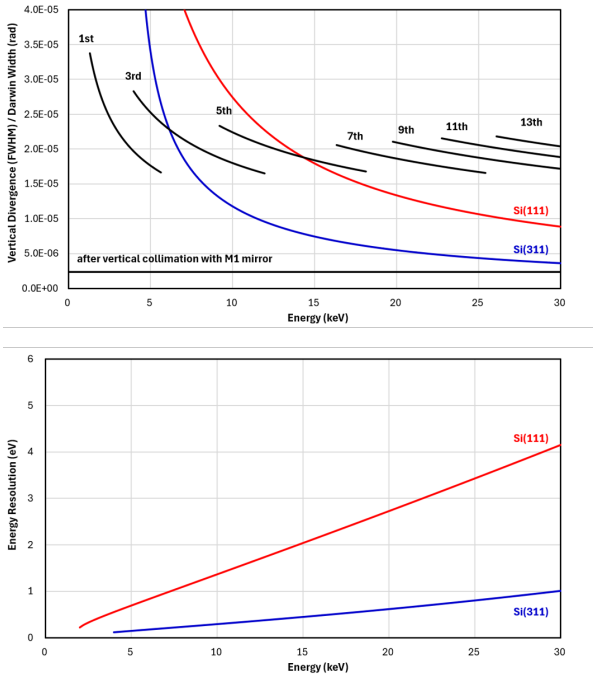
The double-crystal monochromator is the high-dynamic direct-drive DCM at 38 m, with LN_2-cooled Si(111) and Si(311) crystal pairs interchangeable by the lateral translation. The DD-DCM operates with a fixed exit with an upward vertical offset of ~15 mm. For the ID23 Real-Time XAFS beamline, vertical deflection monochromator has been chosen to access the lower energy range of ~4–5 keV.

Horizontal deflection double-crystal monochromator can provide exceptional beam stability; however, polarization effects lead to the significant reduction in the photon flux below ~5 keV. The high-dynamic DCM features the direct-drive Bragg axis motors, which replaces the worm-wheel/stepper drive of a conventional DCM. Key advantage involves the fast Bragg axis rotation up to ~4°/s, which corresponds to the ~1 keV/s energy scan capability at ~6 keV (even faster at higher energies, which will be limited by the available vertical translation of 2nd crystal for fixed-exit operation).

Two pairs of Si(111) and Si(311) crystals will be used to produce monochromatic beam at the energy range of ~4–30 keV. After the vertical collimation from the HHLM, residual vertical divergence was calculated to be ~2.33 μrad (FWHM), which partly arises from the tangential mirror slope errors of ~0.5 μrad. Figure 4.2.6.4 shows the calculated vertical divergence of the IVU24 and after vertical collimation of HHLM, together with the Darwin width of Si(111) and Si(311) crystals. Resulting energy resolutions for Si(111) and Si(311) crystals are also given below. Over the entire energy range, energy resolution is mostly controlled by the intrinsic resolution of Si(111) and Si(311) crystals of ~1.4×10^{-4} and ~3.0×10^{-5}. The Si(111) will be used for the high-flux XAFS analysis, while Si(311) crystal pairs could be used for the high energy resolution XAFS analysis or energy ranges above ~20 keV. Detailed specifications of the direct-drive DCM are summarized in <Table 4.2.6.4>.

D Toroidal Focusing Mirror

The toroidal focusing mirror (TFM) at 40 m refocuses the beam on the experimental stations. The TFM mirror vertically deflects the monochromatic beam at the nominal grazing incidence angle of ~2.5 mrad. A 2:1 toroidal focusing mirror, when combined with the upstream vertical collimation HHLM, is known to minimize significant aberration, thereby reducing the astigmatic coma. Two toroidal mirrors with Rh- and Pt-coating will be interchangeably used to provide the reflectivity-induced glitch-free XAFS measurements over the entire energy ranges. Such scheme has been widely used at the bending magnet and wiggler beamlines. Based on the grazing incidence angle of ~2.5 mrad, tangential and sagittal radii of the toroidal mirror are ~16 km and ~66.67 mm, respectively. The mirror substrate with pre-figured sagittal spherical curvatures will be mechanically bent to produce the toroidal shape. Because of the significant reduction in the source size, resulting focus spot size is heavily dependent on the surface quality of the mirrors. Target specifications will be slope errors of $\leq$ 0.5 μrad (tangential)



<Figure 4.2.6.4> Undulator vertical divergence and Darwin width of Si(111) and Si(311) crystals, together with the vertical divergence after the HHLM. Calculated energy resolution of ID23 Real-Time XAFS beamline with Si(111) and Si(311) crystals.

and $\leq$ 5 µrad (sagittal) and a surface roughness of $\leq$ 0.2 nm RMS. Particularly, the RMS slope error of the mirror governs the size of the vertical focus. Based on the RMS slope errors of ~0.5 µrad, ray tracing gives the final beam spot size at the focal plane at 60 m of ~50 $\times$ 50 µm^2 (H$\times$V). At the angular acceptance of ~44 $\times$ 44 µrad^2, incident beam size of ~1.61 $\times$ 1.30 mm^2 (4σ) results in the footprint of ~1.61 $\times$ 520 mm^2 on the mirror surface. Detailed specifications of the TFM are also summarized in table 4.2.6.3.

E Harmonic Rejection Mirrors

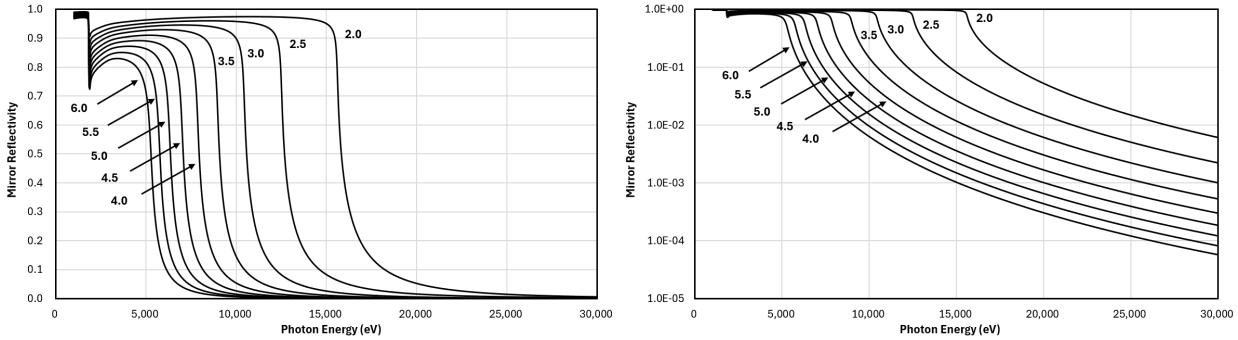
The harmonic rejection mirror pairs (HRM) at ~42, 43 m reduces the harmonic contents from Si(111) and Si(311) double-crystal monochromators. The HRM is flat mirrors (600 mm L $\times$ 50 mm W $\times$ 60 mm H, Si) with three different Si-/Rh-/Pt-coating strips. By adding separate harmonic rejection mirror pairs with variable grazing incidence angles of 2.5–8.0 mrad, ID23 Real-Time XAFS beamline can fully suppress the 3rd harmonic contamination level below ~10^{-6}, which is essential for the high-quality EXAFS measurements. Furthermore, separate harmonic rejection mirror pairs allow the operation of HHLM and TFM without actively changing

<Table 4.2.6.4> Double-crystal monochromator specifications for the Real-Time XAFS beamline.

Item	Specification
Position (m)	38
Deflection / type	Vertical, fixed-exit (upward offset); high-dynamic direct-drive DCM. 1st: Upward reflection; 2nd: Downward reflection
Photon energy range	Fully cover the entire energy range of ~4–30 keV
Crystal / optical element	Si(111) & Si(311) (two pairs, side-by-side), LN_2-cooled
Operating modes	Fixed-exit operation; Si(111) for high-flux XAFS, Si(311) for high energy resolution XAFS or > ~20 keV; crystal pairs interchanged by lateral translation
First crystal	Crystal size (L × W × H) 60 × 25 × 50 mm; upward reflection
Second crystal	Crystal size (L × W × H) 140 × 25 × 30 mm; downward reflection
Beam offset	12–34 mm (variable, upward); nominal ~15 mm
Bragg angle range	−3 to 56°
Slope error	Tangential ≤ 1 μrad (flatness, rms), both crystals
Roughness	≤ 0.5 nm RMS (≤ 5 Å), both crystals
Cooling	Indirect LN_2 (side-cooled OFHC Cu, $h \approx 7{,}000$ W/m^{2}K), both crystals
Motion axes	1st: Bragg (common), roll (Rz), manual perpendicular; 2nd: Bragg (common), perpendicular (Y), pitch (Rx), piezo fine pitch
Incident beam size (H × V, mm)	~1.55 × 1.30 (4σ), both crystals
Angular resolution	< 0.1 μrad (repeatability < 0.5 μrad)
Motor speed (°/s)	Up to 4 (min 0.001)
Pressure (mbar)	$< 5 \times 10^{-8}$ (operating)

pitch angles, which substantially reduces the efforts to align the beamline. For the energy ranges from ~12 keV to ~14 keV, Rh-strip will be mostly used with the grazing incidence angles of ~3 mrad, while above ~14 keV to ~23 keV, the grazing incidence angles will be set to ~2.5 mrad. Beyond ~23 keV, Pt-strip will be chosen with the grazing incidence angles of ~2.5 mrad. Below ~12 keV, bare Si-strip with varying incidence angles will be employed to suppress the 3rd harmonic contamination, depending on the edge energies under consideration. The mirror incidence angles could be fully optimized by tabulating the necessary angles to fully reduce the harmonic contamination level below 10^{-6}, by carefully analyzing the effect of harmonic contamination from standard materials. Figure 4.2.6.5 shows the calculated mirror reflectivity for Si-strip with varying incidence angles from 2 to 6 mrad. In order to suppress the 3rd harmonic contamination below ~10^{-6} at ~4.97 keV at Ti K-edge, grazing incidence angle of 6.0 mrad provides the harmonic suppression of ~10^{-3} at ~15 keV, thus HRM pair enable harmonic suppression of ~10^{-6} without monochromator detuning. Major drawbacks of the

steep grazing incidence angle are the reduction in the mirror reflectivity at ~4.97 keV to ~0.83, resulting in the total flux decrease to ~0.69.



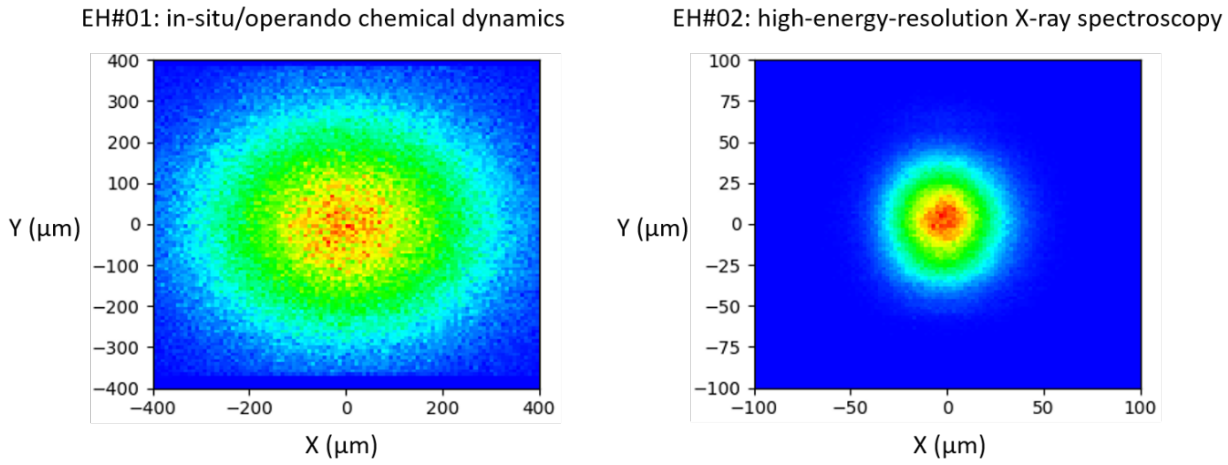
<Figure 4.2.6.5> Mirror reflectivity for Si-strip with varying incidence angles from 2 to 6 mrad.

F Beam Conditions at the Sample Positions

Both experimental stations are served by one common optical configuration. At the EH#01 (50 m), partially focused converging beam will be delivered with the ~717 (H) × 645 (V) μm^2 FWHM. A convergence half-angle of the beam below ~25 μrad is fully useful for the transmission/fluorescence XAFS and well matches to *in-situ*/*operando* studies of batteries and catalysis. At the EH#02 (60 m), TFM with a 2:1 demagnification leads to the ideal focus size of ~20 (H) × 7 (V) μm^2 FWHM; nevertheless, the effective focus size is governed by the slope error of the TFM. Based on the ~0.5 μrad tangential slope error and ~5 μrad sagittal slope error for the HHLM and TFM mirrors, together with the ~0.3 μrad tangential slope errors for HRM, focal spot size at the EH#02 results in ~50 (H) × 50 (V) μm^2 FWHM. Figure 4.2.6.6 briefly shows the simulation results of spot sizes at the experimental hutches. The total flux at the sample positions varies with energy ranges, resulting in the overall total flux of 10^{12}–10^{14} ph/s. Care should be taken on the non-linear response of ionization chambers and saturation of the fluorescence detectors under such high flux conditions. The resulting beam conditions at the two sample positions are summarized in table 4.2.6.5.

G Heat Load

The heat-load management of the Real-Time XAFS beamline is essential for vertical beam collimation and energy resolution of double-crystal monochromator. The HHLM at ~36 m partly absorbs the thermal loads, mitigating the energy resolution degradation of double-crystal monochromators upon direct incidence



<Figure 4.2.6.6> Ray-tracing results for the focal spot sizes at the EH#01 and EH#02.

<Table 4.2.6.5> Beam conditions at the sample positions of the ID23 Real-Time XAFS beamline. Both experimental stations are served by one common optical configuration (HHLM vertical collimation, DD-DCM, TFM 2:1 refocusing, HRM pair). Beam sizes are ray-tracing values including the mirror slope errors.

Configuration	**Photon energy (keV)**	**Beam size, H × V (μm, FWHM)**	**Flux (ph/s)**	**Energy resolution ($\Delta E/E$)**	**Notes**
EH#01 (50 m), Si(111), converging beam	4–30	~717 × 645	10^{12}–10^{14}	~1.4×10^{-4}	Partially focused converging beam; convergence half-angle < ~25 μrad. *In-situ/operando* chemical dynamics station (fast XAFS)
EH#02 (60 m), Si(111), TFM 2:1 focus	4–30	~50 × 50	10^{12}–10^{14}	~1.4×10^{-4}	Effective focus governed by the ~0.5 μrad tangential and ~5 μrad sagittal slope errors of HHLM/TFM and the ~0.3 μrad tangential slope error of the HRM pair
EH#02 (60 m), Si(311), TFM 2:1 focus	4–30 (typically > ~20)	~50 × 50	2.0×10^{11}–2.0×10^{13}	~3.0×10^{-5}	High energy resolution X-ray spectroscopy station; HERFD-XAFS and XES/RXES

of white beam. The heat-load simulations were performed with the OASYS SR-Calc and SRW modules. The maximum power from the IVU24 with minimum mechanical gap of ~5 mm (K = 2.75) at the 1.2 × 1.2 mm^2 aperture at 27 m is ~323.8 W. However, effective minimum gap of Real-Time XAFS beamline corresponds to ~5.62 mm ($K_{\mathrm{max,eff}}$ ~ 2.45) for the Ti K-edge (~4.966 keV) EXAFS at ~4.766 keV with 3rd undulator harmonics. Given the conservative worst-case scenario of effective

minimum gap of ~5.62 mm, maximum power at the 1.2 × 1.2 mm^2 aperture at 27 m is ~287.7 W. With the 125 μm Be filter, total power absorption by the HHLM results in ~93.3 W (< ~0.1 W/mm^2 peak power density) and ~71.7 W (< ~0.08 W/mm^2 peak power density) for Rh- and Pt-strips, respectively. Such heat loads could be effectively handled by conventional side water-cooling, while residual thermal figure errors could be further reduced by the tangential bender. Given the worst-case scenario, first crystal at ~38 m receives the total heat load of ~175.3 W and ~196.9 W for Rh- and Pt-strips for the HHLM, respectively. Peak power density at the Bragg angle of 25° (i.e., ~4.7 and ~9.0 keV for Si(111) and Si(311) crystals, respectively) results in < ~26.5 W/mm^2 and < ~30 W/mm^2 peak power density for Si crystals after the Rh- and Pt-strips of the HHLM, respectively. Such heat loads could be handled by the liquid-nitrogen cooled Si crystals, without significant thermal distortion or degradation in flux and energy resolution. Majority of the heat load is absorbed by HHLM and first Si crystal; therefore, downstream optical components are subject to the minor heat loads. Table 4.2.6.6 summarizes the results of heat load simulations for extreme cases. Under operational conditions, effective minimum gap above ~6.0 mm and moderate decrease in the incidence angle for Si crystals ensure much mild heat load demands for the HHLM and Si crystals, as can be confirmed by the total power and peak power density at ~10, 20, 30 keV with 3rd, 7th, 13th harmonics, respectively.

H Beam Diagnostics and Alignment

The diagnostic modules for beam shape, position, and intensity are critical for the clear delivery of photon beam from front-end to experimental hutch. Two photon beam position monitors (PBPM) in the front-end section identify the white-beam position from the light source, which will be used for orbit correction at the storage ring. For the PTL section, a series of white-, pink-, mono-beam screen monitors and diamond beam monitors, together with several beam-defining slits, will be installed before and after optical components, identifying and monitoring the beam shape and position changes over the PTL. The water-cooled slit and fluorescent screen upstream of the HHLM will be used to monitor the white beam at the PTL. White beam stop, monochromatic beam slits, and fluorescent screen with DBPM, downstream of the DD-DCM define the position of monochromatic beam; continuous position and intensity readings from the DBPM will further be used to provide active feedback of second crystal pitch for beam heights. Each experimental station will have beam position monitoring systems at the entrance

<Table 4.2.6.6> Heat load simulation results under diverse energy ranges. The condition columns give the undulator deflection parameter and the corresponding photon energy; $K = 2.45$ is the worst case at the effective minimum gap of ~5.62 mm, while the 10, 20 and 30 keV cases use the 3rd, 7th and 13th harmonics, respectively. Values are quoted downstream of the 125 μm Be filter, for the 1.2×1.2 mm² front-end aperture at 27 m. The DCM first-crystal peak power density of the worst case is evaluated at a Bragg angle of 25°. "–" marks a combination that is not used in operation.

Component	**Location (m)**	**Parameter**	K = **2.45 (~4.766 keV)**	K = **1.34 (~10 keV)**	K = **1.56 (~20 keV)**	K = **1.87 (~30 keV)**
HHLM (Rh strip)	36	Absorbed power (W)	93.3	19.1	25.4	–
HHLM (Rh strip)	36	Peak power density (W/mm²)	< 0.10	< 0.03	< 0.03	–
HHLM (Pt strip)	36	Absorbed power (W)	71.7	–	–	35.6
HHLM (Pt strip)	36	Peak power density (W/mm²)	< 0.08	–	–	< 0.04
DCM 1st crystal (Rh strip of HHLM)	38	Absorbed power (W)	175.3	117.8 [Si(111)]	134.8 [Si(111)]	–
DCM 1st crystal (Rh strip of HHLM)	38	Peak power density (W/mm²)	26.5	8.9	4.5	–
DCM 1st crystal (Pt strip of HHLM)	38	Absorbed power (W)	196.9	–	–	159.6 [Si(311)]
DCM 1st crystal (Pt strip of HHLM)	38	Peak power density (W/mm²)	30.0	–	–	7.4

point, providing additional channels for beam position feedback. Finally, among a series of three ionization chamber trains for EXAFS acquisition at the experimental hutches, first ionization chamber will measure the incident beam intensity for data normalization and overall monitoring of the beam delivery from PTL.

4.2.6.5 Photon Transfer Line

The photon transfer line (PTL) transfers the beam from the front-end exit to the optical hutch and two experimental hutches at ~50 m and ~60 m. The details on PTL girder, support, and vacuum systems are described in the Common Technical Sections. The PTL is sectorized by gate valves and edge-welded bellows.

A Mechanical Design

The mechanical design for the PTL is to realize the optical layout, while stabilizing the beam size, position, and intensity variations at the sample position. The optical hutch encloses five optical devices (HHLM, DD-DCM, TFM, HRMs) and several diagnostic modules in the 33–45 m ranges. Stable girders for optical devices are essential to minimize the vibrations and ensure the beam stability. Each mirror will be hosted on a granite plinth with a five-axis manipulator (i.e., translation for strip-selection, height translations, three rotations), together with the mechanical benders for the HHLM and TFM. Vacuum vessels will be fully decoupled from the optics supports. The DD-DCM will also be mounted on a granite plinth, because its dynamic performance during fast energy scan dominates the delivered beam stability; downstream diagnostic modules will be used for the closed-loop feedback of beam position by tweaking the pitch of the second crystal.

B Vacuum, Pumps and Valves

The ID23 Real-Time XAFS beamline employs vacuum system common to KLS UHV standards, described in the Common Technical Sections. Sector isolation will be provided by gate valves connected with the safety-interlock system, and a fast-closing shutter and photon shutter protect the storage ring vacuum in the event of a vacuum incident. The Be windows will be used to isolate the front-end and optical hutch (UHV) with experimental hutches (HV), while minimizing the absorption at the low-energy range of 4–5 keV.

C Hutch

The ID23 Real-Time XAFS beamline consists of three hutches: one optical hutch for white-beam and monochromatic beam optics, and two downstream experimental hutches. Experimental Hutch #01 with sample position of ~50 m will be dedicated to the fast-XAFS *in-situ*/*operando* station and Experimental Hutch #02 with sample position of ~60 m will provide the high-energy resolution XAFS measurements. Gas loading systems with multi-channel supply of H_2, O_2, N_2,

CO_2 and safety monitoring system and gas exhaust will be installed to serve two experimental stations. All hutches will be located in the storage-ring experimental hall with a standard hutch configuration. Radiation shielding, exhaust, power, and support facilities (LCW, compressed air, LN_2 for DCM cryocooler) follow the common site-infrastructure standard.

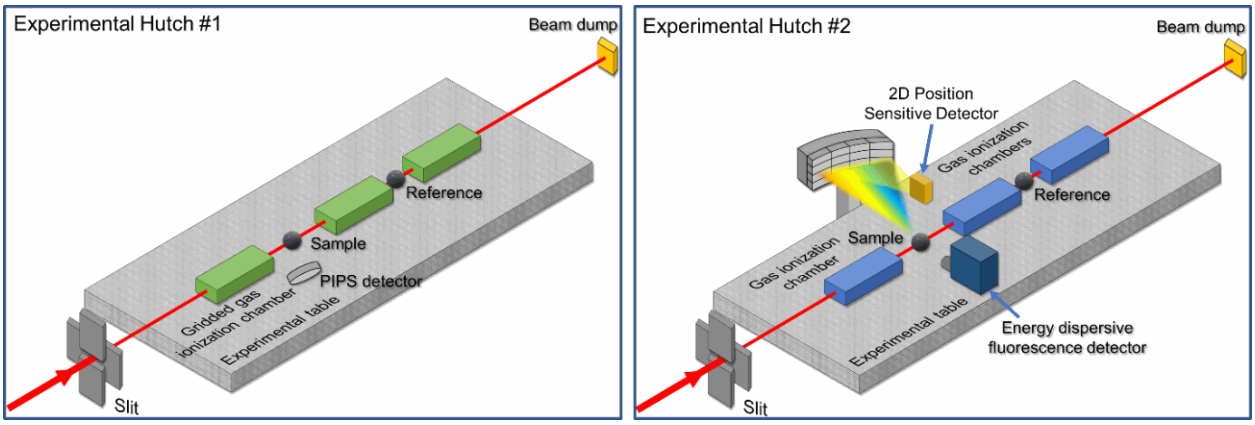
4.2.6.6 End-Station

A Mechanical Design

The ID23 Real-Time XAFS beamline provides two end-stations with distinct features: Experimental Hutch #01 with the *in-situ*/*operando* chemical dynamics program and Experimental Hutch #02 with the high energy resolution X-ray spectroscopy program. Figure 4.2.6.7 shows the schematic overview of the end-stations, where the first experimental hutch mostly focuses on the rapid acquisition of the XAFS spectrum, by using the direct-drive DCM. EH #01 will be built on the stable optical table with a series of gas ionization chambers for I_0, I_t, I_r measurements. PIPS detectors will be used to collect the X-ray fluorescence signal (I_f). The kinematic sample mounts between I_0 and I_t would allow the reproducible exchange of the powder sample or *in-situ*/*operando* cells within a minute. A high-throughput sample holder for a series of standard powder pellets with an automatic sample wheel will support the screening campaigns. The *in-situ*/*operando* sample-environment pool comprises electrochemical/battery cells, a heating stage to 1200 °C with controlled gas environments, a cryogenic stage to liquid-nitrogen temperature, and capillary flow cells for thermo-catalysis. Finally, a gas supplier system with several channels for various gases, such as hydrogen, oxygen, nitrogen, and/or carbon dioxide, will be installed to provide flexible gas controls for *in-situ*/*operando* experiments.

EH #02 provides the X-ray with focal size of ~50 × 50 μm² (H×V) and will be installed on the stable granite slab to minimize the effect of vibrations. A series of gas ionization chambers for I_0, I_t, I_r measurements and energy-dispersive silicon drift detectors will be installed on the mounts to provide standard transmission and fluorescence detection modes. In addition, von Hamos spectrometer with cylindrically bent crystal analyzers and 2D position-sensitive pixel detectors will be used for the X-ray emission spectroscopy. Currently, we consider the von Hamos spectrometer with 16 segmented cylindrically bent crystal analyzers with pitch and yaw adjustments and translations for each crystal. Future upgrade involves the installation of Johann type spectrometer (i.e., Rowland geometry) with spherically bent crystal analyzers with varying bending radius of ~0.5 m and ~1.0 m. Multi-

crystal analyzer mount will be installed on the customized horizontal 2θ arm with the translation stages with long travel distances to move the crystal analyzer mounts. High precision sample stages with three-axis translations and rotation will be installed for the alignment of the sample and *in-situ*/*operando* cells. The instrument specifications of the two experimental hutches are summarized in table 4.2.6.7.



<Figure 4.2.6.7> Schematic overview of the end-stations for ID23 Real-Time XAFS beamline. Upstream experimental hutch (EH #1) will be dedicated to the fast XAFS scan, where a series of gas ionization chambers and passivated implanted planar silicon (PIPS) detectors will be used for transmission and fluorescence modes of XAFS measurements. Downstream experimental hutch (EH #2) will provide the high-energy resolution X-ray spectroscopy capabilities, with a series of gas ionization chambers, multi-element silicon drift detectors, and von Hamos spectrometer enable the collection of XAFS signals from extremely dilute elements. The von Hamos spectrometer would also allow the collection of (non-) resonant X-ray emission spectrum. Diverse *in-situ*/*operando* sample environments, such as electrochemical cells, heating stage with controllable gas environments, and capillary cells, will be available for experimental hutches.

B Detector, Data Acquisition, Computing and Software

Transmission detection uses three gas ionization chamber train (I_0, I_t, I_r), with reference foils providing an internal energy calibration. Fluorescence detection uses either PIPS diodes for high-rate total fluorescence yields or multi-element silicon-drift detectors with digital pulse processors for energy-dispersive partial fluorescence yield for dilute samples. High-resolution fluorescence detection at EH #02 employs a multi-crystal-analyzer spectrometer in von Hamos geometry, accommodating up to 16 (4×4) segmented cylindrically bent analyzer crystals (e.g., Si(100), Si(111), Si(220), Si(311), Si(331)), covering emission energies of ~5–20

<Table 4.2.6.7> End-station instrument specifications for the two experimental hutches of the ID23 Real-Time XAFS beamline.

Parameter	Specification
Experimental Hutch #01: *in-situ*/*operando* chemical dynamics station	
Sample position (m)	50
Instrument support	Stable optical table
Transmission detection	Gas ionization chamber train (I_0, I_t, I_r)
Fluorescence detection	PIPS detectors (total fluorescence yield, I_f)
Sample mount	Kinematic mounts between I_0 and I_t; reproducible exchange of powder samples or *in-situ*/*operando* cells
High-throughput holder	Automatic sample wheel for a series of standard powder pellets
Sample environments	Electrochemical/battery cells; heating stage to 1200 °C with controlled gas environments; cryogenic stage to liquid-nitrogen temperature; capillary flow cells for thermo-catalysis
Gas supply	Multi-channel gas supplier (e.g., H_2, O_2, N_2, CO_2) for flexible gas control in *in-situ*/*operando* experiments
Experimental Hutch #02: high energy resolution X-ray spectroscopy station	
Sample position (m)	60
Instrument support	Stable granite slab (vibration isolation)
Transmission detection	Gas ionization chamber train (I_0, I_t, I_r)
Fluorescence detection	Energy-dispersive multi-element silicon drift detectors
High-resolution spectrometer	von Hamos geometry with cylindrically bent crystal analyzers; up to 16 (4×4) segmented analyzers with per-crystal pitch, yaw and translation adjustment
Analyzer crystals	Si(100), Si(111), Si(220), Si(311), Si(331)
Emission energy range (keV)	~5–20
Emission energy resolution (eV)	0.5–2.0
Analyzer mount	Customized horizontal 2θ arm with long-travel translation stages
Sample stage	High-precision three-axis translation and rotation
Area detector	2D position-sensitive pixel detector for HERFD-XAFS, XES and RXES
Future upgrade	Johann-type spectrometer (Rowland geometry) with spherically bent crystal analyzers of ~0.5 m and ~1.0 m bending radius

keV with 0.5–2.0 eV resolution. The HERFD-XAFS, XES, and RXES techniques will collect the signals from a 2D position-sensitive detector, combined with the von Hamos spectrometer. Future upgrades with the implementation of Johann type spectrometer (Rowland geometry) require additional energy-dispersive silicon drift detectors and/or 2D position-sensitive detectors, where SDD provides exceptional background rejection, suitable for extremely dilute systems, and 2D pixel

detector provides an opportunity to improve the energy resolution by the removal of geometrical aberrations from the spherical crystal analyzers. Finally, additional 2D pixel detectors would be helpful for the multi-modal analysis of energy materials by combining XAFS and XRD techniques. The detector complement of the ID23 Real-Time XAFS beamline is summarized in table 4.2.6.8.

<Table 4.2.6.8> Detector complement of the ID23 Real-Time XAFS beamline. "N/A" marks a quantity that does not apply to the detector type.

Parameter	**Ionization chambers**	**PIPS detectors**	**Silicon drift detectors**	**von Hamos spectrometer**
Role / technique	Transmission XAFS (I_0, I_t, I_r); normalization and internal energy calibration	Total fluorescence yield XAFS at high count rate	Energy-dispersive partial fluorescence yield XAFS for dilute samples	HERFD-XAFS, XES and RXES
Detector type / detection principle	Gas ionization chamber, three-chamber train with reference foils	Passivated implanted planar silicon diode	Multi-element silicon drift detector with digital pulse processors	Multi-crystal-analyzer spectrometer in von Hamos geometry with 2D position-sensitive pixel detector
Sensor material / thickness	Ionization gas	Silicon	Silicon (drift)	Cylindrically bent Si analyzer crystals: Si(100), Si(111), Si(220), Si(311), Si(331); pixel-detector sensor material Si
Pixel format / channels	N/A	N/A	N/A	75 µm
Applicable energy range	4–30 keV (incident)	4–30 keV	4–30 keV	~5–20 keV (emission), 0.5–2.0 eV resolution
Remarks	EH#01 and EH#02	EH#01	EH#02	EH#02; future upgrade to Johann spectrometer with ~0.5 m and ~1.0 m bending radii

Meanwhile, on-the-fly energy scan necessitates a synchronization of undulator gap, Bragg axis of double-crystal monochromator, and detection channels (e.g., ionization chamber readings, fluorescence detector (PIPS/SDD) readings). DAQ structure should ensure the continuous reading of every encoder value from undulator and double-crystal monochromators and detector counts. Time-stamp for each reading will be used to classify, bin, and produce the energy values and detector counts for the XAFS spectra with the on-the-fly energy scan scheme. Software-level orchestration alone may not be able to reach the fast XAFS on-the-

fly scan regime; hardware-level triggering and time-stamping by FPGA will be essential for the on-the-fly energy scan. At the ID23 Real-Time XAFS beamline, data rates will be rather modest, compared to the modern imaging beamlines.

References

[1] Hyungseok Choi and Jongha Park. Beamline Photon Source Analysis Report. Internal Document PAL-INT/ME-2026-007. Pohang Accelerator Laboratory, July 2026.

[2] Jongha Park et al. High Heat Load Front-End Mechanical Design and Thermal Analysis Report. Internal Document PAL-INT/ME-2026-003. Pohang Accelerator Laboratory, June 2026.

4.2.7 Material Structure Analysis (ID24)

The ID24 Material Structure Analysis (MSA) beamline is a powder X-ray diffraction (XRD) beamline of the KLS dedicated to high-resolution structure analysis and fast *in-situ* measurements. This section states the target purpose and objective of ID24 and describes the ID24-specific design of the photon source, the front-end, the beamline optics (overall optical layout, optics parameters and mechanism performance, the double-crystal monochromator, beam conditions at the sample, heat load, and beam diagnostics), the photon transfer line (PTL: mechanical design, vacuum, and hutch), and the end-station (mechanical design, detector, and sample environments). Design elements common to all KLS beamlines are described in the beamline engineering sections (sections 3.1 to 3.6) and are only referred to here. Performance figures in this section are either design values or theoretical values calculated from the design parameters; the calculation basis is stated where the values are given.

4.2.7.1 Target Purpose and Objective

The ID24 MSA beamline delivers high-resolution, high-throughput powder X-ray diffraction; its operating energy range is 17–45 keV, and it is optimized at a fixed energy of 33 keV. Exploiting the high brilliance and low divergence of the KLS source, the beamline provides two dedicated sample stages: a Multi-Analyzer Crystal (MAC)-based high-resolution diffractometer designed for an angular resolution better than 0.01° at 33 keV while reducing the acquisition time from hours to the order of minutes for detailed crystallographic analysis, and a two-dimensional-detector-based optical-table stage (angular resolution $\approx 0.05°$) that further shortens the acquisition time to the order of seconds for *in-situ* measurements. Operation at high energy widens the accessible d-spacing range within a fixed 2θ window, and the high penetrating power of hard X-rays through sample-environment windows and gas atmospheres enables *in-situ*, synthesis, and operating-condition studies.

Battery electrodes, catalysts, ceramics, and pharmaceutical solids are synthesized, processed, and used as polycrystalline materials, so powder diffraction is the principal method by which their crystal structures are determined. At present, precise structure refinement and fast *in-situ* observation are generally obtained on different instruments and seldom on the same sample under the same conditions. ID24 is therefore designed as an industry-priority beamline that delivers quantitative high-resolution structure determination and fast *in-situ* measurement on a

single beamline.

The primary experimental method is high-resolution powder diffraction (HRPD) for the crystallographic analysis of polycrystalline materials, complemented by *in-situ* diffraction under temperature, gas, and electrochemical control. The scientific objectives focus on energy and environmental materials, phase-transition studies, and the quantitative structural analysis of complex functional materials in realistic operating environments. As an industry-priority beamline, ID24 is designed for a multi-sample, high-throughput configuration with automation and high-speed DAQ to meet the industrial demand for analyzing large numbers of samples.

Powder-diffraction beamlines at synchrotron facilities worldwide are increasingly extending their scope toward materials under extreme pressure and temperature, *in-situ* and *operando* studies of rechargeable-battery and energy materials, spatially resolved studies of heterogeneous samples, and, at higher photon energies, total scattering of amorphous and poorly crystalline materials; they also seek to measure the same sample with several complementary techniques. ID24 is designed to remain scalable to such developments in measurement technique and detector technology.

4.2.7.2 Photon Source

The photon source for the ID24 MSA beamline is an In-Vacuum Undulator (IVU16). The insertion devices of the Phase-I beamlines are listed in table 4.1.4.1, and the design basis of the KLS IVU set including the IVU16 (period and gap optimization, K-value, brilliance and power analyses) is given in the photon source analysis report [1]; only the ID24-specific basics are stated here. The undulator has a magnetic period of 16 mm, a total device length of 3.0 m (185 periods), and is installed at the center of the straight section. Owing to its short period, the IVU16 reaches high photon energies through its low-order odd harmonics.

The beamline is optimized for operation at the energy of 33 keV, accessed as the 5th harmonic at a magnetic gap of 5.89 mm (K = 0.94). This high-energy operation broadens the accessible d-spacing range for high-throughput powder diffraction, while a single operating energy supports spectral and mechanical stability. The operating energy range of the beamline is 17–45 keV, and the possibility of extending it toward higher energies is considered in the design (Section 4.2.7.4 C). The source parameters given in this subsection are theoretical values calculated with

SPECTRA for the KLS storage ring (4 GeV, 400 mA), including the electron-energy spread: at 33 keV the source size is 41.2 × 9.14 μm and the divergence 15.0 × 13.9 μrad (H × V, full width at half maximum, FWHM).

Although the undulator can reach a minimum magnetic gap of 5 mm for peak performance, the 33 keV operating point corresponds to a 5.89 mm gap. Under the maximum stored current of 400 mA, the total radiated power is 7.38 kW at the 5 mm minimum gap [1] and 4.71 kW at the operating gap; the power passing through the movable mask (2 × 2 mm^2, the aperture assumed in this calculation) at 23 m from the source is 1.07 kW at the minimum gap and 0.83 kW at the operating gap. The ID24-specific source parameters are summarized in table 4.2.7.1.

<Table 4.2.7.1> Insertion-device source parameters at the minimum (5.0 mm) and 33 keV operating (5.89 mm) gaps, at 400 mA.

Undulator	**Gap size (mm)**	K	**Total power (kW)**	**Power through movable mask (2 × 2 mm^2) at 23 m (kW)**
IVU16	5.0	1.172	7.38	1.07
IVU16	5.89	0.94	4.71	0.83

4.2.7.3 Front-End

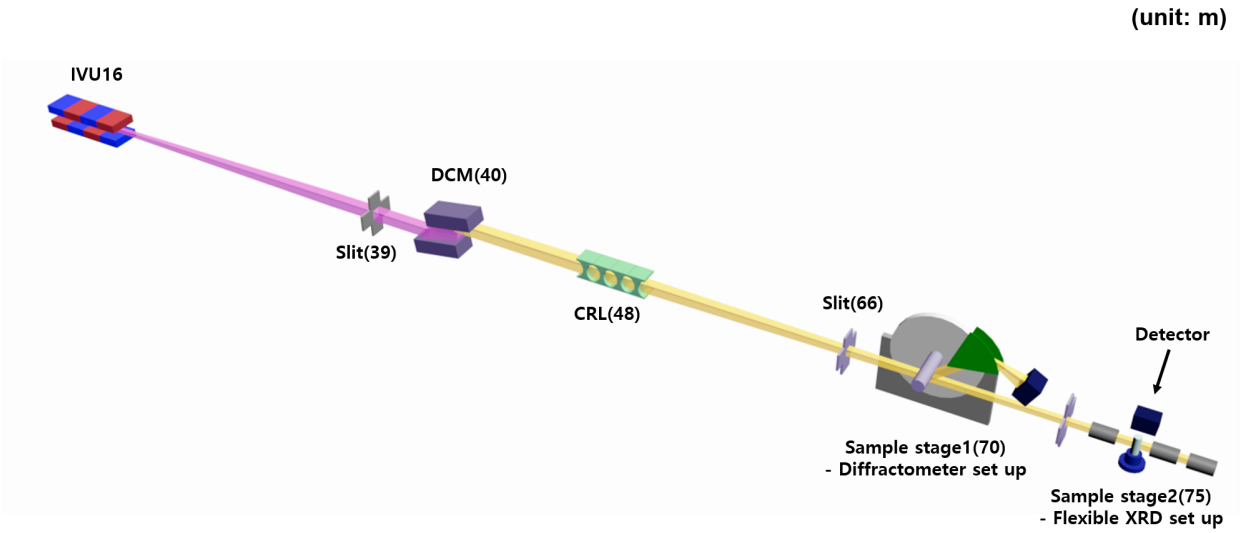
The ID24 MSA beamline adopts the standardized KLS IVU Front-End (FE). The common FE design basis (three-mask heat-load layout, fixed and movable masks, beam stopper, photon shutter, beam-position diagnostics, and the safety magnet) is described in section 3.1; the mechanical design and thermal analysis of the masks, beam stopper, and shutters are given in the high-heat-load front-end report [2]. Only the ID24-specific values that form the basis for the downstream optics are stated here.

The FE is rated for the standard 18 kW heat load defined for the IVU24 reference device [1, 2]. The IVU16 produces a total power of 7.38 kW at the mechanical minimum gap of 5 mm and 4.71 kW at the 33 keV operating gap (5.89 mm); both remain well below the 18 kW rating, confirming that the standardized IVU24-based front-end accommodates the ID24 heat load with substantial margin. The FE photon-beam position monitor detects drift or misalignment of the beam, and the safety magnet deflects any electron beam entering the FE away from the optical hutch. The photon-beam input to the downstream optics is defined by a 1.5 × 1.5 mm^2 white-beam slit at 39 m (38.5 μrad) [3]. The white-beam power transmitted through this slit is 0.22 kW at the minimum gap and 0.17 kW at the operating gap,

forming the heat-load input for the optics analysis in Section 4.2.7.4 E.

4.2.7.4 Beamline Optics

This subsection consolidates the optics design of the ID24 MSA beamline at the nominal operating energy of 33 keV. The beam sizes and divergences at the sample were calculated by Gaussian phase-space propagation of the SPECTRA source of section 4.2.7.2 through the transfocator, including lens absorption and diffraction; they are theoretical values for nominal lens radii and alignment, and the measured values may be larger. The heat load on the monochromator was computed with SRCalc in the OASYS environment.



<Figure 4.2.7.1> Schematic of the ID24 MSA beamline: IVU16 source, DCM (40 m), CRL transfocator (48 m), and the two sample stages (70 m, 75 m); white beam upstream of the DCM, monochromatic downstream.

A Overall optical layout and component roles

The optical layout of the beamline is shown in figure 4.2.7.1, with the component sequence, distances, and roles listed in table 4.2.7.2. The white beam from the IVU16 source passes the shielding wall at 25.4 m into the optical hutch, where it is defined by a white-beam slit at 39 m [3]. The double-crystal monochromator (DCM) at 40 m selects the operating energy, and a single transfocator housing compound refractive lenses (CRL) at about 48 m, optimized for 33 keV, collimates or focuses the beam to the two sample stages: the high-resolution diffractometer at 70 m and

the optical-table stage at 75 m. A monochromatic-beam slit at 66 m conditions the beam entering the experimental hutch, and a second at 74 m conditions the beam incident on the 75 m stage; both block parasitic scattering. Beam-diagnostic screen monitors are placed before and after each major optical element. The detailed optics parameters, the monochromator, the beam conditions at the sample, the heat load, and the beam diagnostics are described below.

<Table 4.2.7.2> Component-by-component layout of the ID24 MSA beamline, in beam order (distances from the source).

Distance (m)	Location	Component	Description
0	Front-End	IVU16	Period 16 mm, length 3.0 m
25.4		Shielding wall	Optical-hutch entrance
39	Optical Hutch	White-beam slit	1.5×1.5 mm^2
39.5		Diamond screen monitor	~1 μm resolution
40		DCM	33 keV, vertical deflection, offset 10 mm, Si(111) double crystal / Si(311) channel-cut
46.5		Diamond screen monitor	~1 μm resolution
48		CRL transfocator	Single-crystal diamond; collimation and focusing (1D and 2D); positioned along the beam per mode (48.2–48.7 m)
49.5		Scintillator screen monitor	Removable
66	Photon Transfer Line	Monochromatic-beam slit	Beam conditioning at the entrance to the experimental hutch
68		Scintillator screen monitor	Removable
69	Experimental Hutch	Ionization chamber	I_0 monitor
70		Diffractometer	High-resolution powder diffraction
74		Monochromatic-beam slit	Beam conditioning for the 75 m stage
75		Optical table	Flexible *in-situ* XRD

B Optics parameters and mechanism performance

The ID24 MSA beamline employs no focusing or collimating mirror. The low divergence of the 33 keV beam permits direct delivery to the sample, and all beam conditioning (collimation and focusing) is provided by a single CRL transfocator located downstream of the DCM at about 48 m. Because the refractive index of the lens material is energy-dependent, the transfocator is optimized for the 33

keV operating energy: the DCM (Section 4.2.7.4 C) selects the energy, while the transfocator sets the beam size and divergence at the sample.

The lenses are single-crystal diamond, selected for its radiation hardness and high thermal conductivity. Eight arms of the transfocator each carry an independent lens stack that is inserted into or withdrawn from the beam: a focusing pair for each of the 70 m and 75 m stages and two collimation pairs, the second being a spare because the collimated beam is expected to be the most frequently used. Each pair consists of a one-dimensional vertical (1D-V) arm, which acts on the vertical plane only, and a two-dimensional (2D) arm, which acts on both planes; the focusing pairs therefore give either a vertical line focus or a point focus at each sample position. The parameters of the arms are listed in table 4.2.7.3.

<Table 4.2.7.3> CRL transfocator arm parameters at 33 keV.

Arm	Function	Lens configuration	N	f (m)	Lens position (m)
1	Collimation, 1D-V	1×R300 + 6×R500	7	48.71	48.71
2	Collimation, 2D	1×R300 + 6×R500	7	48.71	48.71
3	Focusing at 70 m, 1D-V	15×R300	15	14.94	48.40
4	Focusing at 70 m, 2D	15×R300	15	14.94	48.40
5	Focusing at 75 m, 1D-V	13×R300	13	17.24	48.17
6	Focusing at 75 m, 2D	13×R300	13	17.24	48.17
7, 8	Spare collimation (1D-V, 2D)	As arms 1, 2	7	48.71	48.71

Rn: apex radius of curvature (μm); N: lens count; f: focal length; lens position: distance from the source at which the arm is used. The resulting beam conditions at the sample are given in table 4.2.7.6.

In the 1D-V arms the horizontal plane is unfocused and retains the natural beam (about 1054 μm at the 70 m stage), so the horizontal entry in table 4.2.7.6 is the natural beam rather than a focus. Including lens absorption, the transmission is 54–76% in the focusing arms and 73–86% in the collimation arms (table 4.2.7.6). The focal spot is dominated by the geometric demagnification of the source; the diffraction limit (~0.3 μm) is negligible at the resulting spot sizes. The theoretical vertical spot is 4.1 μm at the 70 m stage and 5.1 μm at the 75 m stage, set by the demagnified vertical source size; the DCM does not reduce the vertical divergence of the undulator beam, because each part of the vertical fan is reflected at its own energy within the bandwidth.

By inserting or withdrawing arms, the transfocator provides three operating modes at the sample: a natural (lens-out) mode with a beam of 1054 × 974 μm at the

70 m stage (table 4.2.7.6); a collimation mode that reduces the vertical divergence to 0.19 μrad (arm 1) or both divergences to 0.85 × 0.19 μrad with a beam of 656 × 616 μm (arm 2); and a focusing mode that focuses the beam vertically to 4.1 μm at the 70 m stage (arms 3, 4) or 5.1 μm at the 75 m stage (arms 5, 6), with point foci of 18 × 4.1 μm and 23 × 5.1 μm from the 2D arms (theoretical values). Each mode places its lens stack at a different distance from the source (48.17 m for the 75 m focus, 48.40 m for the 70 m focus, and 48.71 m for collimation), and the effective source point within the 3 m undulator and the lens-radius tolerance shift these positions by amounts of the same order; the depth of focus is only about ±0.17 m. The transfocator is therefore moved along the beam to set each mode, and its support requires sufficient longitudinal travel, forward and backward of the nominal position, to cover these positions and their tolerances; with the transfocator fixed at 48.0 m the 70 m vertical focus would grow to 8.6 μm. Minimizing the change in lens position between modes, and thus the longitudinal alignment travel, requires optimization of the lens radii of curvature for each stack. Because the transfocator operates on the monochromatic beam downstream of the DCM, the absorbed power is low and no active cooling of the lens stack is required (see the heat-load analysis in Section 4.2.7.4 E).

The mechanical layout follows from the requirement to insert variable lens stacks into the beam while preserving the lens-to-lens alignment within each arm. Each lens stack is held in a V-groove cassette (straightness < 2 μm), which fixes the intra-arm alignment without per-lens adjustment. The transfocator is carried on a granite-based support stage, which aligns the whole device to the beam with four axes: lateral (X) and vertical (Y) translation, yaw, and pitch. In addition, a translation along the beam (Z) is required to set the lens position for each operating mode, as described above. The travel ranges are listed in table 4.2.7.4.

<Table 4.2.7.4> CRL transfocator support-stage motions (design values).

Axis	**Type**	**Travel**
Lateral (X)	Linear	± 15 mm
Vertical (Y)	Linear	± 15 mm
Longitudinal (Z)	Linear	Sufficient travel forward and backward of the nominal position to cover the arm positions (48.17–48.71 m) and their tolerances
Yaw (θ_Y)	Rotary	± 2°
Pitch (θ_X)	Rotary	± 2°

C Double-crystal monochromator

The monochromator is a vertical-deflecting DCM located at 40 m, with a nominal exit offset of 10 mm at the 33 keV operating point. It combines a Si(111) double-crystal pair and a Si(311) channel-cut crystal in a single vessel, exchanged by a horizontal translation. A monolithic channel-cut is preferred for the Si(311) reflection; if it cannot be fabricated to the required length, the alternative is a pseudo-channel-cut pair of two separately mounted crystals. Both reflections cover the 33 keV operating point, and the Si(311) pair also covers the upper end of the operating range (40–45 keV); an extension of the range toward higher energies is considered in the design. The beamline is operated at the optimum energy of 33 keV, corresponding to a Bragg angle of 3.43° for Si(111) and 6.59° for Si(311). The Bragg axis is driven by a worm wheel in closed loop.

The crystals are plane and cryogenically cooled with liquid nitrogen near 120 K to suppress thermal distortion of the first-crystal surface, which absorbs the white-beam power transmitted by the white-beam slit (heat-load analysis in Section 4.2.7.4 E). The first crystal accommodates the beam footprint at the smallest Bragg angle, and the second crystal (the second reflecting face of the channel-cut), 95 mm long for both reflections, accommodates the longitudinal beam walk over the energy range of each reflection. Because ID24 has no harmonic-rejection mirror, the dominant higher-order contribution at the 33 keV operating point is the Si(333) reflection at 99 keV, fed by the 15th undulator harmonic; it is estimated at about 2×10^{-5} of the 33 keV flux after the DCM and is further suppressed by the energy discrimination of the detectors. The full DCM specification is given in table 4.2.7.5.

D Beam conditions at the sample

The beam delivered to each sample stage is set by the transfocator mode (Section 4.2.7.4 B): the natural, collimation, and focusing modes give different beam sizes and divergences at the 70 m and 75 m stages. The beam size, divergence, and lens transmission at the sample for each arm, with the lens stack positioned for its mode, are summarized in table 4.2.7.6, together with the photon flux at the sample: about 6.7×10^{12} ph/s in the natural mode and 3.6–5.8×10^{12} ph/s with the lenses inserted (Si(111)). They are theoretical values calculated as described at the beginning of this subsection.

<Table 4.2.7.5> DCM specification. Crystal dimensions are length × width × thickness.

Item	Specification
Position	40 m (source to DCM)
Deflection / type	Vertical deflection, plane crystals
Photon energy range	17–40 keV (Si(111)) / 17–45 keV (Si(311))
Operating energy	33 keV (optimized)
Crystal / optical element	Si(111) double crystal / Si(311) channel-cut (pseudo-channel-cut as the alternative), Bragg, in a single vessel
Operating modes	Si(111) double-crystal mode / Si(311) channel-cut mode, exchanged by horizontal translation
First crystal	$50 \times 25 \times 50$ mm^3
Second crystal	$95 \times 25 \times 30$ mm^3 (Si(111)); second reflecting face 95 mm long (Si(311) channel-cut)
Beam offset	10 mm at 33 keV (nominal); fixed exit in the Si(111) mode
Bragg angle range	2.83°–6.68° (Si(111), 17–40 keV) / 4.83°–12.87° (Si(311), 17–45 keV)
Energy resolution ($\Delta E/E$, intrinsic)	$\approx 1.3 \times 10^{-4}$ (Si(111)) / $\approx 3 \times 10^{-5}$ (Si(311))
Slope error	< 1 μrad RMS
Roughness	≤ 0.5 nm RMS
Figure error	< 1 nm RMS
Cooling	First crystal LN_2-cooled near 120 K; second crystal braid-cooled from the first-crystal exchanger; the channel-cut is cooled as one block
Motion axes	Bragg drive: worm wheel, closed loop, covering the Bragg angle range above; horizontal translation for the reflection exchange; lateral translation for alignment
Sensors and encoders	Bragg encoder: on-axis absolute rotary encoder
Incident beam size (H × V)	1.5×1.5 mm^2, defined by the white-beam slit at 39 m
Heat load	White beam on the first crystal; see Section 4.2.7.4 E
Mounting concept	Goniometer on a granite plinth

E Heat Load

The DCM first crystal is the only optical element exposed to the white beam and carries the entire heat load transmitted by the white-beam slit; the CRL transfocator downstream operates on the monochromatic beam and absorbs negligible power (Section 4.2.7.4 B). Following the common DCM thermal-management approach, which keeps the peak power density low and cryo-cools the first crystal with liquid nitrogen near 120 K (the liquid-nitrogen supply is described in section 3.6), the first-crystal load is evaluated here for the ID24 source and white-beam-slit geometry.

The heat load was computed with SRCalc in the OASYS environment, using the URGENT code for the undulator power density, propagating the IVU16 white

<Table 4.2.7.6> Beam conditions at the sample for each transfocator arm at 33 keV (theoretical values).

Configuration	Beam size, H × V (μm)		Divergence, H × V (μrad)	Transmission (%)	Flux (ph/s, Si(111) bandwidth)
	70 m	75 m			
Natural (lenses out)	1054 × 974	1130 × 1043	15.0 × 13.9	100	6.7×10^{12}
Arm 1 collimation, 1D-V	1054 × 616	as at 70 m	15.0 × 0.19	86	5.8×10^{12}
Arm 2 collimation, 2D	656 × 616	as at 70 m	0.85 × 0.19	73	4.9×10^{12}
Arm 3 focusing at 70 m, 1D-V	1054 × 4.1	–	15.0 × 24.0	74	5.0×10^{12}
Arm 4 focusing at 70 m, 2D	18 × 4.1	–	25.2 × 24.0	54	3.6×10^{12}
Arm 5 focusing at 75 m, 1D-V	–	1130 × 5.1	15.0 × 19.8	76	5.1×10^{12}
Arm 6 focusing at 75 m, 2D	–	23 × 5.1	20.9 × 19.8	57	3.8×10^{12}

Calculated for the source of section 4.2.7.2 with the effective source point at the center of the undulator, nominal lens radii, and the lens positions of table 4.2.7.3. Beam sizes and divergences are FWHM; for the focusing arms the divergence column gives the convergence angle at the focus; –: the arm is not used at that stage. The collimated beam is essentially the same at both stages. Transmission: natural beam at 33 keV through the lens stack, including absorption in diamond (parabolic profile, 25 μm web per lens) and the geometric lens aperture. Flux: SPECTRA flux through the 1.5 × 1.5 mm² white-beam slit at 33 keV (5.16×10^{13} ph/s/0.1%BW at the 5.89 mm gap, 400 mA, ideal undulator field), multiplied by the Si(111) intrinsic bandwidth ($\Delta E/E \approx 1.3 \times 10^{-4}$) for ideal crystals and by the lens transmission.

beam through the 1.5 × 1.5 mm² white-beam slit at 39 m (38.5 μrad acceptance) onto the first crystal at 40 m. The crystal is modeled as bulk silicon, which absorbs essentially the entire incident white-beam power because the Bragg-reflected monochromatic band is a negligible fraction of the broadband load. Although the beamline operates at the optimum energy of 33 keV, the worst-case load is set by the lowest accessible energy at the minimum magnetic gap: at 17 keV the 5 mm gap (K = 1.172) produces the maximum total power. The absorbed power is independent of the selected reflection and Bragg angle, whereas the peak power density increases with the Bragg angle, scaling as $\sin\theta_B$ because the beam meets the crystal at a steeper angle (its footprint on the surface shrinks as $1/\sin\theta_B$).

The full white-beam power absorbed by the first crystal is 223.7 W in the 17 keV minimum-gap worst case and 175.4 W at the 33 keV operating point; this absorbed power, being independent of the reflection, sets the cryogenic cooling capacity. The peak power density, which governs the local surface thermal gradient and the resulting crystal deformation, is highest for the Si(311) reflection at 17 keV, where the largest Bragg angle (12.87°) gives a peak density of 23.17 W/mm^2. At the 33 keV operating point the peak density falls to 4.89 W/mm^2 for Si(111) and 9.39 W/mm^2 for Si(311). All cases are summarized in table 4.2.7.7.

The worst-case peak power density of 23.17 W/mm^2 is the design input for the cooling of the first crystal. The first crystal is cooled with liquid nitrogen near 120 K through an OFHC-copper heat exchanger, and the second crystal is braid-cooled from the same exchanger, while the Si(311) channel-cut is cooled as one block (Section 4.2.7.4 C); operating near 120 K keeps silicon close to the temperature at which its thermal-expansion coefficient crosses zero, minimizing the thermal bump. The steady-state thermal finite-element analysis of the first crystal and the verification of the mounting resonance are part of the engineering design of the monochromator.

<Table 4.2.7.7> DCM first-crystal heat load (theoretical values).

Parameter	**17 keV, Si(111) (6.68°)**	**17 keV, Si(311) (12.87°)**	**33 keV, Si(111) (3.43°)**	**33 keV, Si(311) (6.59°)**
Absorbed power (W)	223.7	223.7	175.4	175.4
Peak power density (W/mm^2)	12.1	23.17	4.89	9.39

SRCalc; IVU16 white beam at 400 mA through the 1.5 × 1.5 mm^2 white-beam slit at 39 m onto the first crystal at 40 m. 17 keV: worst case at the minimum gap of 5.0 mm (K = 1.172); 33 keV: operating point at the 5.89 mm gap (K = 0.94). The Bragg angle of each reflection is given in the column head.

F Beam Diagnostics

The ID24 beam diagnostics use the common KLS photon-beam diagnostic components described in section 3.2; only the ID24-specific layout is given here. The diagnostics provide beam-profile imaging at each major optical transition and an intensity (I_0) reference for normalization, and support optics alignment.

Diamond screen monitors are placed in the optical hutch at 39.5 m (white beam, upstream of the DCM) and 46.5 m (monochromatic beam, downstream of the DCM), each with about 1 μm resolution. Diamond is chosen here because it is transmissive and withstands the white-beam heat load, so the monitors stay permanently in

the beam with negligible attenuation. The 39.5 m monitor characterizes the white beam entering the DCM, while the 46.5 m monitor verifies the monochromatic beam after the DCM.

Downstream of the transfocator the beam is monochromatic and of low power, so removable scintillator (YAG) screen monitors are used at 49.5 m (after the CRL) and 68 m (in the photon transfer line before the experimental hutch). These are inserted for alignment and beam-profile checks and withdrawn during measurement to leave an unobstructed path to the sample.

Beam intensity is monitored by an ionization chamber (I_0 monitor) at 69 m, at the entrance of the experimental hutch immediately upstream of the sample. Any source or monochromator drift that converts into a beam-intensity variation at the sample is recorded by the I_0 chamber and used to normalize the measured diffraction intensities, preserving quantitative accuracy in high-throughput and *in-situ* measurements. For the powder-diffraction stability requirement the screen monitors and the I_0 chamber are sufficient; space is reserved for a continuous X-ray beam-position monitor (XBPM) on the monochromatic beam for a feedback loop. The diagnostic readout and camera interfaces follow the beam-diagnostics and vision framework of section 3.4.

4.2.7.5 Photon Transfer Line

The PTL carries the beam from the front-end exit through the optical hutch to the experimental hutch. The girder and support design and the common PTL components are described in sections 3.1 and 3.2; only the ID24-specific provisions are given here: the white-beam section in the optical hutch (white-beam slit, first diamond screen monitor, DCM) and the monochromatic-beam section downstream of the DCM (through the transfocator to the sample).

A Mechanical Design

The intent of the mechanical design is to realize the optical layout of table 4.2.7.2 while meeting the stability and alignment requirements of the DCM and the transfocator. Because ID24 uses no focusing or collimating mirror, the principal mechanical structures are the DCM at 40 m, mounted on a goniometer on a granite plinth, and the CRL transfocator at about 48 m on a granite-based support stage (table 4.2.7.4). The beam pipes, support girders, vacuum vessels, and their interfaces to the hutch slab are laid out along this component sequence.

B Vacuum, Pumps and Valves

The ID24 vacuum system follows the vacuum design basis described with the front-end (section 3.1), which divides each beamline into front-end, optical-hutch, and experimental-hutch vacuum sections. Gate valves, coordinated with the safety-interlock system (section 3.3), isolate the front-end, optical-hutch, and experimental-hutch sectors so that any sector can be vented independently for maintenance without breaking the vacuum of the adjacent sectors, and the fast-closing shutter in the front-end closes in the event of a vacuum incident to protect the storage-ring vacuum; the interlock signals and the shutdown devices they act on are specified in the beamline interlock system design report [4]. The pumps, valves, and gauges are placed per sector on this layout. A background-pressure analysis of the ID24 optical-hutch and experimental-hutch vacuum sections is given in the front-end vacuum analysis report [5].

C Hutch

ID24 comprises two hutches: an optical hutch that houses and shields the optical components (white-beam slit, DCM, CRL transfocator), and an experimental hutch that houses the sample stages and detectors. The ID24 experimental hutch is located inside the storage-ring experimental hall, in a standard hutch configuration; the positions of the components along the beamline are listed in table 4.2.7.2. Radiation shielding, exhaust, LCW, and LN_2 follow the common infrastructure described in section 3.6.

4.2.7.6 End-Station

The ID24 MSA experimental station comprises two sample stages: a high-resolution diffractometer at 70 m and a flexible optical-table stage at 75 m. The 70 m stage employs a 13-crystal Si(111) MAC combined with a two-dimensional detector for high-resolution powder diffraction (estimated angular resolution in Section 4.2.7.6 B). The realization of the 13-crystal analyzer requires in-house development or collaboration with a manufacturer. The 75 m stage is a flexible optical table carrying a large-area two-dimensional detector for fast, wide-coverage *in-situ* and time-resolved measurements, trading angular resolution for speed and 2θ coverage. The end-station mechanical design and the detector configuration are described below.

A End-Station Mechanical Design

The 70 m high-resolution diffractometer is a 2+1 circle goniometer: a sample (θ) circle, a detector (2θ) arm, and a capillary spinner that rotates powder-filled capillaries for grain-orientation averaging. The 2θ arm carries the 13-crystal Si(111) MAC stage and the two-dimensional detector, which are used in alternation. The mechanical performance targets are summarized in table 4.2.7.8; for combined micro-focus and θ-rotation operation a small sphere of confusion (SOC) is desirable, with a recommended value of ~3 μm. The goniometer bearings and drives, the MAC stage, the sample stages, and the granite support are designed to these targets. The sample environment is centered on capillary samples (glass capillaries of various inner diameters: 0.15, 0.6, 0.8 mm, etc.) at a beam height of 1410 mm, given by the 1400 mm beam height of the source and the 10 mm fixed-exit offset of the DCM.

The 75 m stage is a flexible optical table for multi-sample, *in-situ*, and time-resolved XRD, providing plug-and-play mounting of user sample environments (Section 4.2.7.6 C) and the second two-dimensional detector (Section 4.2.7.6 B). The performance targets are an angular resolution of $\approx 0.05°$, a measurement time below one minute per sample, and second-level time resolution for *in-situ* studies.

<Table 4.2.7.8> High-resolution diffractometer (70 m) mechanical design targets.

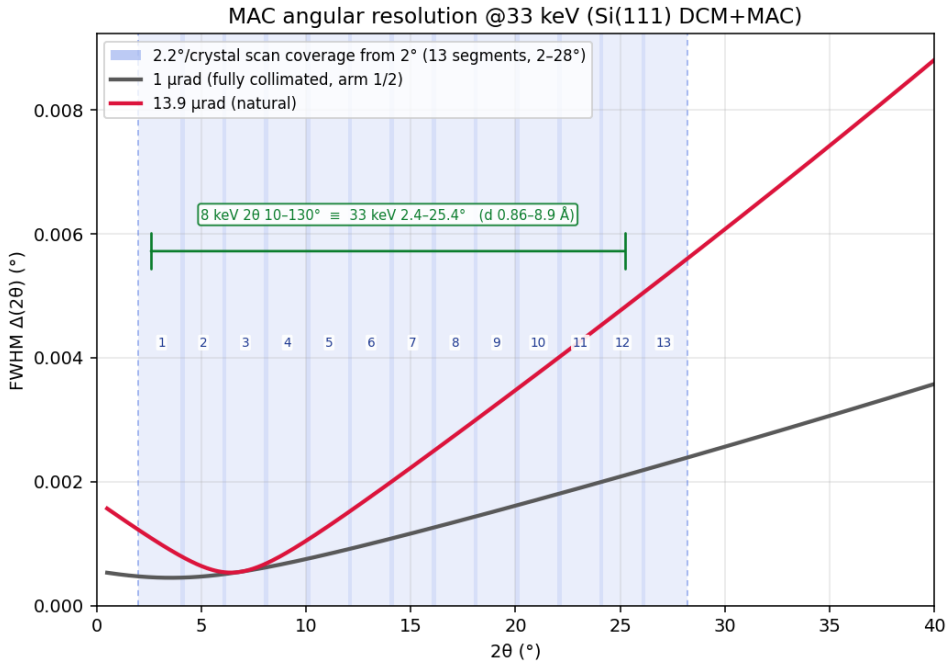
Parameter	Specification
Goniometer axes	
θ (sample) range	$\pm 180°$, continuous
2θ (detector arm) range	$\pm 180°$, continuous; carries the MAC and the 2D detector in alternation
Step resolution (θ, 2θ)	0.00025°
Mechanical repeatability	$\pm 0.0005°$ (unidirectional)
Wobble	< 25 μrad
Encoder	On-axis, absolute
Sphere of confusion (SOC)	~3 μm (recommended)
Sample stage	
Load capacity	$\geq$ 20 kg
Translation range	Ys/Zs $\pm$25 mm, Xs $\pm$10 mm
Step resolution	5 μm
Repeatability	$\pm$10 μm
Beamline interface	
Beam height	1410 mm (source 1400 mm + DCM fixed-exit offset 10 mm)
Capillary spinner	Glass capillaries of various inner diameters (0.15, 0.6, 0.8 mm, etc.)

B Detector

High-resolution detection at the 70 m stage pairs the MAC with a two-dimensional pixel detector, and the value of this combination rests on three points. First, the 13-crystal Si(111) MAC strictly defines the diffraction angle through the narrow angular acceptance (Darwin width) of the analyzer crystals, so the instrumental resolution is set by the crystal optics rather than by the sample or beam size: the estimated in-plane FWHM stays at the level of about 0.006° or better over the 2θ range covered by the analyzer scan (figure 4.2.7.2). Second, the two-dimensional detector maps the thirteen analyzer channels onto distinct regions of the sensor and reads them in parallel. Third, the dual thresholds of the pixel detector provide difference-mode energy discrimination that suppresses harmonics, sample fluorescence, and background. Because these benefits must hold across the entire 17–45 keV band, where a silicon sensor loses absorption efficiency, a high-Z CdTe sensor is essential. In figure 4.2.7.2, the collimated case uses 1 µrad, a conservative value for the 0.19 µrad of the collimation arms (table 4.2.7.6), and the natural case 13.9 µrad. The green bracket shows the energy compression: a full 8 keV scan (2θ 10–130°) covers the same d-range (0.86–8.9 Å) as only 2θ 2.4–25.4° at 33 keV. The blue shading shows the 2θ range covered by a fast 2.2°-per-crystal scan starting at 2°: the 13 channels (2° spacing) tile 2–28° with 0.2° overlaps; the shading marks this scan coverage, not the full accessible range.

Accordingly, both the 70 m diffractometer and the 75 m optical table are equipped with CdTe pixel detectors: a compact detector matched to the MAC channels at the diffractometer, and a large-area detector at the optical table that records full two-dimensional patterns over a wide 2θ range for fast *in-situ* and time-resolved work. The detector parameters are summarized in table 4.2.7.9. Data acquisition, detector control, and the higher-level computing follow the common KLS EPICS and Bluesky/Ophyd frameworks described in sections 3.4 and 3.5.

At the 75 m stage the sample-to-detector distance of the EIGER2 X CdTe 9M is adjustable between 300 and 2,000 mm, trading angular coverage against angular resolution: a short distance widens the 2θ acceptance for fast full-pattern acquisition, while a long distance sharpens the angular resolution. The theoretical angular resolution and d-spacing range at 33 keV are summarized in table 4.2.7.10, for the 0.25 mm reference sample and for a 0.5 mm sample, with the direct beam placed 43 mm from the lower edge of the detector (beam-stop margin). With the 75 µm pixel, the $\approx 0.05°$ stage target is met for $D \geq 372$ mm with the 0.25 mm sample



<Figure 4.2.7.2> Estimated angular resolution of the 70 m high-resolution diffractometer at 33 keV (Si(111) DCM and 13-crystal Si(111) MAC) for collimated and natural vertical divergence.

($D \geq 659$ mm with the 0.5 mm sample).

The angular resolution follows $\Delta(2\theta) = (s + p)/D$ and is dominated by the sample/beam size s (0.25–0.5 mm) rather than the 75 µm pixel, so the stage is sample-limited and the sample-to-detector distance D is the operating knob, trading resolution against the single-frame 2θ coverage ($2\theta_{\max} = \arctan(L/D)$, with L = 201.7 mm the detector height above the direct beam, in the opposite sense). Three regimes result (values for the 0.25 mm reference sample, with the 0.5 mm sample in parentheses): a short distance (~300–500 mm) for fast wide-2θ survey and *in-situ* work (~0.04–0.06°, or 0.07–0.11°; 2θ up to ~34°), a mid distance (~750–1,000 mm) for a balance of resolution and coverage (~0.02–0.025°, or 0.03–0.04°; 2θ ~11–15°), and a long distance (~1,500–2,000 mm) for finer resolution and large-d access (down to ~0.009°, or 0.016°; d up to ~17.5 Å). The travel bounds are physically motivated: the minimum distance by the flat-detector high-angle limit ($2\theta_{\max}$ below ~35°) together with mechanical clearance, and the maximum by the minimum useful single-frame 2θ span and diminishing resolution returns; finer resolution is the role of the 70 m MAC diffractometer.

<Table 4.2.7.9> ID24 end-station detectors.

Parameter	EIGER2 X CdTe 2M-W	EIGER2 X CdTe 9M
Role / technique	HRPD via 13-channel MAC	Large-area *in-situ* XRD
Detector type / detection principle	Hybrid photon-counting pixel detector	Hybrid photon-counting pixel detector
Sensor material / thickness	CdTe, 750 µm	CdTe, 750 µm
Pixel pitch	75 µm	75 µm
Pixel format / channels	4148 × 512	3108 × 3262
Active area	311.1 × 38.4 mm	233.1 × 244.7 mm
Maximum frame rate	2,250 Hz (8 bit) / 1,125 Hz (16 bit)	490 Hz (8 bit) / 245 Hz (16 bit)
Image / dynamic range	32-bit image depth	32-bit image depth
Maximum count-rate capability	10^7 photons/s/pixel	10^7 photons/s/pixel
Detector-supported energy range	8–100 keV	8–100 keV
Sample-to-detector distance	Set by the analyzer geometry on the 2θ arm	300–2,000 mm, adjustable
Remarks	Mounted on the 70 m diffractometer 2θ arm; the 13 MAC channels are read in parallel, and the dual thresholds give difference-mode energy discrimination	Mounted on the 75 m optical table; the distance trades 2θ coverage against angular resolution

The energy range is the detector-supported range, not the beamline operating range.

<Table 4.2.7.10> Theoretical angular resolution and d-spacing range at the 75 m optical-table stage at 33 keV.

Sample-to-detector distance (mm)	Maximum 2θ (°)	Angular resolution, 0.25 mm sample (°)	Angular resolution, 0.5 mm sample (°)	d-spacing range (Å)
300	33.9	0.062	0.110	0.6–2.6
500	22.0	0.037	0.066	1.0–4.4
750	15.1	0.025	0.044	1.4–6.6
1,000	11.4	0.019	0.033	1.9–8.7
1,500	7.7	0.012	0.022	2.8–13.1
2,000	5.8	0.009	0.016	3.7–17.5

Calculated for 33 keV and the EIGER2 X CdTe 9M (75 µm pixel) with the direct beam 43 mm from the lower detector edge, for the 0.25 mm reference sample and a 0.5 mm sample. The angular resolution is the geometric estimate $\Delta(2\theta) = (s + p)/D$, the linear sum of the sample size s and the pixel pitch p divided by the distance D; the 2θ and d-spacing ranges follow from the detector radii between 43 mm and 201.7 mm from the direct beam. Beam divergence and bandwidth (below 0.005°) are not included, nor is the sensor-depth parallax, which grows with 2θ and becomes significant only toward the high-angle edge of the frame at short distances.

C Sample Environments

In-situ measurements are a primary purpose of the end-station, and both stages,

the 70 m diffractometer (capillary-based) and the 75 m flexible optical table, are designed to accommodate a variety of sample environments, for example:

- **Temperature**: hot-air blower and capillary furnace for heating, cryostream for cooling
- **Gas**: gas-flow / gas-dosing cell for adsorption–desorption and reaction studies
- **Pressure**: high-pressure cell
- **Electrochemistry**: *in-situ* battery and electrochemical cells (charge/discharge)
- **External field / light**: electric or magnetic field, and a laser for photo-crystallography
- **Automation**: multi-sample changer and robotic sample exchange for high throughput
- **Custom**: user-supplied chambers, accommodated by the open optical-table layout

References

[1] Hyungseok Choi and Jongha Park. Beamline Photon Source Analysis Report. Internal Document PAL-INT/ME-2026-007. Pohang Accelerator Laboratory, July 2026.

[2] Jongha Park et al. High Heat Load Front-End Mechanical Design and Thermal Analysis Report. Internal Document PAL-INT/ME-2026-003. Pohang Accelerator Laboratory, June 2026.

[3] Jongha Park and Youngduk Yun. White Beam Slit Design Report. Internal Document PAL-INT/ME-2026-004. Pohang Accelerator Laboratory, June 2026.

[4] Minho Seo and Chaesoon Lee. 4GSR Beamline Interlock System Design Report. Internal Document PAL-INT/EE-2026-012. Pohang Accelerator Laboratory, July 2026.

[5] Hyungseok Choi and Jongha Park. 4GSR Front-End Vacuum Analysis Report. Internal Document PAL-INT/ME-2026-009. Pohang Accelerator Laboratory, Aug. 2026.

4.2.8 Nanoscale Angle-Resolved Photoemission Spectroscopy (ID25)

ID25 is a dual-branch soft X-ray ARPES beamline for spatially selective electronic-structure measurements of quantum materials and electrically controlled devices. An EPU98 source and an SX-700-type VLSPGM feed a capillary-focused nanoARPES branch (target beam size $\leq$1 μm FWHM) and a mirror-focused microARPES branch (approximately 10 $\times$ 10 μm FWHM in H/V). The following sections connect the scientific objectives to the source calculation basis, optics and operating modes, transport interfaces, and measurement and preparation systems. Common engineering requirements are referenced to Chapter 3.

4.2.8.1 Target Purpose and Objective

A Mission and Experimental Scope

ID25 combines spatially selective ARPES with photon-energy and polarization control for two-dimensional quantum materials, heterogeneous samples, and electrically controlled devices. The nanoARPES branch uses capillary focusing with a beam-size target of at most 1 μm FWHM. The complementary microARPES branch uses mirror focusing with a target of approximately 10 $\times$ 10 μm FWHM in H/V. Both branches share the EPU98 source and SX-700-type VLSPGM, with independent downstream optics and measurement stations.

The beamline user photon-energy range is 50–2000 eV. HF emphasizes photon throughput, HR has a nominal resolving-power target of approximately 30,000, and HE extends the energy coverage primarily for rapid XPS checks of sample composition and chemical states. The monochromator and sample beam conditions are described in section 4.2.8.4. Each station has a separate analyzer and at least four electrical contacts, with temperature targets of approximately 30 K for nanoARPES and 10 K for microARPES.

B Representative Experiments and Measurement Requirements

The four representative experiment classes in table 4.2.8.1 connect the scientific objectives to spatial selection, energy resolution, photon throughput, polarization, and the sample environment.

C Spatial Selection and Performance Priorities

The focused beam size describes the illumination footprint; achieved spatial resolution also depends on sample scanning, positioning stability, and the measure-

<Table 4.2.8.1> Representative ID25 experiments and their measurement requirements.

Experiment	Measurement requirements
Small exfoliated flakes	Select a flake region within the illumination footprint; HF for throughput or HR for energy resolution; polarization control for matrix-element comparisons; low-temperature measurement and protected transfer for air-sensitive samples
Heterogeneous domains	Correlate real-space position with momentum-resolved spectra; retain beam/sample registration during mapping; compare spectra at common energy and polarization settings; use HF/HR according to signal and energy-scale requirements
Moire and heterostructure regions	Select a distinguishable region of the sample; HR for small spectral energy scales, with flux supporting acquisition at the selected resolution; polarization comparisons and low-temperature operation
Electrically controlled devices	At least four contacts for gate/bias control; stable region selection during electrical and deflector scans; low-temperature wiring and holder compatibility; photon mode and polarization chosen for the spectral contrast of interest

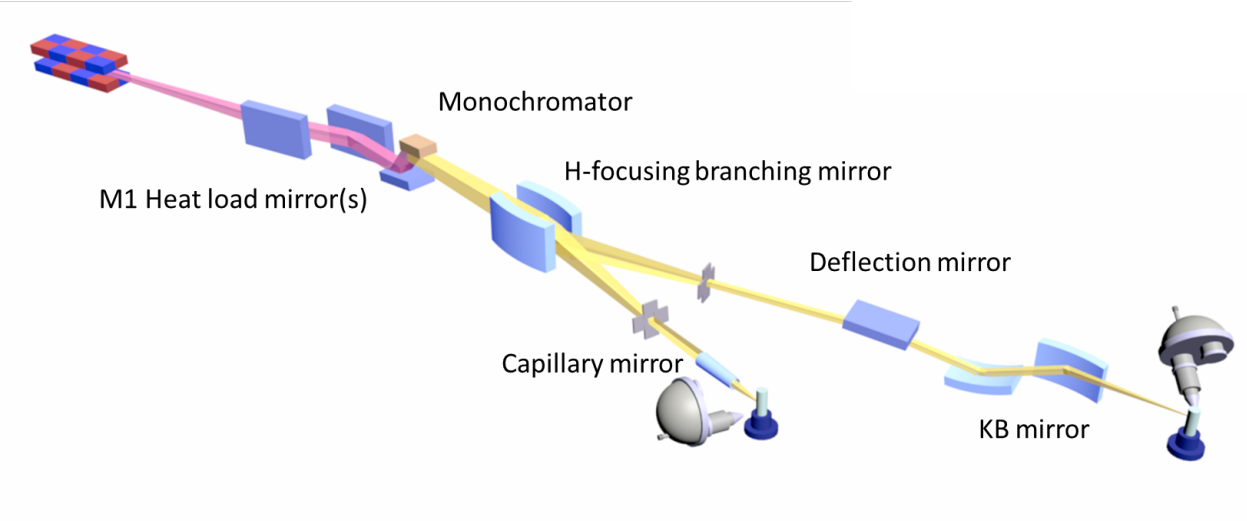
ment response. The capillary baseline supports spatial selection of sample regions comparable to or larger than that footprint. A selected moire or heterostructure region is a sample area for spectroscopy, rather than a claim that the individual moire periodicity is spatially resolved. The microARPES branch serves larger regions and general ARPES workflows.

Photon throughput and energy resolution are balanced through HF and HR modes. Polarization control supports matrix-element-sensitive comparisons, while electrical contacts and low-temperature operation support device measurements. The analyzer-plus-photon FWHM budget is described in section 4.2.8.4; it is distinct from the complete measured spectral width.

D Baseline and Expansion Interfaces

Capillary nanoARPES and mirror-focused microARPES form the baseline. The stations reserve interfaces for spin-ARPES expansion, and the common preparation system reserves an MBE connection. The nano station also reserves future FZP integration. These expansion interfaces carry no FZP beam-size target. The common preparation and transfer workflow and branch-specific instruments are described in Section 4.2.8.6 D and table 4.2.8.21.

The branch separation is 8° in total, implemented by M3 upstream of the independent exit slits. The overall layout is illustrated in figure 4.2.8.1.



<Figure 4.2.8.1> ID25 optical layout: M1 heat-load mirror, monochromator with M2 pre-mirror, M3 horizontal-focusing branching optics, and independent exit slits. The nano branch uses a capillary mirror; the micro branch uses M4M vertical deflection followed by the M5M/M6M focusing pair.

<Table 4.2.8.2> EPU98 insertion-device parameters at a ring current of 400 mA. The total powers are full-fan emitted values at the 15 mm minimum gap for vertical (V), horizontal (H), and circular (C) polarization. The peak angular power density of 38.02 kW/mrad^2 refers to V polarization, as in the common photon-source table. Partial incident power at the M1 condition is listed separately below. The supported polarization states are LH, LV, CR, and CL. The final specification gives 35.75 periods, displayed as the integer 36. The final array length is 3.6316 m. These lengths are distinct from the device and regular-magnet lengths used in the calculation model.

Undulator	Period (mm)	Array length (m)	Gap size (mm)	K_{max}	Total power (kW)	Power density (kW/mrad^2)	Number of periods
EPU98	98	3.6316	15 (min.)	9.238 (V) / 8.043 (H) / 6.070 (C)	13.75 (V) / 10.44 (H) / 11.87 (C)	38.02 (V)	36

4.2.8.2 Photon Source

A Source Overview

The photon source of ID25 is an elliptically polarized undulator with a period of 98 mm (EPU98). The source provides soft X-ray radiation for both the nanoARPES and microARPES branches. The insertion-device geometry and full-fan emitted power are summarized in table 4.2.8.2.

<Table 4.2.8.3> Final EPU98 geometry and magnet specification supplied for this revision. Period count is displayed as 36, with 35.75 retained as the specified value.

Parameter	Final specification
Undulator period	98 mm
Number of periods	36 (specified value: 35.75)
Minimum vertical gap	15 mm
Horizontal airgap	1 mm
Longitudinal airgap	0.1 mm
Magnetic material remanence B_r	1.25 T
Magnet profile W × H	35 × 30 mm
Magnet thickness	24.4 mm (0.1 mm longitudinal airgap)
Array length	3631.6 mm

This section defines the source-side input to the beamline design. Detailed heat-load handling, front-end protection, and downstream optical heat-load calculations are treated in sections 4.2.8.3 and 4.2.8.4.

B Photon Energy Range and Polarization

The beamline-level user photon-energy range in the present concept is 50–2000 eV. Some individual grating modes have wider or narrower design coverage, as described in Section 4.2.8.4 E.

The beamline provides linear horizontal (LH), linear vertical (LV), circular right (CR), and circular left (CL) polarization modes.

C Source Performance Parameters

The source performance table (table 4.2.8.4) lists photon flux, source size, and source divergence at 50, 100, and 200 eV. The 100 eV condition is used as the representative photon energy for the beamline design discussion. The retained source calculation curves are shown in figure 4.2.8.2.

D Calculation Conditions and Traceability

The source calculation conditions are 400 mA, LH polarization, and full angular acceptance of 135 μrad in each of H and V. The source-size and divergence curves in figure 4.2.8.2 are RMS, whereas table 4.2.8.4 reports FWHM. For a Gaussian profile, FWHM equals $2\sqrt{2\ln 2}\,\sigma \simeq 2.355\,\sigma$; the source size and divergence use this width-convention distinction.

The SPECTRA 12.2.1 calculation model uses 36 regular periods, a regular

<Table 4.2.8.4> Retained EPU98 source calculation values at 50, 100, and 200 eV; source size and divergence are labeled FWHM in the existing table. These are source-side values, not delivered sample fluxes. The calculation conditions are recorded in table 4.2.8.5.

Photon energy	Photon flux	Source size FWHM	Source divergence FWHM
50 eV	9.97×10^{14} ph/s/0.1%BW	90.0 μm (H) × 78.9 μm (V)	139.9 μrad (H) × 139.7 μrad (V)
100 eV	9.95×10^{14} ph/s/0.1%BW	70.9 μm (H) × 56.3 μm (V)	98.9 μrad (H) × 98.7 μrad (V)
200 eV	9.84×10^{14} ph/s/0.1%BW	59.1 μm (H) × 40.3 μm (V)	70.2 μrad (H) × 69.9 μrad (V)

magnet length of 3.528 m (36×98 mm), and a model device length of 3.8 m. These calculation inputs are recorded separately from the final undulator specification of 35.75 periods, displayed as 36, and array length 3631.6 mm. The recorded 50 eV first-harmonic operating point uses a 22.3684 mm gap. This distinction preserves the calculation geometry used for the source results.

<Table 4.2.8.5> Source calculation conditions and width conventions.

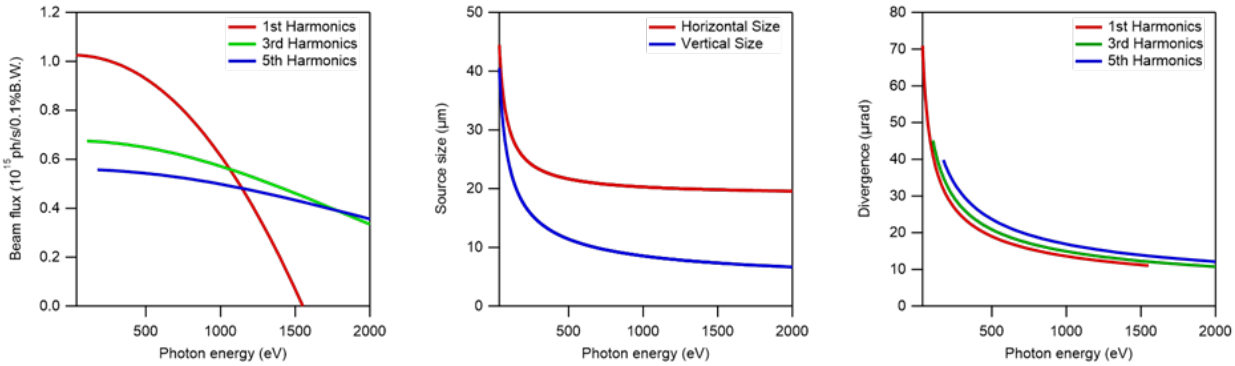
Item	Calculation conditions
Source-performance table	Flux per 0.1% bandwidth; size and divergence FWHM. Supplied conditions: 400 mA, LH, nominal acceptance 135 × 135 μrad.
Source figure	Flux per 0.1% bandwidth; RMS source size/divergence. Supplied conditions: 400 mA, LH, nominal acceptance 135 × 135 μrad. SPECTRA 12.2.1 model: 36 regular periods, regular magnet length 3.528 m, device length 3.8 m.
M1 heat-load condition	400 mA, LH, first harmonic at 50 eV, gap approximately 22.37 mm, H/V full angular acceptance 135 × 135 μrad. Partial incident power within the specified acceptance: 546.9 W; incident peak angular power density: 33.78 kW/mrad²

E Source Acceptance for Beamline Design

The beamline design acceptance is 135 μrad full angle in each of the horizontal and vertical directions. This acceptance is used as a common boundary condition for the front-end interface, heat-load calculation, grating footprint evaluation, and downstream clipping analysis (table 4.2.8.6).

<Table 4.2.8.6> ID25 source acceptance used as the beamline-design boundary condition.

Parameter	Value	Use in design
Horizontal full-angle acceptance	135 μrad	Beamline aperture, footprint, and power-transmission basis
Vertical full-angle acceptance	135 μrad	Beamline aperture, footprint, and power-transmission basis



<Figure 4.2.8.2> Retained EPU98 source calculation curves: flux per 0.1% bandwidth and divergence for the first, third, and fifth harmonics, and horizontal/vertical source sizes. Source size and divergence are RMS. The supplied conditions are 400 mA, LH polarization, and nominal H/V acceptance of 135 × 135 μrad. The supplied SPECTRA 12.2.1 calculation model uses 36 regular periods and a regular magnet length of 3.528 m. The source table reports FWHM, whereas the figure reports RMS widths.

F Heat-Load Input Condition

The M1 heat-load condition is 400 mA, LH polarization, and a first-harmonic photon energy of 50 eV at a gap of approximately 22.37 mm, with full angular acceptance of 135 μrad in each of H and V. At this operating point, the partial incident power within the specified acceptance is 546.9 W and the incident radiation has a peak angular power density of 33.78 kW/mrad^2. The partial incident power is integrated over the specified acceptance, whereas the angular density describes its peak. The M1 surface projection of the incident density is given in Section 4.2.8.4 B; the full-fan emitted powers in table 4.2.8.2 refer separately to minimum-gap source operation.

4.2.8.3 Front-End

A Common Design and ID25 Scope

The ID25 front-end uses the EPU front-end concept described in section 3.1. That section provides the common component layout, EPU extra fixed mask, protection components, mechanical design, and front-end vacuum discussion. Common interlock architecture is described in section 3.3. The high-heat-load front-end report is a related design reference [1].

This section records the ID25 source acceptance, retained power inputs, and downstream interface requirements.

B Acceptance and Aperture Interface

The ID25 full angular acceptance is 135 μrad horizontally and 135 μrad vertically. Its definition is maintained in table 4.2.8.6; the front-end interface summary is given in table 4.2.8.7. The front-end aperture must preserve this full angular acceptance around the reference trajectory.

<Table 4.2.8.7> ID25 full-angle front-end acceptance and aperture requirement.

Item	Input / status
Horizontal acceptance	135 μrad (full angle)
Vertical acceptance	135 μrad (full angle)
Angular convention	Full angle
Defining aperture	Preserve the specified full angular acceptance and alignment allowance about the reference trajectory

The common front-end description includes a millimeter-scale central-cone aperture. Its opening and source distance must be checked against the ID25 angular acceptance and beam trajectory before adopting it for ID25. The ID25 aperture requirement is set by the specified full angular acceptance.

C Radiation and Heat-Load Interface

The M1 condition is 400 mA, LH, and a 50 eV first-harmonic setting at a gap of approximately 22.37 mm, with H/V full angular acceptance of 135 × 135 μrad. The partial incident power within the specified acceptance is 546.9 W; the incident radiation peak angular density is 33.78 kW/mrad^2. The partial power is integrated over the specified acceptance. Front-end aperture and protection integration must preserve the specified acceptance and account for the source radiation distribution.

The M1 incident-density projection is given in Section 4.2.8.4 B.

D Protection and Downstream Handover

The common design provides the basis for masks, absorber or stopper elements, photon and safety shutters, diagnostics, and vacuum protection. ID25 implementation requires an agreed front-end exit reference trajectory and aperture, downstream vacuum connection, beam-permit logic, and diagnostic readback interface. Component placement and aperture settings must satisfy these handover requirements. These handover items are tracked with the optical and endstation boundaries in table 4.2.8.18.

4.2.8.4 Beamline Optics

A Optical Layout Overview

The current optical layout places the radiation shielding wall at 26 m from the source and the first heat-load mirror M1 at 29 m. The VLSPGM monochromator is positioned downstream of M1, followed by the M3 switching and horizontal focusing mirror. The nanoARPES and microARPES branches use independent exit slits and are separated by switching mirrors upstream of the slit positions.

The current layout coordinates are summarized in table 4.2.8.8. The coordinates define the source-referenced layout. The microARPES sample is 1.5 m downstream of M6M at 46.1 m, giving a source-referenced sample position of 47.6 m. The nanoARPES sample is 6 mm downstream of the capillary reference; its listed 41.006 m coordinate is derived from the 41 m capillary position.

B M1 Plane Heat-Load Mirror

M1 is a plane heat-load mirror located 29 m from the source. In the current design, M1 is not used as a focusing optic. Its principal role is to receive the high-power undispersed beam and define a thermally manageable optical input for the monochromator and downstream optics.

The M1 operating condition is 400 mA, LH polarization, and a 50 eV first harmonic at a gap of approximately 22.37 mm, with H/V full angular acceptance of 135×135 μrad. The partial incident power within the specified acceptance is 546.9 W. This is the worst-case M1 heat-load condition within the intended operating envelope, using the highest-load polarization and the minimum operating photon energy. The incident radiation peak angular power density is 33.78 kW/mrad^2; it

<Table 4.2.8.8> Component-by-component layout of the ID25 nanoARPES beamline, in beam order (positions from the source).

Distance (m)	Location	Component	Description
0	Front-End	EPU98	Photon source
26	Optical Hutch	Shielding wall	Fixed shielding boundary
29		M1	Plane heat-load mirror
31.8		M2	Plane monochromator pre-mirror
32		Gratings, VLSPGM	SX-700-type variable-line-spacing plane grating monochromator
34		M3	Switching and horizontal focusing mirror; branch separation upstream of exit slits
39		Exit slits	Independent branch exit slits; HF/HR nominal opening 40×20 μm^2 (H×V); HE adjustable opening
41	nanoARPES branch	Capillary mirror	Baseline capillary focusing optic
41.006	nanoARPES branch	nanoARPES sample	6 mm downstream of the capillary reference at 41 m
44.5	microARPES branch	M4M	microARPES branch vertical deflecting mirror
45.3		M5M	microARPES branch vertical focusing mirror
46.1		M6M	microARPES branch horizontal focusing mirror
47.6		microARPES sample	1.5 m downstream of M6M at 46.1 m

describes the incoming radiation rather than the absorbed-power distribution.

At the 29 m source-to-M1 distance, 1 mrad corresponds to 29 mm. The incident peak density on a plane normal to the beam is therefore $33{,}780/29^2 \simeq 40.2$ W/mm^2. Projection onto the mirror at a grazing angle of 1.8° gives $40.2 \sin(1.8°) \simeq 1.26$ W/mm^2. These two densities are incident quantities and must not be interpreted as peak absorbed surface densities. The partial incident power and incident-density projection are listed in table 4.2.8.9.

C Variable Line Spacing Plane Grating Monochromator

The monochromator is an SX-700-type variable-line-spacing plane grating monochromator (VLSPGM). The monochromator provides the photon-energy selection and focusing required to deliver the target resolving power at the exit slits.

The monochromator is operated through discrete grating modes optimized

<Table 4.2.8.9> M1 partial incident power and incident-density projection at 400 mA, LH polarization, a 50 eV first harmonic, gap approximately 22.37 mm, and H/V full angular acceptance of 135 × 135 μrad. The 546.9 W value is partial incident power within the specified acceptance; the angular and projected densities also describe incident radiation.

Component	Location (m)	Parameter	400 mA, 50 eV
M1	29	Partial incident power within acceptance (W)	546.9
Incident radiation	0	Peak angular power density (kW/mrad²)	33.78
M1	29	Grazing angle (°)	1.8
M1	29	Incident peak power density on a plane normal to the beam at 29 m (W/mm²)	40.2
M1	29	Incident peak power density on the mirror surface (projected at 1.8° grazing incidence) (W/mm²)	~1.26

for high flux, high resolving power, and high-energy coverage. These modes are defined by their grating density, nominal Cff value, energy coverage, and target performance.

D Monochromator Operation Modes

The monochromator operation is described in terms of HF, HR, and HE modes rather than as branch-specific Cff operation. The HF mode sacrifices resolving power to increase photon flux. The HR mode targets high resolving power for measurements where photon-energy broadening must be kept small compared with the analyzer contribution. The HE mode provides extended photon-energy coverage up to approximately 2 keV, primarily for rapid XPS checks of sample composition and chemical states. The three modes are summarized in table 4.2.8.10.

<Table 4.2.8.10> Monochromator operation modes (HF, HR, HE).

Mode	Primary objective	Nominal resolving power target	Use case
HF	High flux	~15,000	Photon-flux-limited measurements at low photon energy
HR	High energy resolution	~30,000	High-resolution ARPES near low kinetic energy
HE	High-energy coverage	—	Rapid XPS checks up to approximately 2 keV

E Grating Set and Energy Coverage

The monochromator uses G1/G2 substrates carrying the HF, HR and HE grating patterns. The common substrate, coating, metrology and motion requirements apply to all three patterns. The HF and HR gratings are designed to cover 35–215 eV, even though the official beamline user energy range starts at 50 eV. This lower design coverage provides margin at the low-energy end. The HE grating covers 115–2005 eV and provides the extended high-energy capability required for the 50–2000 eV beamline range. The grating set and its energy coverage are summarized in table 4.2.8.11.

<Table 4.2.8.11> Grating design coverage and its overlap with the 50–2000 eV beamline user range. The overlap is a range definition, not validation of flux, resolution, or polarization coverage throughout that range.

Mode	Groove density	Nominal Cff	Grating design coverage	Within user range	Design purpose
HF	250 l/mm	2.23	35–215 eV	50–215 eV	High flux; RP ~15,000
HR	600 l/mm	3.24	35–215 eV	50–215 eV	High resolution; RP ~30,000
HE	750 l/mm	1.51	115–2005 eV	115–2000 eV	Rapid XPS checks

F Grating Mechanical Aperture

The grating clear aperture is 160 mm and the substrate length is 180 mm (table 4.2.8.12). The optical design must maintain beam footprints within this clear aperture under the selected operating modes for the grating patterns summarized in Section 4.2.8.4 E.

<Table 4.2.8.12> Grating mechanical aperture.

Parameter	Value
Grating clear aperture	160 mm
Grating substrate length	180 mm

G Exit Slit and Energy Resolution

The nominal exit-slit opening is $40 \times 20\ \mu m^2$ for both the HF and HR modes. The exit slit is a key determinant of the finite-slit photon-energy resolution, while the zero-slit resolution provides the intrinsic monochromator contribution.

The following illustrative budget indicates the scale of photon broadening appropriate for HR operation; it is not a finite-slit performance calculation for the

nominal opening. The HR concept uses an analyzer contribution of approximately 4 meV at pass energy PE = 10 eV and a photon contribution intended to limit the combined analyzer-plus-photon width to 110% of the analyzer-only value. For the adopted budget of two independent Gaussian contributions, with both analyzer and photon widths expressed as FWHM,

$$\Delta E_{\mathrm{a+ph}}^2 = \Delta E_{\mathrm{a}}^2 + \Delta E_{\mathrm{ph}}^2, \qquad \Delta E_{\mathrm{ph}} = \Delta E_{\mathrm{a}} \sqrt{1.10^2 - 1} \simeq 1.83 \text{ meV}. \qquad \text{(Eq. 4.2.8.1)}$$

The quoted 4 meV analyzer contribution and 1.83 meV photon contribution are both FWHM. The analyzer target is specified at PE = 10 eV. This two-component budget excludes sample, temperature, and other measurement contributions and is not a prediction of the complete measured energy resolution.

With the resolving-power convention $R = E/\Delta E$, using the 1.83 meV FWHM photon width as ΔE at 60 eV gives $R \simeq 32{,}800$. The nominal HR target of $R \simeq 30{,}000$ instead corresponds to $\Delta E = 2.00$ meV at 60 eV. The nominal target and the conditional 1.83 meV budget are therefore recorded separately; they are not interchangeable performance results.

HF has a nominal resolving-power target of approximately 15,000. Slit-dependent throughput and finite-slit resolution are evaluated with photon energy, polarization, and optical-error contributions. The HF/HR opening is specified in H×V; HE uses an adjustable exit slit. No increase in sample flux or spot size is quantified from a slit change without the branch calculation.

<Table 4.2.8.13> Exit slit and target energy resolution per mode.

Mode	Nominal exit slit	Target resolving power	Resolution note
HF	40 × 20 μm²	~15,000	Higher flux; reduced resolving power
HR	40 × 20 μm²	~30,000	Conditional photon budget 1.83 meV at 60 eV; see resolution discussion
HE	Adjustable	—	Rapid XPS checks

H Monochromator Specification Summary

The monochromator specifications are summarized in table 4.2.8.14. This summary complements the mode, grating, and exit-slit tables given above and collects the present design values in a single monochromator specification list.

Entries that apply only to crystal monochromators are marked as not applicable for the grating configuration.

<Table 4.2.8.14> ID25 VLSPGM monochromator specifications.

Item	Specification
Position (m)	M2 pre-mirror: 31.8; gratings: 32
Deflection / type	SX-700-type variable-line-spacing plane grating monochromator (VLSPGM)
Photon energy range	50–2000 eV (official beamline range); grating design coverage 35–215 eV (HF, HR) and 115–2005 eV (HE)
Energy resolution	HF: resolving power ~15,000; HR: nominal resolving power ~30,000 (2.00 meV at 60 eV); conditional photon budget 1.83 meV at 60 eV; HE: high-energy coverage
Crystal / optical element	HF, HR and HE variable-line-spacing grating patterns on G1/G2 substrates: HF 250 l/mm (nominal Cff 2.23), HR 600 l/mm (nominal Cff 3.24), HE 750 l/mm (nominal Cff 1.51); see table 4.2.8.11
Operating modes	HF (high flux, photon-flux-limited measurements at low photon energy), HR (high energy resolution for ARPES near low kinetic energy), HE (rapid XPS checks with coverage up to approximately 2 keV); see table 4.2.8.10
First crystal	n/a (grating); the SX-700-type configuration uses a plane pre-mirror (M2) at 31.8 m together with the plane grating
Second crystal	n/a (grating)
Beam offset	32 mm
Bragg angle range	n/a (grating); pre-mirror and grating angles are set by the nominal Cff of each mode (2.23 / 3.24 / 1.51)
Slope error	M2 and common grating-substrate specification: tangential < 0.2 µrad RMS; sagittal < 5 µrad RMS, over spatial wavelengths from 1 mm to the corresponding clear-aperture length
Roughness	M2 and common grating-substrate specification: < 1 nm RMS
Cooling	M2 side cooling; G1/G2 substrates: no cooling
Motion axes	Motorized pitch, roll, yaw, x and y; manual support pitch, roll, yaw, x, y and z
Grating clear aperture	160 mm
Grating substrate length	180 mm
Exit slit	Nominal opening 40×20 µm^2 in H$\times$V for HF and HR (HE adjustable); independent nanoARPES and microARPES exit slits at 39 m, implemented as a translatable slit and gas-cell assembly; see table 4.2.8.13

I M3 Switching and Horizontal Focusing Mirrors

M3 comprises the M3N and M3M horizontal-focusing branching mirrors for nanoARPES and microARPES, respectively. The system separates the beam into the nanoARPES and microARPES branches. The physical branch separation is

$\pm 4°$, corresponding to a total angular separation of 8°. The branch separation is implemented upstream of the independent exit slits so that the nanoARPES and microARPES branches can use branch-specific slit assemblies.

This configuration allows the downstream optical paths to be optimized independently while preserving a shared upstream source and monochromator.

J Branch Optical Designs

(a) nanoARPES Branch Optics

The nanoARPES branch is optimized for sub-micron beam delivery. The baseline focusing optic is a capillary mirror located at approximately 41 m from the source. The target focused beam size for the baseline nanoARPES operation is at most 1 μm FWHM. The capillary focusing concept uses a nominal focal-length scale of approximately 6 mm, with the sample 6 mm downstream of the capillary reference. This branch is intended for measurements on device samples, exfoliated flakes, moire systems, and locally inhomogeneous quantum materials.

The endstation layout will preserve compatibility with future FZP-based nanofocusing optics. FZP integration is reserved as a future expansion option. The expansion interface accommodates the optic, order-sorting aperture, alignment motion and vacuum integration.

(b) microARPES Branch Optics

The microARPES branch uses a mirror-based optical system consisting of M4M, M5M, and M6M before the sample position at 47.6 m. The target beam size at the microARPES sample is approximately 10×10 μm FWHM in H$\times$V. The microARPES branch supports general ARPES experiments and provides a complementary measurement mode for samples that do not require sub-micron focusing.

The branch design allows the incorporation of a sample camera to simplify beam and sample alignment. The working distance is treated as a layout and integration parameter rather than as the primary scientific performance metric.

K Mirror Specification Summary

The mirror specifications of the shared upstream optics and of the two branch optical systems are collected in table 4.2.8.15. The table summarizes the optical roles and mirror specification targets. M2, M3N and M3M are listed separately. M2 is the plane monochromator pre-mirror; M3N and M3M provide branch switching

and horizontal focusing. The capillary baseline is described separately in the nanoARPES branch design.

<Table 4.2.8.15> ID25 substrate-mirror specifications. M3N and M3M are the nanoARPES and microARPES horizontal-focusing branching mirrors. Slope-error specifications are RMS over spatial wavelengths from 1 mm to the corresponding clear-aperture length. Substrate mirrors use nominal 50 nm Au coating with Cr adhesion. Reflection directions follow the beamline hall/ring convention. M4M produces a 3° downward deflection at 1.5° grazing incidence, lowering the beam by approximately 42 mm before M5M; M5M restores horizontal propagation. The footprint-area entries are rounded reference dimensions; the specified optical clear areas will exceed these footprints.

Parameter	**M1**	**M2**	**M3N**	**M3M**	**M4M**	**M5M**	**M6M**
Installation location (m)	29	31.8	34	34	44.5	45.3	46.1
Height of incident beam	1400 mm	1400 mm	1432 mm	1432 mm	1432 mm	1390 mm	1390 mm
Reflection direction	Hall (right)	Up	Hall	Ring (left)	Down	Up	Hall
Mirror surface shape	Plane	Plane	Elliptic cylinder	Elliptic cylinder	Plane	Elliptic cylinder	Elliptic cylinder
Grazing incidence angle	1.8 °	2.4–8.2 °	2 °	2 °	1.5 °	1.5 °	0.8 °
Tangential radius	∞ (plane)	∞ (plane)			∞ (plane)		
Sagittal radius	∞ m	∞ m	∞ m	∞ m	∞ m	∞ m	∞ m
Substrate material	Si	Si	Si	Si	Si	Si	Si
Mirror size (L × W × T)	180 × 50 × 50 mm	420 × 50 × 50 mm	180 × 50 × 50 mm	180 × 50 × 50 mm	600 × 50 × 50 mm	600 × 50 × 50 mm	600 × 50 × 50 mm
Reference footprint area (L × W)	130 × 8 mm	340 × 9 mm	140 × 20 mm	140 × 20 mm	420 × 11 mm	490 × 12 mm	470 × 17 mm
Beam size at optic (H × V)	3.92 × 3.92 mm	4.3 × 4.3 mm	4.59 × 9.99 mm	4.59 × 9.99 mm	5.05 × 10.99 mm	5.79 × 12.59 mm	6.52 × 8.21 mm

(continued on next page)

(Table 4.2.8.15 continued)

Parameter	M1	M2	M3N	M3M	M4M	M5M	M6M
Coating and thickness	Au 50 nm nominal; (Cr adhesion)	Au 50 nm nominal; (Cr adhesion)	Au 50 nm nominal; (Cr adhesion)	Au 50 nm nominal; (Cr adhesion)	Au 50 nm nominal; (Cr adhesion)	Au 50 nm nominal; (Cr adhesion)	Au 50 nm nominal; (Cr adhesion)
Tangential slope error	<0.5 µrad RMS	<0.2 µrad RMS	<0.5 µrad RMS	<0.5 µrad RMS	<0.2 µrad RMS	<0.2 µrad RMS	<0.35 µrad RMS
Sagittal slope error	<5 µrad RMS	<5 µrad RMS	<5 µrad RMS	<5 µrad RMS	<5 µrad RMS	<5 µrad RMS	<5 µrad RMS
Roughness	<1 nm RMS	<1 nm RMS	<1 nm RMS	<1 nm RMS	<1 nm RMS	<1 nm RMS	<1 nm RMS
Cooling method	Side	Side	None	None	None	None	None
Mirror bender	No bender	No bender	No bender	No bender	No bender	No bender	No bender
Coating strip number		1			1	1	1
Coating stripe width	10 mm (W), per stripe	10 mm (W), per stripe			10 mm (W), per stripe	10 mm (W), per stripe	10 mm (W), per stripe
Motor axes	Pitch, roll, yaw, x, y	Pitch, roll, yaw, x, y	Pitch, roll, yaw, x, y	Pitch, roll, yaw, x, y	Pitch, roll, yaw, x, y	Pitch, roll, yaw, x, y	Pitch, roll, yaw, x, y
Manual support axes	Pitch, roll, yaw, x, y, z	Pitch, roll, yaw, x, y, z	Pitch, roll, yaw, x, y, z	Pitch, roll, yaw, x, y, z	Pitch, roll, yaw, x, y, z	Pitch, roll, yaw, x, y, z	Pitch, roll, yaw, x, y, z
Branch	Common upstream	Common upstream	nanoARPES	microARPES	microARPES	microARPES	microARPES

L Beam Conditions at the Sample

The beam conditions delivered to the nanoARPES and microARPES sample positions are summarized in table 4.2.8.16 for each combination of branch and monochromator operation mode. It records branch design targets, rather than energy-resolved calculated or measured performance. The listed energy intervals are grating design coverages; their overlap with the user range is given in table 4.2.8.11.

<Table 4.2.8.16> ID25 beam conditions at the nanoARPES and microARPES sample positions. The official beamline photon-energy range is 50–2000 eV; the values quoted per row are the design coverages of the HF/HR and HE gratings. The polarization modes are LH, LV, CR, and CL. HF and HR have a nominal exit-slit opening of 40×20 μm^2, in H×V; HE uses an adjustable exit slit. Beam sizes are FWHM design targets.

Configuration	Photon energy (eV)	FWHM spot target (μm)	Nominal RP target	Notes
nanoARPES branch, HF mode	35–215	≤ 1	~15,000	Capillary focusing; high flux for photon-flux-limited measurements
nanoARPES branch, HR mode	35–215	≤ 1	~30,000	Conditional photon budget 1.83 meV at 60 eV; see resolution discussion
nanoARPES branch, HE mode	115–2005	≤ 1	—	Rapid XPS checks up to approximately 2 keV
microARPES branch, HF mode	35–215	~10 × 10	~15,000	M4M/M5M/M6M mirror focusing; high flux
microARPES branch, HR mode	35–215	~10 × 10	~30,000	High-resolution ARPES near low kinetic energy
microARPES branch, HE mode	115–2005	~10 × 10	—	Rapid XPS checks up to approximately 2 keV

M Sample-Performance Definitions

The nanoARPES spot target is at most 1 μm FWHM. The microARPES target is approximately 10×10 μm FWHM in H×V. The illumination footprint and achieved spatial resolution are distinct quantities; sample scanning, positioning stability and measurement response also determine spatial selectivity.

Source flux is specified per 0.1% bandwidth. Delivered sample flux depends on the selected energy bandwidth, full angular acceptance, grating efficiency, coating reflectivity, slit opening, clipping and final-optic transmission. Sample spot and

resolving-power evaluations use these same branch and mode conditions. The capillary and KB optics provide the respective final focusing geometries.

N M2 Pre-Mirror Heat Load and Optical Tolerances

The worst-case heat-load design inputs for the M2 monochromator pre-mirror are 30 W and a maximum power density of 0.1 W/mm^2. These values apply to the pre-mirror at its worst-case operating angle.

Thermal design uses absorbed power and its spatial distribution, with coating properties, footprint and optical transmission. Thermal deformation and slope-error effects are evaluated against the energy-resolution and sample-spot requirements. The mirror-table metrology values provide the corresponding optical specification inputs.

O Optical-Element Motion and Supports

Substrate-mirror pitch control is divided into coarse alignment and fine adjustment. The coarse specifications describe positioning range, resolution and repeatability; the fine-stage command increment and angular stability are separate design targets. The first-stage mirror-motion targets are summarized in table 4.2.8.17. Command resolution is the smallest requested angular increment and does not by itself specify positioning accuracy, repeatability or vibration.

<Table 4.2.8.17> ID25 coarse and fine mirror-motion requirements and first-stage design targets. Fine-stage targets guide the support design; their implementation is adapted to each optic.

Parameter	Requirement / target
Coarse pitch travel	±5 mrad; M2 pre-mirror: ±3°
Coarse pitch resolution / repeatability	Each <5 µrad
Fine pitch travel	Approximately ±50 µrad
Fine pitch command resolution	≤0.02 µrad
Fine pitch stability	≤0.05 µrad; evaluation time and bandwidth specified for acceptance
Angular vibration	≤0.1 µrad; distinct from command resolution and positioning repeatability
Coarse roll / yaw	±5 mrad; resolution <50 µrad, repeatability <250 µrad
Mirror x travel	±5 mm
Mirror y travel	±20 mm for M3N/M3M; ±5 mm for other substrate mirrors
Translation resolution / repeatability	Each <10 µm

The initial support concept for the 600 × 50 × 50 mm Si mirrors (M4M, M5M and M6M) uses a mirror mass of approximately 3.5 kg, a longitudinal leg baseline of 400 mm and a transverse baseline of 200 mm. The support-level translation assumptions are ±5 mm in Y and Z; their mapping to the optical-element coordinates is established during mechanical integration. The coarse vertical actuator stroke is at least ±6 mm, with ±7.5 mm preferred, and the coarse horizontal stroke is approximately ±6–7 mm. These actuator strokes include the accommodation needed for the support geometry and are distinct from the mirror translation ranges above.

Fine pitch adjustment uses three high-stiffness piezo actuators with a metrology baseline of 400–450 mm. PI P-844.30 is an initial candidate, with the supplied nominal values of 45 µm stroke and 75 N/µm stiffness; actuator selection is finalized against the installed load, preload and usable stroke. The initial roll/yaw accuracy target for this support concept is approximately 1–2 µrad, separate from the coarse-drive resolution and repeatability. The first structural mode is required to exceed 100 Hz, with a design goal of at least 150 Hz. This support concept is a first-stage design basis for the 600 mm mirrors; support dimensions and actuator arrangements for M1, M2 and M3N/M3M are adapted to their individual geometry and loads.

The common grating-substrate motion requirements retain pitch travel of ±5°, with pitch resolution and repeatability each below 2 µrad, and x travel of ±50 mm. These are separate from the mirror fine-stage targets. Grating roll and yaw retain ±5 mrad ranges, resolution below 50 µrad and repeatability below 250 µrad; y travel is ±5 mm with translation resolution and repeatability each below 10 µm. The drives use vendor-standard drivers. Manual chamber-support adjustment provides ±1° in pitch, roll and yaw and ±10 mm in x, y and z. Coordinates follow the optical-element coordinate convention.

4.2.8.5 Photon Transfer Line

A Scope and Common Engineering Basis

The Photon Transfer Line (PTL) integrates the transport vacuum, supports, diagnostics, alignment, controls, and utilities from the front-end exit through the optical hutch to the experimental stations. Optical prescriptions and branch performance targets are maintained in section 4.2.8.4. Common PTL component examples are in section 3.2, interlocks in section 3.3, motion and control infrastruc-

ture in section 3.4, acquisition infrastructure in section 3.5, and cooling and hutch infrastructure in section 3.6. These sections provide the common engineering basis for ID25 integration.

B Boundary Interfaces and Responsibilities

The boundaries in table 4.2.8.18 organize the subsystem requirements and participating engineering functions. M3 provides branch switching and horizontal focusing upstream of the independent exit slits. Branch operation uses the shared source and monochromator, with beam-permit logic coordinated with the switching state.

<Table 4.2.8.18> ID25 subsystem interface requirements.

Boundary	Participating functions	Interface requirements
FE to upstream optics	FE, optics, vacuum, protection	Exit trajectory/aperture, transmitted spectrum and power, flange, isolation and beam permit; common FE/interlock basis
Monochromator to branch slits	Optics, mechanics, controls	M3 trajectories and switching state, focus reference, slit opening and longitudinal travel, diagnostics; common PTL/control basis
Branch transport to station	Branch optics, vacuum, station integration	Final optic and sample references, working distance, support/fiducials, alignment and isolation; ID25 geometry required
Preparation to stations	Preparation, station, vacuum, controls	Transfer paths to both stations, compatible holders, contacts, valves, pressure recovery and transfer permissions
Hutch and services	Civil, utilities, controls, experiment	Floor/support interfaces, service loads and routing, access/maintenance envelopes; common utility basis and ID25 service inputs

C Exit-Slit and Gas-Cell Assembly

Each branch has an independent exit slit. The concept includes a translatable slit/gas-cell assembly for longitudinal focus adjustment and energy calibration. HF/HR use the nominal H×V opening in table 4.2.8.13; HE uses an adjustable exit slit.

The mechanical design must define longitudinal stroke, transverse alignment, aperture H/V conventions, position readback, fiducials, and bellows accommodation. The calibration procedure must specify gas species and reference features, operating pressure, pumping and isolation, and how the fitted energy reference is applied to the monochromator control. The assembly must integrate gas handling, control permissions, and vacuum recovery before measurement.

D Diagnostics, Alignment, and Stability

Diagnostic functions include beam viewers, photodiodes or drain-current monitors, exit-slit cameras, and gas-cell calibration. Diagnostic integration must coordinate insertion states, signal readout, and station acquisition. The control and acquisition interfaces should follow the available common architectures in sections 3.4 and 3.5.

Supports and fiducials must preserve the optical reference coordinates and provide installation and commissioning alignment. A stability budget must allocate relative beam-to-sample motion among optical supports, slit assemblies, final optics, and the manipulator. Vibration, thermal drift, and position reproducibility limits must be derived from the selected spot target, region of interest, scan dwell time, and permissible acquisition drift. The angular-vibration requirement for the optical elements is 0.1 µrad or less. The fine-pitch command-resolution target is $\leq$0.02 µrad and the pitch-stability target is $\leq$0.05 µrad, as summarized in table 4.2.8.17. These targets are distinct from coarse positioning resolution and repeatability. Acceptance definitions will specify the evaluation time, frequency band and amplitude convention for stability and vibration. The stability allocation connects those measurement requirements to the mechanical design.

E Vacuum Sectors and Transfer Protection

The front-end vacuum basis is described in section 3.1; the common protection logic is in section 3.3. The ID25 upstream optics, gas-cell region, two branch lines, measurement stations, and preparation/transfer system require a coordinated sector and isolation design. Sector isolation must coordinate valve locations, pumping and gauges, bake-out compatibility, venting and recovery, and station pressure requirements. Gas-cell operation and sample introduction must be isolated as required by that design; no vacuum window is assumed in the soft X-ray transport concept.

F Hutch, Supports, and Utilities

Cooling and hutch infrastructure are described in section 3.6. ID25 must define service demand and routing for cooling, cryogenic systems, power, compressed air where required, cabling, gas supply/exhaust, and control racks. Support choice, floor interfaces, thermal management, and maintenance access require coordination with the final optical and station envelopes. The microARPES sample reference

is 47.6 m, 1.5 m downstream of M6M. The floor plan must accommodate the common preparation connection to both stations and the required maintenance and transfer envelopes.

4.2.8.6 End-Station

A Endstation Overview

The ID25 endstation design includes nanoARPES and microARPES capabilities. The nanoARPES capability is the primary identity of the beamline, while the microARPES branch provides a complementary mode for general ARPES measurements. Both branches share the same source and monochromator. HF and HR support ARPES measurements, while HE primarily provides rapid XPS checks of sample composition and chemical states, as described in Section 4.2.8.4 D.

B nanoARPES Endstation

(a) Capillary-Based nanoARPES

The baseline nanoARPES focusing optic is a capillary mirror. The target beam size is at most 1 μm FWHM at the sample. This focusing mode is intended for spatially selective ARPES on small devices, exfoliated flakes, moire materials, and heterogeneous quantum materials. The capillary configuration is the baseline, with a focal-length scale of approximately 6 mm. Its working distance and sample geometry must integrate the capillary focus with the analyzer entrance.

(b) Future Fresnel Zone Plate Upgrade Path

The nanoARPES endstation reserves mechanical and vacuum integration possibilities for a future Fresnel zone plate (FZP) upgrade. FZP is included as an expansion interface. Spin-ARPES and MBE expansion interfaces are also to be reserved; these future capabilities are not baseline installed equipment.

(c) Sample Manipulator and Low-Temperature Capability

The nanoARPES endstation targets low-temperature operation with a sample-temperature goal of approximately 30 K. The nanoARPES manipulator uses a 5-axis configuration. Fermi-surface mapping is expected to be performed primarily using the detector deflector scan rather than relying entirely on mechanical sample rotation.

(d) Device and Operando Capability

The nanoARPES endstation will support device-oriented measurements with at least four electrical contacts. This capability enables gate-voltage, bias-voltage, and related electrical-control experiments on nanoscale and mesoscopic device samples. The broader operando capability is therefore described as an endstation capability rather than as a separate beamline-level operating mode.

C microARPES Endstation

(a) microARPES Beam Delivery

The microARPES endstation targets a beam size of approximately 10×10 μm FWHM in H×V at the sample. Both HF and HR modes are intended to support this beam size target. The microARPES branch is designed for general ARPES experiments that benefit from a larger beam and a more conventional sample environment.

(b) Sample Alignment and Camera System

A sample camera is planned to support beam and sample alignment in the microARPES branch. The camera system is expected to improve the efficiency of finding the beam on the sample and aligning the region of interest before ARPES acquisition.

(c) Low-Temperature Capability

The microARPES endstation targets a sample temperature of approximately 10 K. The cryostat, manipulator and holder must support low-temperature alignment and sample transfer.

D Common Requirements for the Two ARPES Analyzers

Each station has a separate ARPES analyzer. The requirements below apply to both analyzers. The principal requirement is compatibility with a future spin-ARPES upgrade. The analyzer system should also support deflector-based momentum-space mapping, which is particularly important for nanoARPES measurements where large mechanical sample rotations may be limited by device wiring, focusing optics, or compact endstation geometry. The common analyzer requirements are given in table 4.2.8.19.

<Table 4.2.8.19> Common requirements for the separate nanoARPES and microARPES analyzers.

Parameter	Requirement
Configuration	Separate analyzer at each station
Kinetic-energy coverage	Electron kinetic-energy coverage matched to the beamline experiments
Energy resolution	Target approximately 4 meV FWHM at PE = 10 eV; performance evaluated with the electron kinetic energy, entrance slit, lens mode and acquisition conditions
Angular resolution and acceptance	Angular performance evaluated with electron kinetic energy and lens/deflector conditions
Deflector mapping	Deflector scan with calibrated angular mapping
Acquisition and control	Energy/angle mapping coordinated with sample position and electrical control
Spin expansion interface	Analyzer exit geometry, mounting, vacuum connection and clearance compatible with future spin-ARPES
Detector hardware	Detector readout integrated with energy/angle mapping and acquisition
Sample/analyzer geometry	Working distance, entrance axis and photon incidence compatible with electrical contacts and cryogenic clearances

E Sample Preparation and Transfer System

The sample-preparation infrastructure will include a glovebox, load-lock, vacuum suitcase interface, preparation chamber, cleaver, and evaporator. These elements form the agreed baseline common preparation system, connected to both measurement stations; both destinations use compatible transfer interfaces. A future MBE connection is reserved as an expansion path rather than as a baseline requirement. The preparation and transfer components are listed in table 4.2.8.20.

The intended workflow is glovebox handling of air-sensitive samples, introduction through the load-lock, preparation such as cleaving or evaporation as required, and vacuum transfer to either measurement station. A vacuum-suitcase interface provides an alternative vacuum-compatible entry path. Holder compatibility, orientation, electrical-contact engagement, transfer reach, sector valves, and pressure recovery must be defined for both destinations. Cleaving and evaporation are experiment-dependent operations rather than mandatory steps for every sample.

<Table 4.2.8.20> ID25 sample preparation and transfer components.

Preparation / transfer component	Status	Function
Glovebox	Baseline	Air-sensitive sample handling
Load-lock	Baseline	Rapid sample introduction
Vacuum suitcase interface	Baseline	Vacuum-compatible sample transfer
Preparation chamber	Baseline	In-vacuum sample preparation
Cleaver	Baseline	Fresh surface preparation
Evaporator	Baseline	*in-situ* deposition or dosing workflow
MBE connection	Future expansion	Extended growth/transfer capability

F Endstation Instrument Summary

The photon-energy range, beam size and resolving-power targets to each station are not repeated here; they are given once, for every branch and monochromator mode, in table 4.2.8.16. The instrument-side specifications of the two stations are summarized in table 4.2.8.21.

<Table 4.2.8.21> Comparison of the two ID25 stations; entries are concept requirements and targets.

Item	nanoARPES	microARPES
Baseline final optics	Capillary mirror	M4M/M5M/M6M branch mirrors
Analyzer	Separate analyzer; common requirements in table 4.2.8.19	Separate analyzer; same common requirements
Sample temperature target	Approximately 30 K	Approximately 10 K
Manipulator	5-axis manipulator with alignment and region-position retention	Manipulator and holder compatible with alignment and transfer
Electrical contacts	At least four; gate/bias experiments	At least four; gate/bias experiments
Momentum mapping	Primarily deflector scan to limit sample motion	Deflector mapping
Alignment	Beam/sample mapping and position retention	Sample camera for alignment
Preparation and transfer	Connected to common baseline preparation system	Connected to same common preparation system
Expansion	FZP integration reserved, with no spot target; spin/MBE interfaces reserved	Spin interface reserved; common preparation system accommodates future MBE connection

G Integrated Low-Temperature and Electrical Operation

Both stations require at least four electrical contacts. The sample holders, vacuum feedthroughs, wiring and thermal anchoring must be compatible with

the respective temperature targets and with sample transfer. Contact engagement, signal isolation and electrical measurement coordination must support the applied gate/bias conditions and low-temperature operation.

For nanoARPES, the manipulator must retain the selected region within the focused illumination during energy and deflector scans. The capillary, analyzer entrance, cryostat, contacts, and sample camera or mapping diagnostics must be integrated without losing the required alignment access. Relative motion and repositioning requirements are to be allocated through the stability budget described in section 4.2.8.5, rather than assigned arbitrary tolerances.

H Expansion Interfaces

Future FZP integration requires a reserved optic/OSA mounting envelope, alignment access and compatible vacuum interfaces; the interface accommodates the optic and order-sorting aperture. Spin expansion requires analyzer-compatible mounting and vacuum/clearance interfaces at each station. The common preparation system must reserve a future MBE connection with compatible holders, isolation, transfer reach and access. These are provisions for future integration, not installed baseline FZP, spin detection, or MBE equipment.

References

[1] Jongha Park et al. High Heat Load Front-End Mechanical Design and Thermal Analysis Report. Internal Document PAL-INT/ME-2026-003. Pohang Accelerator Laboratory, June 2026.

4.2.9 Soft X-ray Nanoprobe (ID26)

The ID26 Soft X-ray Nanoprobe beamline is an industry-oriented soft X-ray beamline for the KLS project, dedicated to nanoscale imaging and spectroscopy of advanced semiconductor, battery, and energy materials. This chapter describes the ID26-specific design of the photon source (EPU78 undulator), the front-end, the beamline optics (overall optical layout, mirror parameters, the plane grating monochromator, optical performance, and beam diagnostics), the photon transfer line (PTL: design, vacuum, and vibration stability), and the end-station (mechanical design, detector, and DAQ). The beamline integrates two complementary branches: a nano-imaging branch based on STXM and ptychography, and a versatile spectroscopy branch based on XPS and XAS.

4.2.9.1 Target Purpose and Objective

Recent advances in semiconductor devices, batteries, and energy-related technologies have driven rapid increases in device integration and structural miniaturization, resulting in a growing demand for high-resolution analytical techniques capable of probing the structural, chemical, and functional properties of materials at the nanoscale. In particular, fourth-generation synchrotron light sources provide ultra-low-emittance electron beams with emittances on the order of several tens to hundreds of pm·rad, enabling exceptionally high brightness and spatial coherence. These characteristics provide an ideal platform for nanoscale imaging and coherent X-ray–based characterization techniques.

The soft X-ray energy range (90–2600 eV) is particularly well suited for exploiting the ultra-low-emittance characteristics of fourth-generation light sources due to its relatively long wavelength, providing high spatial coherence and enabling advanced imaging techniques such as ptychography and coherent imaging with spatial resolutions well below several tens of nanometers. Furthermore, this energy range encompasses the K absorption edges of light elements such as C, N, and O, the L absorption edges of transition metals, and extends to higher-energy edges such as the S K-edge, making it highly suitable for investigating chemical states, electronic structures, and elemental distributions in functional materials. In particular, soft X-rays offer high sensitivity to light elements and excellent chemical-state contrast, making them an essential analytical tool for next-generation semiconductor, battery, and energy-material research.

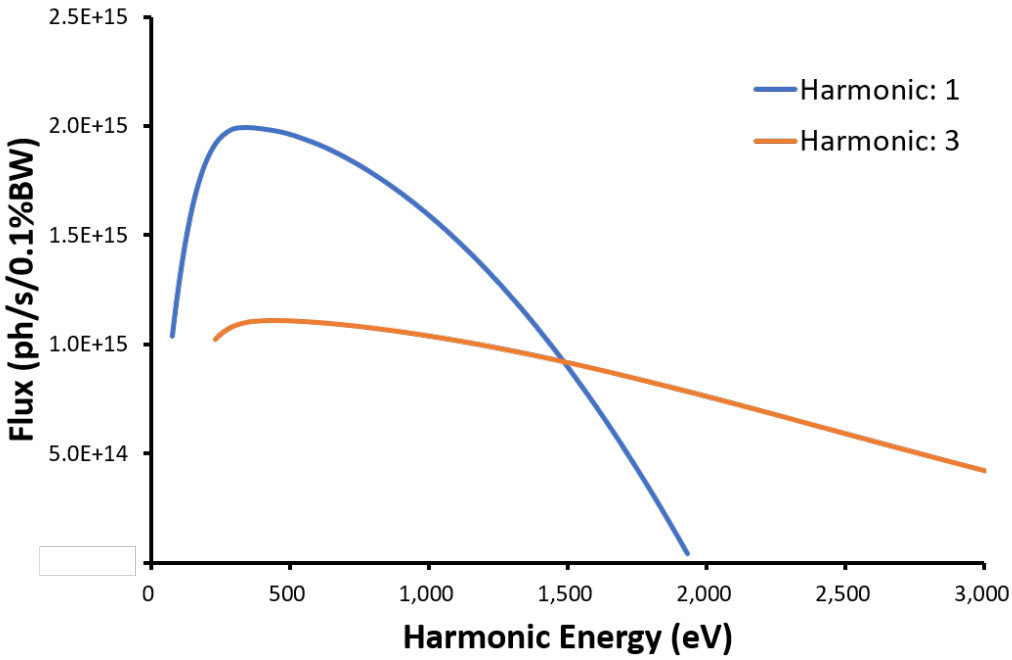
The ID26 Soft X-ray Nanoprobe Beamline is designed to provide nanoscale

imaging capabilities based on Scanning Transmission X-ray Microscopy (STXM) and Ptychography for high-resolution characterization of semiconductors, batteries, and energy materials. STXM combines X-ray Absorption Spectroscopy (XAS) with a nano-focused X-ray beam to visualize elemental distributions and chemical states with nanoscale spatial resolution. Ptychography utilizes coherent X-rays and phase retrieval of scattered diffraction patterns to achieve high-resolution nanoscale imaging beyond the limitations of conventional focusing optics, providing information on electron-density distributions, structural inhomogeneities, strain, and localized defects. STXM enables efficient and quantitative chemical and elemental mapping through direct raster-scanning measurements, while ptychography achieves substantially higher spatial resolution through coherent diffraction imaging and computational reconstruction. Together, these complementary techniques form an integrated nano-imaging platform capable of simultaneously investigating the chemical and structural characteristics of advanced materials. In particular, the beamline will enable direct observation of localized defect distributions and defect dynamics in semiconductor devices, as well as structural and chemical changes occurring in localized regions of battery electrodes and electrolytes during charge–discharge processes, thus supporting key industrial research and development activities.

In addition to the imaging branch, the beamline will include a versatile spectroscopy branch providing high-throughput measurements of chemical states and electronic structures through XAS, XPS, and related spectroscopic techniques. These complementary spectroscopy capabilities will support the quantitative interpretation of the imaging results and provide rapid and efficient analytical services to industrial users. Through the integration of advanced imaging and spectroscopy capabilities, the ID26 Soft X-ray Nanoprobe Beamline will maximize its impact as an industry-oriented beamline dedicated to the characterization of advanced materials.

4.2.9.2 Photon Source

A 3.62 m elliptically polarizing undulator (EPU78, 44 periods of 78 mm) will be installed in the ID26 Soft X-ray Nanoprobe beamline. The undulator provides high coherent photon flux and brightness and supports horizontal, vertical, and circular polarization modes through polarization switching. The photon energy range of 90–2600 eV is covered using fundamental and third harmonic radiation, as shown in <Figure 4.2.9.1>.



<Figure 4.2.9.1> Flux curve for EPU78 undulator in 1st and 3rd harmonics.

The minimum magnetic gap of the undulator is 15 mm, corresponding to a maximum vertical deflection parameter of $K_y = 6.948$ and a peak magnetic field of 0.954 T. Under these conditions, the minimum photon energy achievable from fundamental radiation is 77.5 eV.

Although the undulator can generate photons below 90 eV under selected operating and polarization conditions, the nominal lower energy limit of the beamline is set to 90 eV to include the technologically important EUV energy near 92 eV while maintaining favorable thermal conditions for stable routine operation. Operation at lower photon energies generally requires smaller undulator gaps, resulting in increased total radiated power and heat loads on the downstream front-end and optical components. Although operation under higher heat loads is technically feasible with appropriate cooling, it places greater demands on thermal deformation control and beam stability. The lower limit of 90 eV was therefore selected as a practical operating point that provides access to the EUV regime while maintaining practical thermal conditions for stable and reliable beamline operation. Detailed heat-load considerations are discussed in the front-end section.

The resulting design energy range of 90–2600 eV covers the EUV–soft X-ray transition region and key absorption edges relevant to soft X-ray spectroscopy and

microscopy, including the C, N, and O K-edges, transition-metal L-edges, and the S K-edge. The expected photon flux, brightness, and coherent flux were evaluated using spectral simulations, and the calculated source parameters are summarized in table 4.2.9.1, and the polarization-dependent magnetic and spectral parameters are listed in table 4.2.9.2.

<Table 4.2.9.1> EPU78 undulator specification at the ID26 Soft X-ray Nanoprobe beamline. Magnetic and power values are given at the 15 mm minimum magnetic gap, for the vertical polarization mode that carries the highest power.

Undulator	**Period (mm)**	**Length (m)**	**Gap size (mm)**	$K_{\max}$	**Max total power (kW)**	**Power density (kW/mrad^2)**	**Number of periods**
EPU78	78	3.62	15–100	6.95	12.655	46.5	44

<Table 4.2.9.2> EPU78 magnetic and spectral parameters at the ID26 Soft X-ray Nanoprobe beamline. Magnetic quantities are given at the 15 mm minimum magnetic gap for the three available polarization modes.

Parameter	**Value**
Peak magnetic field, B_0 (T)	0.954 (V) / 0.776 (H) / 0.602 (Circular)
Deflection parameter, K	6.95 (V) / 5.65 (H) / 4.39 (Circular)
First-harmonic energy, E_{1st} (eV)	77.45 (V) / 114.73 (H) / 96.31 (Circular)
Beamline design photon energy range (eV)	90–2600
Photon flux (ph/s/0.1%BW)	1.22×10^{15}
Brilliance (ph/s/mm^2/mrad^2/0.1%BW)	1.52×10^{19}

4.2.9.3 Front-End

The Front-End of the ID26 Soft X-ray Nanoprobe beamline has been designed with careful consideration of beam acceptance, thermal load, vacuum integrity, and machine protection to safely accept synchrotron radiation from the storage ring while protecting both the storage ring and beamline components. The Front-End consists of a fixed mask, movable mask, photon shutter, safety shutter, beam position monitor (BPM), gate valve, and vacuum interlock system.

The beam acceptance was evaluated over the operating energy range, including the low-energy condition where the source divergence is largest. The current Front-End design uses a 3.12 mm mask opening. This corresponds to an acceptance of approximately 2.4σ acceptance at 90 eV (59.3% flux) and approximately 4σ acceptance at 250 eV (91% flux), providing a practical balance between photon acceptance and downstream heat-load control.

To evaluate the thermal stability of the Front-End optics, thermal analyses were performed under the low-energy/high-power operating condition. The movable mask will be equipped with a water-cooling system capable of dissipating the heat load while maintaining the thermal and mechanical stability required for reliable beamline operation. The M1 mirror is located 29 m downstream from the source and operates at a grazing incidence angle of 1°. Spectral/heat-load calculations at 90 eV give an incident heat load of approximately 300 W on M1, corresponding to a peak heat density of approximately 0.574 W/mm^2. After M1, the heat load incident on M2 at 34.5 m is reduced to approximately 24.7 W, with a peak heat density of approximately 0.0481 W/mm^2. Detailed thermo-mechanical verification of the mirror and cooling design will be performed during the engineering design phase.

To evaluate the thermal stability of the Front-End optics, thermal analyses were performed under the maximum heat-load condition. The movable mask will be equipped with a water-cooling system capable of dissipating the heat load while maintaining the thermal and mechanical stability required for reliable beamline operation. The steady-state thermal and structural analysis of the movable mask common to the IVU and EPU Front-Ends, carried out for the worst-case mis-steering heat load that sizes its cooling channels, is given in the high heat load front-end mechanical design and thermal analysis report [1]. After passing through the movable mask, the beam is incident on the M1 mirror located 29 m from the source. The M1 mirror operates at a grazing incidence angle of 1°, resulting in a beam footprint of 199.4 mm (tangential direction) $\times$ 3.5 (sagittal direction) mm. The total incident power on the M1 mirror is 300 W, and the corresponding peak heat density is approximately 0.574 W/mm^2. These values fall within the typical operating range of water-cooled silicon high-heat-load mirrors, and the resulting thermal deformation is expected to have a negligible impact on optical performance.

To protect the ultra-high vacuum (UHV) environment of the storage ring, the Front-End incorporates gate valves and a vacuum interlock system. In addition, a differential pumping section is implemented to isolate the vacuum environments of the storage ring and beamline, thereby minimizing the impact of potential vacuum failures on storage ring operation.

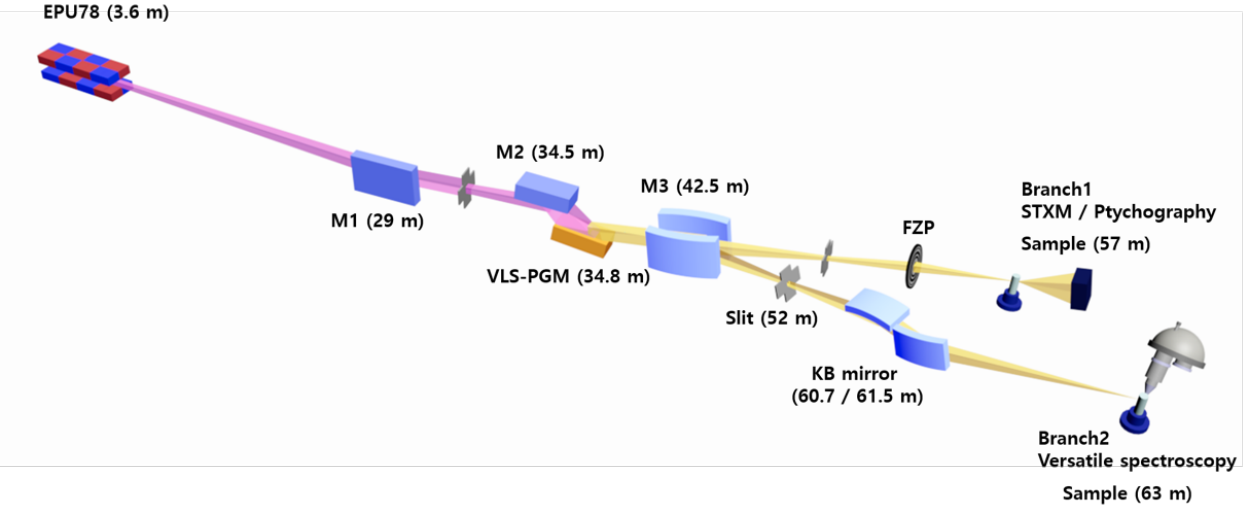
For machine protection and radiation safety, the Front-End is equipped with photon shutters and safety shutters. In the event of abnormal vacuum conditions, cooling-water failure, optical component overheating, BPM faults, or radiation

safety alarms, the interlock system automatically closes the beam shutter to protect both the storage ring and beamline equipment. The trip conditions for the vacuum, cooling-water, temperature and radiation inputs, and the shutdown devices each of them closes, are defined in the beamline interlock system design report [2].

Detailed systems of the Front-End mechanical design, vacuum system, and safety interlock system are provided in Chapter 3. The mechanical design of the EPU-type front-end and of its individual beam-intercepting components is given in the high-heat-load front-end design report [1].

4.2.9.4 Beamline Optics

A Overall Optical Layout and Components Roles



<Figure 4.2.9.2> Optical layout of the ID26 Soft X-ray Nanoprobe beamline. Two branch configurations for nano-imaging beamline using STXM/Ptychography and versatile spectroscopy beamline using XPS/XAS.

The M1 mirror is located 29 m downstream of the undulator source and intercepts the beam transmitted through the movable front-end mask positioned at 26 m. As described in the Front-End section, the mirror is subjected to an absorbed heat load of approximately 300 W and primarily serves to mitigate the thermal load delivered to downstream optical components.

The M2 mirror functions as the pre-mirror of the monochromator system. By controlling the incidence angle on the grating while maintaining a fixed-focus constant (C_{ff}), it enables stable monochromator operation with nearly constant resolving power over the operating energy range. In addition, the M2 mirror

ensures that the diffracted beam remains focused at a fixed exit slit position during energy scans.

The Variable Line Spacing Plane Grating Monochromator (VLS-PGM) provides monochromatization of the incident radiation. The variable groove density profile simultaneously introduces focusing properties and reduces optical aberrations, eliminating the need for additional focusing optics within the monochromator. A detailed description of the monochromator design is provided in Section 4.2.9.4 C.

The M3 optics consist of two independent elliptical branching mirrors that direct the beam to the imaging (Branch 1) and spectroscopy (Branch 2) end-stations, as shown in <Figure 4.2.9.2>. The Branch 1 mirror operates at a grazing incidence angle of 1° to maximize photon flux for coherent imaging experiments, while the Branch 2 mirror operates at 1.5° incidence to achieve greater beam separation and facilitate mechanical integration of the two branches. In addition to beam steering, both mirrors provide horizontal focusing because of their elliptical surface profiles, thereby reducing the demagnification requirements of the downstream focusing optics. The mirrors are located approximately 7.7 m downstream of the grating, providing adequate clearance between optical components. As a result, a lateral separation of approximately 1.3 m is achieved between neighboring beamlines at the end-station position (~57 m from the source), ensuring sufficient space for installation and maintenance while avoiding mechanical interference.

The exit slit, located at approximately 52 m from the source in the current design, serves as both an energy-selecting aperture and a well-defined secondary source. It defines the monochromator energy bandwidth while providing a stable object plane for the downstream focusing optics. The slit width can therefore be selected according to the experimental mode: a narrower slit is used for high-resolution spectroscopy, whereas a moderately wider slit is used for routine STXM operation to increase photon throughput while retaining adequate spectral resolution and coherence.

Fresnel Zone Plates (FZPs) are employed as nano-focusing elements to deliver nanometer-scale X-ray beams to the sample position. The exit-slit-to-FZP distance is set to approximately 5 m to ensure that the incident beam footprint at the FZP is larger than the FZP aperture over the entire operating energy range of 90–2600 eV. This geometry provides sufficient illumination of the zone plate in both the horizontal and vertical directions, avoiding significant underfilling of the FZP and enabling effective utilization of its full numerical aperture for STXM and

ptychographic imaging. Different FZP diameters and zone widths can be selected depending on the photon energy and required spatial resolution.

For the spectroscopy branch, Kirkpatrick–Baez (KB) mirrors are used to provide micrometer-scale focusing on the sample position. The vertical and horizontal focusing functions are provided independently by two orthogonally arranged mirrors. Each KB mirror incorporates two strips with different surface curvatures, providing two distinct operating configurations: a focused mode and a defocused mode. In the focused mode, the KB system is designed to achieve a beam size of approximately 5×5 μm^2 at the sample position for spatially resolved spectroscopy. In the defocused mode, the alternative-curvature strips provide a substantially larger beam of approximately 50–100 $\times$ 50–100 μm^2, enabling measurements requiring a larger illuminated area or reduced photon flux density. Selection between the two modes is achieved by positioning the corresponding mirror strips in the beam path. A summary of the optical components and their functions is provided in table 4.2.9.3.

<Table 4.2.9.3> List of optical components at the ID26 Soft X-ray Nanoprobe beamline, in beam order (distances measured from the source).

Distance (m)	Location	Component	Description
0		EPU78	Period 78 mm, length 3.6 m
29	Optical Hutch	M1	Heat-load mitigation
34.5		M2	Variable included-angle control
34.8		VLS-PGM	Monochromatization
42.5		M3	Beam branching and horizontal focusing
52		Exit slit	Secondary source and energy selection
57	Imaging branch	FZP	Nano-focusing
60.7	Spectroscopy branch	VKB	Vertical micro-focusing
61.5		HKB	Horizontal micro-focusing

B Mirror Parameters

The ID26 Soft X-ray Nanoprobe beamline employs M1, M2, two independent M3 branching mirrors, and a pair of KB mirrors for the spectroscopy branch. All mirrors use silicon (Si) substrates. Au is used as the baseline coating for efficient transport through the soft X-ray range, while an Au/Rh coating option is adopted for M2 to maintain higher-energy throughput. Each mirror is dimensioned to

accommodate the corresponding beam footprint and to preserve wavefront quality and focusing performance.

Mirror surface roughness affects the phase error of the reflected wavefront and contributes to diffuse scattering, both of which are important factors for coherent imaging performance. The RMS phase error induced by mirror roughness can be approximated as

$$\Delta\phi = \frac{2\pi}{\lambda}\left(2\sigma_r \sin\theta_i\right),$$

where σ_r is the RMS surface roughness and θ_i is the grazing incident angle.

For representative operating energies, the optical surface specification has been tightened to an RMS roughness of 0.5 nm. The resulting accumulated wavefront error remains small over the principal soft X-ray operating range and satisfies the diffraction-quality criterion required for coherent imaging. The calculated total RMS phase errors and Strehl ratios are approximately 0.13 rad / 0.983 at 530 eV, 0.177 rad / 0.969 at 850 eV, and 0.453 rad / 0.814 at 2500 eV, respectively. These results show that the total Strehl ratio remains above 0.8 up to approximately 2.5 keV, consistent with the Maréchal criterion for near-diffraction-limited wavefront quality. In addition to phase degradation, surface roughness can produce diffuse scattering and photon-flux loss; therefore, the 0.5 nm RMS roughness specification is adopted for the principal beamline mirrors.

Slope error introduces angular deviations of the reflected beam and directly affects the final beam size and focusing performance. In grazing-incidence optics, the impact of tangential slope error is significantly greater than that of sagittal slope error. Since most mirrors operate at grazing incidence angles below 2°, the influence of sagittal slope error on the reflected beam direction is reduced to approximately 1/30 of that of the tangential slope error. Consequently, tangential slope error must be controlled more strictly from the perspectives of beam focusing and wavefront preservation. Slope error introduces angular deviations that contribute to focal/image blur and energy-resolution degradation. The current design therefore adopts sub-μrad tangential slope-error specifications: 0.5 μrad for M1 and M3, 0.2 μrad for M2, and stringent values for the KB mirrors. These values are selected from the overall focusing and wavefront-error budget rather than from flux transmission alone. For the spectroscopy branch, the KB mirrors constitute the final focusing optics and require particularly stringent slope-error control. The current specifications are 0.2 μrad for the vertical KB mirror and 0.35 μrad for the horizontal KB mirror, with sagittal slope error below 5 μrad. Together

with the upstream optical tolerances, these specifications are intended to preserve the target 5 μm near-round focused beam at the spectroscopy sample position. The detailed mirror specifications are summarized in table 4.2.9.4.

<Table 4.2.9.4> Mirror parameters at ID26 Soft X-ray Nanoprobe beamline. Here p and q are the object and image distances of each focusing mirror. For the horizontally focusing M3 branching mirrors each mirror images the source onto the exit slit, giving $p = 42.5$ m (source to M3 at 42.5 m) and $q = 9.5$ m (M3 to the exit slit at 52 m); for the KB pair the exit slit is imaged onto the sample at 63 m, giving $p = 8.7$ m, $q = 2.3$ m (vertical) and $p = 9.5$ m, $q = 1.5$ m (horizontal). The unbent plane mirrors M1 and M2 and the non-focusing plane of each focusing cylinder are left flat (> 100 km).

Parameter	**M1**	**M2**	**M3**	**VKB**	**HKB**
Installation location (m)	29	34.5	42.5	60.7	61.5
Reflection direction	TBD	Vertical (upward)	Horizontal (branching; Branch 1 towards the hall, Branch 2 towards the ring)	Vertical (upward)	Horizontal (towards the hall)
Mirror surface shape	Plane	Plane	Elliptical cylinder	Elliptical cylinder	Elliptical cylinder
Incident angle	1°	1–5° (variable)	1° (Branch 1) / 1.5° (Branch 2)	1°	1°
Tangential radius	> 100 km (plane)	> 100 km (plane)	889.8 m (1°, Branch 1); 593.2 m (1.5°, Branch 2)	208.5 m	148.5 m
Sagittal radius	> 100 km (plane)	> 100 km (plane)	> 100 km (cylinder)	> 100 km (cylinder)	> 100 km (cylinder)
Substrate material	Si	Si	Si	Si	Si
Mirror size (L × W × T)	600 × 50 × 50 mm	600 × 50 × 50 mm	300 × 50 × 50 mm	600 × 50 × 50 mm	600 × 50 × 50 mm
Coating material	Au	Au	Au	Au	Au
Coating strip number	1	1	1	2	2

(continued on next page)

(Table 4.2.9.4 continued)

Parameter	M1	M2	M3	VKB	HKB
Coating stripe width	10 mm (W), per stripe	10 mm (W), per stripe	10 mm (W), per stripe	10 mm (W), per stripe	10 mm (W), per stripe
Tangential slope error	0.5 µrad RMS	0.2 µrad RMS	0.5 µrad RMS	0.2 µrad RMS	0.35 µrad RMS
Sagittal slope error	5 µrad	$<$ 5 µrad RMS	$<$ 5 µrad RMS	$<$ 5 µrad RMS	$<$ 5 µrad RMS
Roughness	0.5 nm RMS	0.5 nm RMS (HSF)	0.5 nm RMS (HSF)	0.5 nm RMS (HSF)	0.5 nm RMS (HSF)
Cooling method	Water cooling	Side cooling	None	None	None
Mirror bender	None	None	None	None	None
Motor axis	Pitch, roll, yaw, x, y	Pitch, roll, y, scan	Pitch, roll, yaw, x, y	Pitch, roll, yaw, x, y, z	Pitch, roll, yaw, x, y
Manual axis (granite base)	Pitch, roll, yaw, x, y, z	Pitch, roll, yaw, x, y, z	Pitch, roll, yaw, x, y, z	Pitch, roll, yaw, x, y, z	Pitch, roll, yaw, x, y, z
Incident power (total heat load)	300.0 W	24.7 W	<5 W	<5 W	<5 W
Peak heat density	~0.574 W/mm^2	~0.048 W/mm^2	<0.01 W/mm^2	<0.01 W/mm^2	<0.01 W/mm^2
Branch	Common upstream	Common upstream	Branch 1 / Branch 2	Branch 2	Branch 2
Branch separation angle	n/a	n/a	5°	n/a	n/a

C Plane Grating Monochromator

The Variable Line Spacing Plane Grating Monochromator (VLS-PGM) employs a plane diffraction grating with a position-dependent groove density, enabling both spectral dispersion and focusing within a single optical element. The groove density (N) of a VLS grating can be expressed as a polynomial function of the tangential coordinate (w),

$$N(w) = N_0 + N_1 w + N_2 w^2 + N_3 w^3 + \dots ,$$

where N_0 represents the groove density at the grating center and N_1 corresponds to the first-order variation of the groove density, which determines the tangential focusing characteristics of the grating. Tangential focusing is achieved when the

following focusing condition is satisfied:

$$\frac{\cos^2\alpha}{r} + \frac{\cos^2\beta}{r'} - m\lambda N_1 = 0,$$

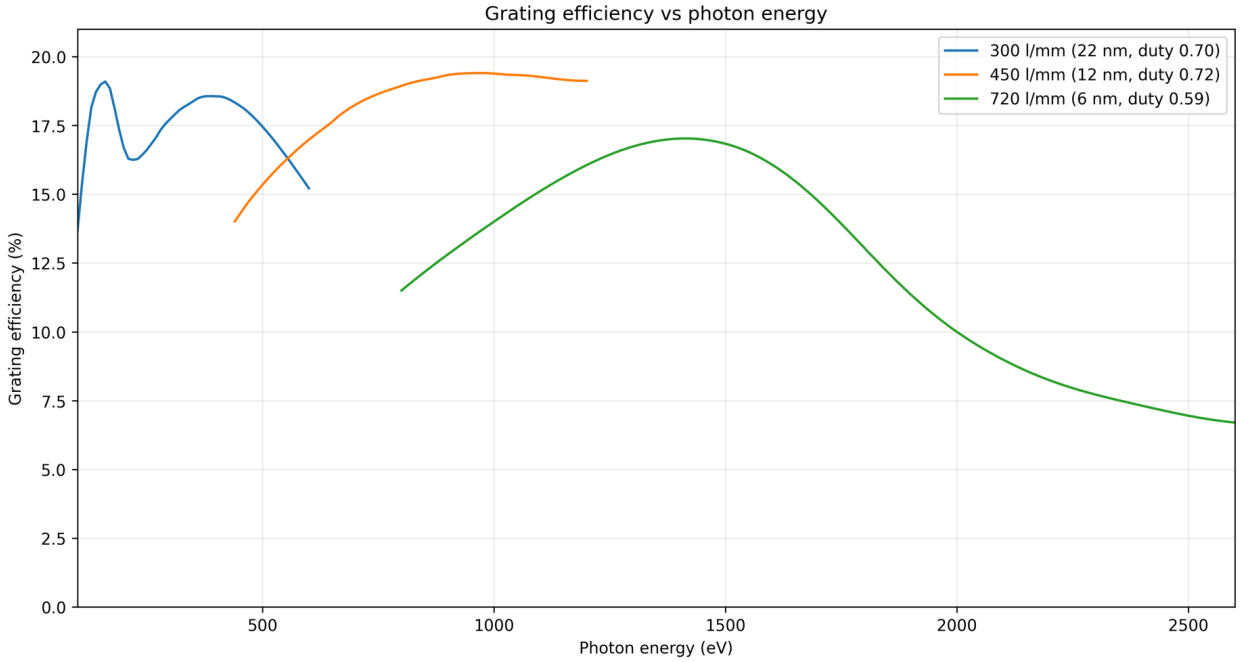
where r is the source-to-grating distance, r' is the grating-to-exit slit distance, α is the incidence angle, β is the diffraction angle, m is the diffraction order, and λ is the wavelength. The higher-order coefficients N_2 and N_3 are used to compensate for optical aberrations such as coma and spherical aberration. These terms improve focusing performance and maintain high energy resolution over a broad photon energy range. In practice, coefficients higher than N_3 provide only marginal performance improvements while significantly increasing fabrication complexity and cost. Therefore, the present design considers terms up to N_3.

The ID26 Soft X-ray Nanoprobe beamline is designed to operate at a fixed-focus constant of $C_{\text{ff}} = 2.2$. A low C_{ff} value results in an enlarged source image and degraded energy resolution, whereas an excessively high C_{ff} reduces photon flux due to decreased grating efficiency and optical acceptance. The STXM and ptychography branch primarily benefits from high photon flux and beam stability, while the spectroscopy branch requires a resolving power exceeding 10,000 in the high-energy region. Therefore, $C_{\text{ff}} = 2.2$ was selected as a compromise operating condition that provides balanced performance between high photon flux for imaging experiments and high energy resolution for spectroscopy applications.

Au coatings are used for the low- and medium-energy gratings, while Rh is used for the high-energy grating to improve throughput in the upper part of the operating range and avoid the reduction in Au reflectivity near the Au M absorption region. This coating strategy supports continuous operation over the 90–2600 eV design range.

The groove densities, VLS coefficients, groove depths, duty cycles, coating materials, and operating ranges of the three gratings were optimized for the target photon-energy ranges and key absorption edges. The detailed specifications are summarized in table 4.2.9.6. Grating diffraction efficiency was additionally evaluated using RAY-UI and cross-compared with independent calculations using GSolver and IGOR-based models to verify the consistency of the optimized groove profiles. The calculated first-order efficiencies are typically in the mid-to-high-teen percentage range over the principal operating bands, with peak values approaching approximately 18–19% for the optimized low- and medium-energy gratings and approximately 17% for the high-energy grating. The calculated energy-dependent

efficiency curves are used together with mirror reflectivity and source flux to estimate the available photon flux at the end-stations.



<Figure 4.2.9.3> Calculated diffraction efficiency of the gratings using RAY-UI

The overall specifications of the VLS-PGM, including the pre-mirror and exit-slit arrangement, are summarized in table 4.2.9.5.

The groove densities and VLS coefficients N_1, N_2, and N_3 of the gratings used in this beamline were optimized based on the target photon energy ranges and key absorption edges. Detailed specifications are summarized in table 4.2.9.6.

D Optical Performance

OASYS simulations were performed to evaluate the beam characteristics of the proposed optical system. Representative simulations include the 530 eV condition, while low-energy cases were also examined because of their larger source divergence. The optical configuration and simulated beam profiles confirm the feasibility of both nanometer-scale focusing on Branch 1 and micrometer-scale focusing on Branch 2. The optical configuration and beam profiles obtained under this condition are presented in figure 4.2.9.4.

For Branch 1 (STXM/Ptychography), the optical design targets a spatial resolution of approximately 20-30 nm using FZP focusing. OASYS simulations at 530 eV yield a representative focused beam size of approximately $19.8 \times 15.4\ \mathrm{nm}^2$ (FWHM)

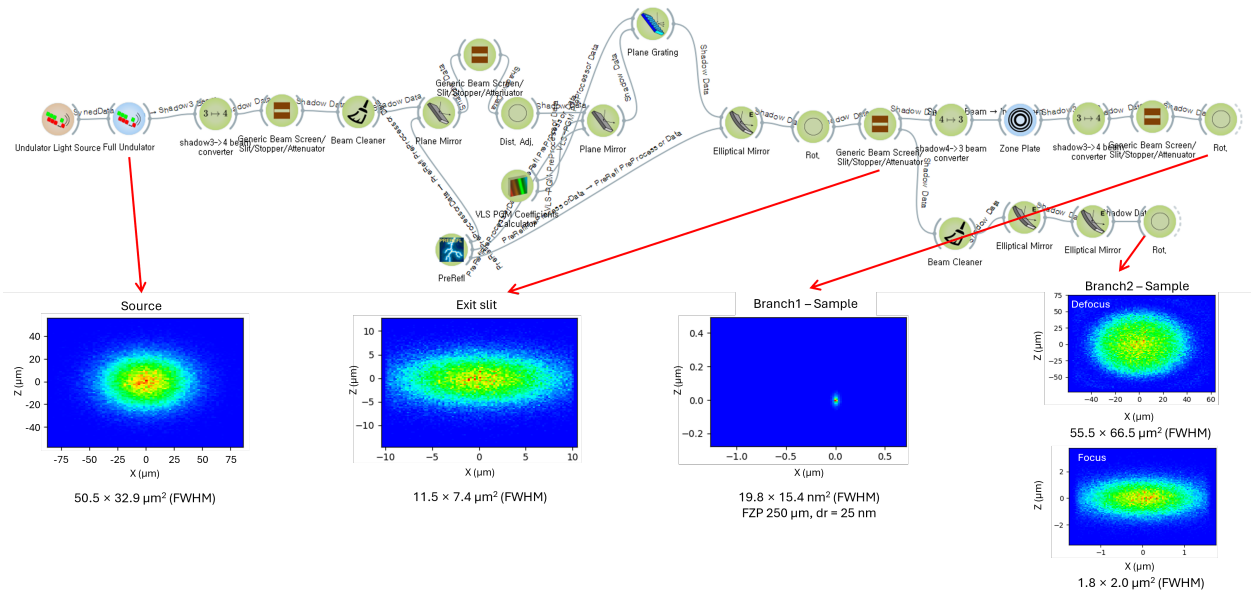
<Table 4.2.9.5> Monochromator (VLS-PGM) specification at ID26 Soft X-ray Nanoprobe beamline.

Item	Specification
Position (m)	34.8 (plane grating); 34.5 (M2 pre-mirror); 52 (exit slit)
Deflection / type	Variable Line Spacing Plane Grating Monochromator (VLS-PGM) with plane pre-mirror; fixed-focus constant $C_{\mathrm{ff}} = 2.2$
Photon energy range	90–2600 eV (beamline design range); LEG 90–600 eV, MEG 400–1200 eV, HEG 1000–2600 eV
Energy resolution	Resolving power above 8,000 over the entire operating energy range
Crystal / optical element	grating: three interchangeable VLS plane gratings, LEG / MEG / HEG, Si (100), 180 × 50 × 50 mm
Operating modes	Fixed-C_{ff} operation ($C_{\mathrm{ff}} = 2.2$) with the included angle set by the M2 pre-mirror; grating selection LEG / MEG / HEG
M2 Pre-mirror	Si substrate, Au coating, 600 × 50 × 50 mm
Grating	VLS plane grating: groove density N_0 = 300000 (LEG) / 450000 (MEG) / 720000 (HEG) lines/m; groove depth 22 / 12 / 6 nm; coating Au (LEG, MEG) / Rh (HEG)
Incident angle range	0.5–5° (grating); M2 pre-mirror incident angle 1–5°
Slope error	M2 pre-mirror: 0.2 µrad tangential, 5 µrad sagittal; grating: 0.2 µrad tangential, 5 µrad sagittal
Roughness	M2 pre-mirror: 0.5 nm RMS; grating 0.5 nm
VLS coefficients	N_1, N_2, N_3 optimized per grating; see table 4.2.9.6
Exit slit	Energy-selecting aperture and secondary source at 52 m; 20 µm opening gives nearly full coherent illumination of the FZP at 2500 eV, 50 µm opening transmits approximately 90% of the flux

<Table 4.2.9.6> Optimized VLS parameters for the PGM.

Parameter	LEG	MEG	HEG
Material	Si (100)	Si (100)	Si (100)
Dimension [mm]	180 × 50 × 50	180 × 50 × 50	180 × 50 × 50
C_{ff}	2.2	2.2	2.2
Groove density, N_0 [lines/m]	300000	450000	720000
Groove density, N_1 [lines/m^2]	48423.7	72650.7	116256.4
Groove density, N_2 [lines/m^3]	3633.9	5453.9	8729.4
Groove density, N_3 [lines/m^4]	303.6	455.8	729.82
Groove depth [nm]	22	12	6
Energy range [eV]	90–600	400–1200	1000–2600
Coating material	Au	Au	Rh

at the Branch 1 sample position. The design therefore provides the nano-focused illumination required for STXM and ptychography over the principal operating range. Spatial coherence is a critical parameter for ptychography experiments. The calculated vertical and horizontal coherent fractions were 0.961 and 0.669, re-



<Figure 4.2.9.4> (Top) Ray-tracing results of the ID26 Soft X-ray Nanoprobe beamline from OASYS simulation. (Bottom) Simulated beam profiles at key optical elements and focal positions.

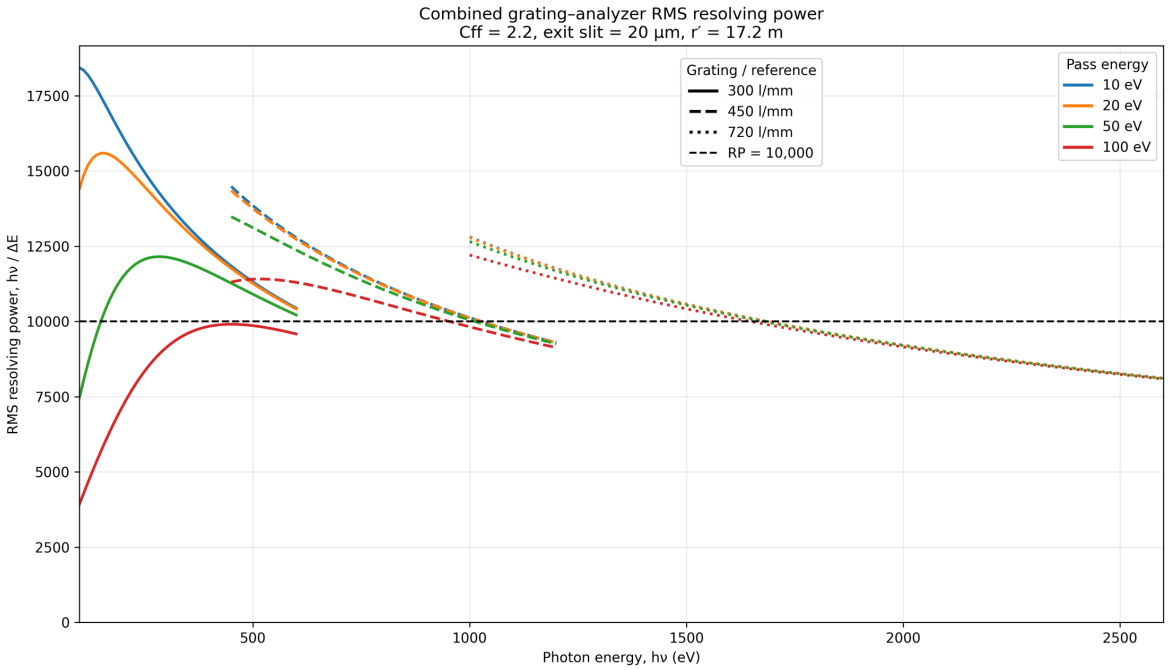
spectively, resulting in a total coherent fraction of 0.643. These results indicate that the beamline provides sufficient spatial coherence for high-quality ptychographic imaging.

For Branch 2, which is dedicated to versatile spectroscopy applications, the KB refocusing optics provide two selectable beam-size configurations to accommodate different experimental requirements. In the focused mode, the optical design targets a beam size of approximately 5×5 μm² or smaller for spatially resolved spectroscopy. OASYS simulations at 530 eV yield a focused beam size of approximately 1.8×2.0 μm² (FWHM) at the sample position. In the defocused mode, the alternative-curvature mirror strips provide a larger beam with a target size of approximately 50-100 × 50-100 μm². The corresponding simulated beam size at 530 eV is approximately 55.5×66.5 μm² (FWHM), satisfying the intended design target. These two operating modes provide flexibility for spatially resolved measurements and large-area illumination, depending on the requirements of XAS, XPS, and scattering experiments.

The simulated beam sizes represent the nominal optical performance without accounting for mirror slope errors. The effects of realistic optical imperfections on the final beam size will be evaluated separately based on the specified mirror tolerances. In addition to beam-size control, energy resolution is a key performance

metric for the spectroscopy branch. The photon-energy resolving power is determined by the combined contributions of the zero-slit monochromator resolution, including source size, optical slope errors, and grating diffraction and aberration effects, and the finite exit-slit contribution. For photoelectron spectroscopy, the electron-analyzer resolution additionally contributes to the overall experimental energy resolution. The exit-slit width is therefore selected according to the required balance between spectral resolution and photon flux. For the spectroscopy branch, the design uses a 20 μm exit slit as the reference high-resolution operating condition. With practical analyzer pass energies of approximately 10–-50 eV, the combined grating/analyzer performance is designed to provide at least RP ≈ 2,000 at 100 eV (ΔE ≈ 0.05 eV), RP ≈ 10,000 at 1,000 eV (ΔE ≈ 0.1 eV), and RP ≈ 8,270 at 2,500 eV (ΔE ≈ 0.3 eV). These values define the practical resolving-power targets of the spectroscopy branch. A 200 eV analyzer pass energy is reserved for exceptional measurements requiring maximum throughput rather than high energy resolution.

For Branch 2, which is dedicated to spectroscopy applications, energy resolution represents a key performance metric. Figure 4.2.9.5 shows the calculated resolving power as a function of photon energy.



<Figure 4.2.9.5> Simulated resolving power as a function of photon energy.

E Beam Diagnostics and Alignment

The ID26 Soft X-ray Nanoprobe beamline will incorporate a beam diagnostics system to monitor beam position, intensity, and stability throughout beamline operation. Diagnostic devices will be installed at key locations along the photon transfer line to facilitate commissioning, alignment, and routine operation. The diagnostics system is expected to include beam position monitors (BPMs), fluorescence screens, intensity monitors, and diagnostic apertures to verify beam transport and optical performance.

Beam alignment will be achieved through motorized optical components and precision positioning stages. Alignment procedures will be developed to ensure accurate positioning of mirrors, gratings, slits, and focusing optics during commissioning and operation. Remote control and automated alignment functions will be implemented where appropriate to improve operational efficiency and reproducibility. In addition, the beam diagnostics system will provide continuous monitoring of beam stability and optical alignment. The possibility of incorporating feedback-based beam stabilization will be evaluated during the detailed design phase.

Detailed specifications and implementation plans for the diagnostics, and alignment systems will be described in Chapter 3.

4.2.9.5 Photon Transfer Line

A Photon Transfer Line Design

The Photon Transfer Line (PTL) of the ID26 Soft X-ray Nanoprobe beamline is currently under detailed design. The PTL is responsible for transporting photons from the Front-End to the experimental stations while preserving photon flux, coherence, wavefront quality, and beam stability. To achieve these objectives, ray-tracing simulations and engineering analyses are being performed to optimize the optical layout and major beamline components.

The PTL consists of mirrors, a monochromator, slits, diagnostic devices, and a vacuum system designed to meet the required optical performance and energy range of the beamline. Mechanical stability, alignment accuracy, and operational accessibility are also considered to facilitate reliable operation and future maintenance.

To ensure safe and reliable operation, the PTL incorporates vacuum interlocks,

cooling-water interlocks, and equipment protection interlocks. In the event of abnormal vacuum conditions, cooling-water failure, overheating of optical components, or equipment malfunction, the interlock system automatically interrupts beam delivery to protect both beamline optics and experimental instruments. The current prototype PTL design serves as the baseline configuration for the detailed design phase. Detailed descriptions of the optical layout, vacuum system, mechanical structure, and expected performance are provided in Chapter 3.

B Vacuum, Pumps, and Valves

The ID26 Soft X-ray Nanoprobe beamline will be operated under ultra-high vacuum (UHV) conditions to ensure stable beam transport, minimize carbon contamination of optical components, and maintain reliable operation of the experimental end-stations. The PTL, monochromator, focusing optics, and experimental chambers will be designed to operate at pressures on the order of 10^{-9} mbar.

The vacuum system will employ a combination of turbomolecular pumps, ion pumps, and dry backing pumps to achieve and maintain the required operating pressure. The pumping configuration and pumping speeds will be optimized during the detailed design phase based on chamber volumes, gas loads, and operational requirements. Particular attention will be paid to minimizing hydrocarbon contamination of optical components and maintaining long-term stability for coherent imaging experiments; the hydrocarbon-free residual-gas acceptance criteria that apply to every beamline UHV component are given in the UHV component fabrication specification appended to the front-end vacuum analysis report [3].

Gate valves and isolation valves will be installed at key locations throughout the beamline to allow independent venting and maintenance of individual sections while protecting adjacent vacuum regions. Vacuum interlock systems will continuously monitor chamber pressure and automatically isolate affected sections in the event of abnormal operating conditions.

Detailed descriptions of the vacuum layout, pumping system, valve configuration, and vacuum performance are provided in Chapter 3.

C Vibration Stability

High-resolution STXM and ptychography require exceptional mechanical and thermal stability to maintain beam alignment, coherent illumination, and

nanoscale positioning accuracy throughout the measurement. The beamline and end-station will therefore be designed as an integrated system to minimize vibration, thermal drift, and long-term mechanical instability.

Optical components, including mirrors, gratings, the exit slit, and focusing optics, will be mounted on rigid support structures with high mechanical stiffness to suppress vibration and maintain alignment. The end-station chamber will be designed with a compact mechanical configuration and vibration-isolated supports to minimize external disturbances while maintaining stable relative positioning between the focusing optics and the sample. The design goal is to achieve a relative vibration of less than 10 nm RMS between the focusing optics and the sample over the measurement bandwidth required for high-resolution imaging.

To minimize thermal drift, the beamline hutch and experimental hutch will be maintained under tightly controlled environmental conditions. Temperature-sensitive components, including the optical support structures, exit slit assembly, and end-station chamber, will be designed to reduce thermal expansion and ensure long-term positional stability. An ambient temperature stability of ± 0.2–0.5 °C is targeted to maintain beam pointing stability and consistent imaging performance during extended STXM and ptychography measurements.

4.2.9.6 End-Station

A End-station Mechanical Design

The end-station is designed to provide flexible experimental environments for both nanoscale imaging and spectroscopy through two dedicated experimental branches. Branch 1 is optimized for scanning transmission X-ray microscopy (STXM) and ptychography, while Branch 2 is designed for versatile X-ray photoelectron spectroscopy (XPS) and X-ray absorption spectroscopy (XAS) measurements. The modular architecture allows future upgrades and the incorporation of additional experimental capabilities while maintaining compatibility with a wide variety of user experiments.

Each branch will be equipped with an independent ultra-high vacuum (UHV) chamber and dedicated pumping system to provide a clean and stable measurement environment. A combination of turbomolecular pumps, roughing pumps, and load-lock systems is planned to enable rapid sample exchange while maintaining UHV conditions and minimizing recovery time. The chamber layout will provide sufficient space for future integration of additional detectors, sample

environments, and specialized experimental equipment.

The imaging branch will employ a compact STXM chamber designed to maximize mechanical stability for high-resolution imaging. The chamber will accommodate the focusing optics, order-sorting aperture, sample stage, and transmitted X-ray detector within a rigid mechanical structure to minimize relative motion between optical components and the sample. A high-precision piezo-driven scanning stage combined with long-travel positioning stages will provide nanometer-scale positioning accuracy required for STXM and coherent diffraction imaging. The sample holder will be compatible with standard TEM grids and commonly used STXM sample holders, allowing users to readily perform transmission measurements with a wide variety of specimens.

The spectroscopy branch will be designed to support general-purpose XPS and XAS experiments on a broad range of materials. The end-station will incorporate a multi-axis UHV sample manipulator capable of precise sample positioning, rotation, and tilt, together with temperature control to accommodate various experimental requirements. Unlike the imaging branch, the spectroscopy chamber will employ a larger sample stage capable of accommodating multiple samples simultaneously, enabling high-throughput measurements and efficient screening of material libraries. The chamber layout will also provide sufficient working distance for an electron analyzer, fluorescence detector, and future experimental accessories.

A dedicated UHV preparation chamber is planned to support sample preparation and surface treatment prior to spectroscopic measurements. The preparation chamber will be designed to accommodate sputter cleaning, thermal evaporation, sample heating, and other commonly used surface preparation techniques. The modular design will also allow future integration of additional preparation tools depending on user requirements. Samples will be transferred between the preparation chamber and the analysis chamber under UHV conditions, minimizing surface contamination and enabling reproducible surface-sensitive measurements. The preparation chamber will also provide a flexible platform for preparing thin films, catalyst model systems, and semiconductor samples, supporting a wide range of *in situ* and *operando* spectroscopy experiments. The spectroscopy end-station is planned to consist of a load-lock chamber, a UHV preparation chamber, and an analysis chamber connected through a vacuum transfer system, allowing rapid sample exchange and contamination-free transfer between preparation and measurement stages.

To support the investigation of air-sensitive materials, the end-station design will provide compatibility with air-free sample handling and transfer systems. The spectroscopy branch is planned to accommodate a glove box interface and vacuum transfer mechanism, enabling contamination-free transfer of moisture- and oxygen-sensitive samples from an inert-gas environment to the UHV analysis chamber without exposure to ambient air. This capability is particularly important for studies of lithium-based battery materials, solid-state electrolytes, catalysts, and other reactive functional materials, ensuring reliable characterization of their intrinsic chemical and electronic properties.

Both branches are planned to support various *in situ* and *operando* sample environments. The mechanical design will provide sufficient space and infrastructure for the future integration of electrochemical cells, electrical biasing, heating and cooling stages, gas reaction cells, and other user-developed sample environments. These capabilities will enable real-time investigations of electrochemical processes, catalytic reactions, semiconductor devices, and other functional materials under realistic operating conditions.

To ensure high spatial resolution and long-term experimental reproducibility, the beamline and end-station will be designed as an integrated mechanically stable system. Optical components, including mirrors, gratings, exit slit assemblies, focusing optics, and experimental chambers, will be mounted on rigid support structures to minimize vibration and thermal drift. Stable relative positioning between the focusing optics and the sample is particularly important for STXM and ptychography measurements, and the mechanical design will target sub-10 nm RMS relative vibration between these components. In addition, the experimental hutch will be maintained under tightly controlled environmental conditions to minimize thermal expansion and preserve beam alignment during long-duration measurements. The baseline specifications of the two end-station instruments are collected in table 4.2.9.7.

<Table 4.2.9.7> Baseline specification of the two end-station instruments of the ID26 Soft X-ray Nanoprobe beamline.

Parameter	Specification
Branch 1: imaging end-station (STXM / ptychography)	
Techniques	STXM; ptychography (coherent diffraction imaging)
Chamber	Compact UHV STXM chamber within a rigid mechanical structure

(continued on next page)

(Table 4.2.9.7 continued)

Parameter	Specification
Operating pressure	~10^{-9} mbar
Pumping and sample exchange	Turbomolecular pumps, roughing pumps, and a load-lock system for rapid sample exchange
In-chamber components	Nano-focusing optics (capillary / FZP), order-sorting aperture, sample stage, transmitted X-ray detector
Sample scanning stage	High-precision piezo-driven scanning stage combined with long-travel positioning stages; nanometer-scale positioning accuracy
Sample holders	Standard TEM grids and commonly used STXM sample holders
Relative vibration (focusing optics to sample)	$<$ 10 nm RMS
Ambient temperature stability	$\pm$0.2–0.5 °C
In situ / *operando* environments	Electrochemical cells, electrical biasing, heating and cooling stages, and gas reaction cells (space and infrastructure reserved)
Branch 2: spectroscopy end-station (XPS / XAS)	
Techniques	XPS; XAS in total electron yield (TEY) and total fluorescence yield (TFY) modes
Chamber configuration	Load-lock chamber, UHV preparation chamber, and analysis chamber connected through a vacuum transfer system
Operating pressure	~10^{-9} mbar
Electron analyzer	Hemispherical electron energy analyzer with MCP + CCD detection
Sample manipulator	Multi-axis UHV manipulator providing precise positioning, rotation, tilt, and temperature control
Sample stage	Large stage accommodating multiple samples simultaneously for high-throughput measurements
Preparation chamber	Sputter cleaning, thermal evaporation, and sample heating; modular for additional preparation tools
Air-free sample handling	Glove-box interface and vacuum transfer mechanism for moisture- and oxygen-sensitive samples
Additional detector ports	Working distance reserved for the electron analyzer, fluorescence detector, and future accessories

(continued on next page)

(Table 4.2.9.7 continued)

Parameter	Specification
In situ / *operando* environments	Electrochemical cells, electrical biasing, heating and cooling stages, and gas reaction cells (space and infrastructure reserved)

B Detector, Data Acquisition, and Software

The detector systems, data acquisition (DAQ), and computing infrastructure of the end-station are designed to support efficient data collection and analysis for both imaging and spectroscopy experiments. Dedicated detector systems and software environments will be implemented for each experimental branch while maintaining a common beamline control and data management framework, as summarized in <Table 4.2.9.8>.

The imaging branch is designed to support both scanning transmission X-ray microscopy (STXM) and ptychography measurements. For STXM experiments, transmitted X-rays will be measured using a high-sensitivity transmission detector, such as a silicon photodiode or avalanche photodiode, providing a large dynamic range and rapid signal acquisition during raster scanning. A silicon photodiode is considered the baseline transmission detector due to its high linearity, large dynamic range, and excellent sensitivity in the soft X-ray energy range. Depending on the final experimental configuration, an avalanche photodiode (APD) may also be considered for applications requiring higher sensitivity or faster signal acquisition. The resulting datasets consist of two-dimensional transmission images acquired at individual photon energies, which can be further processed to generate absorption, elemental, and chemical-state maps through multi-energy image analysis.

For ptychography measurements, coherent diffraction patterns will be recorded at every scan position using a high-speed pixel-array detector with a large dynamic range and high frame rate to enable continuous scanning measurements. The acquired diffraction datasets are expected to be stored in standard scientific data formats suitable for large-volume data processing. Data analysis will be performed through dedicated ptychographic reconstruction software, including detector correction, diffraction preprocessing, phase retrieval, and iterative image reconstruction to recover both the amplitude and phase of the sample transmission function. The beamline computing environment will provide sufficient

computational resources to support large-scale diffraction data processing and image reconstruction using widely adopted reconstruction packages together with user-developed analysis workflows.

The spectroscopy branch will support XPS and XAS measurements using a hemispherical electron energy analyzer equipped with a multi-channel plate (MCP) detector coupled to a CCD camera. The detector system simultaneously records electron kinetic energy and emission angle, enabling high-resolution photoelectron spectroscopy measurements. Detector control and data acquisition will be performed using the SES software platform supplied with the analyzer. The acquired XPS spectra will be stored in both the native SES format and standard text-based data files, allowing subsequent analysis using Igor Pro, Python, or other commonly used data analysis software.

X-ray absorption spectroscopy measurements will be performed using both total electron yield (TEY) and total fluorescence yield (TFY) detection modes. TEY signals will be measured through the sample drain current, while TFY measurements will utilize an appropriate fluorescence detector. The resulting XAS spectra will be recorded as text-based files and can be readily processed using standard XAS analysis software packages. The spectroscopy end-station software will provide integrated control of the monochromator, electron analyzer, sample manipulator, and detectors to facilitate synchronized data acquisition during XPS, XAS, and *operando* measurements.

For both experimental branches, a gold mesh installed upstream of the end-stations will continuously monitor the incident photon flux (I_0). The measured I_0 current will be recorded simultaneously with the experimental data and used for normalization of XAS spectra and STXM transmission measurements, minimizing the influence of storage-ring current decay and beam intensity fluctuations. The I_0 signal will also provide continuous monitoring of beam stability during ptychography experiments, contributing to improved reconstruction accuracy and long-term measurement reproducibility.

The beamline control system and data acquisition software will be designed to provide an integrated experimental environment with synchronized control of beamline optics, detectors, sample positioning systems, and experimental devices. The computing infrastructure will support real-time data visualization, automatic metadata recording, network-based data storage, and remote data access, providing users with an efficient platform for both routine measurements and advanced

nanoscale imaging and spectroscopy experiments. Detector models and detailed specifications will be finalized during the engineering design phase according to the experimental requirements of each branch. Further details on the beamline control system, data acquisition architecture, and software framework are provided in Chapter 3.

<Table 4.2.9.8> Summary of the detector systems, data acquisition, and analysis software for the ID26 end-stations. Detector models and detailed specifications will be finalized during the engineering design phase.

Parameter	**Si photodiode**	**High-speed pixel-array detector**	**Hemispherical electron analyzer**	**Electrometer / fluorescence detector**
Role / technique	STXM transmission imaging	Ptychography, coherent diffraction	XPS	XAS (TEY and TFY)
Detector type / detection principle	Silicon photodiode (avalanche photodiode as an option)	Pixel-array detector	Hemispherical electron energy analyzer with MCP + CCD readout	Electrometer (TEY drain current); fluorescence detector (TFY)
Applicable energy range	90–2600 eV (photon)	90–2600 eV (photon)	<2600 eV (electron)	90–2600 eV (electron, photon)
Remarks	Baseline transmission detector; high linearity and excellent sensitivity in the soft X-ray range	Records a coherent diffraction pattern at every scan position	Records electron kinetic energy and emission angle simultaneously	TEY from the sample drain current; TFY from a fluorescence detector
Data format	Transmission map (Tiff, HDF5)	Diffraction images (HDF5)	Spectrum (TXT, PXT)	Spectrum (TXT)
DAQ / control	EPICS + Bluesky	EPICS + Bluesky	EPICS + Bluesky + SES	EPICS + Bluesky
Analysis software	Python, ImageJ	PtyPy, PyNX	CasaXPS, Igor Pro	Igor Pro, Athena

References

[1] Jongha Park et al. High Heat Load Front-End Mechanical Design and Thermal Analysis Report. Internal Document PAL-INT/ME-2026-003. Pohang Accelerator Laboratory, June 2026.

[2] Minho Seo and Chaesoon Lee. 4GSR Beamline Interlock System Design Report. Internal Document PAL-INT/EE-2026-012. Pohang Accelerator Laboratory, July 2026.

[3] Hyungseok Choi and Jongha Park. 4GSR Front-End Vacuum Analysis Report. Internal Document PAL-INT/ME-2026-009. Pohang Accelerator Laboratory, Aug. 2026.

4.2.10 High Energy Microscopy (BM10)

4.2.10.1 Target Purpose and Objective

The BM10 High Energy Microscopy (HEM) beamline is designed to provide non-destructive full-field X-ray imaging and computed tomography using high-energy synchrotron radiation in the nominal photon-energy range of 20–150 keV. The high penetration of hard X-rays enables three-dimensional investigation of large, dense, and complex specimens in materials science, energy research, engineering, geoscience, and biological applications [1, 2, 3].

The beamline employs a long source-to-sample distance of approximately 100 m and provides a large X-ray beam of up to approximately 200 mm (H) $\times$ 30 mm (V) at the sample position. This geometry enables large-field imaging [4], while complementary detector and microscope configurations provide multi-scale imaging from large-field projection imaging to high-resolution X-ray microscopy.

A major scientific objective is the non-destructive investigation of internal structures and their evolution during processing or operation. Synchrotron X-ray imaging and tomography have demonstrated three-dimensional characterization of electrode morphology and defects [5], direct operando observation of electrochemical processes [6], and time-resolved imaging of dynamic processes under in-situ conditions [7]. The HEM beamline is therefore designed to support in-situ, operando, and time-resolved studies under thermal, mechanical, electrochemical, and other externally controlled environments.

The HEM beamline also supports propagation-based phase-contrast imaging (PBI) for materials and structures with weak absorption contrast. Free-space propagation of coherent or partially coherent X-rays can enhance interfaces and low-contrast features [8, 9]. The long propagation geometry of HEM, together with variable sample-to-detector distance, provides favorable conditions for phase-sensitive imaging, including high-energy phase-contrast microscopy [3].

Multi-scale imaging is also important for biological and biomedical applications. Hierarchical phase-contrast tomography has demonstrated three-dimensional imaging across multiple length scales, from large biological specimens to localized cellular-scale structures [10]. The combination of large field of view, high-energy penetration, phase sensitivity, and high-resolution microscopy therefore provides opportunities for a broad range of HEM applications.

The principal scientific objectives of the HEM beamline are:

- Non-destructive 3D imaging of large, dense, industrial, and functional materials;
- In-situ and operando imaging of internal structural evolution;
- High-speed and time-resolved tomography of dynamic processes;
- Multi-scale imaging from large field of view to high-resolution microscopy;
- High-resolution biological and biomedical imaging; and
- Propagation-based and phase-sensitive imaging of weakly absorbing structures.

To support these objectives, the beamline adopts a simple white-beam photon-transport concept with minimal optical components and integrates flexible sample environments, precision positioning systems, and complementary detector configurations for high-energy multi-scale imaging.

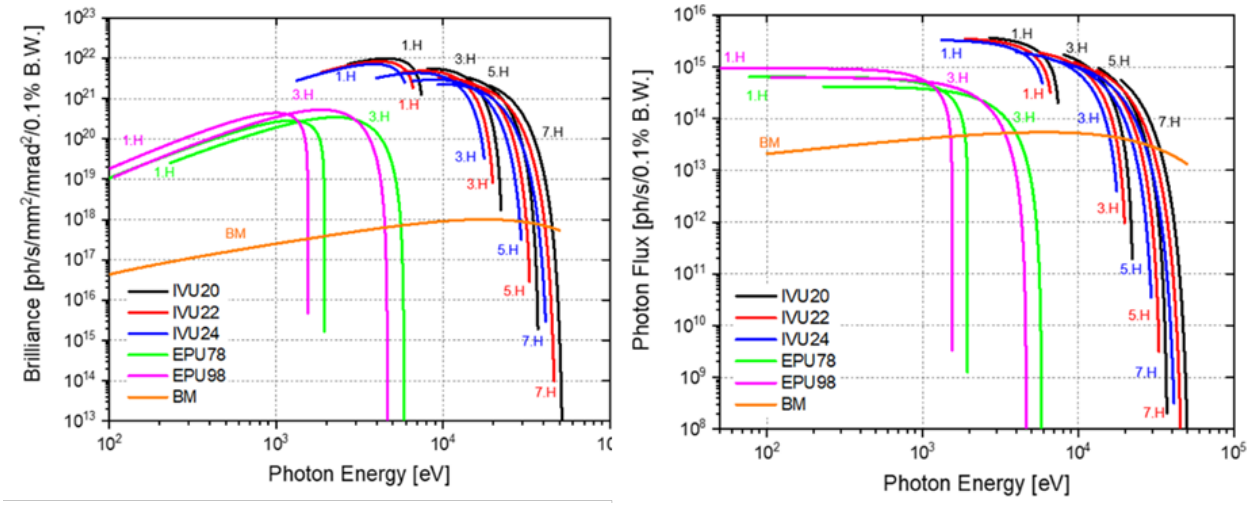
4.2.10.2 Photon Source

The BM10 High Energy Microscopy (HEM) beamline uses synchrotron radiation generated by a 2 T bending magnet of the 4 GeV Korea Light Source (KLS). The source provides high-energy X-rays for full-field projection imaging and computed tomography over the nominal HEM photon-energy range of 20–150 keV.

The principal source parameters are summarized in <Table 4.2.10.1>. The bending magnet has a magnetic field of 2 T and a bending radius of approximately 6.67 m, corresponding to a critical photon energy of approximately 21 keV. The predicted brilliance and photon flux are shown in <Figure 4.2.10.1>.

<Table 4.2.10.1> Bending-magnet source parameters of the High-Energy Microscopy beamline. The usable photon-energy range extends up to 150 keV. At 4 GeV and 400 mA a 2 T bend radiates 0.216 kW per mrad of horizontal fan, so the $\pm$1.5 mrad opening aperture at the exit of the storage-ring vacuum chamber accepts 0.65 kW.

Source type	**Magnetic field (T)**	**Magnetic radius (m)**	**Critical energy (keV)**	**Power through the $\pm$1.5 mrad aperture (kW)**
Bending magnet	2	6.67	21	0.65



<Figure 4.2.10.1> Predicted brilliance and flux of the bending-magnet source.

The high-energy spectral range provides the penetration required for imaging large and dense specimens and supports high-energy projection imaging, computed tomography, and propagation-based phase-contrast imaging.

A future higher-field bending-magnet source may be considered as a possible upgrade to enhance the high-energy spectral performance of the HEM beamline. Such an upgrade is not part of the present baseline design and would require separate evaluation of source performance, beam power, thermal loads, shielding, and beamline compatibility.

4.2.10.3 Front-End

The layout of the beamline is split into two parts separated by a ratchet-shaped storage ring tunnel wall, and the inside of the ring tunnel wall is the Front-end (FE). The FE of the BM10 HEM beamline provides the interface between the 2 T bending-magnet source and the downstream photon transfer line. It defines the accepted synchrotron-radiation beam, manages the thermal load of the white beam, protects downstream components, and maintains the required vacuum boundary between the storage ring and the beamline. The FE is also designed to protect both personnel and equipment on the beamline, as well as the machinery in the event of a vacuum failure on the beamline.

The HEM beamline requires a new high heat load Front-end, designed for a nominal beam acceptance of 2.2 mrad horizontally and 0.6 mrad vertically. At 0.216 kW per horizontal mrad, the $\pm$1.5 mrad opening aperture at the exit of the

storage-ring vacuum chamber admits 0.65 kW into the front-end, of which the parasitic mask (2.2 mrad horizontally by 0.6 mrad vertically) passes 0.48 kW downstream. Because HEM transports a broad polychromatic spectrum for high-energy imaging, the FE components must accommodate the large beam acceptance and the associated heat load. The Front-end of the HEM beamline is designed to respond to beamline issues while minimizing entry and exit. Beam-defining and safety components follow the common KLS front-end design and safety requirements, set out for the BM front-end type in the high heat load front-end mechanical design and thermal analysis report [11]. <Table 4.2.10.2> shows an overview of the components and functions of the HEM beamline Front-end.

<Table 4.2.10.2> Component list of the Front-end in the High-Energy Microscopy beamline, in beam order (distances measured from the source).

Distance (m)	Location	Component	Description
0	Storage ring	Bending magnet	Source (2 T)
12	Front-End	Parasitic mask	(H) 2.2 mrad × (V) 0.6 mrad
12.5		Beam stopper	Absorb of high-energy Bremsstrahlung radiation
13		Diamond window	Vacuum separate
13.5		PBPM1	Diamond-blade
14		Safety magnet	Electron stop
15.3		Photon shutter 1	Main beam blocking
19.5		PBPM2	Diamond-blade
21		Safety shutter 1	Beam diagnostics & shockwave blocking

A beamline-specific component of the HEM front-end is the CVD diamond window, which provides the vacuum boundary while maintaining high transmission of high-energy X-rays. Its high thermal conductivity and low X-ray absorption make diamond suitable for direct exposure to the white beam. The window also absorbs part of the low-energy radiation, reducing the thermal load transmitted to downstream components.

The diamond window is water-cooled and designed with a sufficiently large clear aperture to transmit the accepted HEM beam. X-ray-induced fluorescence from the diamond can also be used for beam observation during commissioning and alignment. The detailed design of the diamond window is described in section 4.2.10.4, Beamline Optics.

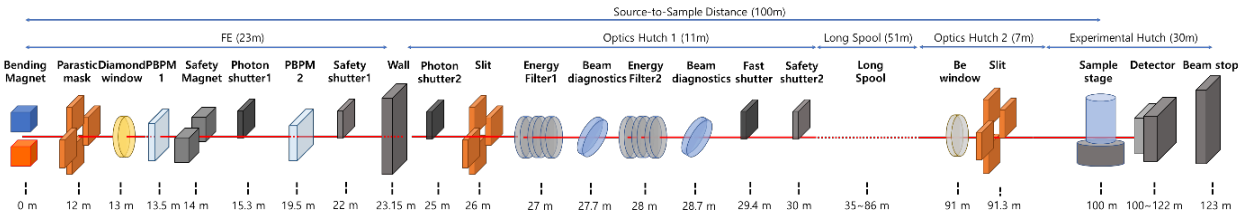
4.2.10.4 Beamline Optics

A Overall optical layout and component roles

The BM10 High Energy Microscopy (HEM) beamline is designed as a long-distance white-beam imaging beamline for high-energy X-ray projection imaging and computed tomography. The bending-magnet radiation is transported to the experimental station located approximately 100 m downstream using a simple and robust optical configuration with minimal components.

The primary projection-imaging beam path does not employ focusing mirrors or a monochromator. Instead, the white beam is conditioned using windows, slits, energy filters, and shutters and transported directly over the long propagation distance. This configuration reduces the number of optical components that can introduce beam-position or wavefront variations and simplifies alignment and maintenance of the long beamline.

The conceptual arrangement of the principal X-ray optical components, beam diagnostics, sample position, and detector system is shown in <Figure 4.2.10.2>.



<Figure 4.2.10.2> Conceptual layout of the High Energy Microscopy beamline indicating diagnostics, X-ray optics, sample position, and detector.

The principal photon-transport sequence is:

Bending-Magnet Source → Diamond Window → White-Beam Slit → Energy Filters → Fast Exposure Shutter → Long Vacuum Transport → Exit Slit → Exit Window → Sample → Detector → Beam Stop

The diamond window provides vacuum separation and initial low-energy attenuation; the white-beam slit defines the accepted beam aperture; the energy-filter system controls the transmitted spectrum and intensity; and the Fast Exposure Shutter (FES) provides intermittent experimental exposure control. After the long vacuum transport section, the exit slit defines the final beam aperture and

the exit window establishes the downstream vacuum boundary before the beam propagates to the sample.

The principal optical and photon-transport components and their functions are summarized in <Table 4.2.10.3>.

<Table 4.2.10.3> BM10 High Energy Microscopy beamline component reference table, in beam order (distances measured from the source).

Distance (m)	Location	Component	Description / comments
0	Front End (0–23 m)	Source	2 T bending-magnet source
12		Parasitic Mask	2.2 mrad (H) × 0.6 mrad (V)
12.5		Beam Stopper	Absorption of high-energy Bremsstrahlung radiation
13		Diamond Window	Vacuum separation, thermal management, and beam observation
13.5		PBPM1	Diamond-blade photon beam position monitor
14		Safety Magnet	Electron-beam stopping
15.3		Photon Shutter 1	Main beam blocking
19.5		PBPM2	Diamond-blade photon beam position monitor
21		Safety Shutter 1	Bremsstrahlung blocking
23.15	Wall (23.15–24.95 m)	Shielding Wall	Front-end radiation shielding; 1.8 m thickness
25	Optical Hutch 1 (24.95–35 m)	Photon Shutter 2	Main beam blocking
26		White-Beam Slit	Defines the accepted beam aperture and reduces unnecessary irradiation of downstream components
27		Energy Filter 1	Spectral and intensity control of the polychromatic beam
27.7		Beam Diagnostics	Beam diagnostics
28		Energy Filter 2	Additional spectral and intensity control of the polychromatic beam
28.7		Beam Diagnostics	Beam diagnostics
29.4		Fast Exposure Shutter	Reduction of radiation damage
30		Safety Shutter 2	Bremsstrahlung blocking

(continued on next page)

(<Table 4.2.10.3> continued)

Distance (m)	Location	Component	Description / comments
35–86	Long spool (35–86 m)	Long spool	Beam transfer (UHV)
91.0	Optical Hutch 2 (86–93 m)	Exit Window	Al window forming the downstream vacuum boundary of the photon transfer line
91.3		Exit Slit	Final definition of the X-ray beam aperture before the experimental station
100	Experimental Hutch (93–123 m)	Sample Stage 1	Heavy-load sample stage for large and heavy specimens
101.2		Sample Stage 2	Small-sample stage for high-resolution imaging and CT
100–122		Detector Positioning System	Variable sample-to-detector distance for projection and propagation-based phase-contrast imaging
100–122		Detector Systems	X-ray microscope and complementary detector systems for multi-scale imaging
123		Beam Stop	Fixed beam stop for the transmitted white beam

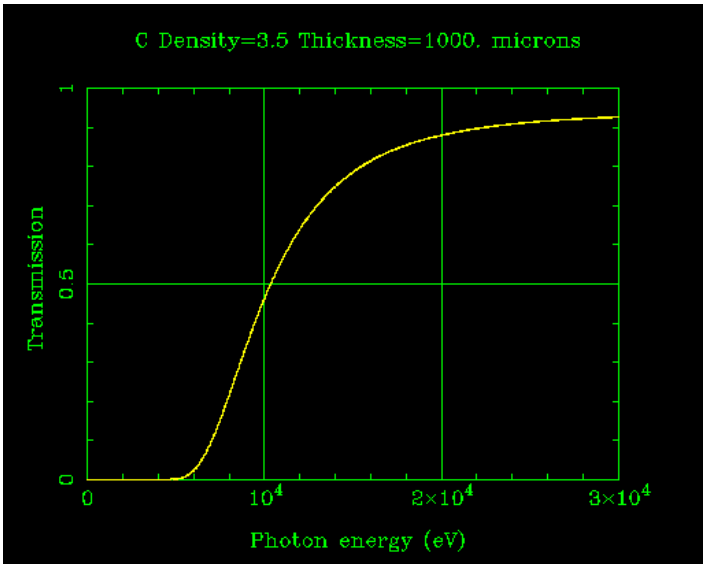
Optical and spectral calculations were performed using SHADOW3/OASYS and SPECTRA, while thermal and structural analyses of white-beam components were performed using ANSYS. Further details on the component specifications, engineering tolerances, and optical, thermal, and structural analyses are described in the following chapter.

B Diamond window

A CVD diamond window is installed at approximately 13 m from the bending-magnet source to provide vacuum separation while maintaining high transmission of the high-energy white beam. Diamond was selected because of its high thermal conductivity, mechanical strength, and relatively low X-ray absorption. The window also preferentially attenuates the low-energy portion of the spectrum, reducing the thermal load transmitted to downstream components.

The baseline window has a thickness of 1.0 mm and a Ø40 mm clear aperture for the accepted beam divergence of approximately 2.2 mrad (H) $\times$ 0.6 mrad (V).

The calculated absorbed power is approximately 150 W, and active water cooling is incorporated into the window assembly. The calculated X-ray transmission of the 1.0-mm-thick diamond window is shown in <Figure 4.2.10.3>.

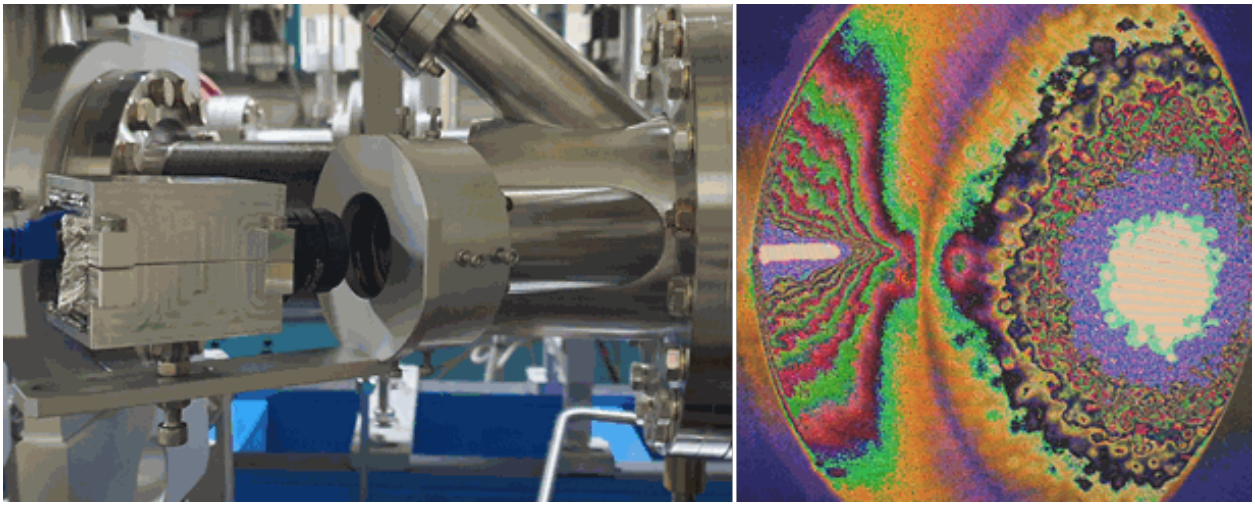


<Figure 4.2.10.3> Calculated X-ray transmission of the 1.0-mm-thick CVD diamond window.

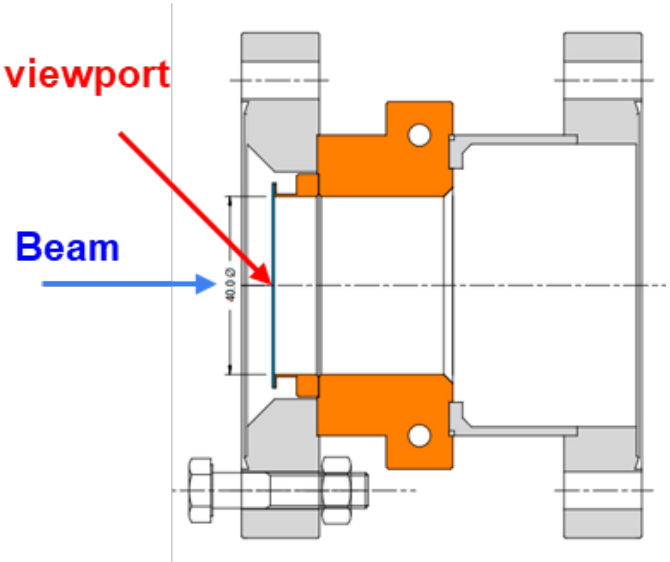
X-ray-induced fluorescence from the diamond is also used for beam-position and beam-footprint observation during commissioning and alignment. A dedicated optical viewport allows the illuminated region of the diamond to be observed using an external camera. A similar fluorescence-based observation method has been used at the PAL BL-6C beamline.

The configuration of the HEM diamond-window assembly is shown in <Figure 4.2.10.5>.

The main specifications of the diamond window are summarized in <Table 4.2.10.4>.



<Figure 4.2.10.4> Diamond-window beam observation at PAL BL-6C: (left) diamond-window assembly and (right) X-ray-induced fluorescence image.



<Figure 4.2.10.5> Configuration of the CVD diamond-window assembly for the BM10 HEM beamline.

<Table 4.2.10.4> Baseline design parameters of the CVD diamond window.

Parameter	Baseline design
Location from source	~13 m
Material	CVD diamond
Thickness	1.0 mm
Clear aperture	Ø40 mm
Accepted beam divergence	2.2 mrad (H) × 0.6 mrad (V)
Absorbed power	~150 W
Cooling	Active water cooling
Primary functions	Vacuum separation, low-energy attenuation, and beam observation

C Slit system

Two slit systems are used to control the white-beam aperture along the HEM photon transfer line. The White-Beam Slit, located in OH1 at approximately 26 m from the source, defines the accepted beam aperture before the energy-filter system and reduces unnecessary irradiation of downstream components. The current design employs a four-blade configuration to define the beam aperture in the horizontal and vertical directions; the mechanical design of the BM-type white beam slit is given in the white beam slit design report [12].

After propagation through the long vacuum transport section, the Exit Slit, located in OH2 at approximately 91.3 m, provides the final definition of the X-ray beam aperture before the experimental station.

The principal functions of the two slit systems are summarized in <Table 4.2.10.5>.

<Table 4.2.10.5> Main functions of the HEM white-beam and exit slit systems.

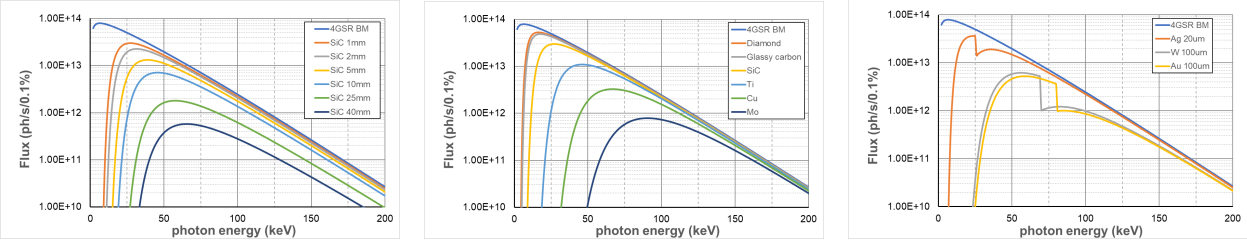
Parameter	White-Beam Slit	Exit Slit
Location	OH1	OH2
Distance from source	~26 m	~91.3 m
Primary function	Accepted beam-aperture definition	Final beam-aperture definition
Additional function	Reduction of unnecessary downstream irradiation	Control of beam aperture delivered toward the experimental station
Configuration	Four-blade slit	Four-blade slit

D Energy filters

The energy-filter system is installed in OH1 at approximately 27–28 m from the source to control the spectral distribution and intensity of the polychromatic white beam. The filters suppress low-energy photons, reduce downstream thermal load, and provide spectral shaping for different experimental conditions.

The transmitted intensity through a filter is described by the Beer–Lambert relation, where $\mu(E)$ is the energy-dependent linear attenuation coefficient and t is the filter thickness. The HEM filter system uses intensity attenuation, low-energy suppression, and K-edge filtering as the principal spectral-conditioning mechanisms.

The filter system is designed for an accepted beam divergence of 2.2 mrad (H)



<Figure 4.2.10.6> Principle of white-beam spectral conditioning using intensity attenuation, low-energy suppression, and K-edge filtering.

× 0.6 mrad (V). At approximately 27 m from the source, the corresponding beam size is approximately 59.4 × 16.2 mm^2. The calculated incident white-beam power is approximately 470 W before the 1.0-mm diamond window and approximately 320 W at the energy-filter system. These design conditions are summarized in <Table 4.2.10.6>.

<Table 4.2.10.6> Design conditions for the HEM energy-filter system.

Parameter	**Design condition**
Filter location	~27–28 m
Accepted beam divergence	2.2 mrad (H) × 0.6 mrad (V)
Beam size at 27 m	~59.4 × 16.2 mm^2
Incident power before diamond window	~470 W
Diamond-window thickness	1.0 mm
Incident power at energy-filter system	~320 W

Based on the thermal-design experience of the PLS-II BL-6C graphite filter, glassy carbon was selected as a primary filter material. Glassy carbon avoids pronounced crystalline diffraction while providing suitable attenuation and thermal characteristics. A conservative absorbed-power criterion of approximately 110 W was used for the initial filter-stage design.

The absorbed-power criteria used for staged glassy-carbon filtering are summarized in <Table 4.2.10.7>.

<Table 4.2.10.7> Absorbed-power design criteria for the glassy-carbon filter stages.

Glassy-carbon thickness (mm)	**Absorbed-power design criterion (W)**
0.5	12
1	25
2	46
4	81
6	110

These values represent design criteria for the staged filter configuration rather than intrinsic thermal limits of the material. Based on spectral and thermal-load calculations, the selected filter materials and thickness ranges are summarized in <Table 4.2.10.8>.

<Table 4.2.10.8> Selected filter materials and thickness ranges. The diamond window, marked *, is a fixed upstream element and is not a selectable filter.

Material	Thickness range (mm)	K-edge (keV)	Primary role
Diamond*	1.0	0.28	Initial spectral filtering
Glassy carbon	1–14	0.28	Primary low-energy filtering
SiC	0.5–40	–	Low-energy suppression
Ti	1–16	4.97	Spectral conditioning
Cu	1–10	8.98	Spectral conditioning
Mo	1–4	20.00	Higher-energy spectral conditioning
W	0.2–2	69.53	K-edge filtering
Au	0.2–0.4	80.72	K-edge filtering

To limit the absorbed power in strongly attenuating metallic filters, the system uses a multi-stage configuration. Glassy carbon and SiC are positioned upstream, while Ti, Cu, Mo, W, and Au are used after appropriate upstream filtering. Representative calculated spectral peak ranges are approximately 26–31 keV for GC, 30–70 keV for SiC, 63–94 keV for Ti, 73–119 keV for Cu, and 95–132 keV for Mo. W and Au provide additional spectral shaping around their K-edges.

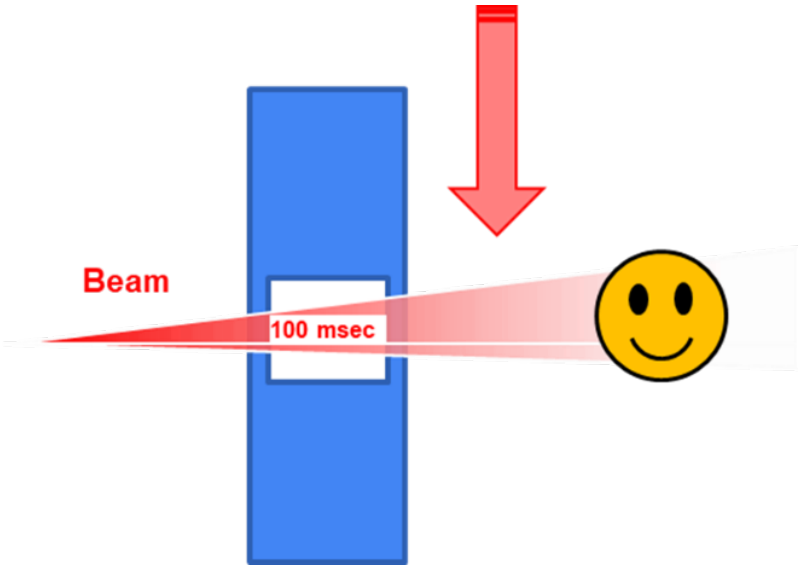
E Fast exposure shutter

A Fast Exposure Shutter (FES) is installed in OH1 at approximately 29.4 m from the source to reduce unnecessary white-beam exposure of the sample and detector during positioning, centering, and alignment. Unlike a conventional fast closing shutter used primarily for protection, the FES is intended for experimental exposure control and is normally maintained in the closed position.

When an X-ray image is required, the FES performs a short snapshot sequence:

$$\text{Closed} \rightarrow \text{Open} \rightarrow \text{Closed}$$

The baseline open duration is approximately 100 ms. During alignment, for example, individual images may be acquired at intervals of 10–20 s, while the shutter remains closed between exposures, thereby reducing accumulated white-beam irradiation.



<Figure 4.2.10.7> Conceptual operating sequence of the Fast Exposure Shutter.

At the FES position, the accepted beam divergence of 2.2 mrad (H) × 0.6 mrad (V) corresponds to a maximum beam size of approximately 64.7 × 17.6 mm^2. The maximum incident beam power is approximately 320 W, while the target beam power during normal FES operation is less than 100 W after appropriate upstream energy filtering. The shutter operates in vacuum and incorporates active water cooling for thermal management. The principal design parameters are summarized in <Table 4.2.10.9>.

<Table 4.2.10.9> Main design specifications of the HEM Fast Exposure Shutter.

Parameter	**Design specification**
Location	~29.4 m
Normal state	Closed
Operating sequence	Closed → Open → Closed
Snapshot open duration	~100 ms
Accepted beam divergence	2.2 × 0.6 mrad
Maximum beam size	~64.7 × 17.6 mm^2
Maximum incident beam power	~320 W
Target power during FES operation	<100 W
Cooling	Active water cooling
Operating environment	Vacuum

F Exit window

The exit window is installed at approximately 91 m from the source at the downstream end of OH2 and forms the final vacuum interface before the X-ray

beam enters the experimental hutch. Because of the long source-to-window distance and large beam acceptance, the window requires a large clear aperture while maintaining adequate X-ray transmission and mechanical reliability.

Aluminum (Al) was selected considering high-energy X-ray transmission, mechanical properties, manufacturability, maintainability, availability, and cost. The initial design considered a 1.0-mm-thick Al1050 window with a Ø260 mm circular aperture. Structural analysis, however, showed excessive stress and deformation because of the large unsupported area.

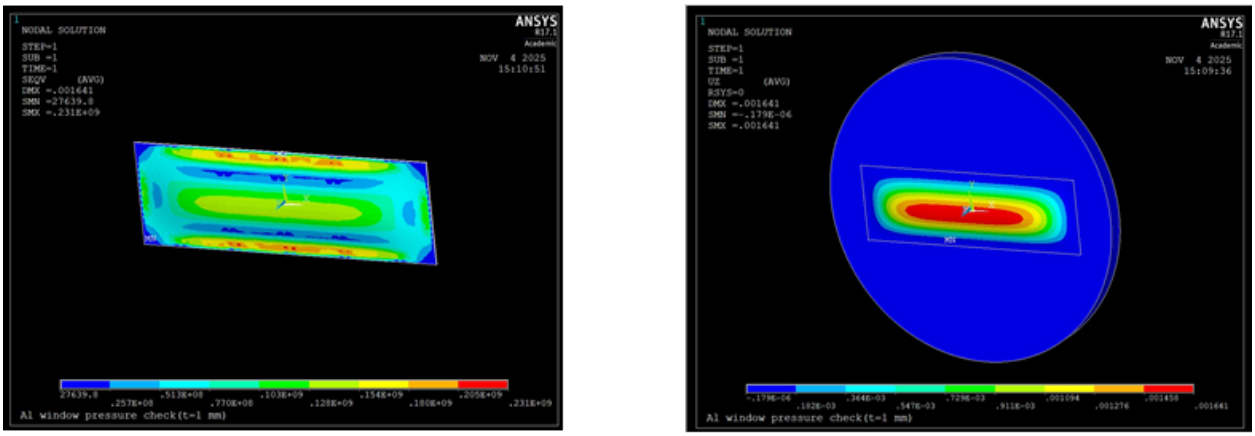
Since the X-ray beam has a strongly asymmetric horizontal-to-vertical aspect ratio, the window geometry was subsequently changed from a circular to a rectangular aperture to reduce the unsupported span while maintaining sufficient beam clearance. The principal structural-analysis results are summarized in <Table 4.2.10.10>.

<Table 4.2.10.10> Structural-analysis results for candidate exit-window geometries.

Aperture	**Thickness (mm)**	**Maximum stress**	**Maximum displacement (mm)**
Ø260 mm	1.0	~3.37 GPa	~41
Ø260 mm	1.5	~1.26 GPa	~15
260 × 80 mm²	1.0	~231 MPa	~1.64
240 × 70 mm²	1.0	~148 MPa	~0.91
220 × 65 mm²	1.0	~130 MPa	~0.68

The calculated beam size at the exit-window position is approximately 200.2 × 54.6 mm². A 220 × 65 mm² rectangular aperture therefore provides sufficient geometrical clearance while significantly reducing the structural load compared with the original circular design.

The current baseline is consequently a 1.0-mm-thick Al1050 window with a 220 × 65 mm² rectangular clear aperture. The calculated maximum stress is approximately 130 MPa, compared with a nominal yield strength of approximately 152 MPa for Al1050-H18. Because the resulting mechanical margin remains limited, the configuration is regarded as a baseline for further mechanical optimization and verification, rather than a fully validated final design.

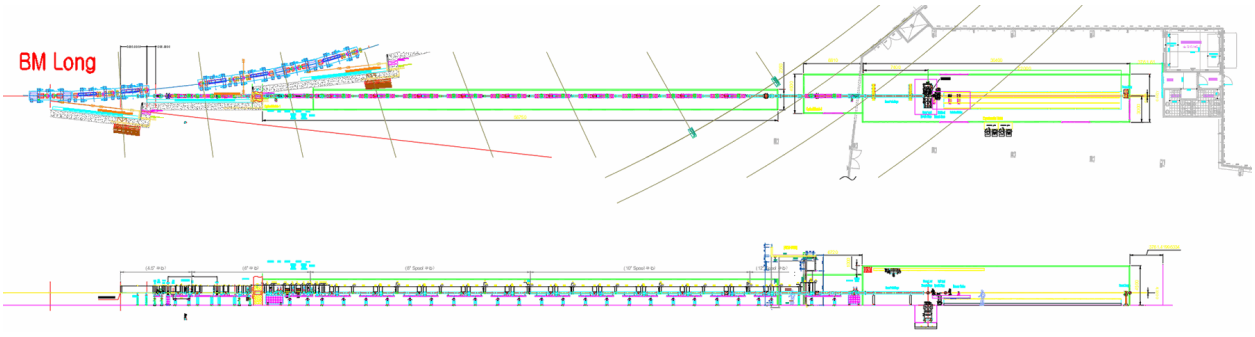


(1 mm equivalent stress) (1 mm Uz displacement)

<Figure 4.2.10.8> Structural analysis of the baseline rectangular Al exit window.

4.2.10.5 Photon Transfer Line

The photon transfer line (PTL) transports the high-energy white beam from the front end through OH1, the long vacuum transport section, and OH2 to the experimental hutch. The primary sample position is located approximately 100 m from the bending-magnet source in the satellite building. The long source-to-sample distance allows the naturally diverging bending-magnet beam to expand to the large field required for full-field imaging and provides the long propagation geometry required for projection and phase-contrast imaging.



<Figure 4.2.10.9> Layout of the BM10 High Energy Microscopy beamline from the storage-ring building to the satellite building, showing OH1, the long photon transfer line, OH2, and the experimental hutch.

The BM10 PTL is designed to transport the large white beam over the long propagation distance without focusing or beam-steering optics. Accordingly, the vacuum transport section uses an increasing clear aperture along the beam propagation direction to accommodate the expanding beam footprint.

The mechanical transport system supports and aligns the long vacuum section between OH1 and OH2 while maintaining sufficient beam clearance for the naturally expanding white beam. The long vacuum system provides the vacuum environment required for white-beam transport between OH1 and OH2. General vacuum requirements and common engineering standards are described in the separate Common Technical Sections document. The PTL passes through OH1 and OH2 before reaching the experimental hutch. OH1 contains the principal beam-conditioning components, while OH2 establishes the final beam aperture and vacuum interface before the beam enters the experimental region.

The detailed pump sizing, valve positions and gauge layout for the BM10 sectors are to be detailed in a later revision (TBD).

4.2.10.6 End-Station

The HEM end-station instruments provide high-energy X-ray imaging across a broad energy range with multiple modalities.

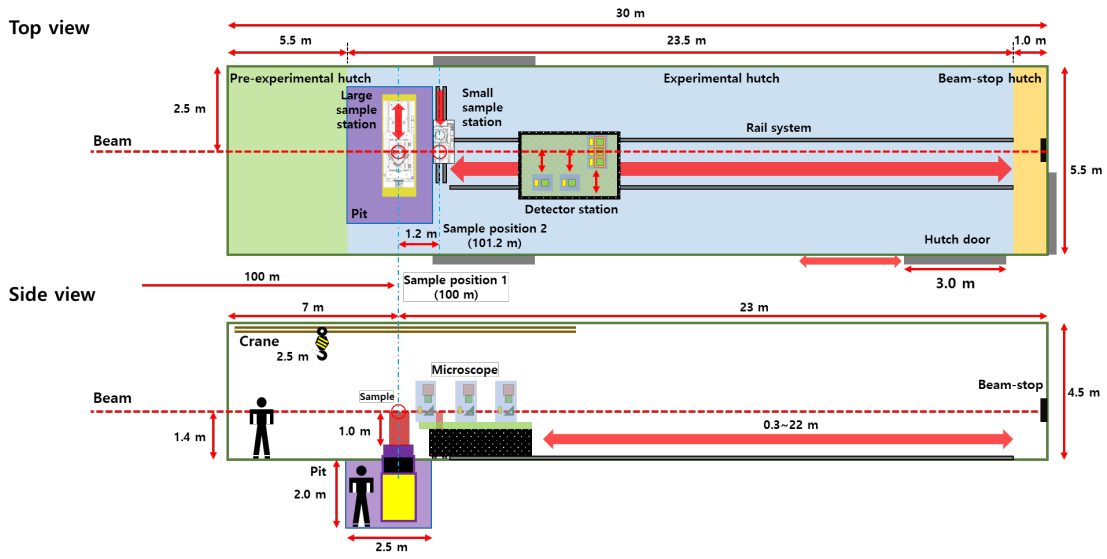
A Instrument Overview

The BM10 HEM end-station is designed to utilize the principal characteristics of the beamline: high-energy X-rays, a large beam field, and propagation-based phase-contrast imaging capability. It therefore supports a broad range of sample dimensions, weights, spatial resolutions, and imaging geometries rather than being optimized for a single experimental configuration.

The Experimental Hutch is located in a satellite building, allowing the primary sample position to be placed approximately 100 m from the source and providing sufficient space for large experimental equipment, heavy samples, in-situ environments, and extended detector travel.

The Experimental Hutch incorporates two complementary sample stations and a movable detector station. The heavy-load station is designed for large and heavy specimens and is installed in a 2-m-deep pit. The small-sample station supports higher-resolution imaging and precise positioning of smaller specimens. The detector station accommodates multiple imaging systems and provides variable sample-to-detector distance for absorption and propagation-based phase-contrast imaging.

The principal end-station instruments are summarized in <Table 4.2.10.11>.



<Figure 4.2.10.10> Conceptual layout of the BM10 HEM end-station, showing the heavy-load large-sample station, small-sample station, movable detector station, and beam stop.

<Table 4.2.10.11> Principal instrumentation of the BM10 HEM end-station.

Instrument	Primary function
Heavy-load sample station	Large/heavy samples and in-situ experiments
Small-sample station	High-resolution imaging of smaller specimens
X-ray imaging systems	Multi-scale projection imaging and CT
Detector positioning system	Variable SDD for absorption and PBI
Beam stop	Termination of transmitted X-ray beam

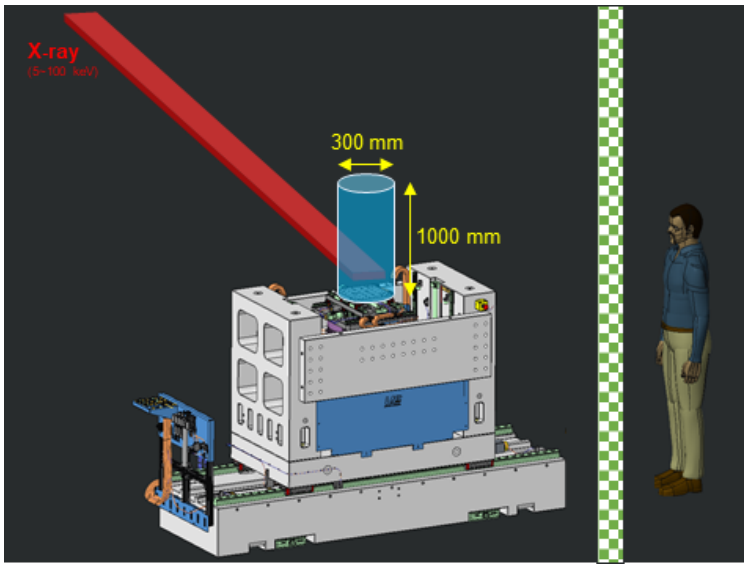
B Sample Positioning Systems

The HEM Experimental Hutch incorporates two complementary sample-positioning systems to accommodate a wide range of sample sizes and weights: a heavy-load sample stage for large and heavy specimens and a small-sample stage for high-resolution imaging of smaller specimens.

(a) Heavy-Load Sample Stage

The heavy-load sample stage is designed for high-energy X-ray CT of large specimens, including industrial components, energy devices, and in-situ experimental systems. The baseline design accommodates samples of approximately 100 kg, 1.0 m in height, and 0.3 m in diameter. The positioning system is installed in a 2-m-deep pit to accommodate the large positioning system while maintaining the sample at the required beam height. An RT500S rotation stage is used as the

principal CT rotation axis.



<Figure 4.2.10.11> Conceptual design of the HEM heavy-load sample positioning system installed in the experimental pit.

The baseline specifications of the heavy-load sample stage are given in <Table 4.2.10.12>.

<Table 4.2.10.12> Baseline specifications of the HEM heavy-load sample stage.

Parameter	Baseline specification
Sample weight	~100 kg
Maximum sample height	~1.0 m
Maximum sample diameter	~0.3 m
Rotation stage	RT500S
Angular accuracy	<2 arcsec
Maximum rotation speed	60 rpm
Installation	2-m-deep pit

(b) Small-Sample Stage

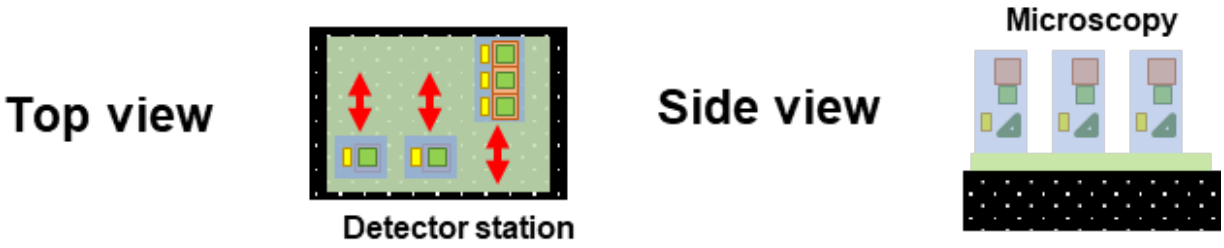
A dedicated small-sample stage is planned for high-resolution imaging and CT of smaller and lighter specimens. This system will complement the heavy-load stage by providing higher positioning precision and flexibility for small-sample experiments. The detailed configuration and technical specifications of the small-sample stage are currently under review and will be updated in a future revision.

C X-ray Imaging System

The HEM beamline is designed to provide multi-scale X-ray imaging over a wide range of fields of view and spatial resolutions. The imaging system combines high-resolution indirect X-ray microscopes with a complementary large-field-of-view detector system.

(a) X-ray Microscope

The X-ray microscope employs an indirect detection scheme consisting of a scintillator, mirror, objective lens, and optical detector. Incident X-rays are converted into visible light by the scintillator, and the optical image is magnified and recorded by the optical detector. For multi-scale imaging, the HEM beamline adopts a multiple-microscope switching concept. Microscope modules with different magnifications are independently configured and aligned, reducing the need for repeated optical realignment when changing the imaging scale.



<Figure 4.2.10.12> Conceptual configuration of the multiple X-ray microscope system for multi-scale imaging.

The baseline microscope configurations are listed in <Table 4.2.10.13>.

<Table 4.2.10.13> Baseline X-ray microscope configurations for multi-scale imaging.

Objective magnification	Field of view (mm^2)	Effective pixel size (μm)
0.5×	38 × 21	9.2
1×	19 × 11	4.6
2×	9.5 × 5.5	2.3
5×	3.8 × 2.1	0.92
10×	1.9 × 1.1	0.46

The effective pixel size represents the spatial sampling of the imaging system and does not directly correspond to spatial resolution. The actual resolution

depends on the scintillator, optical system, X-ray energy, and overall detector response.

(b) Radiation-Damage Considerations

Because the imaging system operates with a high-flux polychromatic X-ray beam, the microscope is designed with modularity and maintainability in mind. Radiation-sensitive components are designed to be accessible and replaceable, and the indirect detection geometry allows sensitive optical components to be positioned away from the direct X-ray beam where practical. Shielding will also be incorporated to reduce unnecessary radiation exposure.

(c) Large-Field-of-View Imaging System

A dedicated large-FOV detector will complement the X-ray microscopes for imaging large samples. The current target field of view is approximately 200 mm in the horizontal direction. Detector technology, final field of view, effective pixel size, acquisition speed, and detailed mechanical configuration remain under technical review.

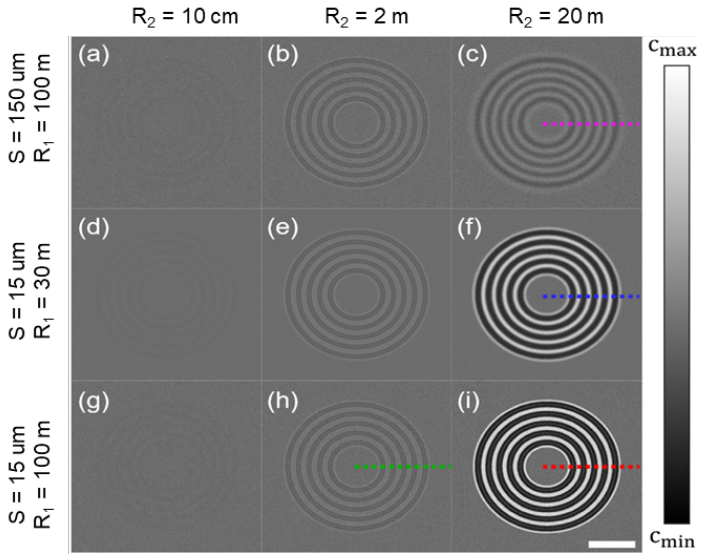
D Detector Positioning System

The HEM detector positioning system provides a variable sample-to-detector distance (SDD) for conventional absorption imaging and propagation-based phase-contrast imaging. The detector station moves along the beam direction using a rail-based positioning system, allowing the imaging geometry to be adjusted according to the sample, X-ray energy, spatial resolution, and required phase-contrast condition.

The SDD design range was investigated through numerical simulations of propagation-based phase contrast [3]. The simulations considered a silicon test structure and a polychromatic high-energy X-ray spectrum of approximately 70–200 keV, with detector distance R_2 varied from approximately 0.1 to 20 m.

For the HEM-like geometry with $R_1 \sim 100$ m, the simulations show increasingly pronounced phase-contrast features with increasing propagation distance under suitable spatial-coherence conditions. The results also demonstrate that source size and source-to-sample distance strongly influence phase-contrast visibility at long SDD.

Based on these results, a maximum SDD of approximately 20–22 m is consid-



<Figure 4.2.10.13> Simulated propagation-based phase-contrast images for different source-size, R_1, and R_2 conditions.

ered for the HEM end-station. The actual SDD is selected according to the X-ray spectrum, sample characteristics, detector performance, and required phase-contrast sensitivity.

E Data Acquisition and Image Reconstruction

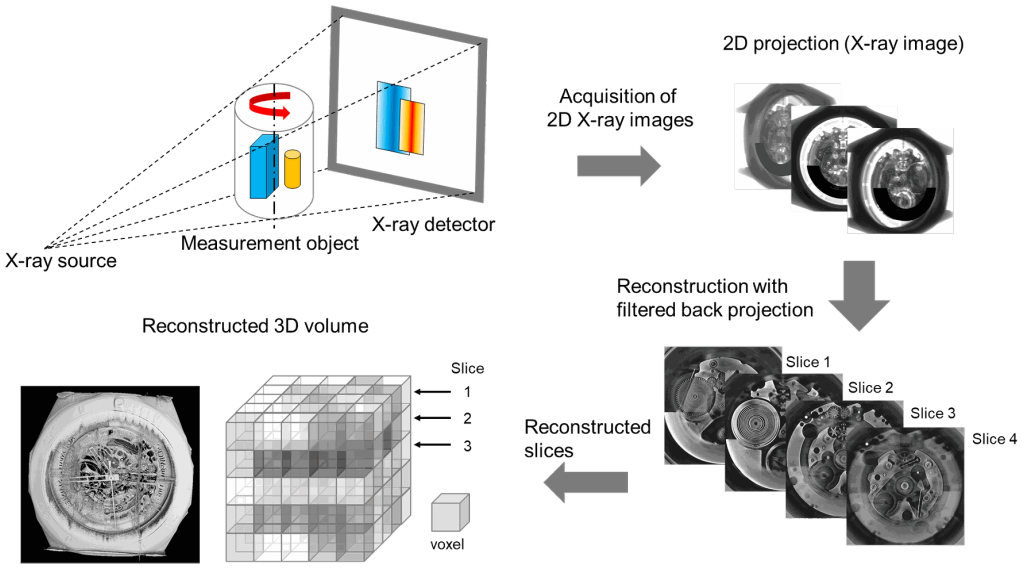
The HEM beamline is designed for high-throughput X-ray imaging and CT using a high-flux polychromatic synchrotron beam. The combination of large detector areas, short exposure times, and high acquisition rates requires a data system capable of coordinating detector acquisition, sample motion, beam exposure, high-speed data transfer, storage, and image reconstruction.

CT data processing follows the general workflow:

> Projection Acquisition → Detector Correction → Projection Preprocessing → Sinogram Generation → CT Reconstruction → 3D Visualization and Analysis

Dark- and flat-field normalization are applied as basic detector corrections, while defective-pixel correction, registration, and artifact correction can be applied as required. For propagation-based phase-contrast imaging, phase retrieval can additionally be performed before CT reconstruction.

A representative detector condition of approximately 18 MB/image at 20 images/s corresponds to a data rate of approximately 360 MB/s, or approximately



<Figure 4.2.10.14> Typical data-acquisition and image-processing workflow for the HEM beamline.

1.2 TB/h. Continuous operation under this reference condition would generate approximately 10 TB over 8 h. These values represent a reference scenario rather than the maximum performance of the HEM detector system. The data system requires high-throughput data transfer, temporary high-speed storage, data management, and computational resources for CT reconstruction and analysis. The corresponding estimate is summarized in <Table 4.2.10.14>.

<Table 4.2.10.14> Estimated data generation for a representative HEM imaging condition.

Parameter	Representative value
Data size	18 MB/image
Acquisition rate	20 images/s
Data-transfer rate	360 MB/s
Data volume	~1.2 TB/h
8-h data volume	~10 TB

References

[1] T. Connolley, C. M. Beavers, and P. Chater. “High-Energy Adventures at Diamond Light Source”. In: Synchrotron Radiation News 33.6 (2020), pp. 31–36.

[2] K. D. Liss and K. Chen. “Frontiers of synchrotron research in materials science”. In: MRS Bulletin 41 (2016), pp. 435–441.

[3] J. Kim et al. “Exploring high-energy X-ray phase-contrast microscopy at a diffraction-limited storage ring”. In: NDT & E International 155 (2025), p. 103395.

[4] K. Uesugi et al. “Large-Field X-ray Imaging at SPring-8 BL20B2”. In: Synchrotron Radiation News 28.5 (2015), pp. 30–35.

[5] P. Blažek et al. “Multiscale 3D Analysis of Defects and Temporal Development of Electrode Morphology in Lithium-Ion Batteries by X-Ray Computed Tomography”. In: ECS Transactions 105.1 (2021), pp. 69–76.

[6] S.-H. Yu et al. “Regulating Key Variables and Visualizing Lithium Dendrite Growth: An Operando X-ray Study”. In: Journal of the American Chemical Society 141.21 (2019), pp. 8441–8449.

[7] F. Marone, C. M. Schlepütz, S. Marti, et al. “Time Resolved in situ X-Ray Tomographic Microscopy Unraveling Dynamic Processes in Geologic Systems”. In: Frontiers in Earth Science 7 (2020), p. 346.

[8] P. Cloetens et al. “Hard x-ray phase imaging using simple propagation of a coherent synchrotron radiation beam”. In: Journal of Physics D: Applied Physics 32.10A (1999), A145–A151.

[9] R. Gradl et al. “Propagation-based Phase-Contrast X-ray Imaging at a Compact Light Source”. In: Scientific Reports 7 (2017), p. 4908.

[10] C. L. Walsh et al. “Imaging Intact Human Organs with Local Resolution of Cellular Structures Using Hierarchical Phase-Contrast Tomography”. In: Nature Methods 18.12 (2021), pp. 1532–1541.

[11] Jongha Park et al. High Heat Load Front-End Mechanical Design and Thermal Analysis Report. Internal Document PAL-INT/ME-2026-003. Pohang Accelerator Laboratory, June 2026.

[12] Jongha Park and Youngduk Yun. White Beam Slit Design Report. Internal Document PAL-INT/ME-2026-004. Pohang Accelerator Laboratory, June 2026.